



**FRIEDRICH-SCHILLER-
UNIVERSITÄT
JENA**

Positional disorder in Huygens' metasurfaces

Dissertation
for the achievement of the academic title
doctor rerum naturalium (Dr. rer. nat.)

submitted to the council of the
Faculty of Physics and Astronomy
of the
Friedrich Schiller University Jena

by Master of Science (M.Sc.) Dennis Arslan
born on 13.06.1989 in Burghausen, Germany

Referees:

1. Prof. Dr. Isabelle Staude
Friedrich Schiller University Jena, Germany
2. Prof. Dr. Georg von Freymann
TU Kaiserslautern, Germany
3. Prof. Dr. Albert Polman
University of Amsterdam, The Netherlands

Date of the disputation:

01.12.2022

Declaration of Academic Integrity

Ehrenwörtliche Erklärung

English

Please refer to the German declaration below.

Deutsch

Ich erkläre hiermit ehrenwörtlich, dass ich die vorliegende Arbeit selbständig, ohne unzulässige Hilfe Dritter und ohne Benutzung anderer als der angegebenen Hilfsmittel und Literatur angefertigt habe. Die aus anderen Quellen direkt oder indirekt übernommenen Daten und Konzepte sind unter Angabe der Quelle gekennzeichnet.

Bei der Auswahl und Auswertung folgenden Materials haben mir die nachstehend aufgeführten Personen in der jeweils beschriebenen Weise unentgeltlich geholfen:

1. Prof. Dr. Isabelle Staude betreute die gesamte Promotion.
2. Stefan Fasold und Katsuya Tanaka waren hauptverantwortlich für die Herstellung der in den experimentellen Studien verwendeten Proben.
3. Aso Rahimzadegan führte alle die auf der T-Matrix Methode basierenden elektromagnetischen Simulationen durch.
4. Matthias Falkner maß Phasenspektren mittels eines von ihm aufgebauten Fourier-Transformations-Interferometers. Wenjia Zhou und Maria Kroychuk halfen mir beim Aufbau des von mir betreuten Phasenschieber-Interferometers und bei der Messung entsprechender Phasenprofile.

Weitere Personen waren an der inhaltlich-materiellen Erstellung der vorliegenden Arbeit nicht beteiligt. Insbesondere habe ich hierfür nicht die entgeltliche Hilfe von Vermittlungs- bzw. Beratungsdiensten (Promotionsberater oder andere Personen) in Anspruch genommen. Niemand hat von mir unmittelbar oder mittelbar geldwerte Leistungen für Arbeiten erhalten, die im Zusammenhang mit dem Inhalt der vorgelegten Dissertation stehen.

Die Arbeit wurde bisher weder im In- noch im Ausland in gleicher oder ähnlicher Form einer anderen Prüfungsbehörde vorgelegt.

Die geltende Promotionsordnung der Physikalisch-Astronomischen Fakultät ist mir bekannt.

Ich versichere ehrenwörtlich, dass ich nach bestem Wissen die reine Wahrheit gesagt und nichts verschwiegen habe.

Jena, 30.06.2022

Dennis Arslan

Abstract

Kurzfassung

English

The primary goal of this thesis was the experimental exploration of certain linear optical properties of positionally disordered Huygens' metasurfaces, which consist of two-dimensional arrangements of specific scattering particles. This goal has been motivated by two recent trends: On the one hand, dielectric Huygens' metasurfaces have proved to be a suitable material platform for holographic and wavefront-shaping applications, and on the other hand, structurally disordered metamaterials have already exhibited features that cannot be attained with ordered structures. However, the influence of positional disorder on Huygens' metasurfaces has not yet been systematically studied, and it thus remained the question if and how Huygens' metasurfaces could benefit from positional disorder.

This thesis characterizes the directional transmission and reflection of positionally disordered Huygens' metasurfaces both experimentally and numerically, provides a simple theoretical model that explains the observation of a disorder-induced phase transition on the basis of effective multipole moments, and confirms that positional disorder is indeed a valuable degree of freedom in the design of holographic and wavefront-shaping devices. Based on these findings, future research may investigate how the directional transmission and reflection of positionally disordered Huygens' metasurfaces can be tailored via their particle arrangements and/or higher multipole moments.

Deutsch

Das Hauptziel dieser Arbeit war die experimentelle Untersuchung bestimmter linearer optischer Eigenschaften positionell ungeordneter Huygens-Metaoberflächen – das sind zweidimensionale Anordnungen spezieller Streupartikel. Dieses Ziel wurde durch zwei aktuelle Forschungstrends motiviert: Einerseits haben sich dielektrische Huygens-Metaoberflächen als eine geeignete Materialplattform für holografische und wellenfrontformende Anwendungen erwiesen, und andererseits wurde bereits gezeigt, dass strukturell ungeordnete Metamaterialien Eigenschaften besitzen, die mit geordneten Strukturen nicht zu erreichen sind. Der Einfluss positioneller Unordnung auf Huygens-Metaoberflächen wurde jedoch noch nicht systematisch untersucht und es verblieb daher die Frage, ob und wie Huygens-Metaoberflächen von positioneller Unordnung profitieren könnten.

In dieser Arbeit wird die gerichtete Transmission und Reflexion positionell ungeordneter Huygens-Metaoberflächen sowohl experimentell als auch numerisch charakterisiert, es wird ein einfaches theoretisches Modell vorgestellt, welches die Beobachtung eines durch Unordnung induzierten Phasenübergangs auf der Grundlage effektiver Multipolmomente erklärt, und es wird bestätigt, dass positionelle Unordnung tatsächlich ein wertvoller Freiheitsgrad in der Gestaltung holografischer und wellenfrontformender Bauelemente ist. Auf diesen Erkenntnissen aufbauend könnte in Zukunft erforscht werden, wie die gerichtete Transmission und Reflexion positionell ungeordneter Huygens-Metaoberflächen über deren Partikelanordnungen und/oder höheren Multipolmomente maßgeschneidert werden kann.

Contents

Declaration of Academic Integrity (Ehrenwörtliche Erklärung)	iii
Abstract (Kurzfassung)	v
1. Introduction	1
2. State of the Art and Motivation	5
2.1. Optical metasurfaces	5
2.2. Towards perfect optical diffusers	9
2.3. Towards disordered metasurface holograms	11
3. Fundamentals of Wave Optics	15
3.1. Fourier transformations	15
3.2. Maxwell's equations	16
3.3. Vector wave equation	17
3.4. Plane vector wave functions	19
3.4.1. Plane wave expansion	20
3.4.2. Area-averaged radiance	21
3.4.3. Directional scatterance	22
3.4.4. Generalized transmission coefficient	23
3.5. Spherical vector wave functions	24
3.5.1. Orthogonality conditions	25
3.5.2. Multipole expansion and scattered field formalism	25
4. Particle Statistics	29
4.1. Structure factor and pair correlation function	29
4.2. Collective coordinate method	30
4.3. Matérn-type distributions	33
5. Simulation Methods	35
5.1. Electromagnetic field solvers	35
5.2. Band-limited angular spectrum method	36
5.3. Iterative Fourier transform algorithm	38
6. Experimental Methods	43
6.1. Fabrication of dielectric metasurfaces	43
6.2. Back-focal-plane imaging	43
6.3. White-light spectroscopy	44
6.4. Phase-shifting interferometry	44
7. Optical Properties of Positionally Disordered Huygens' Metasurfaces	47
7.1. Fundamentals of ordered Huygens' metasurfaces	47
7.2. Design of metasurface types and resonance cases	51
7.3. Zeroth-order transmission and reflection	51
7.3.1. Spectra for oblique incidence	53
7.3.2. Spectra for normal incidence	55
7.3.3. Spatial statistics for normal incidence	57
7.4. Directional scatterance	59
7.4.1. Simulated results	61
7.4.2. Experimental results	63

8. Holograms Based on Positionally Disordered Huygens' Metasurfaces	65
8.1. Design strategies	65
8.2. Experimental results	69
9. Conclusion and Outlook	71
A. Definitions and Derivations	73
A.1. Directional scatterance of ideal scatterers	73
A.2. Spherical vector wave functions	73
A.3. Radial structure factor and pair correlation function	76
A.4. Probability density functions	77
A.5. Disordered Huygens' metasurfaces	78
B. Numerical Methods	81
B.1. Computation of spherical Bessel functions	81
B.2. Computation of associated Legendre polynomials	82
B.3. Simulation of planar multilayer systems	82
B.4. Algorithmic determination of diffraction orders	85
B.5. Computation of structure factor and pair correlation function	88
C. Supplementary Data	91
List of Publications	95
Bibliography	97

1. Introduction

Das Gewebe dieser Welt ist aus Notwendigkeit und Zufall gebildet; die Vernunft des Menschen stellt sich zwischen beide und weiß sie zu beherrschen; sie behandelt das Notwendige als den Grund ihres Daseins; das Zufällige weiß sie zu lenken, zu leiten und zu nutzen ...

The fabric of our life is formed of necessity and chance; the reason of man takes its station between them, and may rule them both: it treats the necessary as the groundwork of its being; the accidental it can direct and guide and employ for its own purposes ...

— J. W. von Goethe, *Wilhelm Meister's Apprenticeship*, Book I, Chapter XVII

The desire to control fate, chance, or randomness seems to be a recurrent theme in human history. However, it was not until the early 20th century that physicists started to understand and manipulate the complex atomic structure of condensed matter; which precluded fundamental investigations on the molecular structure of liquids, amorphous semiconductors, polymer solutions, disordered alloys, and various other disordered media that have led to countless achievements in chemistry and physics [1]. The propagation of classical or even quantum mechanical waves through disordered media is here of particular interest due to its immense significance for modern electronic and photonic systems [2]. Moreover, given the omnipresence of disordered structures in nature, it may not come as a surprise that recent breakthroughs have rekindled the interest in this rich and multidisciplinary subject [3, 4], and reawakened the desire to direct, guide and employ *the accidental* to the benefit of our intellectual and technological advance.

In this thesis, it is studied how light behaves, and how it can be manipulated, when it passes through a two-dimensional arrangement of specific nanoparticles with tailored positional disorder, a so-called Huygens' metasurface. The following paragraphs clarify the terminology, reflect on the current state of the art, and outline the scope of this work.

In everyday language, *disorder* often carries a negative connotation and refers to a dysfunctional or abnormal state, which is why in physics and mathematics, one usually finds less judgmental synonyms such as entropy (thermodynamics), randomness (statistics), or chaos (chaos theory). However, entropy may be understood more accurately as a measure for the dispersion or diffusion of energy or information, in randomness resonates the complete unpredictability of certain quantum mechanical processes that lie at the very heart of our current understanding of reality, and chaos originally symbolized a metaphysical primordial void rather than a complex system. Most importantly, though, neither of these synonyms conveys a nuance that *disorder* does in its most unbiased sense: The prefix *dis-* indicates the removal or reversal of *order*. Intuitively, one may associate *order* with a highly regular structure such as a honeycomb or a snowflake, but already in this example, one may wonder whether a honeycomb is more ordered than a snowflake, or how they compare to the pattern formed by rice spilled on the floor. Hence, disorder not only represents the complete absence of order, but also embodies a continuum of states with different *degrees of disorder*. In the case of the spilled rice, one may further distinguish between irregularities in the size, shape, orientation, or position of each kernel, where the latter is referred to as *positional disorder*. Nevertheless, it remains the question of how to exactly define what an ordered structure is and how to measure the degree by which another structure deviates from it. Unfortunately, since there exists no universally applicable scalar order metric [5], such definitions are inherently subjective and specific to the problem at hand, but by the same token, this also allows one to define the degree of disorder as a posterior measure: When an electromagnetic wave propagates through a disordered structure, it can be more meaningful to evaluate a property of the electromagnetic wave after it has interacted with the disordered structure, as for example the transmission coefficient, than to merely quantify the spatial configuration of the structure. Note that such posterior measures are, more often than not, surjective maps, which means that structures with distinct positional disorder can yield the same optical response. This circumstance presents new degrees of freedom in the deliberate design of disordered structures with prescribed optical responses.

Optical *metamaterials* are synthetic structures with unique physical properties that are usually not found in nature; they consist of three-dimensional arrangements of scattering particles with sizes comparable to the operation wavelength, where the exact size, shape, orientation, position and refractive index of each particle is dictated by the intended functionality [6]. Optical *metasurfaces* are a subclass of metamaterials where the particles are confined to two dimensions, which means to a flat or possibly curved surface. The practical realization of such metamaterials is certainly limited by the available fabrication techniques and natural materials, but due to recent advances in the fabrication of nanoscale structures [7–11], it has already become possible to manipulate light in ways that cannot be achieved with conventional optical elements [12–16].

The natural materials used in a metamaterial generally depend on the application: If the goal is to sense a biological or chemical compound at the surface of a detector, it can be advantageous to use a plasmonic material, as for example a noble metal or graphene, due to its ability to strongly confine light to its surface [17–19]. However, since the high intrinsic absorption losses in plasmonic materials drastically limit the energy efficiency of the resulting metamaterial, which is particularly undesirable in wavefront-shaping applications, current research has recently shifted its focus towards dielectric and semiconductor materials [20].

With the advent of dielectric nanoparticles in metasurfaces, it has become possible to resonantly excite and to selectively tune certain radiative electromagnetic modes, which form an orthogonal set of multipolar basis functions, within the volume of a nanoparticle [21]. This allows one to tune not only the radiation strength of each multipolar order via the size, shape, and refractive index of an individual nanoparticle, but also the electromagnetic coupling strength of neighboring nanoparticles via their spatial arrangement. More precisely, it is the complex interference of the electromagnetic fields radiated by each multipolar order and each nanoparticle that allows one to manipulate the amplitude, phase, polarization and spectrum of an electromagnetic wave as it passes through the metasurface. Moreover, when a carefully balanced combination of these multipolar orders is excited within each nanoparticle, so-called *Huygens sources* can be formed, and the metasurface gains the ability to completely suppress the backscattering of the incident wave [22]. This property makes dielectric *Huygens' metasurfaces* an auspicious material platform for holographic and wavefront-shaping applications [23, 24].

Recently, and quite to the contrary of the long-standing belief that disorder is generally detrimental to the performance of a system, it has been demonstrated that a disordered metamaterial can produce a sharper focal spot than a conventional lens [25], that it can enhance the volume and numerical aperture of holographic displays [26], and that disordered metasurfaces not only inherit these properties but also prove suitable for wavefront-shaping applications [27]. This development strongly suggests that the introduction of positional disorder in Huygens' metasurfaces may not only offer new degrees of freedom in the design of such metasurfaces, but could also reveal novel physical effects and properties that arise from the complex interplay of the excited multipolar orders.

The primary goal of this thesis was the experimental exploration of linear optical properties of positionally disordered Huygens' metasurfaces. Aso Rahimzadegan supported this pursuit on theoretical grounds by conducting multipolar analyses of the studied metasurfaces [28]. Additionally, based on the fundamental discoveries made in the course of this work, two hypotheses with high technological significance were identified and experimentally confirmed:

1. Disordered Huygens' metasurfaces can operate as a perfect optical diffuser at one wavelength and as a transparent window at another. This wavelength-selective functionality may find application in augmented reality displays or multi-functional wavefront-shaping devices.
2. Disordered Huygens' metasurfaces are not only suitable for wavefront shaping, but also for holographic applications. The new degrees of freedom introduced by positional disorder permit the use of identical nanoparticle geometries, which in turn allows for simpler and less error-prone fabrication protocols, or even self-assembly strategies.

Lastly, these objectives required the modification or extension of several numerical methods, and the construction of customized experimental setups.

This thesis is organized as follows:

Chapter 2 provides a much broader overview of the current state of the art and motivates the research goals of this thesis on the basis of important application scenarios.

Chapter 3 presents elementary concepts of modern wave optics, and the notations and conventions used within this thesis, where great importance was placed on the comprehensible derivation of all key aspects from first principles.

Note that the citations in the beginning of each passage generally also apply to the subsequent discussions, and that the presented notations and conventions occasionally deviate from the cited sources. Moreover, the results related to Eqs. (3.43,57,71) are not discussed in the cited sources, were not found in similar literature, and might thus represent novel contributions. Lastly, Secs. 3.4.2–4 introduce concepts that were developed in the course of this thesis, as for example the *directional scatterance*, which is a hypernym for *directional transmittance* and *directional reflectance* and establishes a connection between radiometric quantities and plane wave expansions. This connection was found independently and unknowingly of [29], where such a relationship had already been derived, but in a less general and less rigorous manner that further failed to explain why a plane wave expansion cannot provide a position-dependent radiance.

Chapter 4 first briefly describes certain statistical quantities that are known from statistical mechanics, and then presents two standard methods capable of generating random particle distributions with prescribed statistics. These methods were extended or generalized as to meet additional requirements imposed by the metasurfaces studied in this thesis.

Chapter 5 presents all numerical methods that were used for the simulation of electromagnetic fields. In particular, Secs. 5.2,3 describe two standard methods that were modified or extended in ways that are advantageous for the accurate design of holographic devices.

Chapter 6 provides details on the fabrication of all presented metasurfaces, and on the measurement techniques and setups that were involved in the experiments.

Chapter 7 discusses the optical properties of positionally disordered Huygens' metasurfaces on the basis of comprehensive experimental and numerical data. This data has already been published and concerns the optical properties of ordered Huygens' metasurfaces under oblique incidence [30], the observation of a disorder-induced phase transition in Huygens' metasurfaces [31], and an extensive study of the directional scatterance in positionally disordered Huygens' metasurfaces with the focus on their application as optical diffusers [32].

Chapter 8 presents previously unpublished work that experimentally demonstrates the suitability of positionally disordered Huygens' metasurfaces for holographic applications.

Chapter 9 summarizes this thesis and provides an outlook on future research possibilities that exceeded the scope of this thesis.

Appendix A provides additional definitions and derivations that support Chapters 3 and 7.

Appendix B presents auxiliary numerical methods and considerations.

Appendix C contains supplementary data.

2. State of the Art and Motivation

2.1. Optical metasurfaces

Optical metasurfaces are two-dimensional arrangements of scattering particles with sizes comparable to the operation wavelength [6]. The majority of metasurfaces is operated within or close to the domain of *Mie scattering*, where the particle size and the refractive index contrast with respect to the embedding medium is just about right to allow for the efficient excitation of resonant electromagnetic modes within the particles [33]. However, metasurfaces also reach into the domain of *Rayleigh scattering*, where the particles are so small that their optical response can be modeled in terms of a simple effective medium [6], and touch upon the domain of *geometric scattering*, where the particle size is so large that the scattering is dominated by diffraction or even refraction [34]. Moreover, the inter-particle distance must be comparable to the particle size and not larger than the wavelength in the embedding medium. The former ensures that all of the incident light is scattered and therefore modulated as intended, whereas the latter avoids the excitation of higher diffraction orders in ordered particle arrangements [35]. These requirements distinguish metasurfaces from diffractive optical elements, but since metasurfaces often make use of diffraction and exhibit higher diffraction orders for larger incidence angles, while some diffractive optical elements are based on subwavelength structures [36], a clear distinction can sometimes be difficult.

Mie scattering is named after Gustav Mie, who analytically described how an electromagnetic wave scatters off a homogeneous sphere [37]. This description relies on the expansion of electromagnetic waves in terms of *vector spherical harmonics*, which form an orthogonal set of multipolar basis functions that solve the vector wave equation in spherical coordinates [38]. Resonant electromagnetic excitations of particles that are expressed in terms of such vector spherical harmonics are thus often called *Mie resonances* or *multipole resonances*. In recent years, this formalism has been generalized and developed into the *T-matrix method*, which is currently one of the most powerful methods for the rigorous simulation of electromagnetic scattering in large clusters of arbitrarily shaped particles [39]. The semi-analytical nature of the T-matrix method makes it not only a powerful simulation tool, but also enables theoretical investigations of particle-particle interactions in ordered and disordered arrangements of non-spherical particles. Moreover, since effective media models can be based on the same mathematical framework [40, 41], it usually suffices to discuss optical metasurfaces in the broader context of multipole resonances.

The multipole resonances of an individual particle possess several properties that can be utilized. On the one hand, they exhibit a spectral response that typically resembles that of a Lorentz oscillator [42]. As the wavelength of the incident wave is tuned across the bandwidth of a multipole resonance, both the amplitude and phase of the scattered wave are modulated. This allows for spectral multiplexing or the realization of arbitrary phase shifts at a fixed wavelength. On the other hand, each multipolar order possesses a distinct farfield radiation pattern, which means a very specific directional amplitude, phase, and polarization. Since the scattered wave of a particle is formed by the superposition of all of its multipolar orders, it is possible to shape virtually all directional properties of an electromagnetic wave already on the level of an individual particle. While these properties can be tuned via the particle geometry and refractive index, practical limitations in the available fabrication processes and natural materials generally render only the lowest multipolar orders accessible [43, 44]. Nevertheless, as more particles are added to a metasurface, the complex interference of the electromagnetic fields radiated by each multipolar order and each particle, as well as the intricate electromagnetic particle-particle interactions, provide a great wealth of additional degrees of freedom.

Hence, by using different particle geometries and/or locally different particle arrangements, it is possible to imprint a position-dependent amplitude and phase modulation onto a metasurface. This ultimately combines diffraction-based wavefront-shaping capabilities, as known from diffractive optical elements, with resonant multipolar features [45].

Phase-shifting mechanisms

Resonant metasurfaces are operated within the domain of Mie scattering, where the wavelength-dependent optical response of selected multipolar orders is explicitly made use of. However, since an individual multipole resonance only yields a maximum phase shift of π [22, 46, 47], it is necessary to combine at least two multipole resonances or to introduce an additional phase-shifting mechanism as to obtain full phase coverage [44]. The former approach is usually more appealing, since it often only requires a simple optimization of the particle geometry.

Huygens' metasurfaces, for example, utilize particles with carefully balanced, spectrally overlapping, electric and magnetic dipole resonances to completely suppress backscattering. When such particles are arranged in an array, the transmittance is maximized and the phase covers nearly 2π as the wavelength is tuned across the bandwidth of the dipole resonances [22]. Consequently, Huygens' metasurfaces are interesting for applications that require very high transmission efficiencies. Moreover, since such particles are typically much wider than tall, they are relatively easy to fabricate and to integrate in fibers [48, 49], on-chip photonic devices [50, 51], or multilayer structures [52, 53]. However, since resonantly excited particles are strong scatterers, the electromagnetic inter-particle coupling must be taken into account during the design process. While this is trivial for an infinitely extended array of identical particles, which can be simulated very efficiently with periodic boundary conditions, a large-scale non-periodic metasurface would need to be simulated as a whole. Therefore, current design approaches typically subdivide a large metasurface into smaller pixels, where each pixel is filled with a truncated array of identical particles, but the optical properties of each pixel are still based on simulations of infinite arrays [23, 24]. The idea of this approach is that if sufficiently many particles are contained within each pixel, they can overcome the neglected coupling effects near the pixel boundaries and yield a collective response that is close to that of an infinite array. However, this approach is clearly not suitable for high-performance devices, both due to the neglected coupling effects and the relatively large required pixel sizes of up to 10 times the wavelength of operation.

Positional disorder could mitigate or even resolve this issue: On the one hand, positional disorder could break the strong coupling across pixel boundaries and thus allow for smaller pixel sizes. On the other hand, instead of a subdivision into pixels, one could consider that each particle possesses a local neighborhood with a radius that roughly corresponds to the interaction distance of a particle. Judging from the required pixel sizes of the previously mentioned approach, this interaction distance is likely only slightly larger than the operation wavelength. Hence, each particle could be assigned an effective optical response that depends on the statistical distribution of its local neighbors. Moreover, since different particle arrangements can yield the same optical response, this spatial degree of freedom should allow one to find suitable particle arrangements in regions where the neighborhoods overlap.

Non-resonant metasurfaces operate in the domain of Rayleigh scattering, where the resonance wavelength of each multipole is much smaller than the operation wavelength. In this limit, the particles can usually be treated as an effective medium with an effective refractive index that depends on the volume filling fraction [6]. Hence, the phase of an incident wave can be modulated via position-dependent optical path length differences, and the resulting optical response is very broadband as it only depends on the dispersion of the effective refractive index.

Bordering on the domain of Mie scattering, one finds particles with a very small lateral cross section and a comparatively large height [54]. These *nanowaveguides* are usually more difficult to fabricate than typical Huygens' particles, but their subwavelength lateral cross section allows for a simpler design process: The metasurface can be divided into a regular array of pixels, where each pixel contains only one specific nanowaveguide. Then, if the incident wavefront and the desired spatial phase modulation vary slowly across the width of a nanowaveguide, it generally suffices to simulate the optical response of an infinite array of a given nanowaveguide, and to use this result for the corresponding pixel. Consequently, each pixel can be designed almost independently and with relatively little numerical effort. While some authors perceive this as a fundamental advantage over Huygens' metasurfaces in beam-shaping applications [54], it has not yet been discussed nor demonstrated how positional disorder could enable a truly subwavelength phase control in Huygens' metasurfaces.

The *Pancharatnam-Berry phase*, also known as *geometric phase*, is a residual phase shift that originates from the cyclic evolution of a polarization state, and relates to the concept of parallel transport in differential geometry [55, 56]. More precisely, if the polarization state of an electromagnetic wave is changed along a closed trajectory on the Poincaré sphere, the wave will return to its initial polarization state, but also obtain a phase shift that equals one half of the solid angle enclosed by the trajectory. In practice, the generation of a position-dependent phase shift requires a fixed incident polarization, anisotropic or birefringent nanoparticles, and a position-dependent in-plane rotation of the nanoparticle anisotropy with respect to the incident polarization [35, 57]. Since the Pancharatnam-Berry phase is a purely geometrical effect, it classifies as a non-resonant phase-shifting mechanism. However, it can also be used in resonant metasurfaces, where it may provide an additional position-dependent but wavelength-independent phase bias.

Natural materials

Plasmonic metasurfaces contain conducting particles that support localized surface plasmon resonances, which are coherent free-space excitations of surface waves that couple to the collective motion of the conductor's free electrons [58]. On the one hand, such resonances produce strong electromagnetic field enhancements that are tightly confined to the surface of the particle. On the other hand, the rapid phase shift near the plasmon resonance frequency allows one to tune both the spatial and the spectral dispersion of the metasurface. While plasmonic materials may be an ideal choice for applications that benefit from the enhanced light-matter interaction close to the particle's surface, as for example for biosensing or nonlinear light generation [17, 59], they may be less so for wavefront shaping, where the high intrinsic absorption losses near the plasmon resonance severely limit the energy efficiency. Moreover, since spherical plasmonic particles do not exhibit significant magnetic multipole resonances [6], more complicated particle geometries are required to obtain plasmonic Huygens' metasurfaces [60]. Consequently, many plasmonic metasurfaces rather rely on the Pancharatnam-Berry phase to obtain full phase coverage [35, 61].

Dielectric metasurfaces contain dielectric or semiconducting particles. Contrary to plasmonic particles, dielectric particles not only minimize absorption losses, but also support electric and magnetic multipolar modes that are localized within the particles' volume. Recently, silicon particles embedded in silicon dioxide have become a popular choice for applications in the near-infrared spectral range [20, 21], and with the rapid technological progress in the fabrication of semiconductor devices, silicon-based metasurfaces have already started to enter integrated photonic circuits [62, 63].

More recently, research has also started to investigate resonantly excited dielectric particles for their use in nonlinear or reconfigurable optical devices [64]. These applications benefit from the strong electromagnetic field enhancement within such particles (strong light-matter interaction), the subwavelength thickness of the resulting metasurface (relaxed phase-matching conditions), and the ability to tune the multipole resonances not only via the particle geometry and material, but also the surrounding material. Based on these aspects, a great number of metasurfaces have already been reported with astounding *nonlinear* [65–67], *light-emitting* [68–71], or *tunable* [72–75] properties.

From ordered to disordered Huygens' metasurfaces

So far, the majority of reported optical metasurfaces have used ordered particle arrangements as their fundamental building blocks [76–78]. In the case of non-resonant metasurfaces, it seems that the introduction of positional disorder is neither needed, since disorder in the particle size or shape provides essentially the same control over the effective refractive index as a variation in the local particle density, nor desired, as it would only complicate the simple design approach.

In the case of resonant metasurfaces, however, it seems that the spatial degrees of freedom presented by positional disorder have been widely overlooked so far. One reason for this could be the high computational complexity that comes with positional disorder: While the periodic boundary conditions in arrays of identical particles greatly simplify numerical simulations, and even facilitate the analytical investigation and design of lattice coupling coefficients [79], positionally disordered arrangements of

resonant particles require the position-dependent inter-particle coupling to be fully taken into account. Although the T-matrix method is currently the most suitable tool for this problem, it still requires a great amount of expertise and computational power to simulate hundreds of multipolar particles. Considering that it is already possible to fabricate metasurfaces containing millions of particles, one currently faces the need to spatially discretize large metasurfaces in some smart way.

Ordered Huygens' metasurfaces that are based on a regular grid of pixels, where each pixel is filled with a truncated array of particles, follow a simplistic design idea: Each pixel represents a spatially-invariant transmission coefficient and transmits exclusively along the zeroth diffraction order. The optical response of such a metasurface is then entirely based on the diffraction introduced by the pixel grid, where the largest diffraction angle is limited by the pixel size. However, since the coupling near the pixel boundaries is neglected, the boundaries act as scattering centers that can scatter into the entire hemisphere. Consequently, one may imagine that the desired diffracted wave is superposed with an unaccounted-for scattered wave, where the perturbation increases as the pixel size decreases. While it might still be feasible to simulate a single 3-by-3 neighborhood of small pixels, as to determine a more precise estimate of the transmission coefficient of the central pixel, the use of n unique transmission coefficients would require n^9 of such simulations, which quickly becomes unmanageable. In fact, since ordered Huygens' metasurfaces make explicit use of the lattice constant of their truncated arrays, which means the local particle density, it even seems nonsensical to approach the mode of operation of non-resonant metasurfaces, which means a regular grid of pixels where each pixel contains only one particle. However, in this limit, the control over the local particle density can be regained by transitioning to positionally disordered Huygens' metasurfaces.

In summary, ordered Huygens' metasurfaces require rather large pixel sizes to overcome unconsidered coupling effects, but for some application, as for example for the generation of vortex beams [80], this might not be a problem. Regarding the claim that the inter-particle coupling is the source of "Fundamental limitations of Huygens' metasurfaces for optical beam shaping" [54], it must be kept in mind that although non-resonant metasurfaces provide a subwavelength spatial control that cannot be achieved with ordered Huygens' metasurfaces, they do not offer spectral control. Even more so, positionally disordered Huygens' metasurfaces may fill the gap for applications that require both a spectral and a subwavelength spatial control.

Positionally disordered Huygens' metasurfaces can be discretized as mentioned above in the paragraph "phase-shifting mechanisms". If a pixel-based approach is chosen, each pixel can be filled with a homogeneous particle arrangement that follows a specific statistical distribution. Here, the idea is that different realizations of the same distribution yield, in average, the same optical response, which makes it possible to generate the particle coordinates of one pixel in a way that also takes into account the particle coordinates in neighboring pixels. Since this effectively blends neighboring particle distributions near the pixel boundaries, it may also result in a smooth transition in the optical response of neighboring pixels. Ultimately, this idea can be developed further by switching from a regular grid of pixels to local particle neighborhoods. Alternatively, one could simply rearrange some particles near the pixel boundaries in a way that disrupts the coupling of neighboring pixels.

Certainly, the introduction of positional disorder also leads to scattering into the entire hemisphere, but this is not necessarily detrimental. Since this aspect can be fully taken into account in simulations based on the T-matrix method, and thus during the design process, one can explicitly make use of scattering to significantly enhance the numerical aperture of a metasurface, which has already been demonstrated with non-resonant metasurfaces in the context of wavefront shaping [27].

A brief review of disordered metasurfaces

In the last two decades, photonic devices with various types of disorder have been reported to exhibit a wide range of exceptional properties, but it was not until very recently that research has started to investigate disordered metasurfaces more systematically, both from a technological [81–83], and from a theoretical point of view [84–87]. Hence, the remainder of this section mainly focuses on the reported properties of disordered metasurfaces, categorized in terms of their type of disorder.

Position Positional disorder seems to be the most commonly used type of disorder in early experimental studies that have investigated its impact on the directional scattering of resonant metasurfaces [88–90]. At about the same time, the concept of *hyperuniformity* was introduced as a unifying theoretical framework for the classification and characterization of exotic disordered states of matter [91]. Supported by this framework, it was soon experimentally demonstrated that the directional scattering of resonant metasurfaces can not only be tailored via the particle statistics [10, 92], but also be rendered wavelength-selective [93, 94]. The same has been observed in dielectric Huygens’ metasurfaces, but with an additional control over the transmission-to-reflection energy ratio [31, 32, 95].

Other novel uses and effects of positional disorder include: Geometric-phase plasmonic metasurfaces, where the positional disorder is applied in the sense of spatial multiplexing, enhance the information capacity of multi-functional devices [96, 97]. Dielectric bilayer metasurfaces, where the particles are strongly coupled via guided waves, exhibit an ultrahigh angular selectivity [98]. Plasmonic bilayer metasurfaces, where the particles break the out-of-plane symmetry, show diffuse reflection and reciprocity-protected transmission [99].

Size Resonant plasmonic metasurfaces, where the lateral dimensions of each particle are randomized, demonstrate a tailorable directional reflectance that may find application in high-quality reference structures and engineered diffusers [100]. Similarly, non-resonant dielectric metasurfaces with the same type of size disorder show a tailorable directional transmittance that has been used to enhance the numerical aperture of wavefront-shaping devices [27].

Orientation Plasmonic bilayer metasurfaces with orientational disorder exhibit purely circular eigenstates that enable circular dichroism and optical activity without linear birefringence [101].

Position + Size Fabrication methods based on self-assembly strategies often not only introduce disorder in the position, but also in the size of the particles. This combination has been used in plasmonic and dielectric metasurfaces for angle-independent structural coloration [102, 103], and in dielectric metasurfaces for an optimized chromaticity and light diffusion in organic light-emitting diodes [104].

Position + Orientation The combination of positional and orientational disorder in plasmonic metasurfaces has led to the realization of polarization-independent metalenses [105, 106].

Structural disorder in metamaterials and photonic devices Three-dimensional metamaterials with hyperuniform disorder are expected to exhibit a complete photonic bandgap [7], while two-dimensional metamaterials additionally provide a precise control over the light transport and localization [107–110]. In an even broader context, the incorporation of structural disorder has led to novel photonic devices with unique functionalities in a wide range of fields such as information security, optical computing, spectroscopy, hyperspectral imaging, ultrafast optical pulse measurement, optical sensing, or random lasers [83]. Lastly, considering that nature has had millions of years to optimize disordered biological structures through evolution, as for example for structural coloration, it seems only fair to conclude that research can still learn from nature about how to harness disorder [11].

2.2. Towards perfect optical diffusers

Optical diffusers are key elements in a wide range of applications, as for example in illumination [104, 111, 112], imaging [25, 113–115], screens [116], microscopy [117–121], colorants [103, 122, 123], spectroscopy [124–126], photovoltaics [127–129], or wavefront shaping [27, 130–132]. Their main use is to redistribute incident light across a large solid angle while minimizing or ideally removing high-intensity spots [133, 134]. However, conventional optical diffusers are usually thick volume scatterers (Rayleigh scattering) or microstructured surfaces (geometric scattering) that lack the potential for on-chip integration in photonic devices [135–137]. Positionally disordered Huygens’ metasurfaces, on the other hand, are mechanically-robust ultra-thin embedded layers that are readily integrable.

Conventional optical diffusers can generally be classified as *volume diffusers* [138–140], *microstructured surface diffusers* [141–145], or *holographic diffusers* [146–149]. Volume diffusers, such as opal glass, consist of deep-subwavelength scatterers that provide an almost Lambertian light distribution, but at the cost of a low energy efficiency. Microstructured surface diffusers, such as ground glass, offer relatively high transmission efficiencies, but only limited control over the spatial distribution of scattered light. Holographic diffusers are carefully engineered surface diffusers that offer high transmission efficiencies and tailored spatial light distributions [150]. However, their optical response is usually very sensitive to the incidence angle and polarization, and since most surface diffusers require a defined refractive index contrast at their surface, they cannot readily be deployed in changing environments. All of these conventional optical diffusers are based on non-resonant scattering mechanisms and, thus, provide a broadband diffuser functionality. Only recently, a microstructured surface diffuser and a holographic diffuser have been reported that provide a wavelength-selective diffuser functionality [151, 152], which means that the diffuser turns into a non-diffusing fully-transparent window as the wavelength of the incident wave is tuned away from the operation wavelength. In both cases, this functionality has been achieved via the precise engineering of disordered structures.

Resonant metasurfaces can overcome the limitations of conventional optical diffusers and even provide additional wavelength-dependent and multipolar features [86, 153]. Plasmonic disordered metasurfaces have already shown wavelength-selective diffuser functionalities in combination with unique features such as a tailorable scattering profile or a large optical memory effect [89, 92, 94]. The optical memory effect refers to the observation that if an electromagnetic wave entering a thin scattering layer is tilted or shifted, the transmitted wave tilts and shifts by the same amount while all other aspects of its wavefront remain mostly unchanged [154]. More recently, dielectric disordered metasurfaces have also shown high-numerical-aperture wavefront-shaping capabilities with a large optical memory effect [27], and structural color generation with an improved insensitivity regarding the viewing angle [103, 155].

Furthermore, while ordered Huygens’ metasurfaces completely suppress the zeroth-order reflectance [156–158], positionally disordered Huygens’ metasurfaces can additionally fully suppress the zeroth-order transmittance at the resonance wavelength and for a critical degree of positional disorder [31]. This means that all incident light is completely redistributed across all possible directions [32], which in turn leads to the concept of perfect optical diffusers as discussed in the following paragraph. Moreover, the resonant nature of Huygens’ metasurfaces renders this perfect diffusion wavelength-selective, which offers intriguing new opportunities in applications such as fluorescence microscopy, augmented reality displays [93], or holographic displays [26]. In the case of displays, it would be possible to present information at one wavelength, and to track the motion of a person through the display at a possibly invisible secondary wavelength, which in turn would allow for a relatively simple implementation of interactive features.

What is a perfect optical diffuser?

A *perfect optical diffuser* shall be defined as a device that exhibits zero absorption losses and yields the directional scatterance (Sec. 3.4.3) of a Lambertian surface (Appendix A.1) independently of the incidence angle and polarization. Depending on the width of the wavelength range over which perfect diffusion is achieved, one may distinguish between *wavelength-selective* or *broadband* perfect optical diffusers. Note that this definition seems highly idealistic, as it may already be physically impossible to exactly realize a broadband Lambertian surface, let alone a directional scatterance that does not change with the excitation condition. Hence, this definition should rather be understood as an attempt to generalize the concept of a Lambertian surface that takes into account that metasurfaces are able to shape both the directional transmission and reflection. The definition could be relaxed by requiring that the directional scatterance complies with the concept of the optical memory effect rather than being completely independent of the excitation, or one could argue that a generalized Lambertian surface should allow for an arbitrary ratio of hemispherical transmittance to hemispherical reflectance, but such discussions exceed the scope of this thesis. Nevertheless, since real devices might never exactly meet these requirements, it seems necessary to classify a device on the basis of a performance metric.

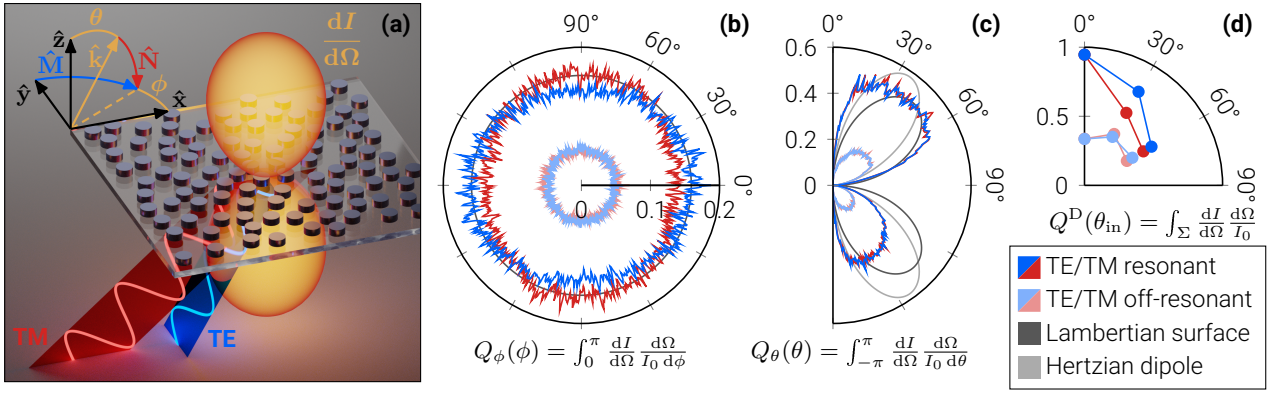


Fig. 2.1 | What is a perfect optical diffuser? (a) Artistic impression of a positionally disordered metasurface with a scattering profile (orange; scattered intensity I per unit solid angle $d\Omega = \sin(\theta) d\phi d\theta$) that hardly changes when excited by generic TE (blue) or TM (red) polarized plane waves. The (b) azimuthal and (c) polar scatterance show the fraction of the incident intensity I_0 per unit angle that is scattered along all polar or azimuthal angles, respectively, when the metasurface is excited by a normally-incident plane wave near (saturated colors) or off (desaturated colors) its resonance wavelength. The scatterance of ideal scatterers is shown for comparison. The (d) diffuse scatterance, as a function of the incidence angle θ_{in} of a plane wave, is the efficiency with which a metasurface redistributes the incident energy across all diffuse directions Σ . For reference: (b–d) show simulations of the soft-core uniform metasurface type for the overlapping resonance case with resonant ($\lambda = 1.38 \mu\text{m}$) and off-resonant ($\lambda = 1.52 \mu\text{m}$) excitation.

Figure 2.1 illustrates the properties of a perfect optical diffuser and motivates the physical quantities that are used in this thesis to judge the performance of diffusers. The artistic impression in Fig. 2.1a depicts a positionally disordered metasurface with a scattering profile, intensity per solid angle $dI/d\Omega$, that hardly changes for different plane wave excitations. Note that a Lambertian surface and a Hertzian dipole are considered for reference, both of which exhibit equal hemispherical transmittance and reflectance (Appendix A.1). For an easier comparison of the shape of $dI(\theta, \phi)/d\Omega$, the scattering profile is normalized by the incident intensity I_0 and integrated over all polar angles θ (Fig. 2.1b), or all azimuthal angles ϕ (Fig. 2.1c). Note that since the differential solid angle $d\Omega \propto \sin(\theta)$ vanishes along the polar axis, Fig. 2.1c inherits the $\sin(\theta)$ factor, and Fig. 2.1b effectively excludes contributions from *regular directions* (here: zeroth-order transmission and reflection). Figures 2.1b,c show the simulated optical response of a metasurface with a disordered particle arrangement as depicted in Fig. 2.1a when the metasurface is excited directly at or slightly off its resonance wavelength by a normally-incident plane wave. Clearly, the optical response is almost independent of the incident polarization, and for off-resonant excitation, the metasurface scatters considerably less light along *diffuse directions*, which means non-regular directions. The latter demonstrates the wavelength-selective diffuser functionality. Moreover, the scattering profile is highly uniform along the azimuthal direction, slightly asymmetric along the polar direction, and has a shape similar to the reference scatterers. Lastly, Fig. 2.1d shows the integral of the normalized scattering profile across all diffuse directions. This quantity measures how efficiently a metasurface diffuses the incident energy. As the incidence angle θ_{in} increases, less light is scattered along diffuse directions and, thus, more light resides in the zeroth diffraction orders. However, while holographic diffusers typically only accept incidence angle deviations of a few degrees, the presented metasurface allows a few tens of degrees.

2.3. Towards disordered metasurface holograms

Holography – from Greek “holos” (whole) and “graphē” (writing, drawing) – may be seen as a generalization of photography where the goal is to record the full three-dimensional optical information of an object in a two-dimensional medium, a *hologram*, from which the object can be reconstructed at any later point in time [159, 160]. While photography only records the intensity distribution of the electromagnetic wave emanated by an object, holography aims to store both the amplitude and phase of the object wave, or additionally its polarization (*polarization holography*). The term “holography” was coined by Dennis Gabor [161–163], who realized that although a photographic plate can only record the intensity of an electromagnetic field, it is still possible to store both the amplitude and phase of an

object wave in an encoded form. To this end, the object wave is interfered with a well-defined reference wave and the intensity of the interference pattern is stored in the hologram. Then, when the hologram is illuminated once again by the reference wave, the interference pattern modulates the amplitude of the reference wave and diffracts it in a way that recreates the object wave. However, since this approach projects a two-dimensional parameter space (amplitude and phase) onto a one-dimensional space (intensity), it is not possible to uniquely reconstruct the object phase, which in turn leads to the appearance of additional unwanted waves. This can be illustrated by considering the intensity of the interference pattern $I(x, y) \propto |1 + o(x, y)|^2$ in the hologram plane (x, y) , where the electric field of the reference wave is normalized to 1 and the object wave is represented by a complex-valued modulation $o(x, y)$. Then, since $I(x, y) \propto 1 + |o(x, y)|^2 + o(x, y) + \overline{o(x, y)}$ modulates the amplitude of the reference wave in the reconstruction process, it can be concluded that the first two terms result in an unwanted background wave, while the last two terms generate the desired object wave, but also its complex conjugate. In an *in-line* configuration, where the reference wave illuminates the hologram under normal incidence, the image of the object wave is generally disturbed by the other waves. However, the different waves can be spatially separated in an *off-axis* configuration, which means for oblique incidence of the reference wave [159, 160].

With the rapid advance of computer technology and nanofabrication, *digital holography* and *computer-generated holography* have largely replaced conventional holography in the fields of optical metrology and wavefront shaping [164–166]. While digital holography generally refers to the digital recording and numerical reconstruction of holograms, computer-generated holography focuses on the numerical design, physical realization, and optical reconstruction of holograms via wavefront-shaping methods. Independent of the used method, one may distinguish here between *amplitude-only*, *phase-only*, and *amplitude-and-phase* holograms [164], which expresses whether the hologram modulates the reference wave’s amplitude, phase, or both. *Computer-generated holograms* can be realized with *spatial light modulators*, which are tunable devices such as digital micromirror devices or liquid crystal cells, or with static structures, as for example diffractive optical elements or metasurfaces [167, 168]. Here, metasurfaces are particularly interesting due to their ability to modulate the amplitude, phase, and polarization on a subwavelength scale, whereas spatial light modulators typically have a coarser spatial resolution and can only modulate either the amplitude or the phase, or require more sophisticated configurations to achieve both simultaneously [169–171]. Moreover, computer-generated holograms are liberated from the need to encode the object wave in the form of an intensity interference pattern, which in turn eliminates unwanted waves and thus allows for simple in-line configurations. For example, to obtain a specific complex-valued electric field distribution in the image plane, one simply has to numerically back-propagate the electric field into the hologram plane, implement the resulting amplitude and phase distribution in terms of a spatially-variant transmission coefficient, and illuminate the resulting hologram with a plane wave. Clearly, this approach generally requires amplitude-and-phase holograms. With amplitude-only and phase-only holograms it is still possible to achieve a desired intensity distribution in the image plane, but without precise control over the resulting phase distribution. Such holograms with constraints are typically generated with an *iterative Fourier transform algorithm* (Sec. 5.3).

Another interesting feature of resonant metasurfaces is their ability to store multiple object waves that can be selectively reconstructed via a change in the wavelength, polarization, or incidence angle of the reference wave [172]. This method, known as multiplexing, can also be applied to the spatial arrangement of the scattering elements in a metasurface. For example, the lateral interleaving of scattering elements can help in situations where a single element cannot provide all required amplitude and phase values for all target wavelengths simultaneously, and the vertical stacking of two metasurfaces can break the out-of-plane symmetry and thus allow for two different object waves to be reconstructed depending on whether the metasurface is illuminated from its front or back side [123]. Moreover, nonlinear holograms have been demonstrated on the basis of all-dielectric resonant metasurfaces, and tunable metasurface holograms have been implemented via the use of phase-change materials, mechanically stretchable substrates, or chemical reactions [123].

The introduction of positional disorder in ordered Huygens' metasurfaces can increase their information capacity in several ways. Firstly, ordered Huygens' metasurfaces are limited to phase-only holograms, because their pixels exhibit a transmittance of one for any phase value. To modulate the amplitude, it is necessary to reduce the scattering strength of the Huygens' particles in some way (Appendix A.5). One way is to spectrally separate the electric and magnetic dipole resonances via the particle geometry or lattice constant, which means by resorting to simple resonant metasurfaces. However, this increases the reflectance and it is not guaranteed that all possible amplitude and phase combinations can be addressed, since an individual multipole resonance only provides a phase range of π . With positionally disordered Huygens' metasurfaces, on the other hand, it is possible to almost independently tune the amplitude via the degree of positional disorder and the phase via the particle density [31], while maintaining a vanishing zeroth-order reflectance [32].

Secondly, the directional scattering typically increases in strength as the degree of positional disorder approaches its critical value, which means as the zeroth-order transmittance approaches zero. Although this may sound detrimental at first, the ability to shape the directional scattering via the particle arrangement can be utilized in several ways. To understand this, consider that the rather large pixel sizes in ordered Huygens' metasurfaces limit the largest achievable diffraction angle and often produce unwanted diffraction orders. With positional disorder, all pixels can be replaced by overlapping particle neighborhoods, where the area average of the transmitted electric field across a local neighborhood determines its zeroth-order transmission coefficient. This effectively reduces the pixel size to a length scale comparable to the average inter-particle distance, which in turn increases the largest achievable diffraction angle. In this context, the object wave is generated by the spatially-variant zeroth-order transmission coefficient. However, the transmitted electric field will generally also exhibit subwavelength spatial modulations within each local neighborhood, which means that it contains spatial frequencies that may lead to scattering into the entire hemisphere. Nevertheless, the low-frequency components can explicitly be used to increase the intensity homogeneity of the zeroth-order object wave in the image plane, mid-frequency components can extend the object wave beyond the largest diffraction angle of the zeroth-order object wave, and high-frequency components could be used to smoothly diffuse unwanted light along all directions that do not interfere with the image of the object wave. The latter may be seen as a compromise that acknowledges that Huygens' metasurfaces can only attenuate the zeroth-order amplitude in transmission via the degree of positional disorder if the remaining light is redistributed along diffuse directions. Compared to ordered Huygens' metasurfaces, which generally exhibit discrete diffraction orders that produce copies of the object wave, this ability to diffuse unwanted light across unimportant directions represents an advantage. Moreover, while non-resonant metasurfaces provide direct control over deep-subwavelength spatial modulations of the electromagnetic field within the hologram plane, it seems that resonant metasurfaces must rely on positional disorder to achieve a comparable subwavelength control.

Lastly, since uniform positional disorder typically renders a metasurface less sensitive to changes in the incidence angle and polarization [32, 105], positionally disordered Huygens' metasurfaces could also be used as amplitude-and-phase *Fourier holograms* [159, 160], which means as the transfer function in a 4-f imaging system [173], where they facilitate the optical processing of large objects.

Note that the preceding discussion generally also applies to the approach where the metasurface is subdivided into pixels with homogeneous positional disorder. However, this pixel-based approach raises two interrelated questions of its own accord: As compared to ordered Huygens' metasurfaces, (i) can positional disorder help reducing the pixel size and (ii) how does the scattering from within a pixel affect the holographic image? These questions are addressed in Chapter 8, where the pixel-based approach was used for the first time in conjunction with positionally disordered Huygens' metasurfaces. This may be seen as a first step towards metasurface holograms with truly inhomogeneous positional disorder.

3. Fundamentals of Wave Optics

3.1. Fourier transformations

Continuous transformations Throughout this thesis, the following one-dimensional non-unitary Fourier transformation pair is used for transformations between time t and angular frequency ω

$$\mathcal{F}_t\{f(t)\}(\omega) = f(\omega) = \int_{\mathbb{R}} f(t) e^{i\omega t} dt \quad (3.1)$$

$$\mathcal{F}_\omega^{-1}\{f(\omega)\}(t) = f(t) = \frac{1}{2\pi} \int_{\mathbb{R}} f(\omega) e^{-i\omega t} d\omega \quad (3.2)$$

and the following D -dimensional non-unitary Fourier transformation pair with a conjugated kernel is used for transformations between space \mathbf{r} and wavevector \mathbf{k} :

$$\mathcal{F}_{\mathbf{r}}\{f(\mathbf{r})\}(\mathbf{k}) = f(\mathbf{k}) = \int_{\mathbb{R}^D} f(\mathbf{r}) e^{-i\mathbf{k}\cdot\mathbf{r}} d\mathbf{r} \quad (3.3)$$

$$\mathcal{F}_{\mathbf{k}}^{-1}\{f(\mathbf{k})\}(\mathbf{r}) = f(\mathbf{r}) = \frac{1}{(2\pi)^D} \int_{\mathbb{R}^D} f(\mathbf{k}) e^{i\mathbf{k}\cdot\mathbf{r}} d\mathbf{k} \quad (3.4)$$

The motivation behind this choice is that harmonic waves of the form $\exp(i\mathbf{k}' \cdot \mathbf{r} - \omega' t)$ with positive frequencies ω' and \mathbf{k}' are mapped to positive frequencies in the Fourier space, which can be seen from the Fourier representation of the Dirac delta function in time $\mathcal{F}_t\{\exp(-i\omega' t)\}(\omega) = 2\pi\delta(\omega - \omega')$ and in space $\mathcal{F}_{\mathbf{r}}\{\exp(i\mathbf{k}' \cdot \mathbf{r})\}(\mathbf{k}) = (2\pi)^D \delta(\mathbf{k} - \mathbf{k}')$. Such positive-frequency waves advance in space along the direction of \mathbf{k}' as the time t increases, which is commonly referred to as the “ $e^{-i\omega t}$ time convention”. Lastly, note that the differentiation property $\mathcal{F}_t\{\partial_t^n f(t)\}(\omega) = (-i\omega)^n f(\omega)$ can be of great help in the solution of partial differential equations, and that the presented notation uses the units of the function arguments to distinguish a function from its Fourier transformation.

Discrete transformations In the development and application of numerical methods, it is advantageous to use a fast implementation of the discrete Fourier transformation [174]. In order to approximate a D -dimensional continuous Fourier transformation, all continuous variables must be sampled on an equidistant grid that takes the shape of a hypercube with $\mathbf{N} = (N_1, \dots, N_D)$ points per side length $\mathbf{p} = (p_1, \dots, p_D)$. Although the choice of sample points is not unique due to the \mathbf{p} -periodicity of the discrete Fourier transformation, the grid coordinates $\mathbf{r}_{\mathbf{n}}$ and $\mathbf{k}_{\mathbf{m}}$ are most commonly defined as

$$\mathbf{r}_{\mathbf{n}} = \Delta\mathbf{r} \circ \left(\mathbf{n} - \left\lceil \frac{\mathbf{N}-1}{2} \right\rceil \right) \quad \Delta\mathbf{r} = \frac{\mathbf{p}}{\mathbf{N}} \quad \mathbf{n} = (n_1, \dots, n_D) \quad (3.5)$$

$$\mathbf{k}_{\mathbf{m}} = \Delta\mathbf{k} \circ \begin{cases} \mathbf{m} & \mathbf{m} \leq \left\lceil \frac{\mathbf{N}-1}{2} \right\rceil \\ (\mathbf{m} - \mathbf{N}) & \text{otherwise} \end{cases} \quad \Delta\mathbf{k} = \frac{2\pi}{\mathbf{p}} \quad \mathbf{m} = (m_1, \dots, m_D) \quad (3.6)$$

where the multi-indices \mathbf{n} and \mathbf{m} can take on integer values in the range of $n_d, m_d \in \{0, \dots, N_d - 1\}$, and the multiplication $\mathbf{a} \circ \mathbf{b}$ and division $\frac{\mathbf{a}}{\mathbf{b}}$ of vectors are element-wise operations. The discrete Fourier transformation pair may then be written as

$$f(\mathbf{k}_{\mathbf{m}}) = \sum_{\mathbf{n}=0}^{\mathbf{N}-1} f(\mathbf{r}_{\mathbf{n}}) e^{-i2\pi\mathbf{m}\cdot\frac{\mathbf{n}}{\mathbf{N}}} \quad (3.7)$$

$$f(\mathbf{r}_{\mathbf{n}}) = \frac{1}{\prod_{d=1}^D N_d} \sum_{\mathbf{m}=0}^{\mathbf{N}-1} f(\mathbf{k}_{\mathbf{m}}) e^{i2\pi\mathbf{m}\cdot\frac{\mathbf{n}}{\mathbf{N}}} \quad (3.8)$$

which can be computed with a time-complexity of $\mathcal{O}(N \log_2 N)$, where $N = \prod_{d=1}^D N_d$ is the total number of sample points and each $N_d = 2^i 3^j 5^k 7^l$ is ideally a product of small primes.

Nonuniform transformations In situations where the spatial or spectral points are non-equidistant, it is advantageous to use fast nonuniform Fourier transformations [175]

$$f(\mathbf{k}_m) = \sum_i f(\mathbf{r}_i) e^{-i\mathbf{k}_m \cdot \mathbf{r}_i} \quad \text{Type 1: Nonuniform to Uniform} \quad (3.9)$$

$$f(\mathbf{r}_i) = \sum_{\mathbf{m}} f(\mathbf{k}_m) e^{i\mathbf{k}_m \cdot \mathbf{r}_i} \quad \text{Type 2: Uniform to Nonuniform} \quad (3.10)$$

$$f(\mathbf{k}_j) = \sum_i f(\mathbf{r}_i) e^{-i\mathbf{k}_j \cdot \mathbf{r}_i} \quad \text{Type 3: Nonuniform to Nonuniform} \quad (3.11)$$

where the nonuniform spatial \mathbf{r}_i and spectral \mathbf{k}_j points are enumerated by $i = 1, \dots, I$ and $j = 1, \dots, J$, respectively, and \mathbf{k}_m is the same as in the discrete Fourier transformation. The type-1 and type-2 transformations each have a time-complexity of $\mathcal{O}(M |\log_{10}(\epsilon)|^D + N \log_2 N)$, where $M = I, J$ is the number of nonuniform points, N the number of uniform points, and ϵ the targeted relative precision. The time-complexity of type 3 scales with the space-frequency product of \mathbf{r}_i and \mathbf{k}_j .

3.2. Maxwell's equations

Maxwell's macroscopic equations, which model the interaction of electromagnetic fields with matter on a scale that exceeds and therefore ignores most of the matter's atomic structure, are defined as [176]

$$\nabla \times \mathbf{E}(\mathbf{r}, t) = -\partial_t \mathbf{B}(\mathbf{r}, t) \quad \text{Faraday's law} \quad (3.12)$$

$$\nabla \times \mathbf{H}(\mathbf{r}, t) = \partial_t \mathbf{D}(\mathbf{r}, t) + \mathbf{j}(\mathbf{r}, t) \quad \text{Ampere's law} \quad (3.13)$$

$$\nabla \cdot \mathbf{D}(\mathbf{r}, t) = \rho(\mathbf{r}, t) \quad \text{Gauss's law} \quad (3.14)$$

$$\nabla \cdot \mathbf{B}(\mathbf{r}, t) = 0 \quad \text{Gauss's law for magnetism} \quad (3.15)$$

where \mathbf{E} is the electric field strength, \mathbf{H} the magnetic field strength, \mathbf{D} the electric flux density, \mathbf{B} the magnetic flux density, \mathbf{j} the free current density, and ρ the free charge density. The flux densities account for bound currents and charges via the material equations

$$\mathbf{D} = \varepsilon_0 \mathbf{E} + \mathbf{P} \quad (3.16)$$

$$\mathbf{B} = \mu_0 \mathbf{H} + \mu_0 \mathbf{M} \quad (3.17)$$

where ε_0 is the vacuum permittivity, μ_0 the vacuum permeability, \mathbf{P} the polarization field, and \mathbf{M} the magnetization field. For the special case of linear and isotropic dielectrics ($\mathbf{j} = \mathbf{0}$, $\rho = 0$), the polarization and magnetization fields can be modeled in the frequency domain as

$$\mathbf{P}(\mathbf{r}, \omega) = \varepsilon_0 \chi_e(\mathbf{r}, \omega) \mathbf{E}(\mathbf{r}, \omega) \quad (3.18)$$

$$\mathbf{M}(\mathbf{r}, \omega) = \chi_m(\mathbf{r}, \omega) \mathbf{H}(\mathbf{r}, \omega) \quad (3.19)$$

where χ_e and χ_m are the material's electric and magnetic susceptibility, respectively. Since these material models require the evaluation of convolution integrals in the time domain, it is much more convenient to Fourier-transform Maxwell's macroscopic equations into the frequency domain

$$\nabla \times \mathbf{E}(\mathbf{r}, \omega) = i\omega \mu_0 \mu(\mathbf{r}, \omega) \mathbf{H}(\mathbf{r}, \omega) \quad \text{Faraday's law} \quad (3.20)$$

$$\nabla \times \mathbf{H}(\mathbf{r}, \omega) = -i\omega \varepsilon_0 \varepsilon(\mathbf{r}, \omega) \mathbf{E}(\mathbf{r}, \omega) \quad \text{Ampere's law} \quad (3.21)$$

$$\nabla \cdot [\varepsilon(\mathbf{r}, \omega) \mathbf{E}(\mathbf{r}, \omega)] = 0 \quad \text{Gauss's law} \quad (3.22)$$

$$\nabla \cdot [\mu(\mathbf{r}, \omega) \mathbf{H}(\mathbf{r}, \omega)] = 0 \quad \text{Gauss's law for magnetism} \quad (3.23)$$

where $\varepsilon = 1 + \chi_e$ and $\mu = 1 + \chi_m$ are the relative permittivity and permeability, respectively. Note that although most dielectric materials typically exhibit $\mu \approx 1$, it is convenient to explicitly retain μ in all equations as to preserve the self-dual symmetry of Maxwell's equations.

Duality Principle The duality principle states that Maxwell's equations (Eqs. (3.20–23)) map back onto themselves given the following substitutions [38]:

$$\mathbf{E} \rightarrow \mathbf{H} \qquad \mathbf{H} \rightarrow -\mathbf{E} \qquad \varepsilon \rightarrow \frac{\mu_0}{\varepsilon_0} \mu \qquad \mu \rightarrow \frac{\varepsilon_0}{\mu_0} \varepsilon \qquad (3.24)$$

The duality principle can be used to quickly transform known expressions for \mathbf{E} into complementary expressions for \mathbf{H} , and vice versa. Due to this reason, the remainder of this thesis avoids the explicit discussion of those properties of \mathbf{H} that can easily be derived from the duality principle.

Boundary conditions At material interfaces, ε and μ generally exhibit jump discontinuities that are, by definition, not differentiable but still integrable. Consequently, Maxwell's equations (Eqs. (3.20–23)) must be stated in their integral form in order to derive continuity conditions for the electromagnetic field at such interfaces [38]:

$$\oint_{\partial S} \mathbf{E}(\mathbf{r}, \omega) \cdot d\mathbf{r} = i\omega\mu_0 \iint_S \mu(\mathbf{r}, \omega) \mathbf{H}(\mathbf{r}, \omega) \cdot d\mathbf{S} \qquad \text{Faraday's law} \qquad (3.25)$$

$$\oiint_{\partial V} \varepsilon(\mathbf{r}, \omega) \mathbf{E}(\mathbf{r}, \omega) \cdot d\mathbf{S} = 0 \qquad \text{Gauss's law} \qquad (3.26)$$

By considering sufficiently short integration paths across the interface of two media (subscripts 1,2), such that all quantities are effectively constant, the tangential components of the field strengths and the normal components of the flux densities are found to be continuous at the interface:

$$\mathcal{P}_{\parallel} (\mathbf{E}_1 - \mathbf{E}_2) = \mathbf{0} \qquad (3.27)$$

$$\mathcal{P}_{\perp} (\varepsilon_1 \mathbf{E}_1 - \varepsilon_2 \mathbf{E}_2) = \mathbf{0} \qquad (3.28)$$

The tangential projection (\mathcal{P}_{\parallel}), normal projection (\mathcal{P}_{\perp}), and reflection (\mathcal{R}) of an arbitrary vector with respect to the unit normal $\hat{\mathbf{n}}$ or tangential plane of a surface can be expressed in terms of operators

$$\mathcal{P}_{\parallel} = (\mathbf{I} - \hat{\mathbf{n}}\hat{\mathbf{n}}) \cdot \qquad (3.29)$$

$$\mathcal{P}_{\perp} = (\hat{\mathbf{n}}\hat{\mathbf{n}}) \cdot \qquad (3.30)$$

$$\mathcal{R} = \mathcal{P}_{\parallel} - \mathcal{P}_{\perp} = (\mathbf{I} - 2\hat{\mathbf{n}}\hat{\mathbf{n}}) \cdot \qquad (3.31)$$

where \mathbf{I} is the identity matrix, $\hat{\mathbf{n}}\hat{\mathbf{n}}$ is a dyadic product, and hats represent unit vectors $\hat{\mathbf{n}} = \mathbf{n}/\sqrt{\mathbf{n} \cdot \mathbf{n}}$. Note that all operators become position-dependent if the surface is curved.

3.3. Vector wave equation

Faraday's and Ampere's law (Eqs. (3.20,21)) can be combined to a single vector wave equation

$$\left[\nabla \times \nabla \times - (\nabla \ln \mu(\mathbf{r}, \omega)) \times \nabla \times - k^2(\mathbf{r}, \omega) \right] \mathbf{E}(\mathbf{r}, \omega) = \mathbf{0} \qquad (3.32)$$

where $k^2 = \omega^2 \varepsilon_0 \mu_0 \varepsilon \mu$ is, at first, only a symbolic abbreviation. However, in the following sections it will become apparent that the wavenumber k dictates the spatial frequency of an electromagnetic wave and asserts a constraint on the wavevector \mathbf{k} of plane waves. Hence, it is convenient to explicitly define the wavenumber k and the refractive index n as

$$k(\mathbf{r}, \omega) = \frac{\omega}{c_0} n(\mathbf{r}, \omega) \qquad n(\mathbf{r}, \omega) = \sqrt{\varepsilon(\mathbf{r}, \omega) \mu(\mathbf{r}, \omega)} \qquad (3.33)$$

where $c_0 = 1/\sqrt{\varepsilon_0 \mu_0}$ is the speed of light in vacuum, and the definition of the refractive index involves the principal square root that satisfies $\text{Re} \sqrt{z} \geq 0$ and $\text{sgn}(\text{Im} \sqrt{z}) = \text{sgn}(\text{Im} z)$ for any $z \in \mathbb{C}$. Lastly, it should be noted that $n^2 = \varepsilon \mu$ and $\sqrt{n^2} = n$ hold by definition, even though generally $\sqrt{z^2} \neq z$.

Homogeneous media The vector wave equation simplifies greatly for homogeneous media:

$$\left[\nabla^2 + k^2(\omega)\right] \mathbf{E}(\mathbf{r}, \omega) = \mathbf{0} \quad (3.34)$$

A common approach to the solution of such vectorial differential equations is to reduce the vectorial problem to a scalar problem by assuming and confirming that \mathbf{E} can be expressed in terms of a rather complicated scalar potential $\psi(\mathbf{r})$ and a simple pilot vector $\mathbf{v}(\mathbf{r})$ [38]. The purpose of the pilot vector is to establish, together with $\nabla\psi$, a vector basis for the polarization states of \mathbf{E} , and to provide any additional spatial dependencies with which the ansatz ultimately satisfies the vector wave equation. The search for a suitable pilot vector can be simplified by requiring that \mathbf{v} itself arises from a scalar potential ν , and that ψ is the general solution of the associated scalar wave equation:

$$\mathbf{v}(\mathbf{r}) = \nabla\nu(\mathbf{r}) \quad (3.35)$$

$$\left[\nabla^2 + k^2\right] \psi(\mathbf{r}) = 0 \quad (3.36)$$

Then, to formulate an appropriate ansatz for \mathbf{E} , one should keep in mind that arbitrary vector fields can be separated into a curl-free and a divergence-free part, which is known as the Helmholtz theorem [38, 177, 178]. In homogeneous media, however, the electromagnetic field is purely divergence-free (Eqs. (3.22,23)). Furthermore, in analogy to Faraday's and Ampere's law (Eqs. (3.20,21)), the divergence-free part can be expressed in terms of two vector fields that share the notion of an electric and magnetic field. With these considerations in mind, the vector wave functions \mathbf{M} and \mathbf{N} may be defined as

$$\mathbf{M}(\mathbf{r}) = \frac{1}{k} \nabla \times [\psi(\mathbf{r}) \mathbf{v}(\mathbf{r})] \quad (3.37)$$

$$\mathbf{N}(\mathbf{r}) = \frac{1}{k} \nabla \times \mathbf{M}(\mathbf{r}) \quad (3.38)$$

which immediately implies the following identities

$$\nabla \cdot \mathbf{M} = 0 \quad \nabla \cdot \mathbf{N} = 0 \quad (3.39)$$

$$\nabla \times \mathbf{M} = k\mathbf{N} \quad \nabla \times \mathbf{N} = -\frac{1}{k} \nabla^2 \mathbf{M} \stackrel{!}{=} k\mathbf{M} \quad (3.40)$$

with the exception that the equality with the exclamation mark only holds if \mathbf{M} solves Eq. (3.34). Note that if \mathbf{M} is a solution, it immediately follows that \mathbf{N} is another solution; which can be seen by applying $[\nabla^2 + k^2]$ to Eq. (3.38). Consequently, the equality with the exclamation mark can be used to formulate a condition for ν under which \mathbf{M} and \mathbf{N} are indeed solutions of Eq. (3.34). To this end, the vector wave functions are first brought into a more explicit form

$$\mathbf{M} = \frac{1}{k} \nabla \psi \times \mathbf{v} \quad (3.41)$$

$$\mathbf{N} = \frac{1}{k^2} \nabla [\nabla \psi \cdot \mathbf{v}] + \frac{1}{k^2} [\text{tr}(\nabla \mathbf{v}) \mathbf{I} - 2\nabla \mathbf{v}] \cdot \nabla \psi + \psi \mathbf{v} \quad (3.42)$$

where $\nabla \mathbf{v} = \nabla \nabla \nu$ is the Jacobian matrix of \mathbf{v} or the Hessian matrix of ν , $\text{tr}(\cdot)$ is the trace of a matrix, \mathbf{I} is the identity matrix, and Eqs. (3.35,36) and several vector calculus identities were used. With this, the sought-for condition under which \mathbf{M} and \mathbf{N} solve Eq. (3.34) is quickly found:

$$\nabla \times \{[\text{tr}(\nabla \nabla \nu) \mathbf{I} - 2\nabla \nabla \nu] \cdot \nabla \psi\} = \mathbf{0} \quad (3.43)$$

Note that this condition is trivially satisfied when $\nabla \nabla \nu = m\mathbf{I}$ reduces to a constant multiple m of the identity matrix. In Cartesian coordinates, this is the case for

$$\nu = \frac{m}{2} \mathbf{r}^2 + \mathbf{c} \cdot \mathbf{r} \quad \mathbf{v} = m\mathbf{r} + \mathbf{c} \quad m \in \mathbb{R}, \mathbf{c} \in \mathbb{R}^3 \quad (3.44)$$

where $m = 0$ yields a particularly simple pilot vector. In spherical coordinates, however, it is more convenient to choose $\mathbf{c} = \mathbf{0}$, which can be seen when changing the basis of \mathbf{v} .

3.4. Plane vector wave functions

The scalar wave equation (Eq. (3.36)) reads in Cartesian coordinates (x, y, z) as:

$$\left[\partial_x^2 + \partial_y^2 + \partial_z^2 + k^2 \right] \psi(x, y, z) = 0 \quad (3.45)$$

After assuming that the scalar potential is separable in each coordinate $\psi(x, y, z) = X(x)Y(y)Z(z)$, performing the separation of variables by introducing the arbitrary constants k_x^2 and k_y^2 , and abbreviating $k_z^2 = k^2 - k_x^2 - k_y^2$, the scalar wave equation splits into the following set of differential equations and general solutions with integration constants c_i :

$$\left[\partial_x^2 + k_x^2 \right] X(x) = 0 \quad X(x) = c_1 e^{\mathbf{i}k_x x} + c_2 e^{-\mathbf{i}k_x x} \quad (3.46)$$

$$\left[\partial_y^2 + k_y^2 \right] Y(y) = 0 \quad Y(y) = c_3 e^{\mathbf{i}k_y y} + c_4 e^{-\mathbf{i}k_y y} \quad (3.47)$$

$$\left[\partial_z^2 + k_z^2 \right] Z(z) = 0 \quad Z(z) = c_5 e^{\mathbf{i}k_z z} + c_6 e^{-\mathbf{i}k_z z} \quad (3.48)$$

By defining the wavevector as $\mathbf{k} = (k_x, k_y, k_z)$, where $\mathbf{k}^2 = k_x^2 + k_y^2 + k_z^2 = k^2$ establishes the connection with the wavenumber k , it is possible to write the scalar potential as

$$\psi_{\mathbf{k}}(\mathbf{r}) = e^{\mathbf{i}\mathbf{k}\cdot\mathbf{r}} \quad (3.49)$$

$$\nabla\psi_{\mathbf{k}}(\mathbf{r}) = \mathbf{i}\mathbf{k}\psi_{\mathbf{k}}(\mathbf{r}) \quad (3.50)$$

but since the ‘‘magnitude’’ $\mathbf{k}^2 = k^2$ is fixed by the material, only the direction of \mathbf{k} is a free parameter. Together with the pilot vector $\mathbf{v} = \hat{\mathbf{n}}/\sin(\theta)$, where $\cos(\theta) = \hat{\mathbf{k}} \cdot \hat{\mathbf{n}}$ represents the angle between $\hat{\mathbf{k}} = \mathbf{k}/k$ and the normal vector $\hat{\mathbf{n}}$ of an arbitrary reference plane, the plane vector wave functions become

$$\mathbf{M}_{\mathbf{k}}(\mathbf{r}) = \mathbf{i}\psi_{\mathbf{k}}(\mathbf{r}) \hat{\mathbf{M}}_{\mathbf{k}} \quad \hat{\mathbf{M}}_{\mathbf{k}} = \frac{\hat{\mathbf{k}} \times \hat{\mathbf{n}}}{\sin(\theta)} \quad (3.51)$$

$$\mathbf{N}_{\mathbf{k}}(\mathbf{r}) = -\psi_{\mathbf{k}}(\mathbf{r}) \hat{\mathbf{N}}_{\mathbf{k}} \quad \hat{\mathbf{N}}_{\mathbf{k}} = \hat{\mathbf{k}} \times \hat{\mathbf{M}}_{\mathbf{k}} = \frac{\cos(\theta) \hat{\mathbf{k}} - \hat{\mathbf{n}}}{\sin(\theta)} \quad (3.52)$$

and the projections of the plane wave unit vectors with respect to the reference plane read as

$$\mathcal{P}_{\perp} \hat{\mathbf{M}}_{\mathbf{k}} = \mathbf{0} \quad \mathcal{P}_{\parallel} \hat{\mathbf{M}}_{\mathbf{k}} = \hat{\mathbf{M}}_{\mathbf{k}} \quad \mathcal{R} \hat{\mathbf{M}}_{\mathbf{k}} = \hat{\mathbf{M}}_{\mathcal{R}\mathbf{k}} = \hat{\mathbf{M}}_{\mathbf{k}} \quad (3.53)$$

$$\mathcal{P}_{\perp} \hat{\mathbf{N}}_{\mathbf{k}} = -\sin(\theta) \hat{\mathbf{n}} \quad \mathcal{P}_{\parallel} \hat{\mathbf{N}}_{\mathbf{k}} = \frac{\hat{\mathbf{k}} - \cos(\theta) \hat{\mathbf{n}}}{\tan(\theta)} \quad \mathcal{R} \hat{\mathbf{N}}_{\mathbf{k}} = -\hat{\mathbf{N}}_{\mathcal{R}\mathbf{k}} \quad (3.54)$$

where \mathcal{P}_{\perp} , \mathcal{P}_{\parallel} and \mathcal{R} are the operators from Eqs. (3.29–31). Since $\mathbf{M}_{\mathbf{k}}$ has no normal component and is typically associated with the electric field, it is customary to refer to $\mathbf{M}_{\mathbf{k}}$ and $\mathbf{N}_{\mathbf{k}}$ as the transverse electric (TE) and transverse magnetic (TM) plane wave, respectively. These waves are orthogonally polarized $\hat{\mathbf{M}}_{\mathbf{k}} \cdot \hat{\mathbf{N}}_{\mathbf{k}} = (\mathcal{P}_{\parallel} \hat{\mathbf{M}}_{\mathbf{k}}) \cdot (\mathcal{P}_{\parallel} \hat{\mathbf{N}}_{\mathbf{k}}) = 0$ and form a right-handed system with $\hat{\mathbf{M}}_{\mathbf{k}} \times \hat{\mathbf{N}}_{\mathbf{k}} = \hat{\mathbf{k}}$.

Lastly, for the special case of $\hat{\mathbf{n}} = \hat{\mathbf{z}}$, and by expressing $\mathbf{k}(\theta, \phi) = k\hat{\mathbf{k}}(\theta, \phi)$ in terms of polar $\text{Re } \theta \in [0, \pi]$ and azimuthal $\phi \in [-\pi, \pi]$ propagation angles, the unit vectors can be written as:

$$\hat{\mathbf{k}}(\theta, \phi) = \begin{pmatrix} \sin(\theta) \cos(\phi) \\ \sin(\theta) \sin(\phi) \\ \cos(\theta) \end{pmatrix} \quad \hat{\mathbf{M}}_{\mathbf{k}}(\theta, \phi) = \begin{pmatrix} \sin(\phi) \\ -\cos(\phi) \\ 0 \end{pmatrix} \quad \hat{\mathbf{N}}_{\mathbf{k}}(\theta, \phi) = \begin{pmatrix} \cos(\theta) \cos(\phi) \\ \cos(\theta) \sin(\phi) \\ -\sin(\theta) \end{pmatrix} \quad (3.55)$$

Often it is not only convenient but even necessary to require $\text{Im } \mathcal{P}_{\parallel} \mathbf{k} = \mathbf{0}$ (cf. Appendix B.3), which demands $\text{Im } \theta$ to be determined by $\tanh(\text{Im } \theta) = -\tan(\arg(k)) \tan(\text{Re } \theta)$ and results in

$$\hat{\mathbf{k}}(\theta, \phi) = \cosh(\text{Im } \theta) \hat{\mathbf{k}}(\text{Re } \theta, \phi) + \mathbf{i} \sinh(\text{Im } \theta) \hat{\mathbf{N}}_{\mathbf{k}}(\text{Re } \theta, \phi) \quad (3.56)$$

$$\mathbf{k}(\theta, \phi) = \left[\frac{|k|^2 \cosh(\text{Im } \theta)}{\text{Re}(k)} \mathcal{P}_{\parallel} + \frac{\text{Re}(k)}{\cosh(\text{Im } \theta)} \mathcal{P}_{\perp} \right] \hat{\mathbf{k}}(\text{Re } \theta, \phi) + \mathbf{i} \frac{\text{Im}(k) \cosh(\text{Im } \theta)}{\cos(\text{Re } \theta)} \hat{\mathbf{n}} \quad (3.57)$$

where $\text{Re } \theta = \frac{\pi}{2} \pm \arg(k) \Leftrightarrow \text{Im } \theta = \pm\infty$ is in fact the largest achievable angle due to refraction at a planar interface when the refractive index of the medium on the incident side tends to infinity.

3.4.1. Plane wave expansion

Without loss of generality, one may assume a standard Cartesian coordinate system where the reference plane is identical to the x - y plane ($z = 0$, $\hat{\mathbf{n}} = \hat{\mathbf{z}}$), require $\text{Im } \mathcal{P}_{\parallel} \mathbf{k} = \mathbf{0}$ for simplicity, and introduce the following abbreviation for a two-dimensional integral across the reference plane:

$$\langle f \rangle_{\xi} = \int_{\mathbb{R}^2} f(\xi) \, d\xi_x \, d\xi_y \quad (3.58)$$

The orthogonality conditions of the plane vector wave functions (Eqs. (3.51,52)) read then as

$$\langle \overline{\mathbf{M}_{\mathbf{k}'}} \cdot \mathbf{N}_{\mathbf{k}} \rangle_{\mathbf{r}} = \langle \overline{\mathbf{N}_{\mathbf{k}'}} \cdot \mathbf{M}_{\mathbf{k}} \rangle_{\mathbf{r}} = 0 \quad (3.59)$$

$$\langle \overline{\mathbf{M}_{\mathbf{k}'}} \cdot \mathbf{M}_{\mathbf{k}} \rangle_{\mathbf{r}} = \langle \overline{\mathbf{N}_{\mathbf{k}'}} \cdot \mathbf{N}_{\mathbf{k}} \rangle_{\mathbf{r}} = (2\pi)^2 \delta(\mathbf{k} - \mathbf{k}') \quad (3.60)$$

$$\langle \overline{\mathbf{M}_{\mathbf{k}'}} \times \mathbf{N}_{\mathbf{k}} \rangle_{\mathbf{r}} = \langle \overline{\mathbf{N}_{\mathbf{k}'}} \times \mathbf{M}_{\mathbf{k}} \rangle_{\mathbf{r}} = \mathbf{i} \hat{\mathbf{k}} (2\pi)^2 \delta(\mathbf{k} - \mathbf{k}') \quad (3.61)$$

$$\langle \overline{\mathbf{M}_{\mathbf{k}'}} \times \mathbf{M}_{\mathbf{k}} \rangle_{\mathbf{r}} = \langle \overline{\mathbf{N}_{\mathbf{k}'}} \times \mathbf{N}_{\mathbf{k}} \rangle_{\mathbf{r}} = \mathbf{0} \quad (3.62)$$

where the overline denotes complex conjugation. With this, the plane wave expansion of an electric field $\mathbf{E}(\mathbf{r})$ in a homogeneous medium, and its Fourier transformation $\mathbf{E}(\mathbf{k})$, may be defined as

$$\mathbf{E}(\mathbf{r}) = E_0 \frac{1}{(2\pi)^2} \langle a_{\mathbf{k}} \mathbf{M}_{\mathbf{k}}(\mathbf{r}) + b_{\mathbf{k}} \mathbf{N}_{\mathbf{k}}(\mathbf{r}) \rangle_{\mathbf{k}} \quad (3.63)$$

$$\mathbf{E}(\mathbf{k}) = E_0 \left[\mathbf{i} a_{\mathbf{k}} \hat{\mathbf{M}}_{\mathbf{k}} - b_{\mathbf{k}} \hat{\mathbf{N}}_{\mathbf{k}} \right] \quad (3.64)$$

where $a_{\mathbf{k}}$ and $b_{\mathbf{k}}$ are expansion coefficients with units of square meters, and E_0 is a reference electric field strength. Given \mathbf{E} , the expansion coefficients can be found from scalar projections:

$$a_{\mathbf{k}} = \frac{1}{E_0} \langle \overline{\mathbf{M}_{\mathbf{k}}} \cdot \mathbf{E} \rangle_{\mathbf{r}} = -\frac{\mathbf{i}}{E_0} \hat{\mathbf{M}}_{\mathbf{k}} \cdot \mathbf{E}(\mathbf{k}) \quad (3.65)$$

$$b_{\mathbf{k}} = \frac{1}{E_0} \langle \overline{\mathbf{N}_{\mathbf{k}}} \cdot \mathbf{E} \rangle_{\mathbf{r}} = -\frac{1}{E_0} \hat{\mathbf{N}}_{\mathbf{k}} \cdot \mathbf{E}(\mathbf{k}) \quad (3.66)$$

Faraday's law (Eq. (3.20)) provides an expression for the associated magnetic field

$$\mathbf{H}(\mathbf{r}) = -\frac{\mathbf{i} E_0 n}{c_0 \mu_0 \mu} \frac{1}{(2\pi)^2} \langle a_{\mathbf{k}} \mathbf{N}_{\mathbf{k}}(\mathbf{r}) + b_{\mathbf{k}} \mathbf{M}_{\mathbf{k}}(\mathbf{r}) \rangle_{\mathbf{k}} \quad (3.67)$$

$$\mathbf{H}(\mathbf{k}) = \frac{E_0 n}{c_0 \mu_0 \mu} \left[\mathbf{i} a_{\mathbf{k}} \hat{\mathbf{N}}_{\mathbf{k}} + b_{\mathbf{k}} \hat{\mathbf{M}}_{\mathbf{k}} \right] \quad (3.68)$$

where n is the refractive index of the homogeneous background medium. Note that all orthogonality conditions and the expressions for $\mathbf{E}(\mathbf{r})$ and $\mathbf{H}(\mathbf{r})$ can be evaluated at any point in space, but if the reference plane is shifted along the z -axis, the expansion coefficients $a_{\mathbf{k}}(z)$ and $b_{\mathbf{k}}(z)$ and the Fourier transformations $\mathbf{E}(\mathbf{k}; z) = \mathbf{E}(\mathbf{k}) e^{\mathbf{i} k_z z}$ and $\mathbf{H}(\mathbf{k}; z) = \mathbf{H}(\mathbf{k}) e^{\mathbf{i} k_z z}$ become dependent on z . Nevertheless, a mere multiplication with $e^{\mathbf{i} k_z z}$ in the frequency domain suffices to propagate any electromagnetic field in a homogeneous medium from the $z = 0$ to the $z \neq 0$ plane.

Lastly, an individual plane wave of arbitrary polarization, defined in terms of its electric field

$$\mathbf{E}(\mathbf{r}) = E_0 \left[\cos(\gamma) e^{\mathbf{i}\alpha} \mathbf{M}_{\mathbf{k}}(\mathbf{r}) + \sin(\gamma) e^{\mathbf{i}\beta} \mathbf{N}_{\mathbf{k}}(\mathbf{r}) \right] \quad (3.69)$$

$$\mathbf{H}(\mathbf{r}) = -\frac{\mathbf{i} E_0 n}{c_0 \mu_0 \mu} \left[\cos(\gamma) e^{\mathbf{i}\alpha} \mathbf{N}_{\mathbf{k}}(\mathbf{r}) + \sin(\gamma) e^{\mathbf{i}\beta} \mathbf{M}_{\mathbf{k}}(\mathbf{r}) \right] \quad (3.70)$$

with a given wavevector \mathbf{k} , electric field amplitude $E_0 \in \mathbb{C}$, and polarization parameters $\alpha, \beta, \gamma \in \mathbb{R}$, possesses an intensity $I = \mathbf{S} \cdot \hat{\mathbf{n}}$ (see Eq. (3.72)) that is invariant across the reference plane

$$I(z) = \frac{|E_0|^2}{2c_0 \mu_0 \mu} \text{Re}(n \cos(\theta)) \left[\cosh^2(\text{Im } \theta) - \cos(2\gamma) \sinh^2(\text{Im } \theta) \right] e^{-2 \text{Im}(k \cos(\theta)) z} \quad (3.71)$$

where it was assumed that $\mu \in \mathbb{R}$. The term in the square brackets shows that TM waves can yield higher intensities than TE waves, but since it expands to $1 + 2 \sin^2(\gamma) (\text{Im } \theta)^2 + \mathcal{O}((\text{Im } \theta)^4)$ for $\text{Im } \theta \approx 0$, this effect can be neglected in media with small gain or loss.

3.4.2. Area-averaged radiance

The time-averaged Poynting vector is defined as [176]

$$\mathbf{S}(\mathbf{r}) = \frac{1}{2} \operatorname{Re}(\mathbf{E}(\mathbf{r}) \times \overline{\mathbf{H}(\mathbf{r})}) \quad (3.72)$$

and the net energy flux (radiant flux) $P = \langle \mathbf{S} \cdot \hat{\mathbf{n}} \rangle_{\mathbf{r}}$ that passes through the reference plane of a plane wave expansion (Eqs. (3.63,64,67,68)) can be computed both in the spatial and the frequency domain $\langle \mathbf{E} \times \overline{\mathbf{H}} \rangle_{\mathbf{r}} = (2\pi)^{-2} \langle \mathbf{E} \times \overline{\mathbf{H}} \rangle_{\mathbf{k}}$. However, since either approach requires the evaluation of integrals that span across the entire reference plane, P can be infinite even if \mathbf{S} is finite everywhere. For example, an individual plane wave possesses an infinite energy flux, but its intensity is spatially-invariant and finite. Hence, to avoid such mathematical singularities, it is better to consider the area average of \mathbf{S} instead. The area-time-averaged Poynting vector $\langle \mathbf{S} \rangle$ may then be defined as

$$\langle \mathbf{S} \rangle = \lim_{\mathcal{R} \rightarrow \mathcal{A}} \frac{\langle \chi_{\mathcal{R}} \mathbf{S} \rangle_{\mathbf{r}}}{\langle \chi_{\mathcal{R}} \rangle_{\mathbf{r}}} \quad \chi_{\mathcal{A}} \mathbf{S} = \mathbf{S} \quad \mathcal{A} \subseteq \mathbb{R}^2 \quad (3.73)$$

where \mathcal{A} represents a physical aperture that is either fully transparent ($\mathcal{A} = \mathbb{R}^2$) or that truncates the electromagnetic field such that $\mathbf{S}(\mathbf{r}) = \mathbf{0}$ for $\mathbf{r} \notin \mathcal{A} \subset \mathbb{R}^2$, and the indicator function

$$\chi_{\mathcal{R}}(\mathbf{r}) = \begin{cases} 1 & \mathbf{r} \in \mathcal{R} \\ 0 & \mathbf{r} \notin \mathcal{R} \end{cases} \quad (3.74)$$

can be understood as a generalization of the Heaviside step function to higher dimensions. However, in situations where $\langle \mathbf{S} \rangle$ vanishes although \mathbf{S} is nonzero everywhere, or where \mathbf{S} is not known everywhere, one is forced to choose a smaller, virtual aperture $\mathcal{A}' \subset \mathcal{A}$ that approximates the exact area average in a meaningful way

$$\langle \mathbf{S} \rangle \approx \frac{\langle \mathbf{S} \rangle_{\mathbf{r}}}{A} \quad \chi_{\mathcal{A}'} \mathbf{S} \approx \mathbf{S} \quad A = \langle \chi_{\mathcal{A}'} \rangle_{\mathbf{r}} \quad (3.75)$$

where A is the transparent area of the virtual aperture \mathcal{A}' . With this, the area-averaged intensity (irradiance) $I = |\langle \mathbf{S} \rangle \cdot \hat{\mathbf{n}}|$ of a plane wave expansion can be expressed in terms of an integral, where the integrand can be interpreted as the following differential

$$\frac{d^2 I(\mathbf{k})}{dk_x dk_y} = \frac{|E_0|^2 n |a_{\mathbf{k}}|^2 + |b_{\mathbf{k}}|^2}{2c_0 \mu_0 \mu} \frac{1}{(2\pi)^2 A} |\hat{\mathbf{k}} \cdot \hat{\mathbf{n}}| \quad (3.76)$$

and the limit $\mathcal{A}' \rightarrow \mathcal{A}$ must be kept in mind. Here, it was assumed that $n, \mu \in \mathbb{R}$, and the choice of making I non-negative only affected the sign of $\hat{\mathbf{k}} \cdot \hat{\mathbf{n}}$. Furthermore, after a change of variables

$$dk_x dk_y = k_0^2 |\cos(\theta)| d\Omega \quad (3.77)$$

$$d\Omega = \sin(\theta) d\phi d\theta \quad (3.78)$$

where k_0 is the wavenumber of the homogeneous background medium and $d\Omega$ is the unit solid angle, and by comparison with the position-dependent radiance $L(\mathbf{r}, \theta, \phi) = dP(\mathbf{r}) / [\cos(\theta) dA d\Omega]$ where P is the energy flux along the direction of (θ, ϕ) into a unit solid angle $d\Omega$ that emerges from a surface element dA at the point \mathbf{r} of the radiating surface [176], an opportunity arises to identify and define the area-averaged radiance L in terms of the area-averaged intensity (irradiance) I :

$$L(\theta, \phi) = \frac{dI(\theta, \phi)}{|\cos(\theta)| d\Omega} = k_0^2 \frac{d^2 I(\mathbf{k})}{dk_x dk_y} \Big|_{\mathbf{k}=\mathbf{k}(\theta, \phi)} \quad (3.79)$$

The necessity for the area average can also be understood from the uncertainty principle of the Fourier transformations in the plane wave expansions: All quantities are either absolutely sharp in space or in frequency, but never simultaneously. In other words, the use of plane waves only allows for the knowledge of $I(\mathbf{r})$ or $I(\mathbf{k})$, but not $I(\mathbf{r}, \mathbf{k})$ as it would be required by $L(\mathbf{r}, \theta, \phi)$.

3.4.3. Directional scatterance

Since a planar structure transmits and reflects light into two distinct hemispheres, the hemispheres may as well be unified by composing the area-averaged intensity I in the form of

$$\frac{d^2 I(\mathbf{k})}{dk_x dk_y} = \frac{d^2}{dk_x dk_y} \begin{cases} I^T(\mathbf{k}) & \hat{\mathbf{k}} \cdot \hat{\mathbf{n}} \geq 0 \\ I^R(\mathbf{k}) & \hat{\mathbf{k}} \cdot \hat{\mathbf{n}} < 0 \end{cases} \quad (3.80)$$

where I^T is the transmitted and I^R the reflected area-averaged intensity on the respective side of the structure. Any plane wave expansion coefficients $(a_{\mathbf{k}}, b_{\mathbf{k}})$ can be unified in the same manner. Motivated by the differential forms in Eq. (3.79), the directional scatterance $Q_\Omega = L/I_0$ may be defined as

$$Q_\Omega(\mathbf{k}) = \frac{k_0^2}{I_0} \frac{d^2 I(\mathbf{k})}{dk_x dk_y} = \begin{cases} Q_\Omega^T & \hat{\mathbf{k}} \cdot \hat{\mathbf{n}} \geq 0 \\ Q_\Omega^R & \hat{\mathbf{k}} \cdot \hat{\mathbf{n}} < 0 \end{cases} \quad (3.81)$$

$$Q_\Omega(\theta, \phi) = \frac{1}{I_0} \frac{dI(\theta, \phi)}{|\cos(\theta)| d\Omega} = Q_\Omega(\mathbf{k}(\theta, \phi)) \quad (3.82)$$

where I_0 is the intensity of an arbitrarily-polarized plane wave that illuminates the structure, and Q_Ω^T and Q_Ω^R are the directional transmittance and reflectance, respectively. Physically, one may interpret Q_Ω as the fraction of the incident intensity that is scattered along (θ, ϕ) into a projected unit solid angle, or equivalently, as the normalized intensity recorded in the back-focal-plane of a lens that collects the light transmitted or reflected by the planar structure. Given the unified plane wave expansion coefficients $(a_{\mathbf{k}}, b_{\mathbf{k}})$, the directional scatterance of a plane wave expansion is then found to equal

$$Q_\Omega(\mathbf{k}) = k_0^2 \frac{|a_{\mathbf{k}}|^2 + |b_{\mathbf{k}}|^2}{(2\pi)^2 \cos(\theta_0) A} |\hat{\mathbf{k}} \cdot \hat{\mathbf{n}}| \quad (3.83)$$

where θ_0 is the incidence angle of the illuminating plane wave. Since $a_{\mathbf{k}}$ and $b_{\mathbf{k}}$ correspond to TE and TM polarized plane waves, respectively, it is trivial to separate their contributions as in $Q_\Omega = Q_\Omega^{\text{TE}} + Q_\Omega^{\text{TM}}$. Furthermore, the azimuthal scatterance Q_ϕ and the polar scatterance Q_θ may be defined as the definite integral of Q_Ω with respect to either θ or ϕ

$$Q_\phi(\phi) = \frac{dQ(\phi)}{d\phi} = \int_0^\pi Q_\Omega(\theta, \phi) \sin(\theta) |\cos(\theta)| d\theta \quad (3.84)$$

$$Q_\theta(\theta) = \frac{dQ(\theta)}{d\theta} = \int_{-\pi}^\pi Q_\Omega(\theta, \phi) \sin(\theta) |\cos(\theta)| d\phi = \frac{|\sin(2\theta)|}{2} \int_{-\pi}^\pi Q_\Omega(\theta, \phi) d\phi \quad (3.85)$$

which can also be interpreted as the azimuthal $dQ = Q_\phi d\phi$ and polar $dQ = Q_\theta d\theta$ contributions to the total scatterance Q . Note that due to energy conservation, $Q = 1$ in the absence of gain and loss. Moreover, the sectorial scatterance $Q(\theta)$ may be defined as the antiderivative of Q_θ

$$Q(\theta) = \int_0^\theta Q_\theta(\theta') d\theta' + \Delta(\theta) \quad (3.86)$$

which represents the fraction of the incident intensity that is scattered into a spherical sector with an half-angle of $\theta \in [0, \pi]$ with respect to $\hat{\mathbf{n}}$. Since the determinant of the Jacobian matrix vanishes for the given coordinate transformation at the critical points $\theta \in \{0, \pi\}$, the piecewise constant function

$$\Delta(\theta) = \lim_{\mathcal{K} \rightarrow \{\mathbf{0}\}} \left[\frac{\langle \chi_{\mathcal{K}} Q_\Omega^T \rangle_{\mathbf{k}}}{k_0^2} + \delta_{\theta, \pi} \frac{\langle \chi_{\mathcal{K}} Q_\Omega^R \rangle_{\mathbf{k}}}{k_0^2} \right] \quad (3.87)$$

with the Kronecker delta $\delta_{i,j}$ was included as to capture any Dirac deltas that may be present at the critical points. In other words, Δ can be understood as an integration constant that vanishes due to Sard's theorem if Q_Ω is finite at the critical points [179], or introduces jump discontinuities otherwise.

With this, the hemispherical transmittance Q^T and reflectance Q^R

$$Q^T = \frac{\langle Q_\Omega^T \rangle_{\mathbf{k}}}{k_0^2} = Q\left(\frac{\pi}{2}\right) \quad Q^R = \frac{\langle Q_\Omega^R \rangle_{\mathbf{k}}}{k_0^2} = Q(\pi) - Q\left(\frac{\pi}{2}\right) \quad (3.88)$$

trivially satisfy $Q^T + Q^R = Q(\pi) = Q$. See Appendix A.1 for a definition of ideal scatterers. Lastly, it is desirable to define a quantity that measures how efficiently a structure diffuses all incident light. Here, diffusion shall be understood as the capability of a structure to redistribute the optical energy from the zeroth order in transmission and reflection along all other directions. Hence, one may simply compute Q from Q_Ω while excluding the zeroth orders, but since certain structures scatter mainly or even exclusively along directions that can be associated with diffraction orders, a fairer comparison of different structures can be achieved if not only the zeroth orders, but also all higher diffraction orders are excluded. To this end, the diffuse scatterance Q^D may be defined as

$$Q^D = Q - \lim_{\mathcal{K} \rightarrow \mathcal{K}^T} \frac{\langle \chi_{\mathcal{K}} Q_\Omega^T \rangle_{\mathbf{k}}}{k_0^2} - \lim_{\mathcal{K} \rightarrow \mathcal{K}^R} \frac{\langle \chi_{\mathcal{K}} Q_\Omega^R \rangle_{\mathbf{k}}}{k_0^2} \quad (3.89)$$

where \mathcal{K}^T and \mathcal{K}^R are sets of wavevectors that are associated with the zeroth and, if applicable, all higher diffraction orders of the structure. In this context, the countably many directions represented by \mathcal{K}^T and \mathcal{K}^R are referred to as the *regular directions*, and their continuum-forming complement constitutes the *diffuse directions*. Note that in the absence of gain and loss, for negligible cross-polarization, and if no higher diffraction orders are excited, the diffuse scatterance simplifies to $Q^D = 1 - T - R$, where T and R are the transmittance and reflectance (cf. Sec. 3.4.4), respectively.

3.4.4. Generalized transmission coefficient

Given that a planar structure is excited by a TE or TM polarized plane wave with an electric field of

$$\mathbf{E}_0^X(\mathbf{r}) = E_0^X \begin{cases} \mathbf{M}_{\mathbf{k}_0}(\mathbf{r}) & \text{X: TE} \\ \mathbf{N}_{\mathbf{k}_0}(\mathbf{r}) & \text{X: TM} \end{cases} \quad (3.90)$$

where E_0^X is the complex-valued amplitude, \mathbf{k}_0 the wavevector, and X the polarization state of the incident wave, the generalized transmission coefficient of the structure may then be defined as

$$t_{\mathbf{k}}^{X,Y} = \lim_{\mathcal{R} \rightarrow \mathbb{R}^2} \frac{1}{E_0^X \langle \chi_{\mathcal{R}} \rangle_{\mathbf{r}}} \begin{cases} \langle \chi_{\mathcal{R}} \overline{\mathbf{M}}_{\mathbf{k}} \cdot \mathbf{E} \rangle_{\mathbf{r}} & \text{Y: TE} \\ \langle \chi_{\mathcal{R}} \overline{\mathbf{N}}_{\mathbf{k}} \cdot \mathbf{E} \rangle_{\mathbf{r}} & \text{Y: TM} \end{cases} \approx \frac{1}{A} \begin{cases} a_{\mathbf{k}} & \text{Y: TE} \\ b_{\mathbf{k}} & \text{Y: TM} \end{cases} \quad (3.91)$$

where \mathbf{E} is the total electric field transmitted by the planar structure, Y is the polarization state of a transmitted plane wave with wavevector \mathbf{k} , and the limit represents an area-averaging operation that is analogous to that introduced in Sec. 3.4.2. The approximate equality applies to the situation where \mathbf{E} is only known over a finite area A , in which case the generalized transmission coefficient can be computed from an area-average of the plane wave expansion coefficients.

In the remainder of this thesis, the zeroth-order co-polarized transmission coefficient is simply referred to as the transmission coefficient t , and the transmittance T and phase φ are defined as:

$$t = t_{\mathbf{k}_0}^{X,X} \quad T = |t|^2 \quad \varphi = \arg(t) \quad (3.92)$$

The zeroth-order reflection coefficient r and the reflectance $R = |r|^2$ are defined analogously to Eqs. (3.91,92), with the exception that \mathbf{k}_0 must be replaced by its reflection $\mathcal{R}\mathbf{k}_0$.

Moreover, the definitions of the transmission coefficient profile $t(\mathbf{r})$, the transmittance profile $T(\mathbf{r})$, and the phase profile $\varphi(\mathbf{r})$ are obtained by omitting the integrals in Eqs. (3.91,92).

Lastly, the spatial statistics of transmittance and phase profiles are expressed in terms of means μ_T, μ_φ and variances $\sigma_T^2, \sigma_\varphi^2$, where the ring accents emphasize on the circular nature of the phase angle and the use of corresponding circular moments. See Appendix A.4 for the definition of statistical quantities that are based on standard, folded, and wrapped normal distributions.

3.5. Spherical vector wave functions

The scalar wave equation (Eq. (3.36)) reads in spherical coordinates (r, θ, ϕ) as:

$$\left[r^2 \partial_r^2 + 2r \partial_r + \partial_\theta^2 + \frac{\cos(\theta)}{\sin(\theta)} \partial_\theta + \frac{1}{\sin^2(\theta)} \partial_\phi^2 + k^2 r^2 \right] \psi(r, \theta, \phi) = 0 \quad (3.93)$$

After assuming that the scalar potential is separable in each coordinate $\psi(r, \theta, \phi) = R(r) \Theta(\theta) \Phi(\phi)$ and performing the separation of variables by introducing the polar mode number n and azimuthal mode number m , the scalar wave equation splits into the following set of differential equations and general solutions with integration constants c_i

$$\left[r^2 \partial_r^2 + 2r \partial_r + k^2 r^2 - n(n+1) \right] R(r) = 0 \quad R(r) = c_1 j_n(kr) + c_2 y_n(kr) \quad (3.94)$$

$$\left[\partial_\theta^2 + \frac{\cos(\theta)}{\sin(\theta)} \partial_\theta + n(n+1) - \frac{m^2}{\sin^2(\theta)} \right] \Theta(\theta) = 0 \quad \Theta(\theta) = c_3 P_n^m(\cos \theta) + c_4 Q_n^m(\cos \theta) \quad (3.95)$$

$$\left[\partial_\phi^2 + m^2 \right] \Phi(\phi) = 0 \quad \Phi(\phi) = c_5 e^{im\phi} + c_6 e^{-im\phi} \quad (3.96)$$

where j_n and y_n are spherical Bessel functions with integers $n \geq 0$, and P_n^m and Q_n^m are associated Legendre polynomials with integers $-n \leq m \leq n$. If the mode numbers were not integers, P_n^m would exhibit singularities at $\theta \in \{0, \pi\}$ and thus produce nonphysical solutions along the entire polar axis. Moreover, since Q_n^m remains to exhibit logarithmic singularities even for integer mode numbers, this solution can be rejected altogether. Hence, the scalar potential may be defined as

$$\psi_n^m(\mathbf{r}; k, i) = \check{z}_n(kr; i) \Psi_n^m(\cos \theta) e^{im\phi} \quad (3.97)$$

$$\nabla \psi_n^m(\mathbf{r}; k, i) = \left[\hat{\mathbf{r}} \partial_r + \hat{\boldsymbol{\theta}} \frac{1}{r} \partial_\theta + \hat{\boldsymbol{\phi}} \frac{im}{r \sin(\theta)} \right] \psi_n^m(\mathbf{r}; k, i) \quad (3.98)$$

where Ψ_n^m represents a convenient normalization factor, and \check{z}_n enumerates linear combinations of spherical Bessel functions including the spherical Hankel functions $h_n^{(1)}$ and $h_n^{(2)}$:

$$\Psi_n^m = \sqrt{\frac{1}{2\pi} \frac{2n+1}{2n(n+1)} \frac{(n-m)!}{(n+m)!}} \quad \check{z}_n(kr; i) = \begin{cases} j_n(kr) & i = 1 \\ y_n(kr) & i = 2 \\ h_n^{(1)}(kr) = j_n(kr) + \mathbf{i} y_n(kr) & i = 3 \\ h_n^{(2)}(kr) = j_n(kr) - \mathbf{i} y_n(kr) & i = 4 \end{cases} \quad (3.99)$$

Finally, with the radial pilot vector $\mathbf{v} = k\mathbf{r}$, the spherical vector wave functions can be written as:

$$\mathbf{M}_n^m(\mathbf{r}; k, i) = \left[\hat{\boldsymbol{\theta}} \frac{im}{\sin(\theta)} - \hat{\boldsymbol{\phi}} \partial_\theta \right] \psi_n^m(\mathbf{r}; k, i) \quad (3.100)$$

$$\mathbf{N}_n^m(\mathbf{r}; k, i) = \frac{1}{kr} \left[\hat{\mathbf{r}} n(n+1) + \hat{\boldsymbol{\theta}} \partial_\theta [r \partial_r + 1] + \hat{\boldsymbol{\phi}} \frac{im}{\sin(\theta)} [r \partial_r + 1] \right] \psi_n^m(\mathbf{r}; k, i) \quad (3.101)$$

Note that without Ψ_n^m , the functions $\mathbf{M}_0^0 = \mathbf{N}_0^0 = \mathbf{0}$ vanish everywhere since n and m appear as prefactors and $\partial_\theta \psi_0^0 = 0$. Consequently, one may as well require $n \geq 1$ and introduce a Ψ_n^m that is singular at $n = 0$. The motivation behind the presented Ψ_n^m is to simplify the orthogonality conditions of the vector wave functions and to render $\psi_n^{\pm m}$ more symmetric.

Lastly, \mathbf{N}_n^m and \mathbf{M}_n^m are commonly referred to as the electric and magnetic vector spherical harmonics, respectively. The reason for this convention is that only \mathbf{N}_n^m can represent a directed vector field due to its radial component, and if it is used to represent a directed electric field, it is accompanied by a purely circulating magnetic field in the shape of \mathbf{M}_n^m . Moreover, since n represents electromagnetic modes with up to 2^n poles, the first few orders $n = 0, 1, 2, 3$ are commonly referred to as: monopole, dipole, quadrupole, octopole. Since the monopole cannot be expressed in terms of divergence-free vector wave functions, it must be associated with a curl-free field. This makes the dipole the fundamental mode in homogeneous media.

3.5.1. Orthogonality conditions

The following abbreviations represent volume and solid angle integrals in spherical coordinates:

$$\langle f \rangle_V = \int_0^\infty \langle f \rangle_\Omega r^2 dr \quad \langle f \rangle_\Omega = \int_0^\pi \int_0^{2\pi} f(r, \theta, \phi) \sin(\theta) d\phi d\theta \quad (3.102)$$

With the help of several additional identities (Appendix A.2), the scalar products are found to equal

$$\langle \overline{\mathbf{M}}_{n'}^{m'} \cdot \mathbf{N}_n^m \rangle_\Omega = 0 \quad (3.103)$$

$$\langle \overline{\mathbf{M}}_{n'}^{m'} \cdot \mathbf{M}_n^m \rangle_\Omega = \overline{\zeta}_n(k'r; i') \zeta_n(kr; i) \delta_{m, m'} \delta_{n, n'} \quad (3.104)$$

$$\langle \overline{\mathbf{N}}_{n'}^{m'} \cdot \mathbf{N}_n^m \rangle_\Omega = \frac{(n+1) \overline{\zeta}_{n-1}(k'r; i') \zeta_{n-1}(kr; i) + n \overline{\zeta}_{n+1}(k'r; i') \zeta_{n+1}(kr; i)}{2n+1} \delta_{m, m'} \delta_{n, n'} \quad (3.105)$$

and the special case for $i = i' = 1$

$$\langle \overline{\mathbf{M}}_{n'}^{m'} \cdot \mathbf{M}_n^m \rangle_V = \langle \overline{\mathbf{N}}_{n'}^{m'} \cdot \mathbf{N}_n^m \rangle_V = \frac{\pi}{2k^2} \delta_{m, m'} \delta_{n, n'} \delta(k - k') \quad (3.106)$$

can be seen as an integral representation of the Dirac delta function $\delta(k - k')$. For the computation of the energy flow through a spherical surface, it is convenient to note that

$$\langle [\mathbf{M}_n^m \times \overline{\mathbf{N}}_{n'}^{m'}] \cdot \hat{\mathbf{r}} \rangle_\Omega = \frac{(n+1) \overline{\zeta}_{n-1}(k'r; i') - n \overline{\zeta}_{n+1}(k'r; i')}{2n+1} \zeta_n(kr; i) \delta_{m, m'} \delta_{n, n'} \quad (3.107)$$

$$\langle [\mathbf{M}_n^m \times \overline{\mathbf{M}}_{n'}^{m'}] \cdot \hat{\mathbf{r}} \rangle_\Omega = 0 \quad (3.108)$$

$$\langle [\mathbf{N}_n^m \times \overline{\mathbf{N}}_{n'}^{m'}] \cdot \hat{\mathbf{r}} \rangle_\Omega = 0 \quad (3.109)$$

and the special case for $i = i' = 3$ and $k = k'$

$$\text{Im} \langle [\mathbf{M}_n^m \times \overline{\mathbf{N}}_{n'}^{m'}] \cdot \hat{\mathbf{r}} \rangle_\Omega = \text{Im} \langle [\mathbf{N}_n^m \times \overline{\mathbf{M}}_{n'}^{m'}] \cdot \hat{\mathbf{r}} \rangle_\Omega = -\frac{1}{k^2 r^2} \delta_{m, m'} \delta_{n, n'} \quad (3.110)$$

relies on a property of spherical Hankel functions (Appendix A.2).

3.5.2. Multipole expansion and scattered field formalism

The main idea behind the scattered field formalism is to utilize the superposition principle of the vector wave equation in piecewise homogeneous media (Eq. (3.34)) for the separation of the total electric field \mathbf{E} into a background electric field \mathbf{E}_b and a scattered electric field \mathbf{E}_s [38, 176]

$$\mathbf{E}(\mathbf{r}, \omega) = \mathbf{E}_b(\mathbf{r}, \omega) + \mathbf{E}_s(\mathbf{r}, \omega) \quad k^2(\mathbf{r}, \omega) = k_b^2(\omega) + \chi_V(\mathbf{r}) k_s^2(\omega) \quad (3.111)$$

where k_b is the wavenumber of the homogeneous background medium, k_s represents a scattering structure that modulates the refractive index of the background medium within a finite volume V , and χ_V is the indicator function of this volume (Eq. (3.74)). Given that \mathbf{E} and \mathbf{E}_b are governed by homogeneous wave equations, $[\nabla^2 + k^2] \mathbf{E}$ splits into an inhomogeneous wave equation for \mathbf{E}_s :

$$[\nabla^2 + k^2(\omega)] \mathbf{E}(\mathbf{r}, \omega) = \mathbf{0} \quad k^2(\omega) \in \mathbb{C} \quad (3.112)$$

$$[\nabla^2 + k_b^2(\omega)] \mathbf{E}_b(\mathbf{r}, \omega) = \mathbf{0} \quad k_b^2(\omega) \in \mathbb{R} \quad (3.113)$$

$$[\nabla^2 + k_b^2(\omega)] \mathbf{E}_s(\mathbf{r}, \omega) = -\chi_V(\mathbf{r}) k_s^2(\omega) \mathbf{E}(\mathbf{r}, \omega) \quad k_s^2(\omega) = k^2(\omega) - k_b^2(\omega) \quad (3.114)$$

The scattered field can be understood as a superposition of outgoing wavelets that originate from within the scattering volume and are generated by the total field. Since the total field may in turn be understood as the superposition of the background field and all scattered wavelets, the scattered field represents a self-consistent solution that readily takes into account how all wavelets influence each

others generations due to interference effects within the scattering volume. The background field can be seen as an external wave that excites the scattering structure. Although it is admissible to use a piecewise constant background medium, which is typically very easy to simulate with electromagnetic field solvers, the presented formalism assumes a single background medium that extends to infinity. The reason for this assumption is related to the fact that the orthogonality conditions of the spherical vector wave functions only hold in a homogeneous background and that the derivation and evaluation of the Green's dyadic for a piecewise constant background can be very challenging.

With these considerations in mind, the scattered electric field and its associated magnetic field can be expanded in terms of spherical vector wave functions

$$\mathbf{E}_s(\mathbf{r}) = E_0 \sum_{n=1}^{\infty} \sum_{m=-n}^n [a_n^m \mathbf{N}_n^m(\mathbf{r}; k_b, 3) + b_n^m \mathbf{M}_n^m(\mathbf{r}; k_b, 3)] \quad (3.115)$$

$$\mathbf{H}_s(\mathbf{r}) = -\frac{\mathbf{i}E_0 k_b}{\omega \mu_0 \mu_b} \sum_{n=1}^{\infty} \sum_{m=-n}^n [a_n^m \mathbf{M}_n^m(\mathbf{r}; k_b, 3) + b_n^m \mathbf{N}_n^m(\mathbf{r}; k_b, 3)] \quad (3.116)$$

where E_0 is a reference electric field strength and a_n^m and b_n^m are the multipole expansion coefficients. Note that since the spherical Hankel function of first kind ($i = 3$) is singular at the origin, this expansion should only be used outside of the scattering volume. For expansions within the scattering volume, the spherical Bessel function of first kind ($i = 1$) should be used instead.

Multipole expansion based on orthogonality Given the scattered electric field \mathbf{E}_s on a spherical surface with a radius of r_0 that encloses the entire scattering volume, the multipole coefficients

$$a_n^m = \frac{1}{E_0} \frac{\langle \overline{\mathbf{N}_n^m} \cdot \mathbf{E}_s \rangle_{\Omega}}{\langle \overline{\mathbf{N}_n^m} \cdot \mathbf{N}_n^m \rangle_{\Omega}} \Big|_{r=r_0} \quad b_n^m = \frac{1}{E_0} \frac{\langle \overline{\mathbf{M}_n^m} \cdot \mathbf{E}_s \rangle_{\Omega}}{\langle \overline{\mathbf{M}_n^m} \cdot \mathbf{M}_n^m \rangle_{\Omega}} \Big|_{r=r_0} \quad (3.117)$$

are easily found from Eq. (3.115) with the help of the orthogonality conditions Eqs. (3.103–105). The origin of the coordinate system is often placed at the geometric center of the scattering volume.

Multipole expansion based on impulse response The inhomogeneous wave equation of the scattered electric field (Eq. (3.114)) can be solved with the help of the Green's dyadic \mathbf{G} [38]

$$[\nabla^2 + k_b^2] \mathbf{G}(\mathbf{r}, \mathbf{r}') = -\mathbf{I} \delta(\mathbf{r} - \mathbf{r}') \quad (3.118)$$

where \mathbf{I} is the identity matrix and \mathbf{G} can be understood as the impulse response of the scattering structure given a point-like excitation at \mathbf{r}' . The solution can be written as

$$\mathbf{E}_s(\mathbf{r}) = k_s^2 \int_{\mathbb{R}^3} \mathbf{G}(\mathbf{r}, \mathbf{r}') \cdot \mathbf{E}(\mathbf{r}') \chi_V(\mathbf{r}') \, d\mathbf{r}' = k_s^2 \int_V \mathbf{G}(\mathbf{r}, \mathbf{r}') \cdot \mathbf{E}(\mathbf{r}') \, d\mathbf{r}' \quad (3.119)$$

which can be confirmed by applying $[\nabla^2 + k_b^2]$ to this equation and substituting Eq. (3.118). Hence, once the explicit form of \mathbf{G} is known, the scattered field outside of the scattering volume can be computed from the total field within the scattering volume. With the Dirac delta representation from Eq. (3.106) and several other considerations (Appendix A.2), the Green's dyadic is found to equal

$$\mathbf{G}(\mathbf{r}, \mathbf{r}') = \mathbf{i}k_b \sum_{n=1}^{\infty} \sum_{m=-n}^n \left[\mathbf{M}_n^m(\mathbf{r}; k_b, 3) \overline{\mathbf{M}_n^m(\mathbf{r}'; k_b, 1)} + \mathbf{N}_n^m(\mathbf{r}; k_b, 3) \overline{\mathbf{N}_n^m(\mathbf{r}'; k_b, 1)} \right] \quad (3.120)$$

which, however, is only valid for $r \geq r'$ where the radius r' represents the smallest sphere that encloses the entire scattering volume. Hence, it is best to choose the geometric center of the scattering volume as the origin of the spherical coordinate system.

When Eq. (3.120) is inserted into Eq. (3.119) and compared with Eq. (3.115), it is found that the multipole expansion coefficients must equal:

$$a_n^m = \mathfrak{i} \frac{k_b k_s^2}{E_0} \int_V \overline{\mathbf{N}_n^m(\mathbf{r}'; k_b, 1)} \cdot \mathbf{E}(\mathbf{r}') \, d\mathbf{r}' \quad (3.121)$$

$$b_n^m = \mathfrak{i} \frac{k_b k_s^2}{E_0} \int_V \overline{\mathbf{M}_n^m(\mathbf{r}'; k_b, 1)} \cdot \mathbf{E}(\mathbf{r}') \, d\mathbf{r}' \quad (3.122)$$

It is important to note that this multipole expansion is only exact if the homogeneous background medium extends to infinity, but it can still be performed even if the background medium is piecewise constant. Due to this reason, it is worth to discuss the physical implications of the latter: The total field induces currents inside the scattering volume that, in turn, generate the scattered field. However, by using this multipole expansion, it is as if the induced currents were taken out of the piecewise constant background and placed into a homogeneous background. The resulting scattered field can again be thought of as being generated by these currents, but with the important difference that it does not couple back to the currents. The scattered field obtained in this way is therefore not a self-consistent solution and it is not identical to the actual scattered field in the piecewise constant medium. Despite these differences, it is often still possible to obtain a qualitatively correct decomposition of the actual scattered field.

Scattering cross section The energy flux of the scattered field through a spherical surface that encloses the entire scattering volume can be written as

$$P_s = \frac{1}{2} \operatorname{Re} \langle [\mathbf{E}_s \times \overline{\mathbf{H}_s}] \cdot \hat{\mathbf{r}} \rangle_{\Omega} r^2 \quad (3.123)$$

where r is the radius of the sphere, and the factor of r^2 stems from the surface element $dS = r^2 d\Omega$. The scattering cross section C_s is defined as [34, 39]

$$C_s = \frac{P_s}{I_0} \quad I_0 = \frac{|E_0|^2 n_b}{2c_0 \mu_0 \mu_b} \quad (3.124)$$

where I_0 is interpreted as the incident intensity of an arbitrarily polarized plane wave (cf. Eq. (3.71)). With this, the scattering cross section of a multipole expansion

$$C_s = \frac{1}{k_b^2} \sum_{n=1}^{\infty} \sum_{m=-n}^n [|a_n^m|^2 + |b_n^m|^2] \quad (3.125)$$

is found by inserting Eqs. (3.115,116) into Eq. (3.123) and applying Eq. (3.110) and $\operatorname{Re}(\mathfrak{i}z) = -\operatorname{Im}(z)$. Lastly, this expression motivates the definition of partial scattering cross sections

$$C_s = \sum_{n=1}^{\infty} [C_{s,n}^E + C_{s,n}^M] \quad C_{s,n}^E = \frac{1}{k_b^2} \sum_{m=-n}^n |a_n^m|^2 \quad C_{s,n}^M = \frac{1}{k_b^2} \sum_{m=-n}^n |b_n^m|^2 \quad (3.126)$$

where $C_{s,n}^E$ and $C_{s,n}^M$ represent the contributions of electric-type and magnetic-type n -poles to the full scattering cross section, respectively.

4. Particle Statistics

4.1. Structure factor and pair correlation function

In statistical mechanics [180], the n -particle density $\rho_N^{(n)}(\mathbf{r}^n)$ of a system of N identical particles with random coordinates $\mathbf{R}^N = \mathbf{R}_1, \dots, \mathbf{R}_N$ is defined as a probability density function that quantifies how likely it is to find a specific configuration of n particles at the query coordinates $\mathbf{r}^n = \mathbf{r}_1, \dots, \mathbf{r}_n$ per combined volume element $d\mathbf{r}^n = d\mathbf{r}_1 \cdots d\mathbf{r}_n$. To construct this probability density function, one may first count how often a given particle configuration occurs in each concrete realization of the system, and then take the ensemble average across all possible realizations. For example, the single-particle density $\rho_N^{(1)}$ and the pair density $\rho_N^{(2)}$ can be written as

$$\rho_N^{(1)}(\mathbf{r}_1) = \left\langle \sum_{i=1}^N \delta(\mathbf{r}_1 - \mathbf{R}_i) \right\rangle \quad (4.1)$$

$$\rho_N^{(2)}(\mathbf{r}_1, \mathbf{r}_2) = \left\langle \sum_{i=1}^N \sum_{\substack{j=1 \\ j \neq i}}^N \delta(\mathbf{r}_1 - \mathbf{R}_i) \delta(\mathbf{r}_2 - \mathbf{R}_j) \right\rangle \quad (4.2)$$

where $\langle \cdot \rangle$ denotes the ensemble average with respect to \mathbf{R}^N . Consequently, the integral of $\rho_N^{(n)}$ over all $d\mathbf{r}^n$ yields the number of permutations of n -particle configurations present in the system:

$$\int_V \rho_N^{(n)}(\mathbf{r}^n) d\mathbf{r}^n = \frac{N!}{(N-n)!} \quad (4.3)$$

In a homogeneous and isotropic ideal gas that consists of non-interacting and uniformly-distributed particles with a number density of $\rho = N/V$, all n -particle densities are spatially invariant and approach $\lim_{N \rightarrow \infty} \rho_N^{(n)} = \rho^n$. This motivates the definition of the n -particle distribution function

$$g_N^{(n)}(\mathbf{r}^n) = \frac{\rho_N^{(n)}(\mathbf{r}^n)}{\prod_{i=1}^n \rho_N^{(1)}(\mathbf{r}_i)} \quad (4.4)$$

which quantifies by how much the system deviates from the completely random ideal gas. Note that the denominator simplifies to ρ^n for homogeneous systems. Furthermore, since the absolute position of \mathbf{r}^n is irrelevant in homogeneous systems, it is convenient to marginalize one coordinate and to define the pair correlation function as

$$g(\mathbf{r}) = \frac{1}{V} \int_V g_N^{(2)}(\mathbf{r}_1, \mathbf{r}_1 + \mathbf{r}) d\mathbf{r}_1 = \frac{1}{\rho} \left\langle \frac{1}{N} \sum_{i=1}^N \sum_{\substack{j=1 \\ j \neq i}}^N \delta(\mathbf{r} - [\mathbf{R}_j - \mathbf{R}_i]) \right\rangle \quad (4.5)$$

where \mathbf{r} has now the meaning of a difference vector as in $\mathbf{r} = \mathbf{r}_2 - \mathbf{r}_1$. The structure factor $S(\mathbf{k})$ is essentially the Fourier transformation of the pair correlation function

$$S(\mathbf{k}) = 1 + \rho \int_{\mathbb{R}^D} [g(\mathbf{r}) - 1] e^{-i\mathbf{k} \cdot \mathbf{r}} d\mathbf{r} \quad (4.6)$$

$$g(\mathbf{r}) = 1 + \frac{1}{(2\pi)^D \rho} \int_{\mathbb{R}^D} [S(\mathbf{k}) - 1] e^{i\mathbf{k} \cdot \mathbf{r}} d\mathbf{k} \quad (4.7)$$

where small modifications were introduced to render S and g both unitless and square-integrable. Moreover, by inserting the explicit form of g from Eq. (4.5) into Eq. (4.6), it is possible to write S and g alternatively as

$$S(\mathbf{k}) = \langle \tilde{S}(\mathbf{k}) \rangle - (2\pi)^D \rho \delta(\mathbf{k}) \quad (4.8)$$

$$g(\mathbf{r}) = \frac{1}{(2\pi)^D \rho} \int_{\mathbb{R}^D} [\langle \tilde{S}(\mathbf{k}) \rangle - 1] e^{i\mathbf{k} \cdot \mathbf{r}} d\mathbf{k} \quad (4.9)$$

where $\tilde{S}(\mathbf{k})$ is the microscopic structure factor

$$\tilde{S}(\mathbf{k}) = \frac{|\tilde{\rho}(\mathbf{k})|^2}{N} \quad \tilde{\rho}(\mathbf{k}) = \sum_{n=1}^N e^{-i\mathbf{k}\cdot\mathbf{R}_n} \quad (4.10)$$

and $\tilde{\rho}(\mathbf{k})$ is the Fourier transformation of the microscopic particle density $\tilde{\rho}(\mathbf{r})$. The tilde accents and the term *microscopic* shall emphasize that these quantities do not characterize the macrostate (ensemble average) of the system, but rather only one concrete microstate (realization) for which all coordinates \mathbf{R}^N are fixed. Lastly, note that S and g inherit the Hermitian symmetry of $\tilde{\rho}(-\mathbf{k}) = \overline{\tilde{\rho}(\mathbf{k})}$, $\tilde{S}(\mathbf{0}) = \tilde{\rho}(\mathbf{0}) = N$ count all particles, \tilde{S} can also be written as a nonuniform cosine transformation

$$\tilde{S}(\mathbf{k}) = 1 + \frac{2}{N} \sum_{i=1}^{N-1} \sum_{j=i+1}^N \cos(\mathbf{k} \cdot [\mathbf{R}_j - \mathbf{R}_i]) \quad (4.11)$$

which requires the explicit computation of $N(N-1)/2$ pair distances, and see Appendix A.3 for the definition of the radial functions $S(k)$ and $g(r)$, and Appendix B.5 for numerical considerations.

4.2. Collective coordinate method

This section presents an extension of the collective coordinate method [181–183]. The collective coordinate method is formulated as an optimization problem that seeks a finite number of particle coordinates in a finite-sized simulation domain such that the corresponding structure factor takes a prescribed shape. The method was extended by a simultaneous constraint on the pair correlation function, which can not only be used to ensure a minimum distance between all particles, but also to fine-tune the system's short-range order.

The computational efficiency of this method stems from the use of fast Fourier transformations and the observation that for a large number of particles, it is considerably more favorable to obtain the structure factor from Eq. (4.10) than from Eq. (4.11) or a histogram of the pair correlation function as in Eq. (4.5). Contrary to histogram-based approaches, the direct computation of the structure factor further provides continuously differentiable analytic expressions that are needed by gradient-based large-scale optimization routines such as the Broyden-Fletcher-Goldfarb-Shanno algorithm [184–187] and its memory-limited variants. Lastly, the periodic boundary conditions of the fast Fourier transformations also resolve the paradoxical situation of simulating a homogeneous particle system on a finite-sized domain: Any finite system would be inhomogeneous if it was not extended to infinity by suitable boundary conditions. In fact, even if the simulation domain was surrounded by a sufficiently large but finite number of other particles, and only those directed distances that start from within the simulation domain were taken into account, the system would still classify as inhomogeneous. This can be seen in the derivation of Eq. (4.11) from Eq. (4.10), where the structure factor would become complex-valued if not all bi-directional pair distances were accounted for. Hence, it seems that periodic boundary conditions are the only suitable boundary conditions for this method.

The main input parameters of a D -dimensional particle system can be summarized as

$$\rho = \frac{N}{\prod_{d=1}^D p_d} \quad \Delta\mathbf{r} = \frac{\mathbf{p}}{\mathbf{L}} \quad \mathbf{0} \leq \mathbf{R}_n^m < \mathbf{p} \quad n = 1, \dots, N \quad m = 1, \dots, M \quad (4.12)$$

where ρ is the particle density, N is the number of particle coordinates in each realization, M is the number of independent realizations for the computation of the ensemble average, $\mathbf{p} = (p_1, \dots, p_d)$ represents the side lengths of the periodic simulation domain, $\Delta\mathbf{r}$ is the spatial resolution of the simulation domain and of the pair correlation function, \mathbf{L} represents the number of sample points in each dimension, and all particle coordinates \mathbf{R}_n^m require suitable initial guesses. With this, the ensemble average of the microscopic structure factor $\langle \tilde{S} \rangle$ can be computed from nonuniform Fourier transformations of the particle coordinates

$$\langle \tilde{S}(\mathbf{k}) \rangle = \frac{1}{M} \sum_{m=1}^M \tilde{S}_m(\mathbf{k}) \quad \tilde{S}_m(\mathbf{k}) = \frac{|\tilde{\rho}_m(\mathbf{k})|^2}{N} \quad \tilde{\rho}_m(\mathbf{k}) = \sum_{n=1}^N e^{-i\mathbf{k}\cdot\mathbf{R}_n^m} \quad (4.13)$$

where \tilde{S}_m and $\tilde{\rho}_m$ are the microscopic structure factors and particle densities of each realization, respectively. The derivatives with respect to a specific particle coordinate can be written as:

$$\frac{d\langle\tilde{S}(\mathbf{k})\rangle}{d\mathbf{R}_n^m} = \frac{1}{M} \frac{d\tilde{S}_m(\mathbf{k})}{d\mathbf{R}_n^m} \quad \frac{d\tilde{S}_m(\mathbf{k})}{d\mathbf{R}_n^m} = -\frac{2}{N} \mathbf{k} \operatorname{Im}(\tilde{\rho}_m(\mathbf{k}) e^{i\mathbf{k}\cdot\mathbf{R}_n^m}) \quad (4.14)$$

The proposed objective function $F = F_S + F_g$ consists of two terms

$$F_S = \int_{\mathbb{R}^D} w_S(\mathbf{k}) [\langle\tilde{S}(\mathbf{k})\rangle - S_0(\mathbf{k})]^2 d\mathbf{k} \quad \int_{\mathbb{R}^D} w_S(\mathbf{k}) d\mathbf{k} = 1 \quad w_S(-\mathbf{r}) = w_S(\mathbf{r}) \geq 0 \quad (4.15)$$

$$F_g = \int_{\mathbb{R}^D} w_g(\mathbf{r}) [g(\mathbf{r}) - g_0(\mathbf{r})]^2 d\mathbf{r} \quad \int_{\mathbb{R}^D} w_g(\mathbf{r}) d\mathbf{r} = 1 \quad w_g(-\mathbf{r}) = w_g(\mathbf{r}) \geq 0 \quad (4.16)$$

where F_S and F_g demand that $\langle\tilde{S}\rangle$ and g approach the target functions S_0 and g_0 in regions where the weight functions w_S and w_g are nonzero, respectively. For convenience, $S_0(\mathbf{0}) = N$ should be enforced irrespective of the user input. Regarding the choice of weights, it was found that the optimizer converges faster if the weight functions have suitable gradients in regions where S_0 or g_0 are constant. For example, a minimum distance R between all particles can be enforced by setting $g_0(\mathbf{r}) = 0$ and $w_g(\mathbf{r}) = \max(0, 1 - |\mathbf{r}|/R)$. Physically, one may interpret $w_g [g - g_0]^2$ as a scalar potential with a repelling force that is larger for smaller pair distances. If w_g was constant as well, this potential could have shallow local minima due to g , in which the optimizer can be trapped.

The derivative of the objective function with respect to the particle coordinates can be written as

$$\frac{dF}{d\mathbf{R}_n^m} = -\frac{4}{MN} \operatorname{Im} \left(\int_{\mathbb{R}^D} \mathbf{k} f(\mathbf{k}) \tilde{\rho}_m(\mathbf{k}) e^{i\mathbf{k}\cdot\mathbf{R}_n^m} d\mathbf{k} \right) \quad (4.17)$$

where the integral can be computed with a nonuniform Fourier transformation, and f is given by:

$$f(\mathbf{k}) = w_S(\mathbf{k}) [\langle\tilde{S}(\mathbf{k})\rangle - S_0(\mathbf{k})] + \frac{1}{(2\pi)^D \rho} \int_{\mathbb{R}^D} w_g(\mathbf{r}) [g(\mathbf{r}) - g_0(\mathbf{r})] e^{i\mathbf{k}\cdot\mathbf{r}} d\mathbf{r} \quad (4.18)$$

Note that when g is computed with a discrete Fourier transformation from Eq. (4.9), it may be necessary to multiply $[\langle\tilde{S}\rangle - 1]$ with a window function that renders this term periodic and continuous at the Nyquist frequency. The second sum term in f must then also be multiplied with this window function. The computation of multiple realizations can, to some extent, be parallelized. Lastly, even if an unconstrained optimizer algorithm is used, one may simply enforce $dF/d\mathbf{R}_n^m = \mathbf{0}$ for specific particles to keep these coordinates fixed throughout the optimization.

Special case If one only requires $S = 0$ and/or $g = 0$ in specific regions and is indifferent about their shape in the remainder, it is possible to exploit the fact that S and g are non-negative by definition, which ensures that the following $F = F_S + F_g$ will minimize S and g to zero

$$F_S = \int_{\mathbb{R}^D} w_S(\mathbf{k}) \langle\tilde{S}(\mathbf{k})\rangle d\mathbf{k} \quad (4.19)$$

$$F_g = \int_{\mathbb{R}^D} w_g(\mathbf{r}) g(\mathbf{r}) d\mathbf{r} = \int_{\mathbb{R}^D} \frac{w_g(\mathbf{k})}{(2\pi)^D \rho} [\langle\tilde{S}(\mathbf{k})\rangle - 1] d\mathbf{k} \quad w_g(\mathbf{k}) = \int_{\mathbb{R}^D} w_g(\mathbf{r}) e^{-i\mathbf{k}\cdot\mathbf{r}} d\mathbf{r} \quad (4.20)$$

and the same comments about the weight functions and the computation of g apply as mentioned above. With this, the objective function gradients become

$$\frac{dF}{d\mathbf{R}_n^m} = -\frac{2}{MN} \operatorname{Im} \left(\int_{\mathbb{R}^D} \mathbf{k} \left[w_S(\mathbf{k}) + \frac{w_g(\mathbf{k})}{(2\pi)^D \rho} \right] \tilde{\rho}_m(\mathbf{k}) e^{i\mathbf{k}\cdot\mathbf{R}_n^m} d\mathbf{k} \right) \quad (4.21)$$

which can be computed with a nonuniform Fourier transformation for each realization m individually and the term in the square brackets needs to be evaluated only once. This special case not only allows for a better code optimization and higher parallelization, but it can also be used to quickly generate particle coordinates that serve as excellent initial guesses for the general method mentioned above.

Implications Figure 4.1 illustrates the capabilities of the collective coordinate method for a realistic set of parameters. Here, five types of particle distributions (Stealthy, Box, Ring, Liquid, Chain) were generated to demonstrate the possibility of realizing *stealthy configurations* [86, 91] that not only respect a minimum pair distance and contain fixed particle coordinates (Stealthy), but additionally exhibit an anisotropy (Box), a fine-tuned short-range order (Ring), or strikingly different emerging patterns due to a particular long-range order (Liquid, Chain).

In a disordered Huygens' metasurface, the short-range order could have a strong influence on the nearfield-coupling of neighboring particles and, therefore, on their multipolar composition, whereas the long-range order could have a dominant influence on the shape of the farfield diffraction pattern. However, such a distinction may prove elusive, since the particles in a Huygens' metasurface are generally strongly coupled via both the nearfield and farfield. Moreover, the first-order Born approximation [176], which ignores all particle-particle couplings, does not apply and the scattered field of such a metasurface cannot immediately be deduced from the structure factor alone. Nevertheless, future research may reveal how the optical response of a disordered Huygens' metasurface depends on its particle statistics.

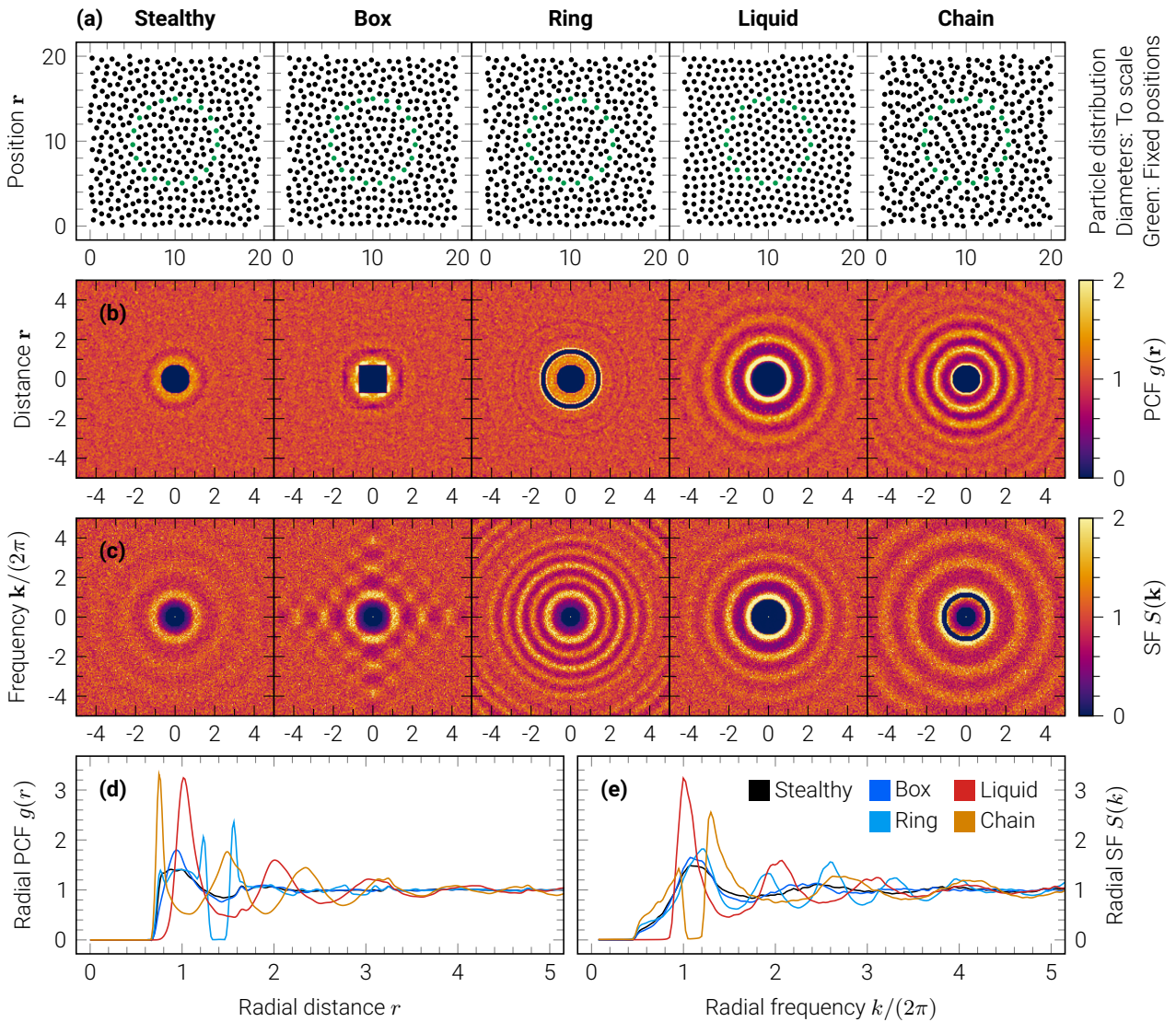


Fig. 4.1 | A demonstration of the collective coordinate method. (a) Visualizations of five generic distributions (column titles) of cylindrical particles with diameters of 0.6 and densities of $\rho = 1$, and their (b,c) two-dimensional and (d,e) radial pair correlation function (PCF) and structure factor (SF). All distributions require the same minimum pair distance ($g(\mathbf{r}) = 0$ for $|\mathbf{r}| < 0.7$), stealthy configuration ($S(\mathbf{k}) = 0$ for $|\mathbf{k}| < \pi$) and fixed particle coordinates (Stealthy), or extend these requirements to $\|\mathbf{r}\|_\infty < 0.7$ (Box), $|\mathbf{r}| \in [1.3, 1.5]$ (Ring), $|\mathbf{k}| < 1.8\pi$ (Liquid), or $|\mathbf{k}| \in [2\pi, 2.5\pi]$ (Chain). The initial coordinates of the Stealthy distribution were taken from a uniform distribution, and those of all other distributions from the resulting Stealthy distribution. Each simulation involved $M = 24$ realizations.

4.3. Matérn-type distributions

This section presents the three types of uniform hard-core distributions introduced by Matérn [188], their generalizations by Teichmann *et al.* [189], and the modifications used in this thesis. In the jargon of a physicist, *uniform* means homogeneous and isotropic, and *hard-core* refers to a minimum pair distance R ($g(r) = 0$ for $r \leq R$). Although the collective coordinate method is capable of generating Matérn-type distributions, a direct generation of these distributions is often faster to implement and in certain situations also faster to execute.

Matérn's idea was to apply a thinning rule to an initial homogeneous Poisson point process that enforces the minimum pair distance but maintains the uniformity of the initial process. For example, one may first uniformly fill a region in space with a specific initial point density $\hat{\rho}$, and then remove all points that are too close to each other. In general, more sophisticated thinning rules are necessary to keep the resulting point density $\rho \leq \hat{\rho}$ as large as possible.

The idea of Teichmann *et al.* was to introduce a deletion probability function $f(r)$ that controls how likely a point is deleted depending on its distance r to another point. This allows for the generation of *soft-core* distributions, where f has the notion of a far-reaching repulsive pair potential, whereas for a hard-core distribution, f resembles a step-like pair potential. In this thesis, the following deletion probability functions with positive parameters $R, \alpha, \beta, \gamma > 0$ were used for all hard-core (subscript hc) and soft-core (subscript sc) distributions:

$$f_{\text{hc}}(r; R) = \begin{cases} 1 & 0 \leq r < R \\ 0 & R \leq r \end{cases} \quad f_{\text{sc}}(r; \alpha, \beta, \gamma) = \begin{cases} 1 & 0 \leq r < \alpha \\ \left(\frac{\beta-r}{\beta-\alpha}\right)^\gamma & \alpha \leq r < \beta \\ 0 & \beta \leq r \end{cases} \quad (4.22)$$

A central term in [189] is the volume integral $V = 2\pi^{D/2}/\Gamma(D/2) \int_0^\infty f(r) r^{D-1} dr$ in D dimensions, and the discussion in [188] suggests that the packing density τ of a hard-core distribution is given by $\tau = \rho V_{\text{hc}}/2^D$. The remainder of this section is limited to $D = 2$ dimensions, where

$$V = 2\pi \int_0^\infty f(r) r dr \quad V_{\text{hc}} = \pi R^2 \quad V_{\text{sc}} = \pi \left[\alpha^2 + 2 \left(\alpha + \frac{\beta}{\gamma+1} \right) \frac{\beta-\alpha}{\gamma+2} \right] \quad (4.23)$$

and preliminary considerations of ordered Huygens' metasurfaces show that rather large packing densities of about $\tau \approx 0.40$ are required (jamming limit: $\tau = 0.547$ [188]). Lastly, the main focus in the following paragraphs is on the rapid generation of large numbers of points. Although perfect simulations are possible [188], where edge effects at the boundaries of the simulation domain and other subtleties are fully accounted for, they tend to be computationally more complex.

Matérn type I In this thinning rule, a point is marked if there is at least one other point within a distance of R . The marked points are deleted after all points were checked. The resulting densities

$$\rho = \hat{\rho} e^{-\hat{\rho}V} \leq \frac{1}{eV} \quad \hat{\rho} \leq \frac{1}{V} \quad \tau \leq \frac{1}{4e} \approx 0.09 \quad (4.24)$$

are rather low due to excessive deletion. For example, given a dense cluster of points where each point is within the R -neighborhood of another point, this rule causes the deletion of the entire cluster.

Matérn type II In this thinning rule, each initial point is assigned a random weight drawn uniformly from $[0, 1]$. A point is marked if there is at least one other point within a distance of R that has a lower weight. The marked points are deleted after all points were checked. As compared to the type-I thinning rule, considerably higher densities can be achieved

$$\rho = \frac{1 - e^{-\hat{\rho}V}}{V} < \frac{1}{V} \quad \hat{\rho} = -\frac{\ln(1 - \rho V)}{V} < \infty \quad \tau < \frac{1}{4} \quad (4.25)$$

but the maximum packing density requires an infinite initial point density. In a dense cluster of points, this rule retains the point with the lowest weight.

Matérn type III In this thinning rule, each initial point is assigned a random weight drawn uniformly from $[0, 1]$. A point is marked if there is at least one other point within a distance of R that has a lower weight and is not (yet) marked. Contrary to the type-I and II thinning rules, the order in which the points are checked has now an influence on the result. For example, if the points are checked in the order of decreasing weights, all points with lower weights are always unmarked and this rule reduces to the type-II rule. However, if the points are checked randomly or in the order of increasing weights, a dense cluster of points might break up into smaller clusters. When a cluster cannot be broken down any further, similarly to the type-II rule, the point with the lowest weight is retained. The marked points can be deleted immediately as the algorithm progresses, or after all points were checked.

Unfortunately, the $\hat{\rho}$ - ρ -dependency cannot be expressed in closed form, which makes it difficult to predict the initial density $\hat{\rho}$ that is needed for a desired resulting density ρ . However, it was shown that this thinning rule is capable of reaching the jamming limit $\tau = 0.547$ [188], and it is still possible to establish the required $\hat{\rho}$ - ρ -dependency numerically.

Matérn type III (generalized) Teichmann *et al.* generalized the Matérn point process of type I and II, and likely skipped III due to its “rather formidable mathematics” [188]. Nevertheless, given a purely numerical interest, it is straight forward to apply the same ideas to the type-III rule.

Each initial point is assigned a retention probability $p = 1$ and a random number p_0 drawn uniformly from $[0, 1]$. To accelerate the search for other points in the $r \leq \beta$ neighborhood of a selected point, the simulation domain is split into a grid with a cell size $\geq \beta$, and the initial points are associated with their enclosing cell. Hence, only the 3-by-3 cell-neighborhood of a selected point needs to be checked. While the list of points is traversed in a random permutation, all points that remain to be checked are assumed to have a higher weight than the currently selected point. Hence, the currently selected point cannot be deleted by its neighbors, but may cause their deletion. For the currently selected point, the retention probability $p \leftarrow p \cdot (1 - f(r))$ of each unmarked neighbor in a distance of $r \leq \beta$ is updated, and then the neighbor is marked if $p < p_0$. This is repeated with the next unmarked point in the list. The marked points are deleted after all points were checked.

Figure 4.2a demonstrates the $\hat{\rho}$ - τ -dependency of this rule for a hard-core (blue) and soft-core (red) distribution with a fixed minimum pair distance. The soft-core distribution cannot reach the desired packing density ($\tau = 0.4$), and the maximum packing density ($\tau = 0.567$) slightly exceeds the jamming limit due to edge effects. Figure 4.2b shows resulting point distributions for selected initial densities.

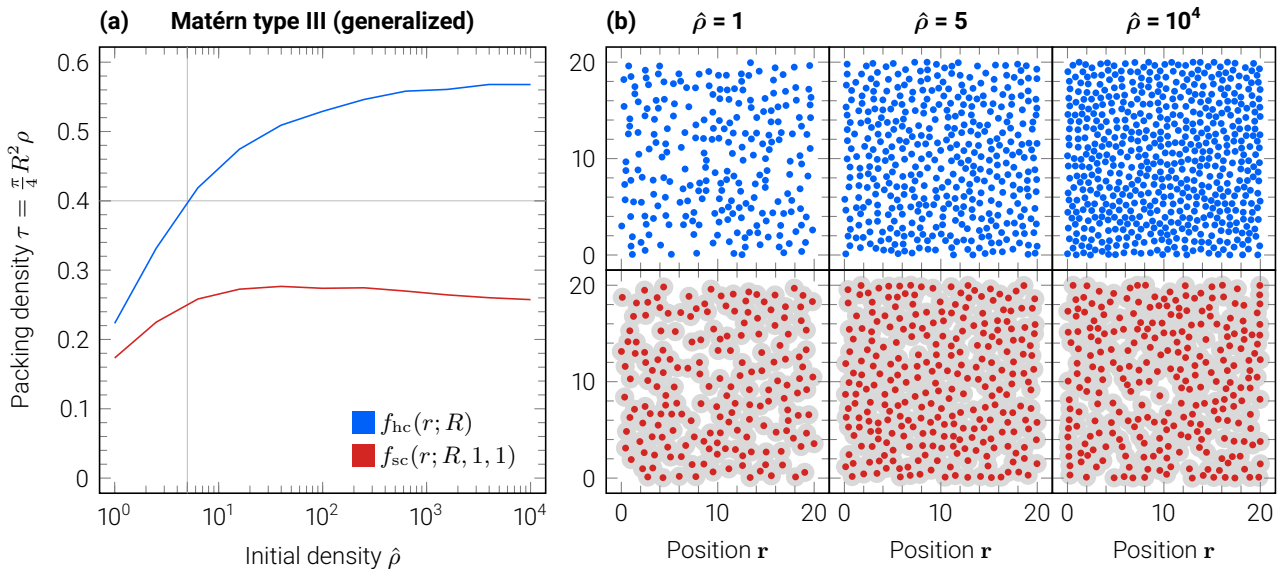


Fig. 4.2 | A demonstration of the generalized Matérn type-III thinning rule. (a) The input-output density characteristics of a hard-core (blue) and soft-core (red) distribution with $R = 0.7125$. Gray lines indicate the required initial density $\hat{\rho}$ for a desired packing density of $\tau = 0.4$. **(b)** Resulting point distributions for selected $\hat{\rho}$ (column titles). Colored circles have radii of $R/2$, so that an intersection would indicate the violation of the minimum pair distance. Overlapping gray circles have radii of 1.

5. Simulation Methods

5.1. Electromagnetic field solvers

Electromagnetic field solvers directly solve Maxwell’s equations (Sec. 3.2) or the vector wave equation (Sec. 3.3) for the full or scattered electromagnetic field. This can be done both in the time and frequency domain and requires the simulation to be discretized in some way. For example, the finite-difference time-domain (FDTD) method stores electric and magnetic field vectors at the vertices of a staggered rectangular grid [190]. While it is a simple yet powerful method, its computational complexity grows quickly with the simulation volume, since the accurate simulation of structures with curved surfaces typically requires a spatial resolution of about one tenth of a wavelength.

The following paragraphs introduce the solvers that were used in this thesis for the simulation of infinite arrays and disordered arrangements of cylindrical scatterers.

Finite element method The finite element method (FEM) not only discretizes the simulation volume, but also approximates the electromagnetic field within each volume element by a low-order polynomial [191, 192]. These volume elements, the *finite elements*, commonly take the shape of tetrahedra or hexahedra and can be transformed to exactly represent curved surfaces. The electromagnetic field is stored at a few special points within each finite element, which are usually the nodes of a particular quadrature rule, since this allows for the rapid evaluation of the polynomial at arbitrary points within the finite element. The electromagnetic problem is then solved by matching the global boundary conditions and those of all finite elements, which results in a large matrix equation. Due to the use of polynomials, a spatial resolution of about one half of a wavelength is often sufficient for finite elements of quadratic order. Hence, the FEM is capable of solving complicated structures more accurately and efficiently than the FDTD method, but since the numerical handling of finite elements is rather intricate, its computational complexity still grows quickly with the simulation volume.

Here, the proprietary software “COMSOL Multiphysics” was used to simulate an individual cylindrical scatterer or infinite arrays of such scatterers. The main derived quantities were the transmission and reflection coefficients of all diffraction orders (Sec. 3.4.4 and Appendices B.3,4), and the multipole coefficients and scattering cross sections (Sec. 3.5.2).

Local-coordinate T-matrix method In the local-coordinate T-matrix method [28, 39], each scatterer is assigned its own scattered electromagnetic field, namely a truncated series of spherical vector wave functions (Eqs. (3.115,116)) with multipole coefficients a_n^m and b_n^m . The origin of each series is taken to be $\mathbf{r} = \mathbf{0}$, which means that each scatterer is, at first, treated within its own local frame of reference. The global coordinates of all scatterers are introduced in a later step. Then, by expressing the incident field in terms of multipole coefficients p_n^m and q_n^m , and collecting the multipole coefficients in vectors $\begin{pmatrix} \mathbf{a} \\ \mathbf{b} \end{pmatrix}$ and $\begin{pmatrix} \mathbf{p} \\ \mathbf{q} \end{pmatrix}$, the optical response of an isolated scatterer to the incident field can be written as a matrix product $\begin{pmatrix} \mathbf{a} \\ \mathbf{b} \end{pmatrix} = \mathbf{T} \cdot \begin{pmatrix} \mathbf{p} \\ \mathbf{q} \end{pmatrix}$ with the scatterer’s transition matrix (T-matrix) \mathbf{T} .

The T-matrix of arbitrarily-shaped scatterers can be assembled from FEM simulations in which the scatterer is excited by one spherical vector wave function at a time for a range of polar and azimuthal orders [193]. It often suffices to compute \mathbf{T} up to the octopolar order ($n = 3$).

Given a cluster of scatterers with known T-matrices, the effective multipole coefficients \mathbf{a}_{eff} and \mathbf{b}_{eff} of each scatter are found by considering that each scatterer is not only excited by the incident wave but also by all other scatterers. In other words, the effective multipole coefficients represent the self-consistent solution of the scattering problem in the context of the scattered wave formalism. To solve this problem, the addition theorem of spherical wave functions must be used to express the global coordinate of one scatterer within the local coordinate system of each other scatterer [194, 195]. Ultimately, this leads to a large system of linear equations that can be solved for \mathbf{a}_{eff} and \mathbf{b}_{eff} .

Here, the local-coordinate T-matrix method was used to simulate disordered arrangements of cylindrical scatterers with often more than 200 scatterers. This provided the same quantities as the finite element method, plus the directional scatterance (Sec. 3.4.3) and effective dipole moments (Appendix A.5).

5.2. Band-limited angular spectrum method

This section presents an adaptation of the band-limited angular spectrum method [196, 197]. The angular spectrum method is based on the idea that any electromagnetic field in a homogeneous medium can be propagated from one plane into another via its plane wave expansion (cf. Sec. 3.4.1). Without loss of generality, one may assume a standard Cartesian coordinate system where the input plane is identical to the x - y -plane and the output plane lies parallel to the input plane in a distance of $z \neq 0$. With this, the angular spectrum method can be summarized in three steps:

1. Expansion of the electric field in the input plane $\mathbf{E}(\mathbf{r})$ into its plane wave spectrum $\mathbf{E}(\mathbf{k})$.
2. Propagation of $\mathbf{E}(\mathbf{k})$ into the output plane via a simple multiplication $\mathbf{E}(\mathbf{k}; z) = \mathbf{E}(\mathbf{k}) e^{\mathbf{i}k_z z}$.
3. Reconstruction of the electric field in the output plane $\mathbf{E}(\mathbf{r}; z)$ from $\mathbf{E}(\mathbf{k}; z)$.

The band-limited aspect of the method takes into account that the discrete Fourier transformations used in the numerical simulations generally suffer from aliasing. The goal is to exclude those regions of $\mathbf{E}(\mathbf{k}; z)$ at the end of step 2 that would otherwise lead to aliasing artifacts in $\mathbf{E}(\mathbf{r}; z)$.

In mathematical terms, the method can be summarized as

$$\mathbf{E}(\mathbf{r}; z) = \mathcal{F}_{\mathbf{k}}^{-1} \{ h(\mathbf{k}; z) \mathcal{F}_{\mathbf{r}} \{ \mathbf{E}(\mathbf{r}) \}(\mathbf{k}) \}(\mathbf{r}) \quad \mathbf{k} = (k_x, k_y) \quad \mathbf{r} = (x, y) \quad (5.1)$$

$$h(\mathbf{k}; z) = \chi_{\mathcal{K}}(\mathbf{k}) \exp(\mathbf{i} \sqrt{k^2 - \mathbf{k}^2} z) \quad k = \frac{2\pi}{\lambda} n \quad (5.2)$$

where λ is the vacuum wavelength, n the real-valued refractive index of the homogeneous background medium, h the propagator kernel, $\chi_{\mathcal{K}}$ the indicator function (Eq. (3.74)), and \mathcal{K} the set of points \mathbf{k} for which no aliasing occurs (Eq. (5.4)). In the following paragraph it will become clear that $\chi_{\mathcal{K}}$ takes the role of a specific low-pass filter. For numerical purposes, the continuous Fourier transformations must be replaced by discrete transformations, the simulation domain must be truncated to a finite but periodic window $\mathbf{p} = (p_x, p_y)$, and all functions must be sampled at $\mathbf{N} = (N_x, N_y)$ points with corresponding discretized coordinates $\mathbf{r}_{\mathbf{n}}$ and $\mathbf{k}_{\mathbf{m}}$ as mentioned in Eqs. (3.5,6).

The set \mathcal{K} is found from an investigation of the instantaneous frequency ℓ , which is defined as the derivative of the local phase of the non-truncated ($\mathcal{K} = \mathbb{R}^2$) kernel h

$$\ell(\mathbf{k}; z) = \frac{1}{2\pi} \frac{d}{d\mathbf{k}} \arg(h(\mathbf{k}; z)) = -\frac{\mathbf{k}z}{2\pi \sqrt{k^2 - \mathbf{k}^2}} \quad (5.3)$$

where the product $\ell \cdot d\mathbf{k}$ equals the number of periods that the phase of h would advance at the point \mathbf{k} for an infinitesimally small step along $d\mathbf{k}$. In other words, this quantity measures how rapidly h oscillates at each point of the \mathbf{k} -plane. When $d\mathbf{k}$ is replaced by the resolution $\Delta\mathbf{k}$ of the discrete Fourier transformation, the inverse $(|\ell_d| \Delta k_d)^{-1}$ can be interpreted as the number of sample points per one period of ℓ_d along the dimension d . According to the Nyquist criterion, there must be at least two sample points per period $(|\ell_d| \Delta k_d)^{-1} \geq 2$ to avoid aliasing. This criterion must be met along all dimensions simultaneously and requires \mathbf{k} to lie within the intersection of two ellipses

$$\mathcal{K} = \left\{ \mathbf{k} \left| \frac{k_x^2}{[k \sin(\theta_x)]^2} + \frac{k_y^2}{k^2} \leq 1 \wedge \frac{k_x^2}{k^2} + \frac{k_y^2}{[k \sin(\theta_y)]^2} \leq 1 \right. \right\} \quad (5.4)$$

where $k \sin(\theta_d)$ carries the notion of a numerical aperture as it determines the largest possible spatial frequency in the output plane, and the angle

$$\theta_d = \arctan\left(\frac{p_d}{2|z|}\right) \quad (5.5)$$

can be interpreted geometrically as the half-angle under which one period of the input plane appears when viewed from the output plane, or vice versa.

Additionally, the spatial resolution $\Delta \mathbf{r}$ should be chosen small enough such that the Nyquist frequency $\frac{1}{2}N_d \Delta k_d$ is slightly larger than the band limit $k \sin(\theta_d)$, which ensures that the kernel is not artificially truncated and therefore propagates the maximum possible amount of information:

$$\frac{1}{2}N_d \Delta k_d \geq k \sin(\theta_d) \quad \Leftrightarrow \quad N_d \geq 2n \sin(\theta_d) \frac{p_d}{\lambda} \quad \Leftrightarrow \quad \Delta r_d \leq \frac{\lambda}{2n \sin(\theta_d)} \quad (5.6)$$

Considering that discrete Fourier transformations are usually most efficient for array sizes that are products of small primes, N_d should be rounded up to such an integer. Moreover, since the discrete Fourier transformations are inherently periodic, the propagation of the electric field becomes a circular convolution with the propagator kernel. Depending on the frequency content of the electric field in the input plane and the propagation distance, this can introduce significant errors due to diffracted waves that wrap around the simulation domain. However, the circular convolution can be turned into a linear convolution by zero-padding the simulation domain to twice its original size ($\mathbf{p} \rightarrow 2\mathbf{p}$) while maintaining the spatial resolution ($\mathbf{N} \rightarrow 2\mathbf{N}$). This also results in a finer frequency resolution of the kernel, but all other preceding considerations remain valid (see [196] for more technical details).

Optimal parameters Equation (5.6) reveals that the optimal spatial resolution is bounded by

$$\frac{\lambda}{2n} \leq \Delta r_d \leq \frac{\lambda}{2n \sin(\theta_d)} = \frac{\lambda}{2n} \sqrt{\left(\frac{2|z|}{p_d}\right)^2 + 1} \quad (5.7)$$

where the lower limit stems from the fact that any features in the electric field with sizes smaller than $\lambda/(2n)$ originate from evanescent waves that cannot propagate into the farfield. Hence, although possible, the use of an even smaller spatial resolution is not meaningful. The upper limit represents the smallest possible feature size in the output plane due to the low-pass-filter characteristic of the propagator kernel. In other words, the limited numerical aperture $n \sin(\theta_d)$ causes blurring in the output plane. Moreover, the upper limit is identical to the *Abbe diffraction limit* [166], and its violation implies that the electric field in the output plane is undersampled. While the use of the upper limit results in the most efficient numerical implementation, the considered range can be used to accommodate additional requirements as mentioned in the following paragraph. This concludes the standard band-limited angular spectrum method.

The following discussion seeks optimal parameters for the sampling of an object in the input plane that is represented by I pixels, where each pixel may be further divided into J sub-pixels. For example, such an object may be a metasurface where each pixel consists of a particular arrangement of scattering particles, and the subdivision allows one to further take into account the internal structure of each pixel. Since the following discussion applies to each dimension individually, the corresponding subscripts are dropped in favor of readability.

Additionally to Eq. (5.7), one may require a minimum number of sub-pixels J_{\min} , that the size of the simulation domain $p = N \Delta r$ is larger than both the size of the object s_{obj} and the image s_{img} , and that N is an integer power of two

$$\Delta r = \frac{s_{\text{obj}}}{IJ} \quad \max\left\{J_{\min}; 2n \sin(\theta_{\text{obj}}) \frac{s_{\text{obj}}}{I\lambda}\right\} \leq J \leq 2n \frac{s_{\text{obj}}}{I\lambda} \quad I, J, J_{\min} \in \mathbb{Z}_{>0} \quad (5.8)$$

$$N = 2^m \quad \log_2\left(\max\left\{1; \frac{s_{\text{img}}}{s_{\text{obj}}}\right\} IJ\right) \leq m \quad m \in \mathbb{Z}_{\geq 0} \quad (5.9)$$

where $\theta_{\text{obj}} = \arctan(s_{\text{obj}}/(2|z|))$ is half of the object's apparent size, and $J_{\min} \leq 2ns_{\text{obj}}/(I\lambda)$ must not be exceeded. Since the computational workload grows rapidly with N , the goal is to keep N as small as possible, and since the lower bound of the exponent m increases with J , it is best to first determine m from the lower bound of J before concluding with J :

$$m = \left\lceil \log_2\left(\max\left\{1; \frac{s_{\text{img}}}{s_{\text{obj}}}\right\} \max\left\{IJ_{\min}; 2n \sin(\theta_{\text{obj}}) \frac{s_{\text{obj}}}{\lambda}\right\}\right) \right\rceil \quad J = \left\lfloor \frac{2^m}{I} \min\left\{1; \frac{s_{\text{obj}}}{s_{\text{img}}}\right\} \right\rfloor \quad (5.10)$$

This fully determines the optimal choices for \mathbf{N} and $\Delta \mathbf{r}$, as well as \mathbf{p} and $\Delta \mathbf{k}$.

5.3. Iterative Fourier transform algorithm

In the broadest sense, iterative Fourier transform algorithms (IFTAs) represent a class of optimization methods that aim to find an input to a linear system that produces a desired output, but with the important restriction that the output is not fully specified, or otherwise the problem could be solved by a simple back-propagation of the output. In general, the response of a linear system can be written as a convolution integral of the input and the system's impulse response, which in turn can be computed efficiently in the Fourier domain via the convolution theorem; hence the "FT" in IFTA. The iterative aspect of IFTAs is due to their underlying optimization strategy.

The first IFTA, known as Gerchberg-Saxton algorithm, was introduced by Gerchberg & Saxton [198]. There, the focus was on the retrieval of an object's phase information given its intensity diffraction pattern, which is commonly called the phase retrieval problem. Consequently, IFTAs are also known as phase retrieval algorithms, and by now, numerous variations and extensions of the Gerchberg-Saxton algorithm have been reported [199–201]. Two major optimization strategies are projection-based and gradient-search methods [166]. The latter typically offer faster convergence but have problems with discontinuous constraints. The Gerchberg-Saxton algorithm and its improvements, such as the error-reduction algorithm and the input-output algorithm, are projection-based methods. The improved versions offer faster convergence but require careful manual tuning.

In this thesis, a modified Gerchberg-Saxton algorithm was implemented for the generation of a thin transmission hologram that, when illuminated by a light source, produces a specific intensity distribution in a given plane behind the hologram. Figure 5.1 shows a flowchart of the implemented algorithm.

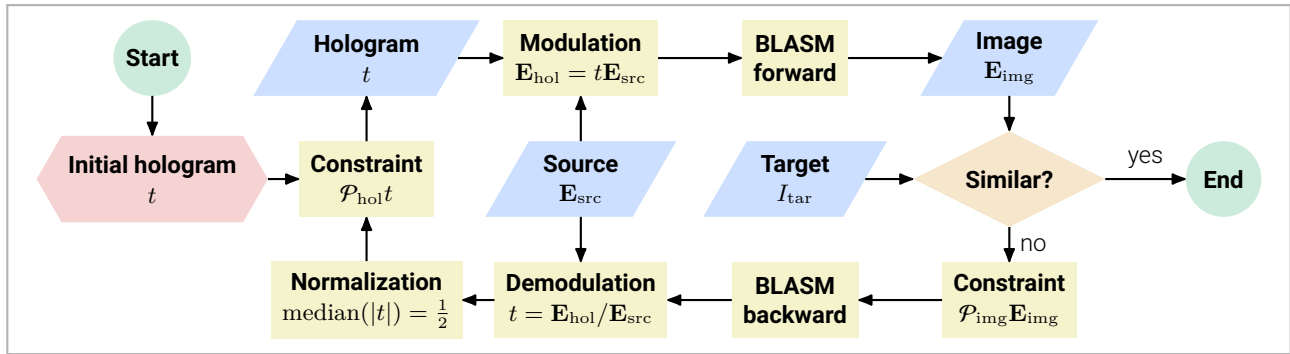


Fig. 5.1 | Flowchart of an IFTA for the generation of a thin transmission hologram. The band-limited angular spectrum method (BLASM) is used for the free-space propagation of the electric field \mathbf{E}_{hol} from directly behind the transmission hologram t into the image plane. The hologram is illuminated by the electric field \mathbf{E}_{src} of a light source. The goal is to generate a hologram for which the intensity of the electric field in the image plane \mathbf{E}_{img} is very similar to the target intensity image I_{tar} . The projection operators \mathcal{P}_{hol} and \mathcal{P}_{img} are explained in the main text. Symbols according to ISO 5807.

More precisely, the thin transmission hologram produces an electric field $\mathbf{E}_{\text{hol}}(\mathbf{r}_{\mathbf{m}}) = t(\mathbf{r}_{\mathbf{m}}) \mathbf{E}_{\text{src}}(\mathbf{r}_{\mathbf{m}})$ in response to the electric field $\mathbf{E}_{\text{src}}(\mathbf{r}_{\mathbf{m}})$ of a light source, where the transmission coefficient profile of the hologram $t(\mathbf{r}_{\mathbf{m}})$ is represented by a rectangular grid of M pixels with two-dimensional multi-indices \mathbf{m} . Each pixel corresponds to a specific arrangement of scattering particles and may be divided further into sub-pixels as to account for scattering effects from within each pixel. The goal of the algorithm depicted in Fig. 5.1 is to generate a hologram that produces an electric field $\mathbf{E}_{\text{img}}(\mathbf{r}'_{\mathbf{m}})$ in a plane $\mathbf{r}'_{\mathbf{m}}$ behind the hologram with an intensity profile that is very similar to a given target intensity image $I_{\text{tar}}(\mathbf{r}'_{\mathbf{m}})$. The free-space propagation between the hologram and the image plane is computed with the band-limited angular spectrum method. The backward propagation can be realized with a complex conjugation of the forward propagator kernel. For the initial guess of the hologram, one may assign each pixel a random amplitude or phase or both, or implement the transfer function of an actual optical element, as for example the parabolic phase of a lens. The latter can help to concentrate more energy into the image area, whereas a random initial guess acts as a strong diffuser. The choice of the initial guess can have a substantial impact on the convergence speed and outcome of the algorithm. The demodulation step requires special care in regions where \mathbf{E}_{src} vanishes. The normalization step applies a constant scaling factor to t such that the median amplitude of t equals $\frac{1}{2}$. This is necessary since the

backward free-space propagation can scatter energy out of the hologram area, and the image projection operator typically introduces an arbitrary amplitude scaling. The image projection operator

$$\mathcal{P}_{\text{img}} \mathbf{E}_{\text{img}} = \sqrt{I_{\text{tar}}} e^{i \arg(\mathbf{E}_{\text{img}})} \quad (5.11)$$

is an integral part of the standard Gerchberg-Saxton algorithm and constrains the electric field amplitude of the holographic image to follow the target image. The main modification introduced in this thesis is the hologram projection operator with the purpose to constrain t to values that can be realized experimentally. The following hologram projection operators were investigated

$$\mathcal{P}_{\text{hol}} t = \begin{cases} t & \text{None} \\ |t| & \text{Amplitude-only} \\ e^{i \arg(t)} & \text{Phase-only} \\ \min(\max(|t|; a_{\min}); a_{\max}) e^{i \min(\max(\arg(t); \varphi_{\min}); \varphi_{\max})} & \text{Sector} \\ \underset{t' \in \mathcal{T}'}{\operatorname{argmin}} |\ln(t/t')| & \text{Discrete} \end{cases} \quad (5.12)$$

where the transmission coefficient $t(\mathbf{r}_{\mathbf{m}})$ of each pixel \mathbf{m} is projected independently, parameters a_{\min} , a_{\max} , φ_{\min} , φ_{\max} define an annular sector, and t' is a member of a finite set of realizable transmission coefficients \mathcal{T}' . If sub-pixels are used, t and t' become matrices, the projection operator must be applied to the spatial average of each $t(\mathbf{r}_{\mathbf{m}})$, and each projected pixel should be filled with the available sub-pixel information. A more detailed descriptions of each operator is in order:

None This is an identity operator. It may be used to rapidly improve an initial hologram or to determine the best possible image quality of a given configuration.

Amplitude-only, Phase-only These constraints allow for the generation of amplitude-only and phase-only holograms. Their purpose is similar to the *none* constraint.

Sector Transmission coefficients outside of the given annular sector are mapped to its nearest boundary. Note that the phase term requires special care regarding phase wrapping around the branch cut. This constraint generalizes *amplitude-only* and *phase-only*, and may serve as a reference case in situations where only a limited phase range can be realized experimentally.

Discrete This constraint assigns each pixel one member of \mathcal{T}' that is closest to t according to the distance measure $|\ln(t/t')|$. If sub-pixel information is used, it must be ensured that the mean value of each matrix in \mathcal{T}' is unique. The distance measure was based on several observations:

- The Euclidean distance $|t - t'|$ often gave unsatisfactory results near the origin of the complex plane, especially when \mathcal{T}' contained only a small number of elements.
- The distance $\sqrt{a[|t| - |t'|]^2 + b[\arg(t) - \arg(t')]^2}$ produced better results, but it was cumbersome to account for phase wrapping and to find good values for the weights a and b .
- The distance $|\ln(t/t')| = \sqrt{[\ln(|t/t'|)]^2 + [\arg(t/t')]^2} = \sqrt{[\ln(|t|) - \ln(|t'|)]^2 + [\arg(t) - \arg(t')]^2}$ is much easier to evaluate and the logarithmic scaling of the amplitudes may even be favorable.

Moreover, to simplify the fabrication of resulting holograms, it can be desirable to reduce the set \mathcal{T}' in a way that tries to preserve the image quality. Two strategies were devised:

Reduction by distance Given a target set $t \in \mathcal{T}$ with N elements, find N elements in $t' \in \mathcal{T}'$ without repetition for which the sum of distances $|\ln(t'/t)|$ is minimal. This fundamental combinatorial optimization problem is also known as the assignment problem. This strategy is most useful when the number of elements in \mathcal{T}' is much larger than N .

Reduction by prevalence Given the hologram t from a previous run of the IFTA, first project it $t' = \mathcal{P}_{\text{hol}} t$, then form a histogram of all t' , and finally retain the N most-frequently used t' . This strategy is most useful when the number of elements in \mathcal{T}' is only slightly larger than N .

In each iteration of the algorithm, the hologram and image are updated. The algorithm terminates after a certain number of iterations or once the image is sufficiently similar to the target. To define a measure for similarity and to quantify the performance of the hologram, consider the intensities in front of the hologram (I_{src}), behind the hologram (I_{hol}), and in the image plane (I_{img})

$$I_{\text{src}}(\mathbf{r}_{\mathbf{m}}) \propto |\mathbf{E}_{\text{src}}(\mathbf{r}_{\mathbf{m}})|^2 \quad I_{\text{hol}}(\mathbf{r}_{\mathbf{m}}) \propto |t(\mathbf{r}_{\mathbf{m}}) \mathbf{E}_{\text{src}}(\mathbf{r}_{\mathbf{m}})|^2 \quad I_{\text{img}}(\mathbf{r}'_{\mathbf{m}}) \propto |\mathbf{E}_{\text{img}}(\mathbf{r}'_{\mathbf{m}})|^2 \quad (5.13)$$

and the following operators

$$\mathcal{M}f(\mathbf{r}_{\mathbf{m}}) = \frac{1}{M} \sum_{\mathbf{m}} f(\mathbf{r}_{\mathbf{m}}) \quad \mathcal{S}f(\mathbf{r}_{\mathbf{m}}) = \sqrt{\frac{1}{M} \sum_{\mathbf{m}} [\mathcal{Z}f(\mathbf{r}_{\mathbf{m}})]^2} \quad \mathcal{Z} = 1 - \mathcal{M} \quad (5.14)$$

where \mathcal{M} produces the spatial mean, \mathcal{S} the spatial standard deviation, and \mathcal{Z} a mean-free function. With this, the zero-normalized cross correlation ZNCC, the total efficiency η_{tot} , and the scattering efficiency η_{sca} can be defined as

$$\text{ZNCC} = \mathcal{M} \left\{ \frac{[\mathcal{Z}I_{\text{img}}][\mathcal{Z}I_{\text{tar}}]}{[\mathcal{S}I_{\text{img}}][\mathcal{S}I_{\text{tar}}]} \right\} \quad \eta_{\text{tot}} = \frac{A_{\text{tar}} \mathcal{M}I_{\text{img}}}{A_{\text{hol}} \mathcal{M}I_{\text{src}}} \quad \eta_{\text{sca}} = \frac{A_{\text{tar}} \mathcal{M}I_{\text{img}}}{A_{\text{hol}} \mathcal{M}I_{\text{hol}}} \quad (5.15)$$

where the $\text{ZNCC} \in [0, 1]$ measures the similarity between the offset-and-scale-normalized intensities I_{img} and I_{tar} , and A_{tar} and A_{hol} are the surface areas of the target and hologram, respectively. Figure 5.2 demonstrates the performance of the IFTA for the five presented constraints. Generally, the introduction of amplitude modulations increases the ZNCC but reduces the total efficiency. Moreover, preliminary tests of the *discrete* constraint indicate that for a fixed cardinality $|\mathcal{T}'|$, target sets \mathcal{T}' that represent a hexagonal or a similarly-spaced cylindrical grid often yield the highest ZNCC.

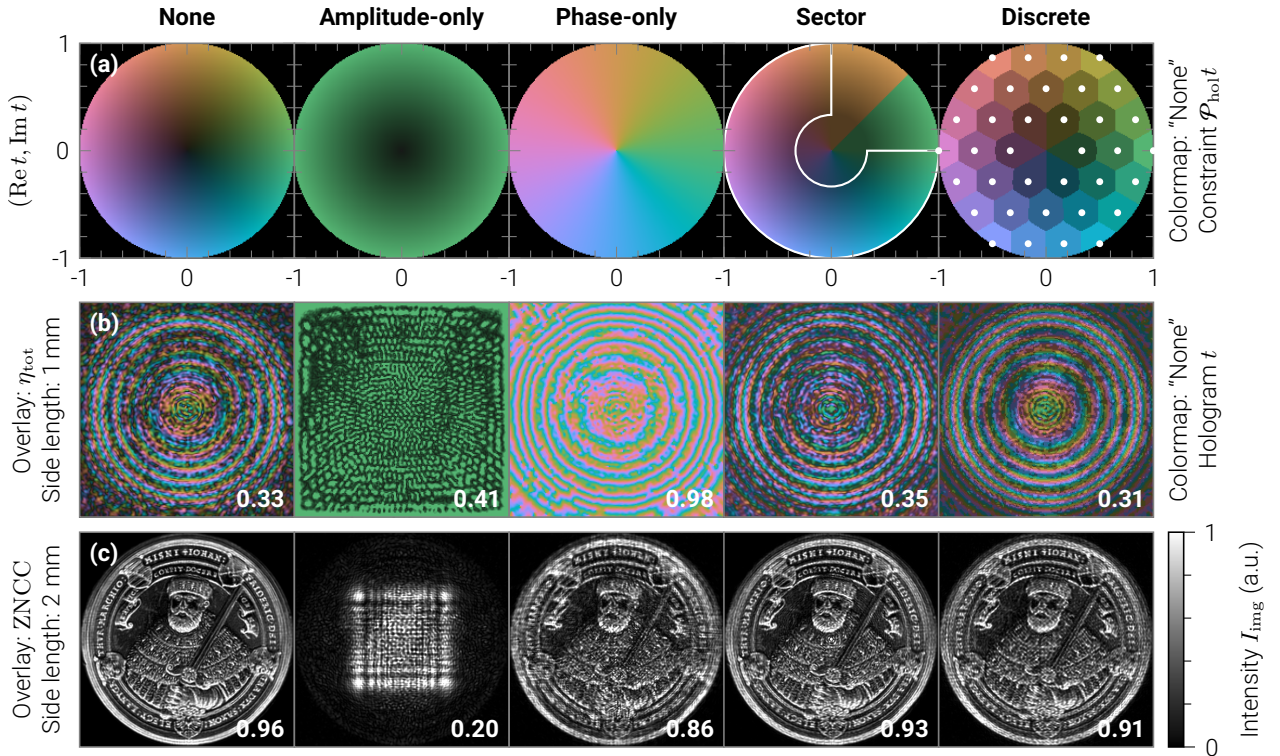


Fig. 5.2 | A demonstration of the presented IFTA. (a) Visualizations of all presented constraints (column titles). The *none* constraint maps each coordinate $(\text{Re } t, \text{Im } t)$ to a unique color and serves as colormap for (a,b). White lines and dots in the *sector* and *discrete* constraint represent their customization parameters. (b) Resulting holograms with 200 pixels per 1 mm side length, each surrounded by a rectangular aperture (not visible) and initialized with a parabolic phase profile that focuses incident light into the image plane. Overlays show the total efficiency η_{tot} . (c) Resulting intensity images I_{img} with side lengths of 2 mm in a distance of 11.44 mm behind the hologram for a plane wave excitation under normal incidence at a vacuum wavelength of 1.5 μm . The intensity in each subplot is normalized with respect to its 99th percentile. Overlays show the zero-normalized cross correlation ZNCC.

Design considerations In the design of in-line holograms, that are a configurations in which the image is generated along the system's optical axis, it must be kept in mind that the hologram's pixelation can act as a diffraction grating and may produce unwanted diffraction orders. Along the direction of these diffraction orders, replicas of the target image can appear that, depending on the distance with respect to the hologram, can spatially overlap and interfere not only with the zeroth diffraction order but also with each other. This overlap is often detrimental to the image quality, since the hologram must not only encode information about the image but also about the compensation of the overlaps within a finite number of pixels. Moreover, since the maximum possible intensity in the image plane typically reduces along larger scattering angles, one has to find a good compromise between the spatial resolution, distance, and intensity homogeneity of the image.

The following discussion applies to each lateral dimension individually and assumes that the hologram is illuminated by a normally incident plane wave with an effective wavelength of $\lambda = \lambda_0/n$, where λ_0 is the vacuum wavelength and n the refractive index of the environment. With this, the polar propagation angle of the m -th diffraction order $\theta_m(\theta)$ in dependence on the scattering angle θ of the zeroth order, the largest possible scattering angle θ_{\max} that extends from one edge of the hologram to the opposing edge of the image, and the opening angle θ_{NA} of the numerical aperture can be written as

$$\theta_m(\theta) = \arcsin\left(\frac{\lambda}{\Lambda}m + \sin(\theta)\right) \quad \theta_{\max} = \arctan\left(\frac{s_{\text{hol}} + s_{\text{img}}}{2d}\right) \quad \theta_{\text{NA}} = \arctan\left(\frac{s_{\text{img}}}{2d}\right) \quad (5.16)$$

where Λ is the size of one pixel, d the image distance, and s_{hol} and s_{img} the hologram and image size, respectively. The first diffraction orders do not overlap with the zeroth order if their critical scattering angle lies just outside of the numerical aperture $\theta_1(-\theta_{\max}) \geq \theta_{\text{NA}}$, which is equivalent to

$$\sin\left(\arctan\left(\frac{s_{\text{img}}}{2d_{\min}}\right)\right) + \sin\left(\arctan\left(\frac{s_{\text{hol}} + s_{\text{img}}}{2d_{\min}}\right)\right) = \frac{\lambda}{\Lambda} \quad (5.17)$$

where $d \geq d_{\min}$ is the minimum image distance required for the separation of the diffraction orders. The exact solution of this equation for d_{\min} is rather unwieldy, but if the image size is much larger than the hologram size, a good approximation can be found:

$$d_{\min} \approx s_{\text{img}} \sqrt{\left(\frac{\Lambda}{\lambda}\right)^2 - \frac{1}{4}} \quad s_{\text{img}} \gg s_{\text{hol}} \quad (5.18)$$

If the image size is large, the minimum image distance is large as well, and the envelope of the farfield intensity distribution produced by the hologram may be interpreted as the Fraunhofer diffraction of a slit. More precisely, using the Fraunhofer intensity diffraction pattern of a slit with a width of Λ [173], the relative intensity I_r at the edge of the image with respect to its center can be written as

$$I_r = \text{sinc}^2\left(\frac{\Lambda}{\lambda} \frac{s_{\text{img}}}{2d}\right) \quad d \gg \frac{\Lambda}{\lambda} \Lambda \quad (5.19)$$

where $\text{sinc}(x) = \sin(\pi x) / (\pi x)$ is the normalized sinc function. Lastly, by setting $d(\mu) = \mu d_{\min}$ as a real multiple $\mu \geq 1$ of the minimum image distance, the relative intensity can be written as:

$$I_r(\mu) = \text{sinc}^2\left(\frac{1}{2\mu}\right) \quad d(\mu) = \mu \frac{\Lambda}{\lambda} s_{\text{img}} \quad \frac{\Lambda}{\lambda} \gg \frac{1}{2} \quad (5.20)$$

The inverse $\mu(I_r)$ can be computed numerically and determines the image distance $d(\mu)$ that is required to achieve a given relative intensity I_r at the image edge. A larger value of μ leads to a more homogeneous intensity envelope, but since it also increases the image distance, it increases (worsens) the achievable spatial resolution Δr in the image plane

$$\Delta r = \frac{\lambda}{2} \sqrt{\left(2\mu \frac{\Lambda}{\lambda} \frac{s_{\text{img}}}{s_{\text{hol}}}\right)^2 + 1} \approx \mu \frac{s_{\text{img}}}{s_{\text{hol}}} \Lambda \quad (5.21)$$

according to the Abbe diffraction limit (cf. Eq. (5.7)).

6. Experimental Methods

6.1. Fabrication of dielectric metasurfaces

The fabrication of all metasurfaces presented in this thesis was based on electron-beam lithography and reactive-ion etching. The starting material was a 1 mm thick amorphous silicon dioxide substrate with a 500 nm thick amorphous silicon cover layer (Tafelmaier Dünnschicht-Technik GmbH). The resulting metasurfaces consisted of ordered and disordered arrangements of nanocylinders with identical height but possibly different radii.

First, the thickness of the amorphous silicon layer was reduced to the desired nanocylinder height of 220 nm using argon ion-beam etching (Oxford Ionfab 300). Then, the substrate was covered by a 30 nm thick chromium layer via ion-beam deposition (Oxford Ionfab 300), followed by a 100 nm thick layer of negative electron-beam resist (ma-N 2401, EN038) via spin-coating. The resist was exposed in a variable-shape electron-beam lithography system (Vistec SB 350) and then developed (AZ 726 MIF, OPD 4262). The resulting resist mask was transferred into the chromium layer via argon ion-beam etching, and then further into the amorphous silicon layer via inductively-coupled plasma reactive-ion etching (Sentech SI-500 C) using carbon tetrafluoride. The chromium mask and any residual resist were removed with a chromium etchant and acetone.

In Chapter 8, each hologram needed to be surrounded by an embedded aluminum aperture. There, the sample was covered by a 300 nm thick layer of negative electron-beam resist (AR-P 617, CSAR) via spin-coating, followed by 10 nm of gold via thermal vapor deposition (VTD Dresden B30). The resist was exposed and developed as mentioned above, which left a protective patch of resist on top of each hologram. Then, a 100 nm thick aluminum layer was deposited using thermal vapor deposition (JEVATEC V700). The protective patches were lifted off using acetone.

Lastly, all samples were covered by a 1 μm thick layer of spin-on glass (Futurrex IC1-200) with a refractive index that matches the amorphous silicon dioxide substrate.

6.2. Back-focal-plane imaging

The directional scatterance $Q_{\Omega}(\mathbf{k})$ (Eq. (3.81)) of an object can be measured in the back-focal plane of a lens with a high numerical aperture that collects the scattered light. Figure 6.1 depicts the setup that was constructed for the measurement of the directional transmittance $Q_{\Omega}^T(\mathbf{k})$.

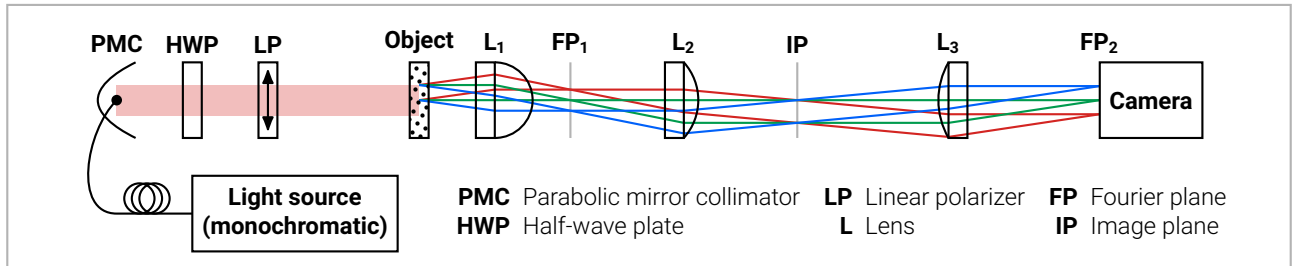


Fig. 6.1 | Back-focal-plane imaging setup. The light source was a fiber-coupled tunable continuous-wave laser. The PMC, HWP and LP produced a weakly-diverging linearly-polarized Gaussian beam (red areas). Lens L_1 was a microscope objective with a numerical aperture of 0.65 and a long working distance that allowed the object to be rotated by up to about 20° as to simulate oblique incidence. The red, green and blue lines represent three distinct scattering angles originating from two points on the object. Note how rays with identical scattering angles meet at unique points in the FP_1 and FP_2 .

When an object is placed in the front-focal plane of lens L_1 , the Fourier transformation of the scattered electromagnetic field can be observed in the back-focal plane, the Fourier plane FP_1 . More precisely, it is the transmitted area-averaged intensity $[d^2 I^T(\mathbf{k})]/[dk_x dk_y]$ (Eq. (3.80)) that can be measured there. However, since the FP_1 was located within the body of L_1 , and due to the large size of the camera chip, lenses L_2 and L_3 were used to project a magnified image of the area-averaged intensity onto the camera in FP_2 . The incident intensity I_0 needed in the calculation of the directional transmittance was obtained from a measurement of the empty setup, which means by removing the object.

6.3. White-light spectroscopy

Figure 6.2 shows the setup that was constructed for the measurement of the zeroth-order transmittance spectrum $T(\lambda, \theta, \phi)$ in dependence on the incidence angle θ and polarization angle ϕ of a collimated beam, and the zeroth-order reflectance spectrum $R(\lambda)$ for normal incidence (Sec. 3.4.4).

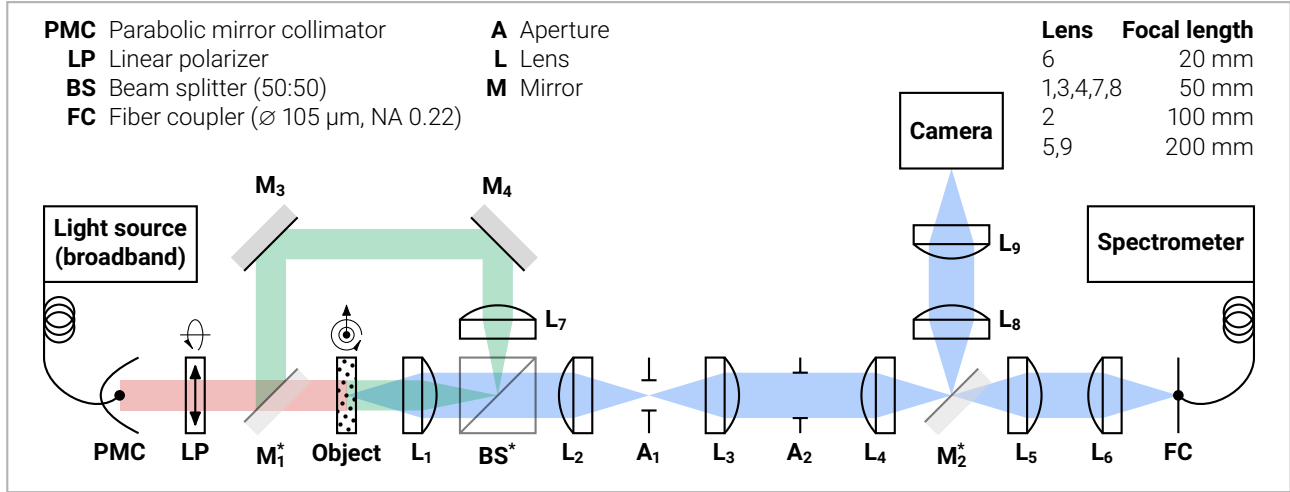


Fig. 6.2 | White-light spectroscopy setup. The light source was a fiber-coupled halogen lamp. The PMC produced a Gaussian beam with a divergence angle of less than 1° . The rotation of the LP, and the rotation and lateral shift of the object were automated. The largest collectible object diameter (525 μ m) and scattering angle (2.52°) can be reduced via apertures A_1 and A_2 , respectively. Elements with a star superscript are removable. Insertion of M_1^* and BS^* switches the setup from transmission to reflection mode. Insertion of M_2^* allows for the inspection and alignment of the object. Red and green areas indicate the illumination path in the transmission and reflection mode, respectively. Blue areas represent the collection path.

The basic idea of this setup is to illuminate the object with a highly collimated beam and then image the object onto the core of a fiber that is connected to a spectrometer. The numerical aperture and the core diameter of the fiber define, together with the magnification factor of the system, the largest collectible object diameter and scattering angle. Aperture A_1 selects the measurement area, which means the region of the object across which the transmittance or reflectance shall be averaged, whereas aperture A_2 reduces the collection angle towards the zeroth order. The insertion of M_1^* and BS^* switches the setup from transmission to reflection mode. Mirror M_2^* was only inserted for the inspection and alignment of the object. Since the spectrometer records the transmitted or reflected intensity spectrum I , it is necessary to perform a reference measurement I_0 to obtain $T, R = I/I_0$, where the object is either removed (transmission mode) or replaced by a mirror (reflection mode). Lastly, to facilitate the measurement of a large number of measurement areas with a fine resolution of θ and ϕ , motorized stages were added to the setup and software was written that enabled a fully automatic acquisition of spectra.

6.4. Phase-shifting interferometry

A phase-shifting interferometer records a set of two-beam interferograms, which means the spatial intensity distribution due to the interference of a known reference beam with a beam that was modulated by the test object, where the phase of the reference beam is shifted in specific steps with the help of a moving mirror or an active optical element [159, 160, 202]. From such a set of interferograms, it is possible to retrieve the phase modulation that was introduced by the test object.

The following discussion focuses on transparent planar objects that generate an output electric field $\mathbf{E}_{\text{out}}(x, y) = t(x, y) \mathbf{E}_{\text{in}}(x, y)$ in response to an input electric field \mathbf{E}_{in} , where $t = \sqrt{T} e^{i\varphi}$, T and φ are the transmission coefficient profile, transmittance profile and phase profile, respectively (Sec. 3.4.4). For this class of objects, it is advisable to use a Mach-Zehnder configuration. Figure 6.3 depicts the setup that was constructed for the measurement of the transmission coefficient profile.

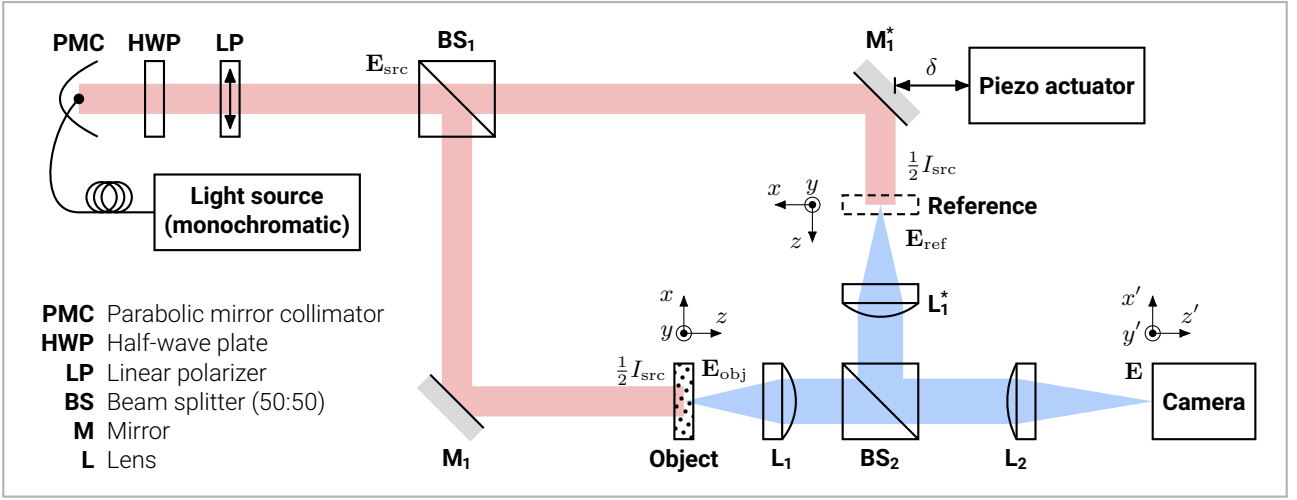


Fig. 6.3 | Phase-shifting interferometer setup. The light source was a fiber-coupled tunable continuous-wave laser. The PMC produced a weakly-diverging Gaussian beam. The HWP and LP prepared the source beam. Elements with a star superscript must be identical to their non-starred counterparts. Since the piezo actuator shifted M_1^* only by fractions of a wavelength, the lateral shift of the reference beam was neglected. The object can be moved along $-\hat{z}$ to measure the phase profile in various planes behind the object. Red and blue areas indicate the paths of the source beam and the imaging system, respectively.

The imaging system, consisting of lenses L_1 , L_1^* and L_2 with respective focal lengths f_1 and f_2 , maps conjugate points $\mathbf{r} = (x, y)$ of the object plane and reference plane into the same point $\mathbf{r}' = -f_2/f_1 \mathbf{r}$ of the camera plane. The non-polarizing beam splitters BS_1 and BS_2 have an intensity splitting ratio of 50:50. Consequently, the electric field \mathbf{E} in the camera plane is the superposition of the electric field \mathbf{E}_{obj} from behind the object plane and the electric field \mathbf{E}_{ref} from behind the reference plane

$$\mathbf{E}(\mathbf{r}') = \frac{1}{\sqrt{2}}\mathbf{E}_{\text{obj}}(\mathbf{r}) + \frac{1}{\sqrt{2}}\mathbf{E}_{\text{ref}}(\mathbf{r}) = \frac{1}{2} [t(\mathbf{r}) + e^{ik\delta}] \mathbf{E}_{\text{src}}(\mathbf{r}) \quad (6.1)$$

$$\mathbf{E}_{\text{obj}}(\mathbf{r}) = t(\mathbf{r}) \frac{1}{\sqrt{2}}\mathbf{E}_{\text{src}}(\mathbf{r}) \quad (6.2)$$

$$\mathbf{E}_{\text{ref}}(\mathbf{r}) = e^{ik\delta} \frac{1}{\sqrt{2}}\mathbf{E}_{\text{src}}(\mathbf{r}) \quad (6.3)$$

where $\mathbf{E}_{\text{src}}/\sqrt{2}$ is the electric field of the source directly in front of the object plane or reference plane, k is the wavenumber of the surrounding medium, δ is the path length difference introduced by the piezo actuator, an ideal imaging system was assumed, and all phase terms that are common to both interferometer arms were ignored. The source field generally diffracts as it propagates into the object and reference plane, but if this happens symmetrically in both interferometer arms, it suffices to only consider $\mathbf{E}_{\text{src}}(\mathbf{r})/\sqrt{2}$ and its intensity profile $I_{\text{src}}(\mathbf{r})/2$ directly in front of the object or reference plane. With this, the intensity profile in the camera plane $I = \frac{1}{2} \text{Re}(\mathbf{E} \times \overline{\mathbf{H}}) \cdot \hat{\mathbf{z}}$ can be written as

$$I(\mathbf{r}'; k\delta) = I_0(\mathbf{r}) [1 + V(\mathbf{r}) \cos(\varphi(\mathbf{r}) - k\delta)] \quad (6.4)$$

$$I_0(\mathbf{r}) = \frac{1 + T(\mathbf{r})}{4} I_{\text{src}}(\mathbf{r}) \quad (6.5)$$

$$V(\mathbf{r}) = \frac{2\sqrt{T(\mathbf{r})}}{1 + T(\mathbf{r})} \quad (6.6)$$

where the visibility $V \in [0, 1]$ measures how strongly the average intensity I_0 is modulated due to interference. In a realistic setup, the beam paths and optical elements in the interferometer arms are rarely identical, which can have the same effect as an additional phase modulation $\Delta(\mathbf{r})$ that leads to a deformed phase profile $\varphi(\mathbf{r}) \rightarrow \varphi(\mathbf{r}) + \Delta(\mathbf{r})$. To compensate for Δ , it is necessary to directly measure Δ by removing the object from the beam path ($\varphi = 0$). Moreover, since the light source and the piezo actuator often drift, it is advisable to repeat this procedure with each new measurement of φ . Instructions for the initial alignment of a Mach-Zehnder interferometer can be found in [202].

Phase retrieval algorithms Least-squares fitting is a standard numerical method for the inversion of an overdetermined nonlinear system, such as Eq. (6.4), where one seeks the phase profile $\varphi(\mathbf{r})$ given N interferograms $I(\mathbf{r}'; k\delta_n)$ that were recorded at specific steps δ_n . Although the steps may have an arbitrary spacing, general least-squares algorithms greatly simplify for equispaced δ_n [203]. In this case, the fitting problem reduces to the computation of the following partial sum

$$I(\mathbf{r}') = \sum_{n=0}^{N-1} I(\mathbf{r}'; k\delta_n) e^{ik\delta_n} = \frac{N}{2} I_0(\mathbf{r}) V(\mathbf{r}) e^{i\varphi(\mathbf{r})} \quad \delta_n = \frac{\lambda}{N} n \quad N \geq 3 \quad (6.7)$$

from which the phase profile can easily be recovered:

$$\varphi(\mathbf{r}) = \arctan\left(\frac{\text{Im } I(\mathbf{r}')}{\text{Re } I(\mathbf{r}')}\right) \quad (6.8)$$

For $N = 4$, this becomes the Carré algorithm [204], and for $N > 4$, there is a close relation to error-correcting algorithms that aim to compensate for certain systematic errors [202]. Note that in this class of algorithms, all spatial points are computed independently of each other.

By making use of the spatial information encoded in the interferograms, an N -step algorithm has been developed that is robust against deviations from the nominal δ_n steps [205]. However, this algorithm typically requires more than four interference fringes to be present in the interferograms, which may require the deliberate introduction of a phase modulation $\Delta(\mathbf{r})$ in the reference beam. This algorithm starts from the same premise as Eq. (6.7), but retrieves the phase profile, up to a constant term, from

$$\varphi(\mathbf{r}_{\mathbf{m}}) = \arctan\left(\frac{\mathcal{N} \{[\mathcal{N} \text{Im} - \mathcal{N} \text{Re}] I(\mathbf{r}_{\mathbf{m}})\}}{\mathcal{N} \{[\mathcal{N} \text{Im} + \mathcal{N} \text{Re}] I(\mathbf{r}_{\mathbf{m}})\}}\right) - \text{const.} \quad \mathcal{N} f(\mathbf{r}_{\mathbf{m}}) = \frac{f(\mathbf{r}_{\mathbf{m}})}{\sqrt{\frac{1}{M} \sum_{\mathbf{m}} [f(\mathbf{r}_{\mathbf{m}})]^2}} \quad (6.9)$$

where the two-dimensional multi-index \mathbf{m} enumerates the M camera pixels, and \mathcal{N} is a normalization operator that divides a function by its spatial root-mean-square value. For a fixed N , the constant term depends only on the (unknown) actual δ_n steps. Hence, as long as the actual δ_n steps are reproducible, the constant term has the same value and can be eliminated altogether with a measurement of $\Delta(\mathbf{r})$.

7. Optical Properties of Positionally Disordered Huygens' Metasurfaces

7.1. Fundamentals of ordered Huygens' metasurfaces

A Huygens' metasurface is a resonant metasurface where each particle sustains a *Huygens source* [22], which in turn is a carefully balanced superposition of vector spherical harmonics that completely suppresses scattering antiparallel to the propagation direction of an incident plane wave. More precisely, the multipole coefficients of a particle must satisfy the *generalized Kerker condition* [206, 207], which can be derived by requiring the differential energy flux along the polar axis to vanish (Appendix A.2). This condition typically also largely suppresses scattering into the backward-facing hemisphere, as demonstrated by the electric field in Fig. 7.1c, where destructive interference occurs along the negative z -axis for the superposition of an x -oriented electric dipole (Fig. 7.1a) and a y -oriented magnetic dipole (Fig. 7.1b). Purely dipolar Huygens sources require electric and magnetic dipole coefficients that satisfy $a_1^1 = b_1^1$ and $a_1^{-1} = -b_1^{-1}$. As higher-order multipoles are introduced, additional combinations of multipole coefficient become available, and the creation of Huygens sources that are based entirely on either electric or magnetic multipoles becomes possible. Lastly, since the multipole coefficients are wavelength-dependent, the involved multipole resonances must be brought into spectral overlap and should ideally have identical lineshapes.

When Huygens sources are arranged in an array, the Floquet-Bloch boundary conditions reduce the continuum of scattered waves to a finite number of diffraction orders, and since resonant metasurfaces are typically operated at wavelengths for which only the zeroth diffraction orders can propagate into the farfield, the ability of Huygens sources to completely suppress backscattering translates into a vanishing reflectance and a maximized transmittance. More precisely, the transmission coefficient of an ordered metasurface can be expressed in terms of effective multipole coefficients (or moments) that result from the multipole coefficients of a single particle, which are fully determined by the particle's geometry and refractive index, and the electromagnetic coupling with the array (Appendix A.5). Hence, the transmission coefficient can be tuned via the particle geometry and lattice constant. Lastly, note that Huygens' metasurfaces generally require particles that have at least two independent geometrical parameters, as for example the radius and height of a cylinder, or otherwise it would be impossible to independently tune the resonance wavelengths of the involved multipolar orders [21]. Moreover, dielectric particles offer not only considerably lower absorption losses than plasmonic particles, but also a simpler and more direct control over both electric and magnetic multipoles [20].

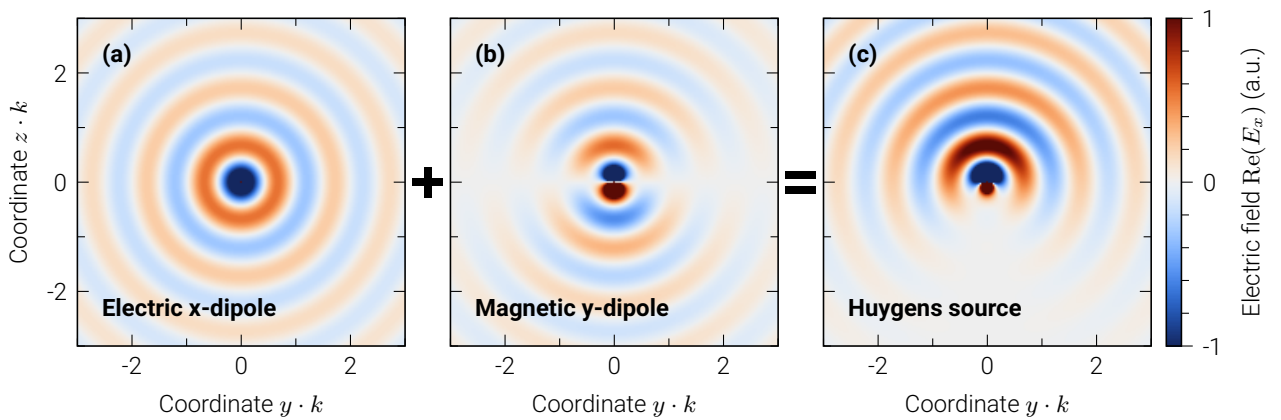


Fig. 7.1 | Electric and magnetic dipoles form a Huygens source. The electric field component $\text{Re}(E_x)$ in the y - z plane of an (a) x -oriented electric dipole, a (b) y -oriented magnetic dipole, and the resulting (c) Huygens source. All coordinates were normalized by the wavenumber k of the homogeneous background medium. The electric field of the depicted Cartesian electric and magnetic dipoles is proportional to $\mathbf{N}_1^1 - \mathbf{N}_1^{-1}$ and $\mathbf{M}_1^1 + \mathbf{M}_1^{-1}$ for $i = 3$, respectively.

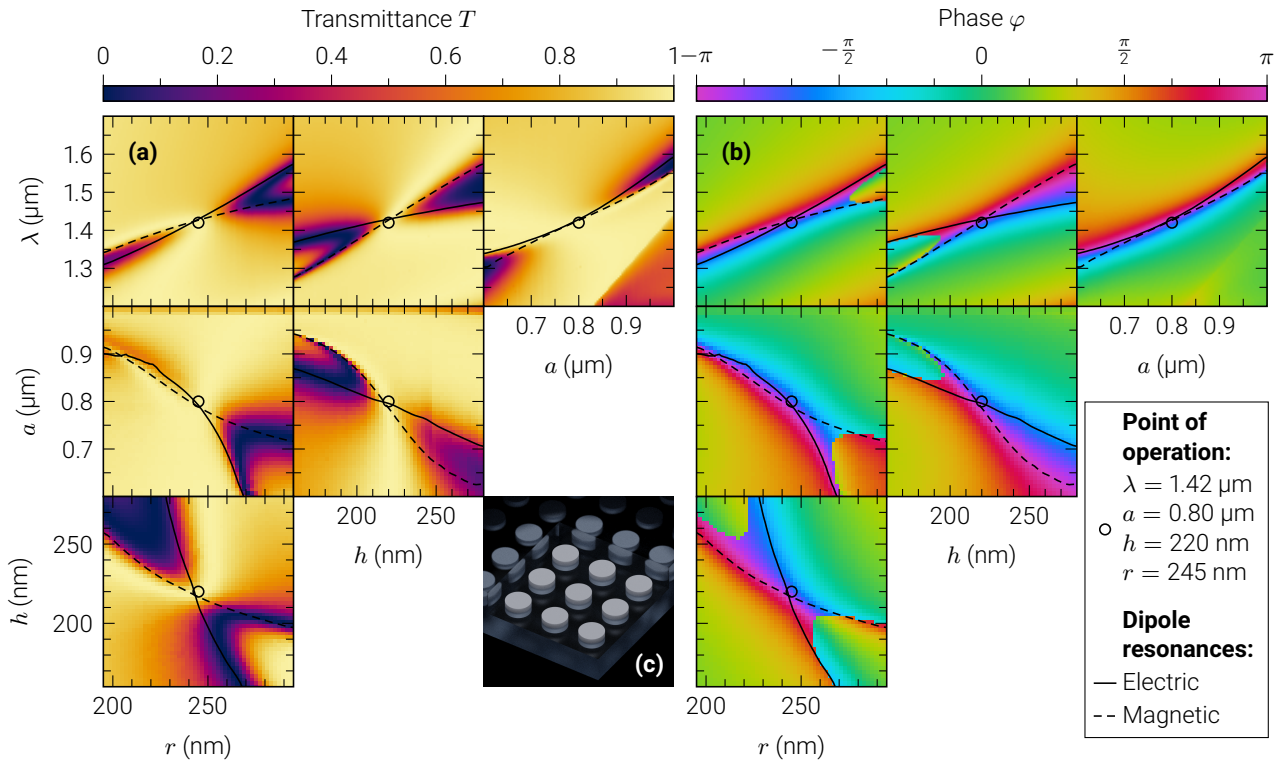


Fig. 7.2 | Design parameters of an ordered Huygens' metasurface. The simulated zeroth-order (a) transmittance and (b) phase of an array of amorphous silicon nanocylinders with radius r , height h , and lattice constant a , embedded in amorphous silicon dioxide and excited by a normally-incident plane wave with vacuum wavelength λ . Each subplot shows six orthogonal planes of the four-dimensional parameter space (λ, a, h, r) that intersect at the point of operation (circular marks). Solid and dashed lines represent ridges (local maxima) in the partial scattering cross sections of electric and magnetic dipoles, respectively. (c) Artistic impression of the array at the point of operation (a, h, r to scale).

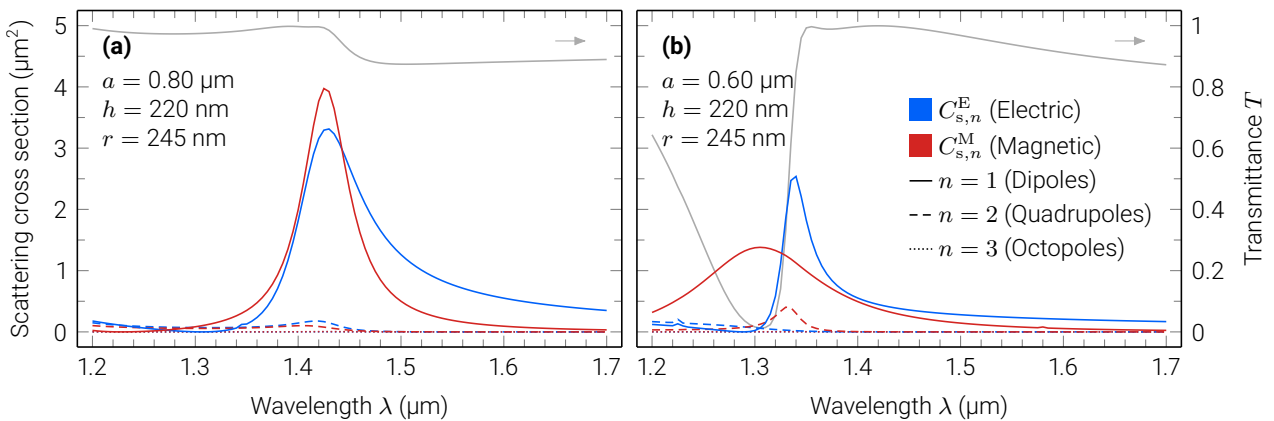


Fig. 7.3 | Partial scattering cross sections of an ordered Huygens' metasurface. The contributions of electric and magnetic multipoles to the scattering cross section of the Huygens' metasurface from Fig. 7.2 at the (a) point of operation and for a (b) smaller lattice constant. Gray lines show corresponding transmittance spectra (cf. a - λ -dependency in Fig. 7.2a).

Figure 7.2 shows the simulated zeroth-order transmittance and phase of a square array of amorphous silicon nanocylinders that are embedded in amorphous silicon dioxide. Each subplot displays realistic parameter ranges for all pairwise combinations of the excitation wavelength λ , the lattice constant a , and the nanocylinder radius r and height h . Solid and dashed lines indicate the resonance positions of electric and magnetic dipoles, respectively. In general, it can be observed that the transmittance approaches 1 and the phase π near overlapping resonances, or 0 and $\pm\frac{\pi}{2}$ near an isolated resonance. Appendix A.5 provides a brief theoretical explanation for this observation in ordered metasurfaces. Moreover, only in the vicinity of overlapping resonances it is possible to obtain phase values of $|\varphi| > \frac{\pi}{2}$. Hence, to attain a Huygens' metasurface, one may search for geometric parameters that yield a transmission coefficient of $t = -1$, which also marks the point of operation.

The r - h -dependency is here of special interest, since it is only due to this geometric anisotropy that the resonance positions of electric and magnetic dipoles can be shifted with respect to each other. For spherical particles, the relative positions are fixed by the sphere's radius and index contrast [6]. The higher sensitivity of the electric dipole with respect to r , or that of the magnetic dipole with respect to h , is due to the pronounced radial or orbital shape of the respective vector spherical harmonics (cf. Figs. 7.1a,b). Hence, by tuning the aspect ratio h/r , the electric and magnetic dipole resonances can be brought into spectral overlap, which then typically also results in the (approximate) fulfillment of the Kerker condition across the entire bandwidth of the dipole resonances.

For a fixed aspect ratio, the a - λ -dependency shows that the resonance wavelengths of the electric and magnetic dipoles shift almost synchronously with a . Deviations only occur for very small a , where the nearfield coupling of neighboring particles dominates, and for very large a , where higher diffraction orders begin to play a role [208]. Moreover, since Maxwell's equations are scale invariant, the resonance wavelengths can also be shifted via an isotropic scaling of the nanocylinders.

In summary, these dependencies allow the point of operation to be realized at arbitrary wavelengths, provided that materials with suitable refractive indices are available at the target wavelength. Other combinations of transmittance and phase values are typically obtained via the r - a -dependency, since height variations are usually more difficult to fabricate.

Figure 7.3 analyses the multipolar contributions to the scattering cross section of the ordered Huygens' metasurface from Fig. 7.2 for different lattice constants. Note that since the scattering cross section was obtained from a multipole expansion of the total electric field within one nanocylinder of the array, which includes the collective response of all nanocylinders, the presented multipolar contributions represent the *effective* response of one nanocylinder inside the array.

At the point of operation (Fig. 7.3a), the electric and magnetic dipole contributions are very similar to each other and reminiscent of Lorentzian and Fano-type lineshapes. The contributions of higher multipolar orders are very small, and hence, the asymmetry in the transmittance spectrum is mostly caused by the asymmetric dipolar lineshapes and the approximate fulfillment of the Kerker condition. However, it is important to keep in mind that $C_{s,n}^E$ and $C_{s,n}^M$ only represent the magnitudes of the excited multipole coefficients, whereas the generalized Kerker condition demands a very specific complex-valued relationship between all multipole coefficients. Hence, identical values for $C_{s,n}^E$ and $C_{s,n}^M$ are merely a good indicator rather than a strict requirement for the achievement of a high transmittance (compare at $\lambda = 1.40 \mu\text{m}$ and $\lambda = 1.44 \mu\text{m}$).

When the lattice constant is reduced (Fig. 7.3b), enhanced nearfield coupling leads to the spectral separation of the maxima in the electric and magnetic dipole contributions, and to the excitation of slightly stronger magnetic quadrupoles. At $\lambda = 1.30 \mu\text{m}$, only magnetic dipoles are excited and the transmittance approaches zero, whereas at $\lambda = 1.34 \mu\text{m}$, the generalized Kerker condition appears to be satisfied due to the interaction with magnetic quadrupoles.

Lastly, note that the resonance width of the electric and magnetic dipoles typically amounts to about 100 nm or less, which may be narrow enough for the realization of certain wavelength-selective or wavelength-multiplexed devices.

(a) Nanocylinder	Resonance case					(b) Metasurface types	
		Overlapping	Separate				
Diameter	d	490 [468]	600 [582]	nm	Array	$\mathbf{p} \in \{a\mathbf{i} \mid \mathbf{i} \in \mathbb{Z}^2\}$	
Height	h	220 [213]	220 [211]	nm	Perturbed array	$\mathbf{p} \in \{a\mathbf{i} + \mathbf{P}_i \mid \mathbf{i} \in \mathbb{Z}^2\}$	
Lattice constant	a	800 [800]	900 [900]	nm	Soft-core uniform	$\mathbf{p} \in \text{Mat3}[f_{\text{sc}}(r; R, a, 1)]$	
Density, soft-core	ρ	1.56 [1.51]	1.23 [1.12]	μm^{-2}	Hard-core uniform	$\mathbf{p} \in \text{Mat3}[f_{\text{hc}}(r; R)]$	
Density, hard-core	ρ	1.56 [1.55]	1.23 [1.22]	μm^{-2}			
						$\mathbf{P}_i = \frac{a-R}{2} \sqrt{U_i} \begin{pmatrix} \cos(2\pi V_i) \\ \sin(2\pi V_i) \end{pmatrix}$	$U_i, V_i \in [0, 1]$
						$R = d + d_{\text{min}}$	$f_{\text{sc}}, f_{\text{hc}}: \text{Eq. (4.22)}$

Table 7.1 | A summary of design parameters. (a) Targeted and actual (in square brackets) nanocylinder parameters for the overlapping and separate resonance case. (b) Particle positions \mathbf{p} of all metasurface types, where U_i, V_i are samples from the continuous uniform distribution, $\text{Mat3}[\cdot]$ is the generalized Matérn type-III point process that uses the deletion probability functions $f_{\text{sc}}, f_{\text{hc}}$, and the fabrication required a minimum edge-to-edge distance of $d_{\text{min}} = 80$ nm between all nanocylinders. Each fabricated metasurface had a size of $(2 \text{ mm})^2$ and contained more than 6 million nanocylinders.

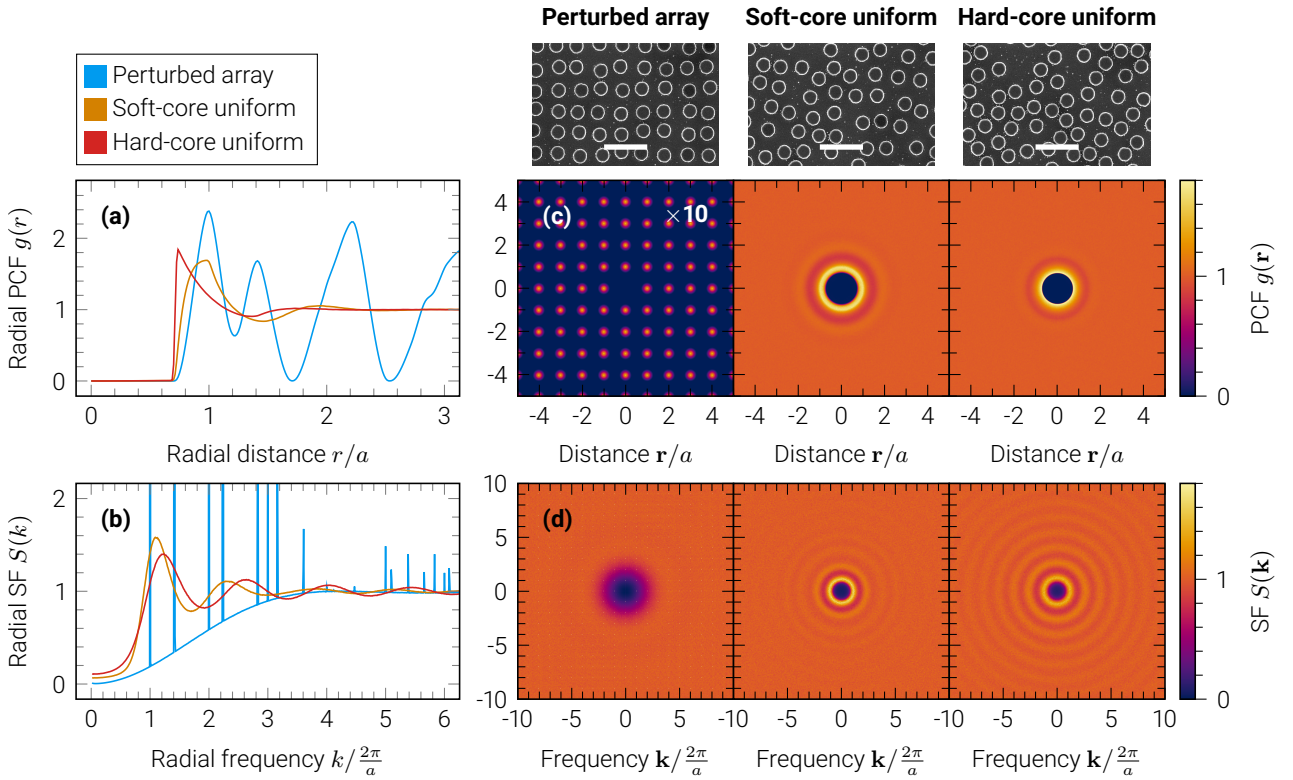


Fig. 7.4 | Particle statistics of disordered metasurface types. (a,b) Radial and (c,d) two-dimensional pair correlation function (PCF) and structure factor (SF) of all disordered metasurface types (column titles) for the overlapping resonance case. The axes of (c) and the above scanning electron micrographs of fabricated metasurfaces (scale bars: $2a$) are true to scale. The PCF of the perturbed array in (c) is ten times larger than indicated by the color bar. All distances and frequencies are normalized with respect to the lattice constant $a = 800$ nm of the array.

7.2. Design of metasurface types and resonance cases

This section presents the design parameters of ordered and disordered Huygens' metasurfaces that were studied throughout the remainder of this chapter. The term *metasurface type* is used to classify the type and degree of disorder in the particle distribution of a metasurface, and the *resonance case* distinguishes between metasurfaces that do or do not sustain Huygens sources.

More precisely, four metasurface types (*array*, *perturbed array*, *soft-core uniform*, *hard-core uniform*) and two resonance cases (*overlapping*, *separate*) were devised that utilize amorphous silicon nanocylinders embedded in amorphous silicon dioxide (fabrication details in Sec. 6.1). The *array* is the only ordered metasurface type and serves as reference. The *overlapping* resonance case was designed such that the electric and magnetic dipole resonances overlap at a wavelength of about $\lambda = 1.4 \mu\text{m}$, whereas in the *separate* resonance case, they are located around $\lambda = 1.6 \mu\text{m}$ and $\lambda = 1.5 \mu\text{m}$, respectively.

Table 7.1 summarizes the geometric parameters of the nanocylinders and illustrates how the particle positions were generated. The particles in the *array* form a square lattice with lattice constant a . The *perturbed array* is based on the *array*, where each particle is translated by a random vector with a maximum magnitude of $(a - R)/2$ for a minimum pair distance of R . The *soft-core uniform* and *hard-core uniform* types were obtained from the generalized Matérn type-III point process with respective deletion probability functions f_{sc} and f_{hc} (Eq. (4.22)) for a target density of $\rho = a^{-2}$.

Figure 7.4 shows the pair correlation function and structure factor of the disordered metasurface types. The *perturbed array* maintains the long-range order of the underlying square lattice (narrow peaks in Figs. 7.4b,d). The *uniform*-type metasurfaces are highly homogeneous and isotropic ($g \approx 1$ for $r/a > 2$ in Figs. 7.4a,c), and nearly classify as *hyperuniform* [91], which requires $\lim_{k \rightarrow 0} S(k) = 0$ (cf. Fig. 7.4b) and implies that the structure does not repeat itself on very large length scales. The main difference between *soft-core uniform* and *hard-core uniform* is their short-range order (Fig. 7.4a for $r/a < 2$): The short-range order of *soft-core uniform* is similar to that of the *perturbed array*, where most particles have a pair distance of $r/a = 1$, as compared to $r/a \approx 0.7$ for *hard-core uniform*. Hence, since these metasurface types resemble crystal-like or liquid-like structures, one may associate increasing positional disorder with the sequence of: *array*, *perturbed array*, *soft-core uniform*, *hard-core uniform*.

7.3. Zeroth-order transmission and reflection

This section presents experimental data that nearly exhaustively characterizes the optical properties of ordered and disordered Huygens' metasurfaces along the zeroth order in transmission and reflection. Most of the experiments are supported and validated by simulations based on the T-matrix method. More specifically, the subsequent sections focus on the following properties of all metasurface types:

Section 7.3.1 presents experimental transmittance spectra in dependence on the incidence angle of a TE or TM polarized incident plane wave. Here, the generalized Brewster effect can be observed in the *array*, and the *uniform*-type metasurfaces exhibit a transmittance that hardly changes with the incidence angle and polarization of the incident wave.

Section 7.3.2 presents experimental and simulated spectra of the transmission coefficient, reflectance, and diffuse scatterance for normally-incident plane wave excitation. Here, a disorder-induced phase transition and a diffuse scatterance of one can be observed in metasurfaces that possess a critical degree of positional disorder. Such a high diffuse scatterance is essential for the realization of perfect optical diffusers, which is investigated in more detail in Sec. 7.4.

Section 7.3.3 presents spatial statistics of the transmission coefficient for the *overlapping* resonance case with resonant or off-resonant excitation by a normally-incident plane wave. Here, experimental evidence indicates that disordered metasurfaces are suitable for wavefront shaping, and simulations of the induced electric and magnetic dipole moments provide a deeper theoretical understanding of how positional disorder affects the optical properties of Huygens' metasurfaces.

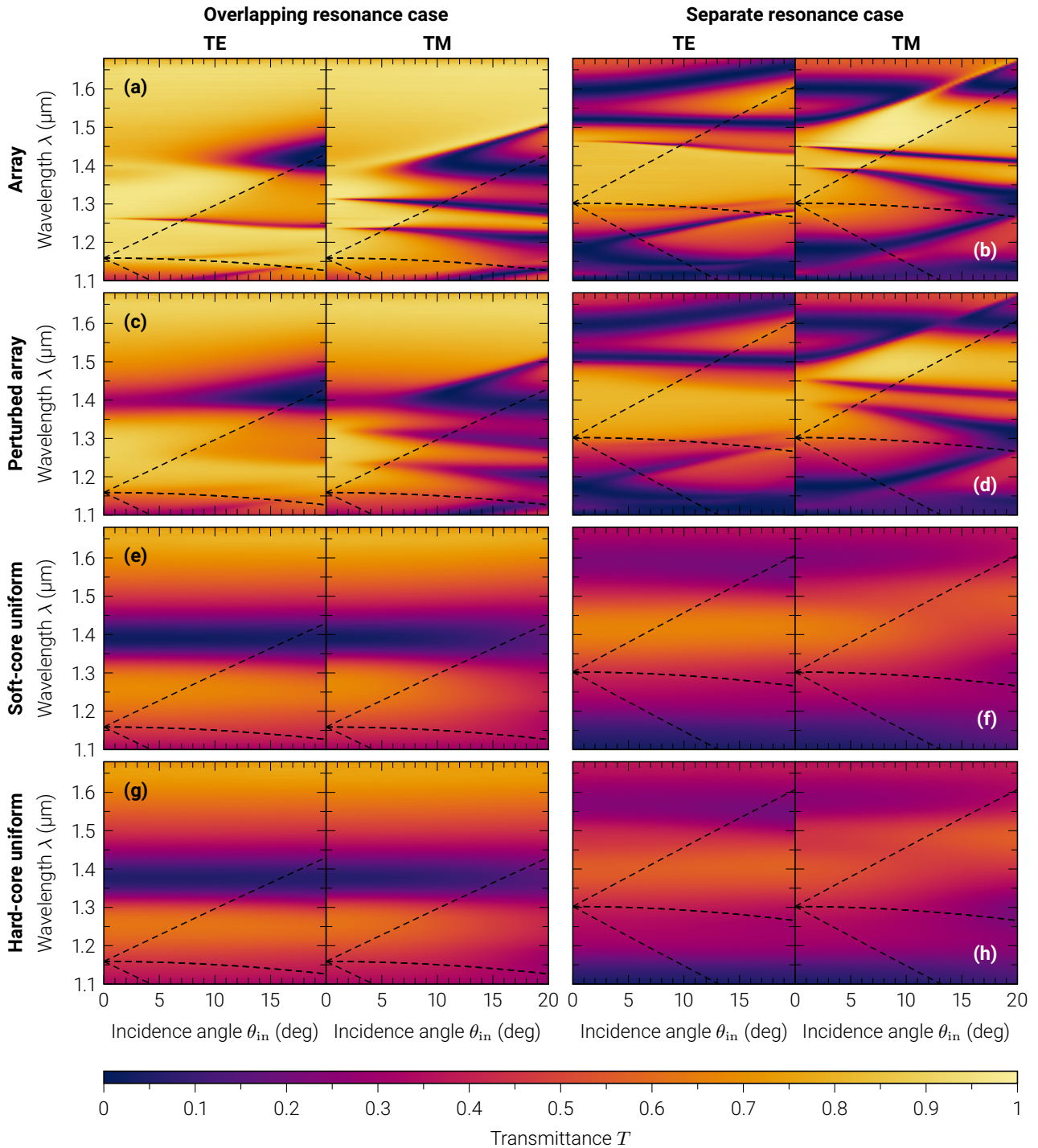


Fig. 7.5 | Experimental transmittance spectra for oblique incidence. Transmittance spectra of the (a,b) array, (c,d) perturbed array, (e,f) soft-core uniform and (g,h) hard-core uniform metasurface type for both resonance cases and TE or TM polarized plane wave excitation (column titles). Dashed lines indicate the onsets of the lowest diffraction orders in the array (top to bottom: $(1, 0)$, $(0, \pm 1)$, $(-1, 0)$). The polar incidence angle θ_{in} is measured in air, and the azimuthal incidence angle $\phi_{\text{in}} = 0$ is measured with respect to the x -axis of the array.

7.3.1. Spectra for oblique incidence

Figure 7.5 shows experimental transmittance spectra of all metasurface types and resonance cases for TE or TM polarized plane wave excitation with incidence angles θ_{in} of up to 20° . The following discussion focuses on how the transmittance changes directly at the resonance wavelength of the electric or magnetic dipole. Hence, to enhance the readability of the following paragraphs, this specification is not repeated and the reader is asked to mentally add the phrase “at the dipole resonance wavelength” after each occurrence of “transmittance”.

The *array* behaves as expected [30]: In the *overlapping* resonance case and for normal incidence (Fig. 7.5a; $\theta_{\text{in}} = 0^\circ$), the electric and magnetic dipole resonances are in spectral overlap at $\lambda = 1.4 \mu\text{m}$, the generalized Kerker condition is satisfied, and the transmittance is nearly one. As the incidence angle increases, the dipole resonances shift apart and separate at about 15° (TE) or 10° (TM), which is accompanied by a reduction of the transmittance to nearly zero. In the *separate* resonance case (Fig. 7.5b) and for TM polarization, the electric and magnetic dipole resonances (near $\lambda = 1.6 \mu\text{m}$ and $\lambda = 1.5 \mu\text{m}$, respectively; $\theta_{\text{in}} = 0^\circ$) shift towards each other and overlap at about $\theta_{\text{in}} = 13.5^\circ$, which leads to a high transmittance due to the generalized Brewster effect [209]. However, the electric dipole resonance shifts significantly less than the magnetic dipole resonance. For TE polarization, the electric and magnetic dipole resonances shift apart, but here it is the magnetic dipole resonance that is less sensitive to the incidence angle. This may qualitatively be understood by considering the volume that the electric and magnetic vector spherical harmonics occupy within a nanocylinder, where a compression or expansion of the mode volume, due to the rotation of the nanocylinder with respect to the incident wave, corresponds to a spectral blue-shift or red-shift, respectively. The comparatively narrow resonances at wavelengths of about 1.25 and $1.30 \mu\text{m}$ in Fig. 7.5a, and 1.40 and $1.45 \mu\text{m}$ in Fig. 7.5b, are higher-order lattice modes that are not excited under normal incidence.

The resonance wavelengths of the *perturbed array* are almost identical to those of the *array*. However, the presence of positional disorder significantly reduces the transmittance when the electric and magnetic dipole resonances are in spectral overlap (compare Figs. 7.5a,c for $\theta_{\text{in}} < 10^\circ$ and Figs. 7.5b,d at $\theta_{\text{in}} = 13.5^\circ$), or slightly increases the transmittance when they are spectrally isolated. Additionally, all spectral features appear slightly broader than in the *array*. The physical reason for the decrease or increase of the transmittance due to disorder will be discussed in Sec. 7.3.2 on the basis of a phase transition, and in Sec. 7.3.3 with the help of spatial statistics of induced dipole moments.

The *soft-core uniform* and *hard-core uniform* types show only minuscule differences when compared to each other, but a much stronger insensitivity with respect to the incidence angle and polarization when compared to the *array* or *perturbed array*. In the *overlapping* resonance case (Figs. 7.5e,g), the transmittance is near zero, and the electric and magnetic dipole resonances hardly shift as the incidence angle increases. In the *separate* resonance case (Figs. 7.5f,h), the transmittance is considerably higher, and the dipole resonances are spectrally much broader than in the *perturbed array*.

In summary, the *array* allows for the realization of angle-selective devices that are, except for a narrow range of incidence angles, highly reflective at the design wavelength (cf. Fig. 7.5b; TM; $\lambda = 1.6 \mu\text{m}$). Moreover, it is possible to obtain the generalized Brewster effect alternatively for TE polarized excitation if the nanocylinder aspect ratio is changed such that the electric dipole resonance occurs, for normal incidence, at a shorter wavelength than the magnetic dipole resonance.

The *uniform-type* metasurfaces of the *overlapping* resonance case exhibit properties that make them promising candidates for optical diffusers: On the one hand, they show a near-zero transmittance, which is a necessary requirement for a high diffuse scatterance and thus a non-trivial directional scatterance. On the other hand, their insensitivity with respect to the incidence angle and polarization of an incident plane wave allows a device to accept more complex input fields. Moreover, since the scattered farfield of the considered metasurfaces can already be taken into account during the design, it seems feasible to utilize such positionally disordered metasurfaces even in wavefront-shaping applications. For example, the angle-insensitive but wavelength-dependent transmittance hints towards the possibility of realizing a metasurface that implements a lens at one wavelength and a diffuser at another.

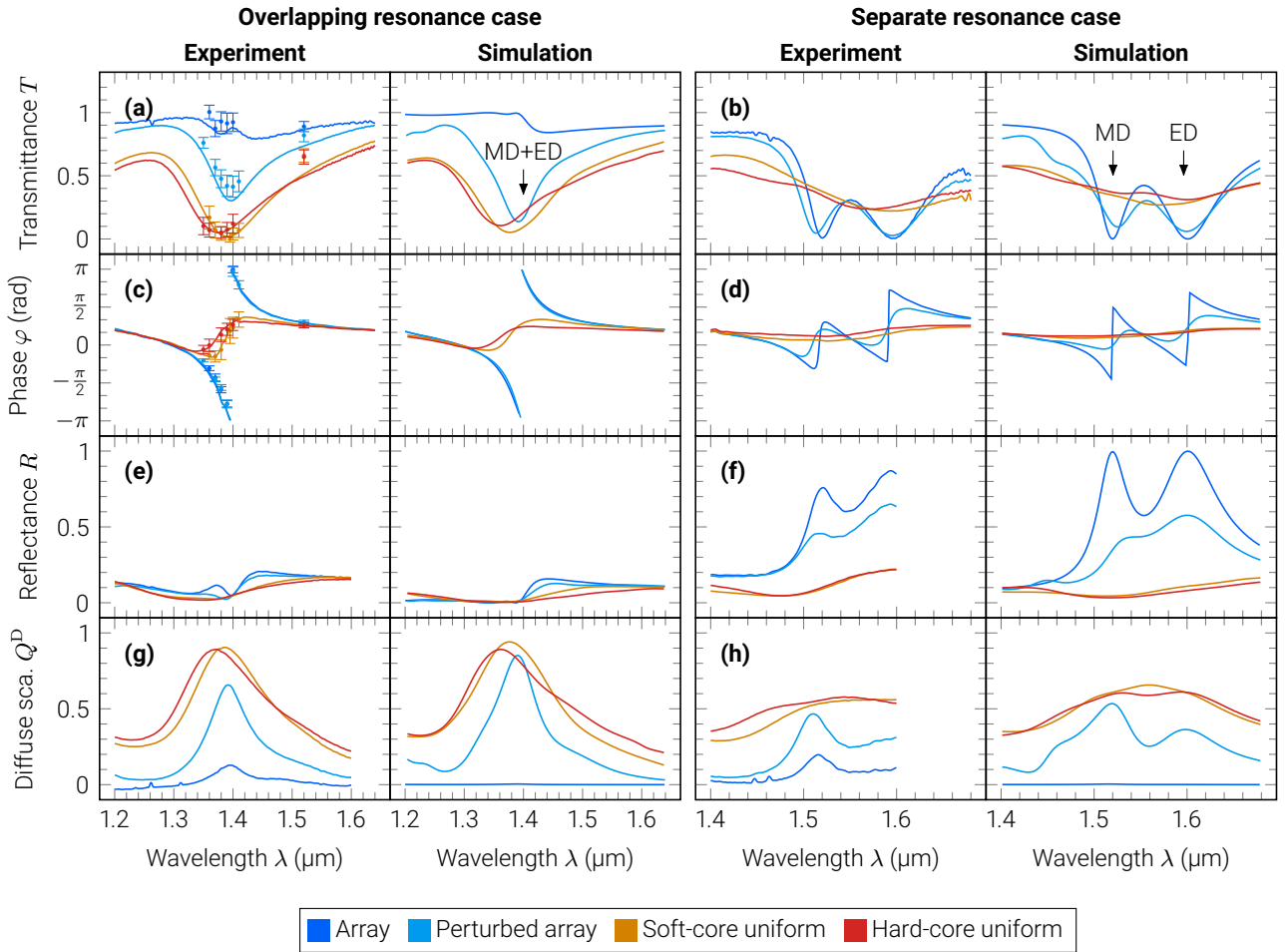


Fig. 7.6 | Spectra for normal incidence. Experimental and simulated (a,b) transmittance, (c,d) phase, (e,f) reflectance and (g,h) diffuse scatterance spectra for both resonance cases (column titles) and TE polarized plane wave excitation under normal incidence. Experimental transmittance and reflectance spectra were measured in the white-light spectroscopy setup (Sec. 6.3). Experimental phase spectra were obtained via Fourier-transform spectral interferometry [210, 211]. Error bars show the spatial mean and standard deviation of experimental transmittance and phase profiles (Fig. 7.8), which were measured in the phase-shifting interferometry setup (Sec. 6.4). Labels MD and ED indicate the resonance wavelength of the magnetic and electric dipole resonance, respectively. Here, the special case $Q^D = 1 - T - R$ applies.

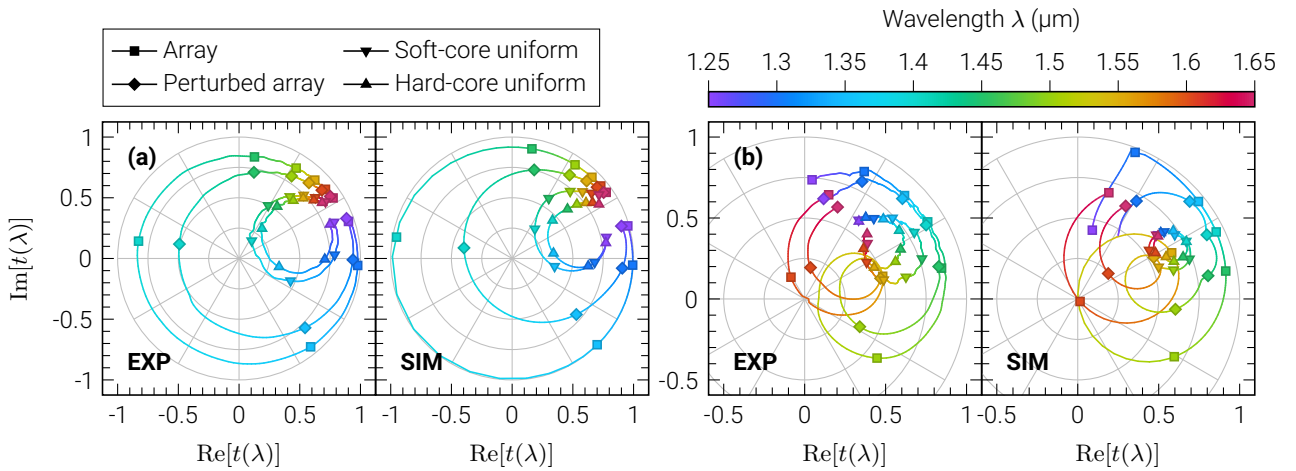


Fig. 7.7 | Parametric plots of transmission coefficients. Experimental (EXP) and simulated (SIM) transmission coefficients $t(\lambda)$ for the (a) overlapping and (b) separate resonance case with TE polarized plane wave excitation under normal incidence. The wavelength λ is color-coded and all marks are placed at nine distinct wavelengths as indicated by the color bar tick labels. The data in this figure is the same as in Figs. 7.6a–d.

7.3.2. Spectra for normal incidence

Figure 7.6 shows the zeroth-order transmittance, phase, reflectance, and diffuse scatterance spectra of all metasurface types and resonance cases for TE polarized plane wave excitation under normal incidence. The transmittance and phase spectra were reused in Fig. 7.7, but presented in a way that is more conducive to the comprehension of the *disorder-induced phase transition* [31].

First, consider the transmittance and phase spectra of the *overlapping* resonance case for increasing wavelengths (Figs. 7.6a,c). For the *array* and *perturbed array*, the transmittance remains relatively high, while the phase shows normal dispersion and a cumulative phase change of about -2π . For the *uniform*-type metasurfaces, the transmittance reaches near zero at the resonance wavelength, the phase exhibits anomalous dispersion, and the cumulative phase change is almost zero. Even more so, the *hard-core uniform* type shows a slightly higher transmittance at resonance than *soft-core uniform*. When this behavior is viewed from the perspective of increasing positional disorder (in the sequence of: *array*, *perturbed array*, *soft-core uniform*, *hard-core uniform*), it may seem paradoxical that the transmittance at resonance first reduces but then increases, or that the phase spectrum is greatly insensitive to disorder until it suddenly switches from normal to anomalous dispersion.

However, this paradox can be resolved by considering a parametric representation of the transmission coefficient spectrum $t(\lambda)$ in the complex plane (Fig. 7.7a). With increasing positional disorder, $t(\lambda)$ contracts towards a point on the positive real half-space. To aid the visualization of this contraction, one may focus on a single wavelength (e.g. marks of identical color) and mentally connect all four metasurface types with a curved line. Hence, along the curve that corresponds to the resonance wavelength ($\lambda \lesssim 1.4 \mu\text{m}$), the transmittance first decreases, becomes zero for a critical degree of positional disorder, and then increases. As the contracting $t(\lambda)$ crosses the origin of the complex plane, the phase abruptly transitions from normal to anomalous dispersion, and the cumulative phase change of about -2π suddenly becomes zero. This disorder-induced phase transition was first demonstrated in the course of this thesis [31], where metasurfaces similar to the *perturbed array* were used to continuously tune the degree of positional disorder, and the winding number of $t(\lambda)$ was used to distinguish between four distinct phase states in a phase diagram that relates positional disorder with the spectral detuning of the electric and magnetic dipole resonances.

In the *separate* resonance case (Figs. 7.6b,d), increasing positional disorder always increases the transmittance at the resonance wavelengths, while the phase spectra flatten and the phase remains in the anomalous dispersion regime.

Similarly to the preceding discussion, this behavior is best understood in the complex plane (Fig. 7.7b). The *array* possesses a $t(\lambda)$ that does not encompass the origin of the complex plane, which corresponds to a phase state that already exceeds the critical degree of positional disorder. Consequently, any increase in positional disorder drives the system only further away from the phase transition, and the previously mentioned effects can be observed.

The reflectance and diffuse scatterance spectra of the *separate* resonance case show that at the resonance wavelengths (Figs. 7.6f,h), increasing positional disorder reduces the reflectance and increases the diffuse scatterance. However, even for maximal positional disorder (*hard-core uniform*), the lowest reflectance still amounts to about 5% and the highest diffuse scatterance only to about 60%.

This is in stark contrast to the reflectance and diffuse scatterance in the *overlapping* resonance case (Figs. 7.6e,g): The reflectance at the resonance wavelength is zero for all metasurface types, and the diffuse scatterance approaches one near the critical degree of positional disorder (*soft-core uniform*). As the wavelength is tuned away from the resonance, the diffuse scatterance reduces significantly. For example, nearly 80% of the incident light passes undisturbed through the *soft-core uniform* metasurface at $\lambda = 1.6 \mu\text{m}$. This demonstrates the wavelength-selective diffuser functionality of the disordered metasurfaces, which could be further engineered with carefully tailored higher-order multipoles [44].

A more fundamental explanation for why the transmission coefficient behaves in the described manner will be given in Sec. 7.3.3, and the question of how the metasurfaces redistribute the incident energy along the diffuse directions will be addressed in Sec. 7.4.

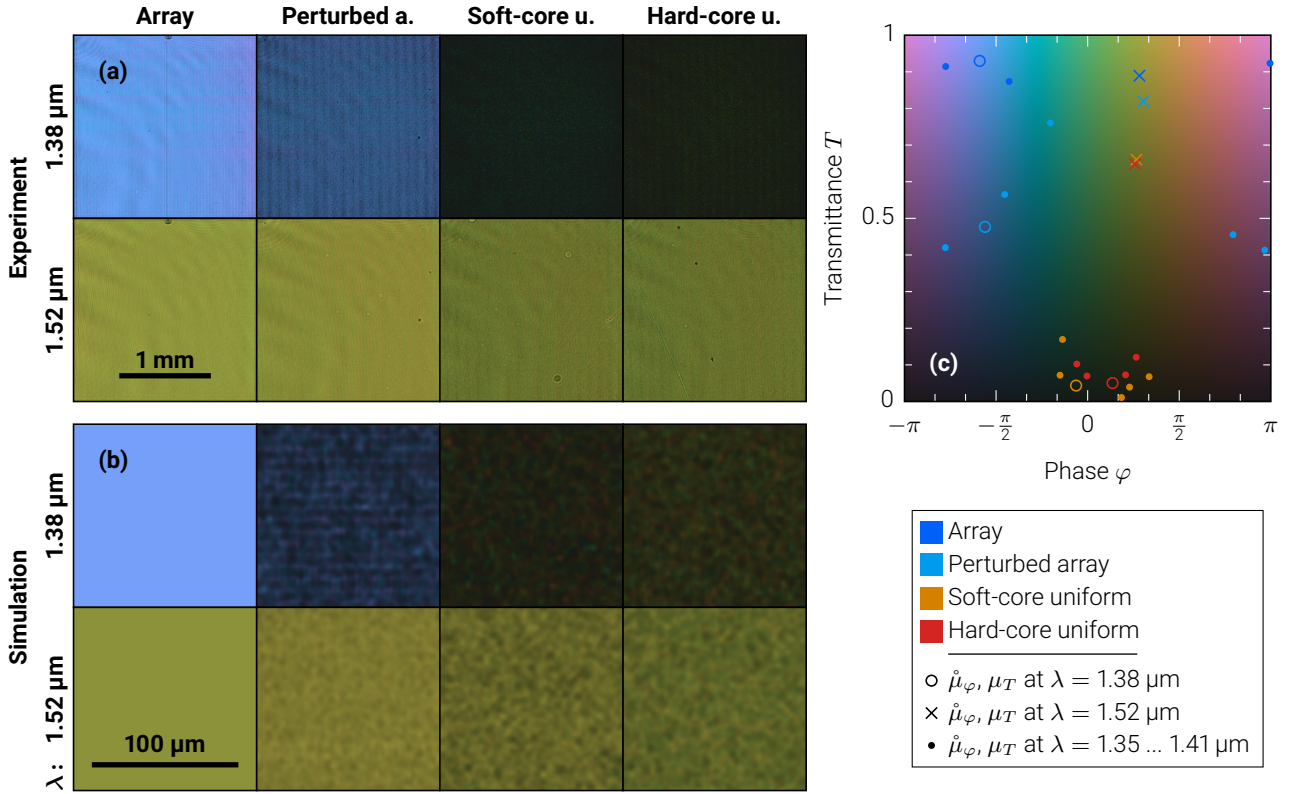


Fig. 7.8 | Transmittance and phase profiles. (a) Experimental and (b) simulated transmittance $T(\mathbf{r})$ and phase $\varphi(\mathbf{r})$ profiles (color-coded via (c)) of all metasurface types (column titles) for the overlapping resonance case with resonant ($\lambda = 1.38 \mu\text{m}$) or off-resonant ($\lambda = 1.52 \mu\text{m}$) excitation (row titles) by a TE polarized plane wave under normal incidence. Each square depicts one profile with side lengths of (a) 2 mm or (b) 125 μm . (c) Color map, where marks indicate the spatial means $\hat{\mu}_{\varphi}, \mu_T$ of experimental profiles: Circles and crosses relate to (a). Dots correspond to error bars in Figs. 7.6a,c (profiles not shown).

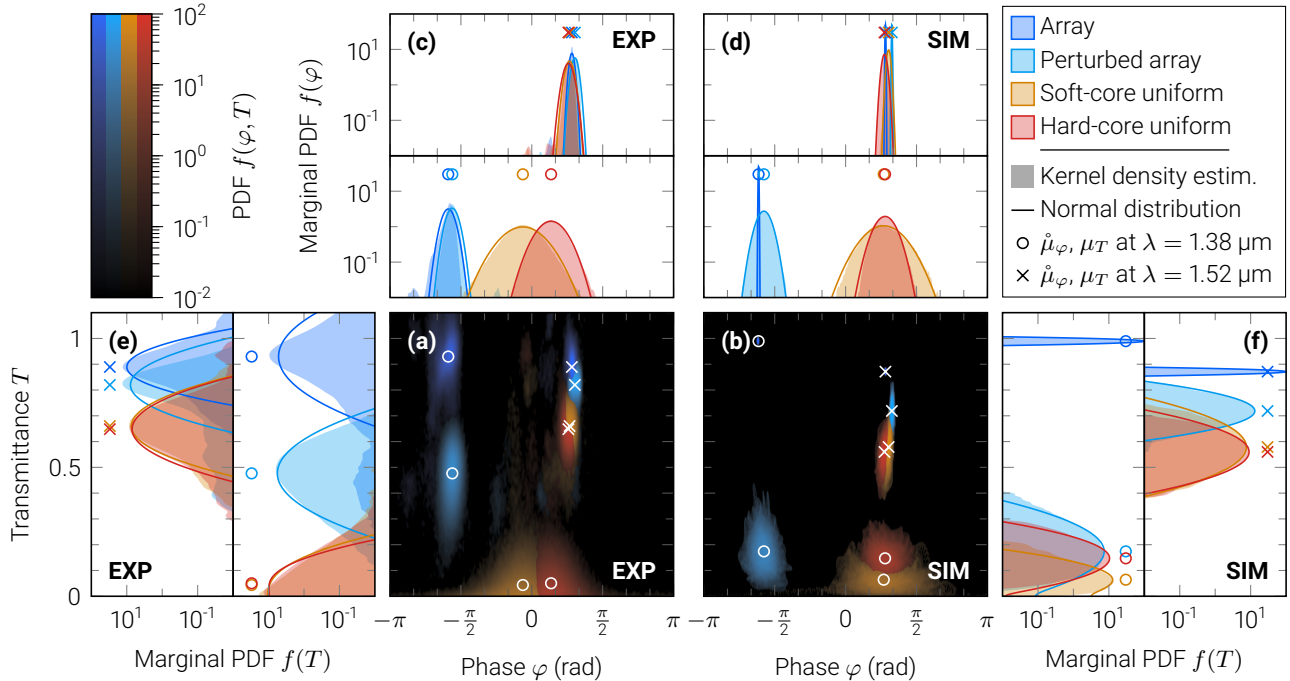


Fig. 7.9 | Probability density functions (PDFs) of transmittance and phase profiles. (a,b) The maximum $\max_{\tau, \lambda} f_{\tau, \lambda}(\varphi, T)$ of the PDFs $f_{\tau, \lambda}$ of all metasurface types τ (colors) for the overlapping resonance case with resonant ($\lambda = 1.38 \mu\text{m}$) or off-resonant ($\lambda = 1.52 \mu\text{m}$) excitation (marks) by a TE polarized plane wave under normal incidence. (c-f) Marginal PDFs, which means definite integrals of $f_{\tau, \lambda}(\varphi, T)$ along φ or T , where shaded areas result from kernel density estimates and solid lines show (c,d) wrapped and (e,f) folded normal distributions with matching means and variances. This figure shows both (a,c,e) experimental (EXP) and (b,d,f) simulated (SIM) data.

7.3.3. Spatial statistics for normal incidence

This section presents spatial statistics of the zeroth-order transmission coefficient and the effective dipole moments of all metasurface types for the *overlapping* resonance case with resonant ($\lambda = 1.38 \mu\text{m}$) or off-resonant ($\lambda = 1.52 \mu\text{m}$) excitation by a TE polarized plane wave under normal incidence. The following paragraphs make use of statistical quantities that are based on the standard normal distribution (Appendix A.4), and of a theoretical model that explains the optical response of disordered Huygens' metasurfaces on the basis of their effective dipole moments (Appendix A.5).

Figures 7.8a,b show experimental and simulated transmittance $T(\mathbf{r})$ and phase $\varphi(\mathbf{r})$ profiles, where Fig. 7.8c associates each tuple (φ, T) with a unique color. Marks indicate the spatial means ($\hat{\mu}_\varphi, \mu_T$) of experimental profiles for resonant and off-resonant (circles and crosses; Fig. 7.8a) or nearly-resonant (dots; also shown as error bars in Figs. 7.6a,c) excitation. The sole purpose of the latter is to visualize the wavelength sensitivity near the resonance. Although the experimental profiles show minor artifacts due to imperfections in the fabrication and measurement system, they appear spatially very homogeneous even on length scales well below 1 mm. In the simulations, $t(\mathbf{r})$ was sampled with a spatial resolution of about $\lambda/3$, and spatial low-pass filters were applied that simulate the limited numerical aperture ($\text{NA} = 0.25$) and the camera pixel size ($5 \mu\text{m}$, square) of the experimental setup. Since the simulations show speckle patterns with a characteristic feature size of about $10 \mu\text{m}$, it can be expected that the experimental profiles just barely resolved such features.

To quantify the spatial variations in the profiles, kernel density estimates of their two-dimensional probability density functions (PDFs) $f(\varphi, T)$ were constructed, marginal PDFs were computed by integrating $f(\varphi, T)$ over the full domain of either φ or T , and normal distributions with matching means and variances were evaluated to verify that the kernel density estimates indeed represent normal distributions. Figures 7.9a,b show experimental and simulated PDFs, where metasurface types are color-coded, and excitation wavelengths and mean values are indicated by marks. The differences between experiment and simulation in terms of the mean values are mainly due to a slight mismatch in the resonance wavelengths, which can also be seen in Figs. 7.6a,c near the excitation wavelengths. The marginal PDFs of the phase $f(\varphi)$ (Figs. 7.9c,d) closely resemble wrapped normal distributions, and the variances in the simulated phase agree well with the experiment. The marginal PDFs of the transmittance $f(T)$ (Figs. 7.9e,f) slightly deviate from a folded normal distribution, and the variances in the simulated transmittance are systematically smaller than in the experiment. However, this is most likely due to experimental imperfections. With these differences in mind, one may still accept that the simulations reliably and accurately predict the optical response of disordered Huygens' metasurfaces. This is an important aspect in the following discussion, since certain quantities, such as the induced effective dipole moments, are only accessible via simulations.

Figure 7.10 reveals correlations in the spatial statistics and examines the influence of positional disorder. In Figs. 7.10a,b, the spatial means μ_T and standard deviations $\hat{\sigma}_\varphi, \sigma_T$ were extracted from Fig. 7.9 and displayed as scatter plots. Figure 7.10a relates σ_T with $\hat{\sigma}_\varphi$, where for off-resonant excitation, both σ_T and $\hat{\sigma}_\varphi$ increase with increasing positional disorder. For nearly-resonant excitation, the *array* and *perturbed array* exhibit a positive correlation between σ_T and $\hat{\sigma}_\varphi$, but in the case of *soft-core uniform* and *hard-core uniform*, $\hat{\sigma}_\varphi$ increases almost independently of σ_T . For resonant excitation, $\hat{\sigma}_\varphi$ is higher the closer a metasurface is to the disorder-induced phase transition. However, the primary cause for this high $\hat{\sigma}_\varphi$ is not positional disorder, but simply a vanishing μ_T . Figure 7.10b shows that $\hat{\sigma}_\varphi$ and μ_T are strongly correlated and almost independent of positional disorder: As μ_T decreases to zero, the phase approaches a uniform distribution and, therefore, $\hat{\sigma}_\varphi$ increases exponentially.

This has two implications. On the one hand, the high similarity in the σ_T - $\hat{\sigma}_\varphi$ -dependency of the *array* and *perturbed array* suggests that they perform similarly well along the zeroth order, which is most likely due to experimental imperfections in the *array* that yield a directional scatterance similar to the *perturbed array*. Hence, it seems feasible to use the *perturbed array* as a direct substitute for the *array* in wavefront-shaping applications that require both transmittance and phase modulations, where the ability to tune the degree of positional disorder replaces the need to precisely vary the particle geometry.

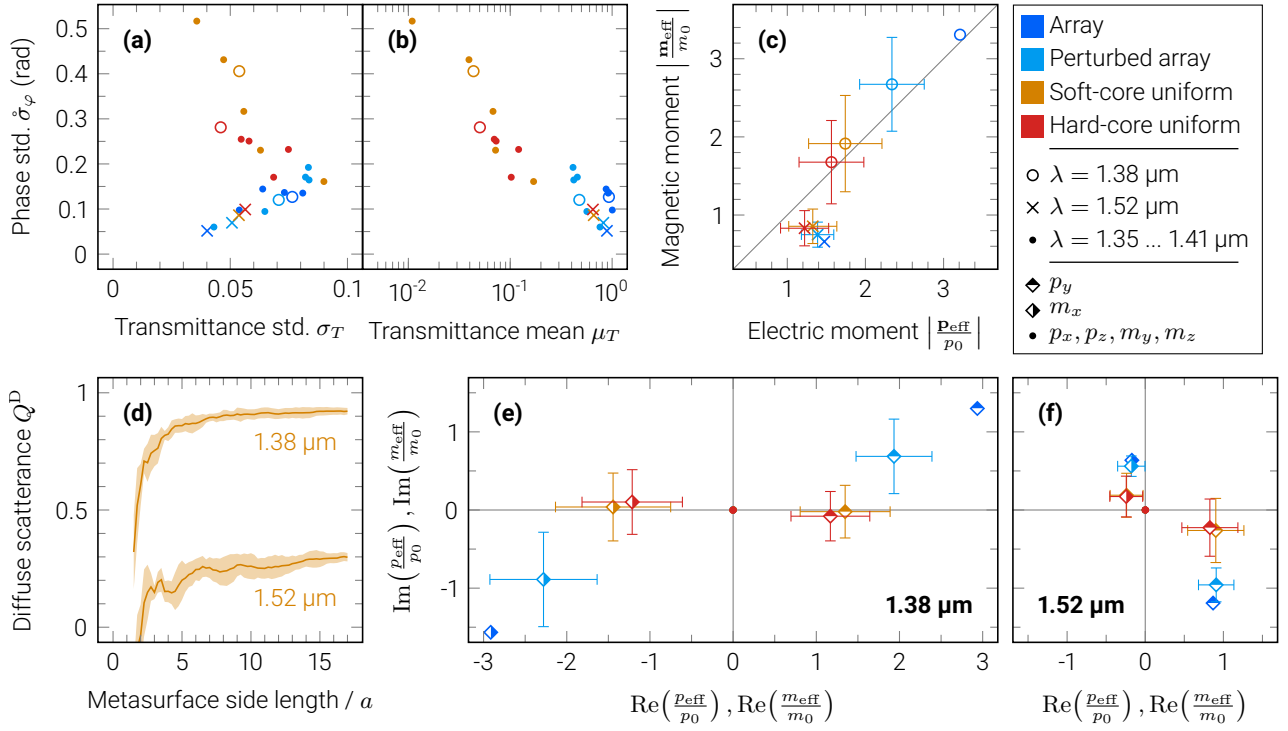


Fig. 7.10 | Correlations in the spatial statistics of Huygens' metasurfaces. (a,b) The standard deviation of experimental phase profiles with respect to the (a) standard deviation and (b) mean of corresponding transmittance profiles. (c) Mean (marks) and standard deviation (error bars) of simulated effective electric and magnetic dipole moments of 100 nanocylinders. (a–c) Circles and crosses indicate resonant ($\lambda = 1.38 \mu\text{m}$) and off-resonant ($\lambda = 1.52 \mu\text{m}$) excitation, dots show additional measurements near the resonance. (d) Simulated diffuse scatterance in dependence on the size of the soft-core uniform metasurface in multiples of the lattice constant $a = 0.8 \mu\text{m}$. The abscissa approximately equals the number of nanocylinders per axis. Solid lines and shaded areas show the mean and standard deviation, respectively, of 8 ($\lambda = 1.38 \mu\text{m}$) and 4 ($\lambda = 1.52 \mu\text{m}$) realizations of the metasurface. (e,f) A different representation of (c) that reveals the complex-valued vector components of all dipole moments for (e) resonant and (f) off-resonant excitation. Dots indicate less important components with near-zero means and standard deviations (not shown for clarity) that are comparable to the other vector components. All dipole moments were normalized with respect to the maximum possible dipole moments (p_0, m_0) of a spherical particle (cf. Appendix A.5).

The use of identical particles may not only be favorable in self-assembly strategies, but also in mask-based lithography systems. On the other hand, since different particle distributions can yield the same zeroth-order transmission coefficient but a vastly different directional scatterance, one can not only optimize the transmission around the zeroth order, but also explicitly design the energy transport along other directions. The important aspect is here that the directional scatterance of a disordered metasurface is mostly determined by the local neighborhood of a particle, whereas that of a pixelated device based on the *array* metasurface type is limited by the pixel size.

The size of such a neighborhood may be estimated from Fig. 7.10d, which shows the simulated diffuse scatterance of the *soft-core uniform* metasurface in dependence on its size. Roughly 5^2 to 10^2 particles may be sufficient to yield an optical response that is comparable to an infinitely large metasurface.

Lastly, to understand how positional disorder affects Huygens' metasurfaces on a more fundamental level, the magnitudes of the effective electric and magnetic dipole moments of 100 nanocylinders of each metasurface type were simulated, and their mean and standard deviation was evaluated (Fig. 7.10c). For off-resonant excitation, the mean and variance of all dipole moments is small, but the electric dipole moments are stronger than the magnetic dipole moments. Hence, all metasurface types are weakly scattering and show a zeroth-order response that is effectively the same as for an *array* composed of electric dipoles. For resonant excitation, the mean and variance of all dipole moments is larger than for off-resonant excitation, but the majority of particles approximately satisfies the Kerker condition (mean values close to the gray diagonal line). An increase in positional disorder reduces the magnitudes of the induced dipole moments, but the majority of particles still sustains Huygens sources.

Figures 7.10e,f show the complex-valued vector components of the dipole moments from Figure 7.10c. The spatial mean and standard deviation of the dominant vector components ($p_{y,\text{eff}}$, $m_{x,\text{eff}}$) are indicated by half-filled marks and error bars. Dots show less important components that vanish in average. Their standard deviation is comparable to that of the dominant components, but was not shown for clarity. As outlined in Appendix A.5, the zeroth-order transmission t and reflection r coefficient of an ordered Huygens' metasurface, excited by a y -polarized plane wave, can be modeled as

$$t = 1 - \frac{3\pi}{k^2 A} \left(\frac{p_{y,\text{eff}}}{p_0} - \frac{m_{x,\text{eff}}}{m_0} \right) \quad r = -\frac{3\pi}{k^2 A} \left(\frac{p_{y,\text{eff}}}{p_0} + \frac{m_{x,\text{eff}}}{m_0} \right) \quad \frac{p_{y,\text{eff}}}{p_0} + \frac{m_{x,\text{eff}}}{m_0} \stackrel{!}{=} 0 \quad (7.1)$$

where A is the unit cell area, k is the wavenumber of the background medium, the leading 1 in t relates to the incident wave, the remaining terms relate to the scattered wave, and the equation with the exclamation mark represents the Kerker condition, in which case $r = 0$ and $|t| = 1$. For resonant excitation, it is known that $t = -1$ [44], which implies that the induced effective dipole moments must generate a scattered wave that exceed the incident wave by a factor of two in amplitude and is shifted by π in phase ($t = 1 + 2e^{i\pi} = -1$). In other words, the induced dipole moments are so strong that they not only cancel the incident wave, but fully replace it by a phase-shifted version of itself. Ultimately, this still only results in an unspectacular phase shift of the incident wave, but this perspective will be the key to understand the influence of positional disorder in Huygens' metasurfaces.

In general, the zeroth-order optical response of any metasurface is intimately linked to the zeroth-order Fourier component of its scattered wave. However, since this Fourier component is simply the area average of the scattered wave, it is reasonable to estimate the zeroth-order transmission t and reflection r coefficient of a disordered Huygens' metasurface via

$$t \approx 1 - \frac{3\pi}{k^2} \left\langle \frac{p_{y,\text{eff}}}{p_0} - \frac{m_{x,\text{eff}}}{m_0} \right\rangle_A \quad r \approx -\frac{3\pi}{k^2} \left\langle \frac{p_{y,\text{eff}}}{p_0} + \frac{m_{x,\text{eff}}}{m_0} \right\rangle_A \quad \left\langle \frac{p_{y,\text{eff}}}{p_0} + \frac{m_{x,\text{eff}}}{m_0} \right\rangle_A \stackrel{!}{\approx} 0 \quad (7.2)$$

where $\langle \cdot \rangle_A$ denotes the area average across the entire metasurface, the less important vector components were readily excluded as they vanish in average, and the equation with the exclamation mark requires the Kerker condition to be fulfilled only in average. Figure 7.10e shows that for resonant excitation, all metasurface types fulfill the Kerker condition in average, which results in $r \approx 0$. However, since increasing positional disorder decreases the effective dipole moments in their magnitude, $|t|$ can now deviate from 1 (recall Fig. 7.7a). Hence, for resonant excitation and a critical degree of positional disorder, it is possible to obtain $t = 0$, which corresponds to a situation where the magnitudes of the induced effective dipole moments equal exactly one half of that in the *array* (compare *array* and *soft-core uniform* in Fig. 7.10e). In other words, the zeroth-order component of the scattered wave interferes destructively with the incident wave ($t = 1 + e^{i\pi} = 0$).

In summary, uniform positional disorder allows one to tune the magnitudes of the electric and magnetic dipole moments in a way that maintains the Kerker condition in average. Hence, for resonant excitation, the zeroth-order reflectance remains zero while the transmittance can be tuned at will. When this feature is combined with more general particle distributions, it seems feasible to design the directional scatterance of perfect optical diffusers, which will be thematized in Sec. 7.4.

7.4. Directional scatterance

This section first presents the simulated directional scatterance of the disordered metasurface types (Sec. 7.4.1), and then the experimental directional transmittance of all metasurface types (Sec. 7.4.2). It is important to note that a strict comparison of simulated and experimental results is not possible, since the simulations assume a homogeneous background, whereas the experiments involve reflections at air/substrate interfaces and other technical complications. Hence, the simulations should be understood as an ideal model that provides a theoretical understanding of the involved physical processes, whereas the experiments assess the performance of the fabricated metasurfaces with respect to the ideal situation. The presented data shows the *overlapping* resonance case with resonant ($\lambda = 1.38 \mu\text{m}$) or off-resonant ($\lambda = 1.52 \mu\text{m}$) excitation by a TE or TM polarized plane wave for normal and oblique incidence.

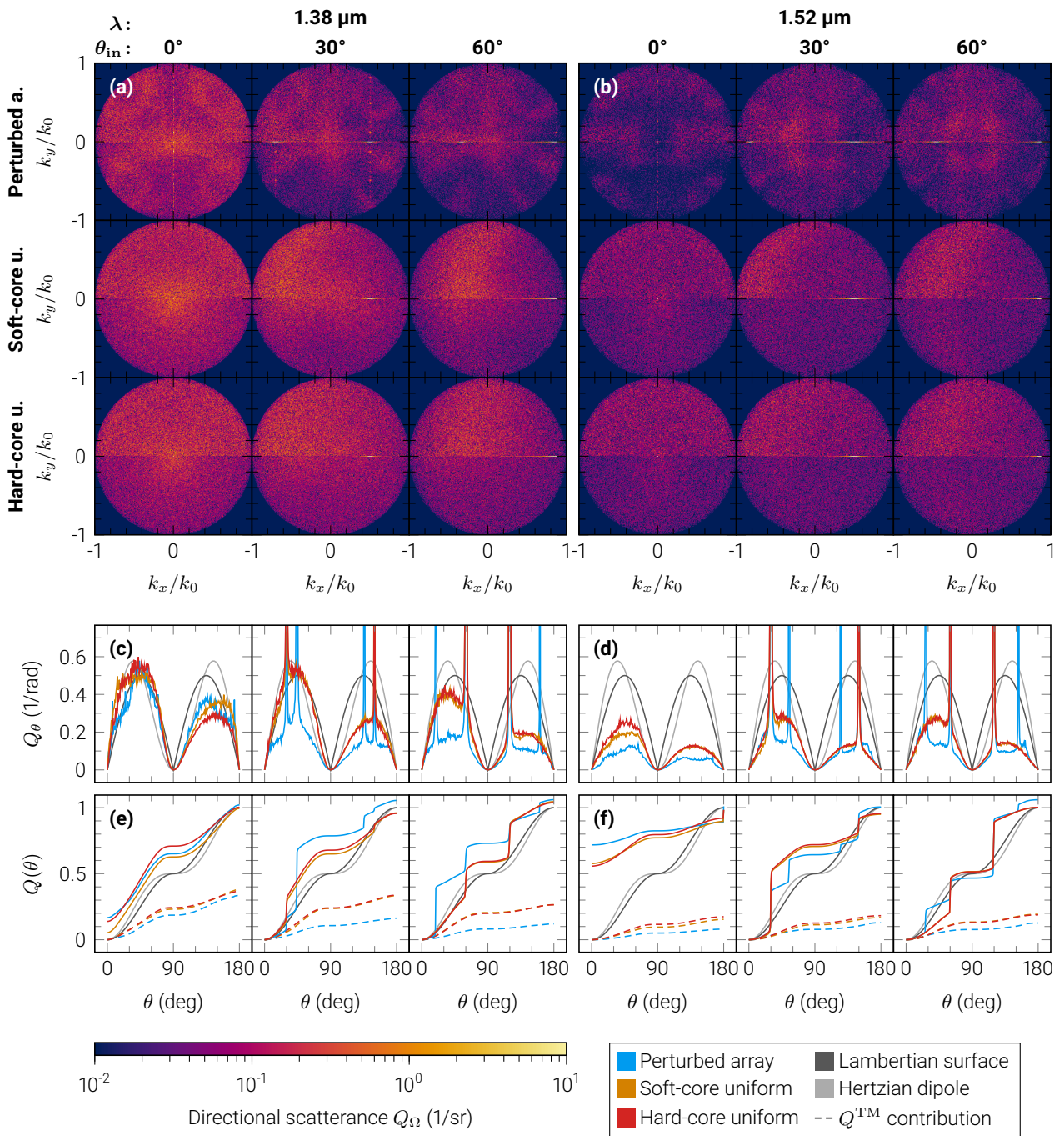


Fig. 7.11 | Simulated scattering for TE polarized excitation. The (a,b) directional Q_Ω , (c,d) polar Q_θ and (e,f) sectorial $Q(\theta)$ scattering of the perturbed array, soft-core uniform and hard-core uniform metasurface type for the overlapping resonance case with (a,c,e) resonant ($\lambda = 1.38 \mu\text{m}$) or (b,d,f) off-resonant ($\lambda = 1.52 \mu\text{m}$) excitation by a TE polarized plane wave incident under $\theta_{\text{in}} \in \{0^\circ, 30^\circ, 60^\circ\}$. Column and row titles indicate all parameter combinations. In (a,b), $k_y > 0$ shows transmission and $k_y < 0$ reflection. In (e,f), Q^{TM} shows the contribution of cross-polarized light to $Q = Q^{\text{TE}} + Q^{\text{TM}}$. All wavenumbers are normalized with respect to the magnitude of the wavevector k_0 in silicon dioxide.

7.4.1. Simulated results

Figure 7.11 shows the simulated scatterance of the disordered metasurface types for TE polarized excitation with incidence angles of $\theta_{\text{in}} = \{0^\circ, 30^\circ, 60^\circ\}$ and $\phi_{\text{in}} = 0^\circ$, where all propagation angles are measured in silicon dioxide. Since the directional scatterance $Q_\Omega(\mathbf{k})$ in Figs. 7.11a,b is mirror-symmetric with respect to the k_x - k_z -plane, the directional transmittance Q_Ω^{T} is displayed only for $k_y > 0$ and the directional reflectance Q_Ω^{R} only for $k_y < 0$. Figure C.1 shows the same for TM polarized excitation.

For resonant excitation and normal incidence, the directional scatterance Q_Ω (Fig. 7.11a) of the *uniform*-type metasurfaces is highly uniform along the azimuthal angle, while that of the *perturbed array* shows a weak azimuthal dependency. As the incidence angle increases, the *uniform*-type metasurfaces transmit slightly more light along directions perpendicular to the incident wave, while the *perturbed array* scatters increasingly more light along regular directions. The same trends can be observed for off-resonant excitation (Fig. 7.11b), with the exception that already at normal incidence, most light is scattered along regular directions. Note that the regular directions can also be seen as peaks in the polar scatterance Q_θ (Figs. 7.11c,d), or as jumps in the sectorial scatterance $Q(\theta)$ (Figs. 7.11e,f). For example, the height of the step $Q(\theta_{\text{in}})$ represents the fraction of the incident energy that is contained within the zeroth order in transmission.

For resonant excitation and an increasing incidence angle, the polar scatterance (Fig. 7.11c) of the *uniform*-type metasurfaces remains almost unchanged and comparable to a Hertzian dipole for up to about $\theta_{\text{in}} \leq 30^\circ$. The *perturbed array* performs similarly well at normal incidence since it adequately suppresses the zeroth orders (cf. Fig. 7.11e). At larger incidence angles, however, the polar scatterance of the *perturbed array* significantly reduces along diffuse directions as the higher diffraction orders of the underlying *array* become available as new radiation channels. These diffraction orders can be seen as additional peaks in the polar scatterance, and are not present in the *uniform*-type metasurfaces. Interestingly, for large transmission angles $\theta \in [45^\circ, 90^\circ]$, the polar scatterance of all disordered metasurface types even exceeds that of a Hertzian dipole and is comparable to a Lambertian surface. However, this surplus in transmission also implies less energy in reflection.

For resonant excitation and an increasing incidence angle, the sectorial scatterance (Fig. 7.11e) further reveals that the fraction of cross-polarized light $Q^{\text{TM}}(180^\circ)$ decreases faster in the *perturbed array* than in the *uniform*-type metasurfaces.

In summary, a redistribution of energy from diffuse directions towards regular directions can be observed as the incidence angle increases, or as the excitation wavelength is tuned away from the resonance. However, with an anisotropic particle distribution and a deliberate spectral detuning of the electric and magnetic dipole resonances at normal incidence, it may be possible to optimize a metasurface for any other incidence angle. More generally, it should be possible to fine-tune the directional scatterance via the particle distribution and/or the introduction of higher-order multipoles.

Perfect optical diffuser Although the presented metasurfaces were not specifically designed as diffusers, the *soft-core uniform* metasurface appears to come very close to the definition of a wavelength-selective perfect optical diffuser: The small jumps in Fig. 7.11e indicate a strong suppression of scattering along regular directions and thus a high diffuse scatterance (Fig. 2.1d), the wavelength-selective diffuser functionality can be seen by comparing Figs. 7.11a,c,e with Figs. 7.11b,d,f, the insensitivity with respect to the incidence angle and polarization can be observed by comparing Fig. 7.11a with Fig. C.1a, and from Figs. 7.11c,e it is evident that the metasurface roughly acts as a Lambertian surface.

Since these results were obtained with a nearly-hyperuniform isotropic particle distribution and a nearly-critical degree of positional disorder, it seems feasible to maximize the diffuse scatterance and to shape the directional scatterance towards a Lambertian surface via the particle arrangement.

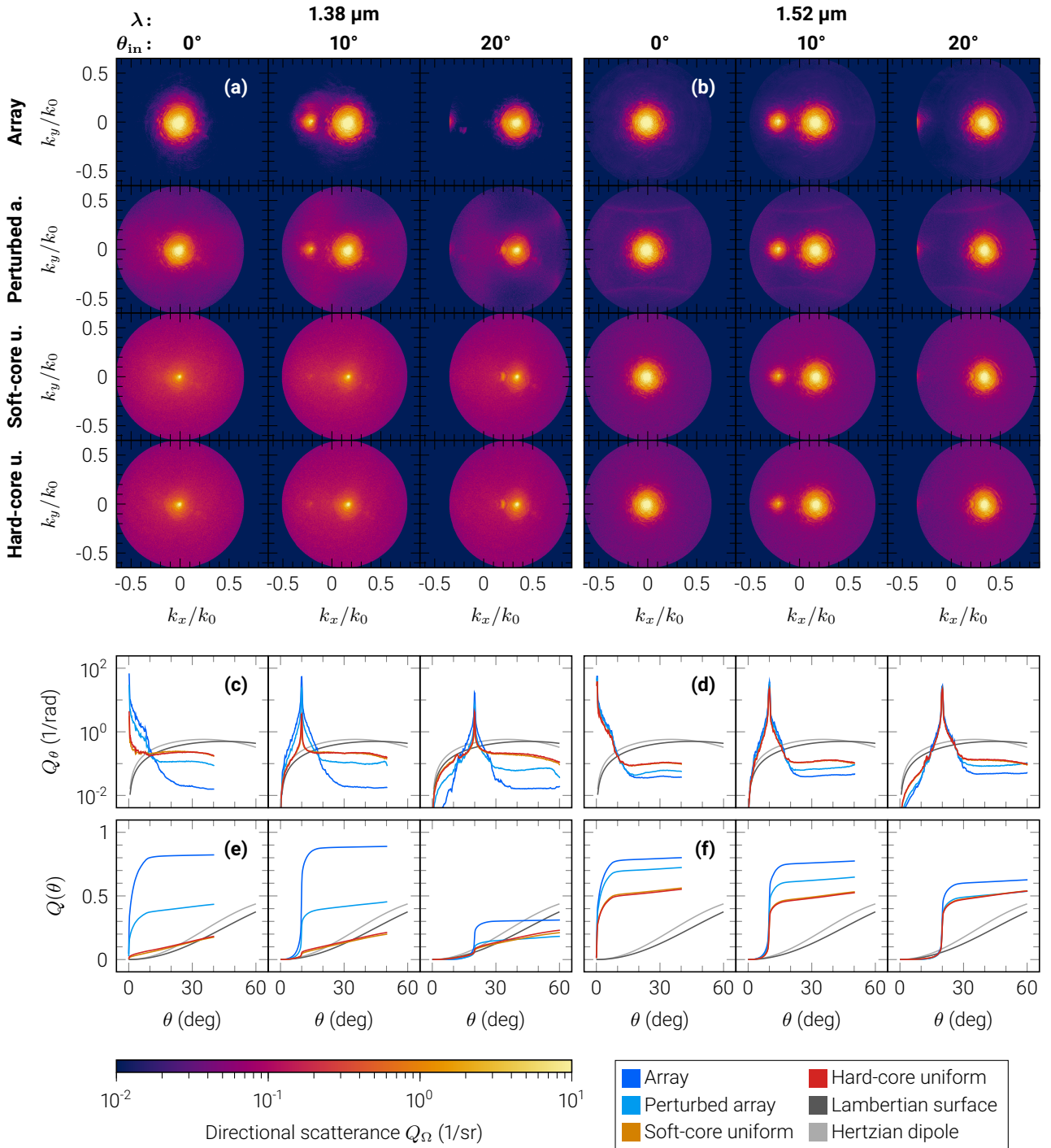


Fig. 7.12 | Experimental scatterance for TE polarized excitation. The (a,b) directional Q_{Ω} , (c,d) polar Q_{θ} and (e,f) sectorial $Q(\theta)$ scatterance of the array, perturbed array, soft-core uniform and hard-core uniform metasurface type for the overlapping resonance case with (a,c,e) resonant ($\lambda = 1.38 \mu\text{m}$) or (b,d,f) off-resonant ($\lambda = 1.52 \mu\text{m}$) excitation by a TE polarized plane wave incident under $\theta_{in} \in \{0^\circ, 10^\circ, 20^\circ\}$. All graphs show transmission ($k_z \geq 0, \theta \leq 90^\circ$). Column and row titles indicate all parameter combinations. All wavenumbers are normalized with respect to the magnitude of the wavevector k_0 in air.

7.4.2. Experimental results

Figure 7.12 shows the experimental scatterance of all metasurface types for TE polarized plane wave excitation with incidence angles of $\theta_{\text{in}} = \{0^\circ, 10^\circ, 20^\circ\}$ and $\phi_{\text{in}} = 0^\circ$, where all propagation angles are measured in air. More precisely, it is the directional transmittance that was measured in the back-focal-plane imaging setup (Sec. 6.2). Figure C.2 shows the same for TM polarized excitation.

Note that the directional scatterance in Figs. 7.12a,b covers different regions of the \mathbf{k} -space for different incidence angles. The reason for this is that the metasurfaces were rotated with respect to the optical axis of the experimental setup as to achieve oblique incidence. Also note that the *array* should ideally exhibit only one Dirac-delta-like peak, but the transfer function of the collecting microscope objective broadened the zeroth-order peak and multiple reflections from the substrate led to the emergence of a secondary peak. However, the microscope objective (Mitutoyo NIR HR 50X, 0.65 NA) was in fact nearly diffraction-limited, and it is due to the clipped logarithmic color scale that one might vastly overestimate the full width at half maximum of the zeroth-order peak ($k_{\text{FWHM}}/k_0 \approx 0.005$ at $\lambda = 1.38 \mu\text{m}$).

Furthermore, in the following discussion, it must be kept in mind that scattered waves with polar angles of about $\theta \geq 44^\circ$ experienced total internal reflection at the substrate-air interfaces. These secondary waves might have been scattered multiple times by the metasurface or could have exited the substrate on its sides. Since this is a non-trivial effect that was not considered in the simulations, the experimental and simulated propagation angles were intentionally not renormalized with respect to a common medium as to prevent misleading comparisons. However, this issue appears to be rather a technological complication than a fundamental limitation, which could be lifted by designing the directional scatterance of an embedded metasurface such that it vanishes for angles that would otherwise undergo total internal reflection, or more trivially, by operating the metasurface in an index-matched environment. The ability to tailor the reciprocal space with positional disorder has already been demonstrated with hyperuniform plasmonic metasurfaces [92], and more recently also with hyperuniform dielectric metasurfaces for which the first-order Born approximation applies [10]. However, although it is already possible to generate particle distributions with prescribed statistics via the collective coordinate method (Sec. 4.2), which would immediately determine the directional scatterance in the first-order Born approximation, it remains the question of how to efficiently and accurately predict the optical response of Huygens' metasurfaces from their spatial statistics. Consequently, the following experimental results were not optimized for a specific directional scatterance, but may nonetheless be seen as a first step towards the realization of perfect optical diffusers.

Overall, the experimental directional scatterance (Figs. 7.12a,b) shows the same dependency on the incidence angle and the excitation wavelength as in the simulations (Figs. 7.11a,b). Moreover, the experimental directional scatterance of the *uniform*-type metasurfaces is also more isotropic and has higher values along diffuse directions than it is the case for the *perturbed array*.

For resonant excitation and large polar angles, the experimental polar scatterance (Fig. 7.12c) of the *uniform*-type metasurfaces appears similar to a Hertzian dipole, which can be seen as a constant offset with respect to the Hertzian dipole curve. However, the sectorial scatterance (Fig. 7.12e) suggests that the *uniform*-type metasurfaces hardly exceed 25% hemispherical transmittance. The *perturbed array* shows a much higher hemispherical transmittance, but this is due to a high zeroth-order transmittance. The lower hemispherical transmittance in the experiments than in the simulations may be explained by secondary waves that are mainly scattered back into the hemisphere associated with reflection, or that are guided to the sides of the substrate.

Nevertheless, the experimental results show that the fabricated *uniform*-type metasurfaces strongly suppress the zeroth-order transmittance, scatter similarly to a Hertzian dipole, tolerate a wide range of incidence angles, and are wavelength-selective.

8. Holograms Based on Positionally Disordered Huygens' Metasurfaces

8.1. Design strategies

This chapter presents the first experimental realization of pixelated holograms with positionally disordered Huygens' metasurfaces and aims to answer the following two interrelated questions: As compared to ordered Huygens' metasurfaces, (i) can positional disorder help reducing the pixel size and (ii) how does the scattering from within a pixel affect the holographic image? This may be seen as a first step towards metasurface holograms with truly inhomogeneous positional disorder.

In general, the design of a hologram can be split into two steps. On the one hand, the IFTA (Sec. 5.3) can find a pixelated transmission coefficient profile that will produce a given holographic image. On the other hand, electromagnetic field solvers (Sec. 5.1) can simulate the transmission coefficient of a given particle arrangement. Hence, it remains the question of how to assign each pixel the correct particle arrangement. One possibility is to parameterize the particle arrangement and to establish a lookup table that relates each parameter combination with the resulting transmission coefficient. Then, the IFTA finds the most optimal transmission coefficient for each pixel, and each pixel is associated with one entry of the lookup table that contains the most similar transmission coefficient. However, this inexact matching generally leads to deviations from the most optimal solution found by the IFTA. The presented IFTA can overcome this issue if the lookup table is provided via the *discrete* constraint. Another possibility is to use inverse design methods to find particle arrangements that exactly yield the transmission coefficients suggested by the IFTA. Although the adjoint method can efficiently solve such inverse problems [212, 213], its numerical implementation can be so intricate that the use of lookup tables remains more practical. In this thesis, all holograms were generated using lookup tables.

The most significant drawback of this two-step design approach is that it does not take into account how neighboring pixels may influence each others transmission coefficient due to electromagnetic coupling near the pixel boundaries. This seems to be an intrinsic problem that could only be overcome with electromagnetic field simulations of larger pixel neighborhoods. Nevertheless, the sub-pixel feature of the presented IFTA can still account for scattering that originates from within each pixel. Moreover, if the particle arrangements are designed such that the coupling across the pixel boundaries is weakened, it may be possible to reduce the pixel size or the strength of unaccounted-for scattering that originates from the pixel boundaries. This aspect will be revisited in the following discussion.

Due to time limitations in this thesis, it was unfortunately not possible to establish how exactly the optical response of positionally disordered Huygens' metasurfaces depends on their particle statistics. Since a haphazard parameterization of the structure factor and/or pair correlation function might not discover all possible transmission coefficients, the presented disordered holograms were not generated with the collective coordinate method, but instead based on arrays with random vacancy defects, which means square arrays of particles from which a given percentage of particles is removed at random.

To address the questions about the impact of positional disorder on the performance of a hologram, several holograms were fabricated that all produce the same target image (Table 8.1d) in a specific distance behind the hologram when illuminated by a normally-incident monochromatic plane wave. More precisely, three *hologram types* (Table 8.1c) were devised that are distinguished by their pixel layout, which means by the way the particles are arranged within each pixel. Each hologram type was realized with five different *pixel sizes* (Table 8.1b), and in accord with the design considerations mentioned in Sec. 5.3, the hologram size and image distance were made to depend on the pixel size, such that the image size, pixel count, relative intensity, and image resolution are identical for all holograms (Table 8.1a). This allows for a fair comparison of all hologram types and pixel sizes, where any deviations from the expected image quality can only be caused by unaccounted-for scattering. Figure 8.1 illustrates the transmission coefficients and pixel layouts of all holograms.

(a) Fixed parameters			(c) Hologram types			
Wavelength	λ	1.42 μm				
Image size	s_{img}	10 mm				
Pixel count	s_{hol}/Λ	310				
Relative intensity	I_r	0.75				
Image resolution	Δr	55.34 μm				
(b) Dependent parameters						
Pixel size	Λ	5.04	8.16	10.37	12.78	16.52 μm
Hologram size	s_{hol}	1.56	2.53	3.21	3.96	5.12 mm
Image distance	d	60.70	98.26	124.94	153.97	199.03 mm



Table 8.1 | A summary of design parameters. All holograms have identical (a) fixed parameters and produce the same (d) target image, but each hologram possesses only one set of (b) dependent parameters and one (c) hologram type. The scanning electron micrographs in (c) illustrate randomly-chosen 3-by-3 pixel neighborhoods of fabricated holograms for a pixel size of 8.16 μm . See Sec. 5.3 for details on the involved symbols and design considerations.

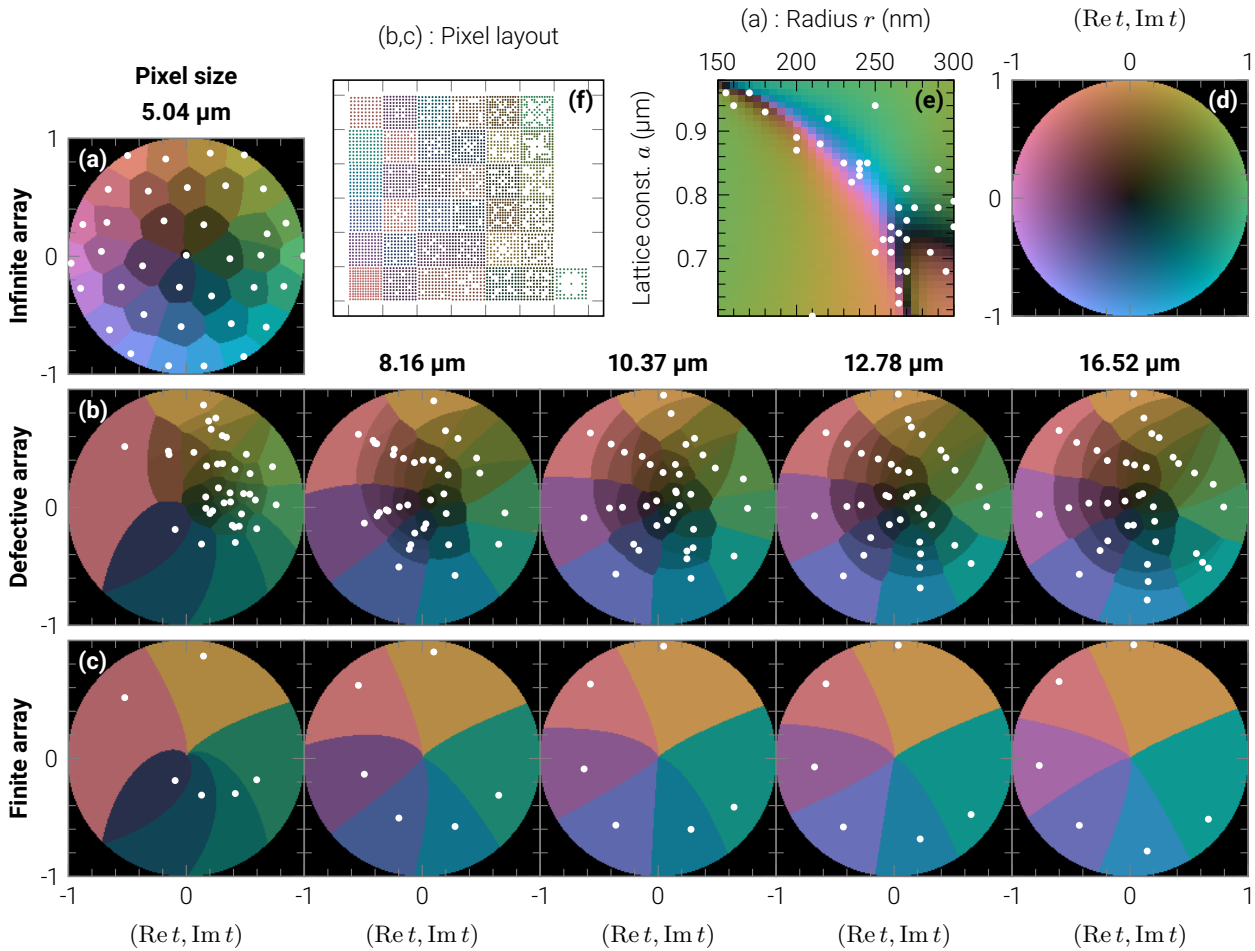


Fig. 8.1 | Constraints of all hologram types and pixel sizes. Visualizations of discrete constraints with simulated zeroth-order transmission coefficients (white points) of the (a) infinite array, (b) defective array, and (c) finite array hologram type for all pixel sizes (column titles). All graphs use the same (d) colormap. The constraint in (a) does not change with the pixel size and is hence shown only once. (e) The zeroth-order transmission coefficient of the infinite array in dependence on the radius and lattice constant of its nanocylinders, where the 37 white points are the same as in (a). (f) A composition of all 37 pixels of size 8.16 μm that are present in (b), where each point represents a nanocylinder and the transmission coefficient of each pixel is color-coded. The left-most column in (f) corresponds to the 6 white points in (c).

The particles in each hologram were the same embedded nanocylinders as described in the previous chapters (*overlapping* resonance case in Sec. 7.2; fabrication details in Sec. 6.1), but the following distinctions apply according to the used hologram type:

Infinite array Each pixel consisted of a truncated array of identical nanocylinders with a radius of $r \in [150, 300]$ nm and a lattice constant of $a \in [0.61, 0.98]$ μm . However, the transmission coefficients were simulated for infinite arrays using the finite element method (Fig. 8.1e), which means that the finite pixel size is completely ignored during the design process. This hologram type represents a common state-of-the-art approach (cf. [23, 24]) and serves as an ordered reference case. Moreover, this hologram type produces amplitude-and-phase holograms.

All holograms of this type were generated using the same 37 discrete transmission coefficients (Fig. 8.1a) that were obtained from Fig. 8.1e via *reduction by distance* (Sec. 5.3), where the target set formed a hexagonal grid. The initial hologram was a parabolic phase profile that focuses the incident wave into the image plane.

Defective array Each pixel consisted of a truncated array of identical nanocylinders with a radius of $r = 245$ nm and a lattice constant of $a \in \{0.61, 0.75, 0.78, 0.81, 0.83, 0.86\}$ μm , where random vacancy defects were introduced with a defect ratio of up to 80%, and a four-fold symmetry was enforced to further suppress backscattering [44, 214]. Moreover, the two outermost columns and rows of particles in each pixel were slightly shifted by typically less than 4% of the lattice constant (cf. Fig. 8.1f) in an attempt to suppress the coupling of neighboring pixels. The shifts were determined from exhaustive simulations of all possible pixel pairs by comparing the transmission coefficients of a pixel pair with those of the individual pixels. The transmission coefficients of all finite-sized pixel layouts were simulated using the T-matrix method. Hence, in this hologram type, the finite size and the coupling of neighboring pixels are partially taken into account. Moreover, this hologram type produces amplitude-and-phase holograms.

For each pixel size of this type, first a temporary hologram was generated that made use of all 78 transmission coefficients (6 variations of the lattice constant; 13 variations of the defect ratio). Then, the 37 most-frequently occurring transmission coefficients of this temporary hologram were extracted via *reduction by prevalence* (Sec. 5.3), and subsequently used to generate the final hologram. Figure 8.1b indicates that as the pixel size is reduced, the simulated transmission coefficients cover an ever smaller region in the complex plane due to the increasing influence of the pixel's finite size. For example, the difference in the spread of the discrete transmission coefficients is more drastic for pixel sizes of 5.04 μm and 10.37 μm than for 10.37 μm and 16.52 μm . The initial hologram was a parabolic phase profile that focuses the incident wave into the image plane, and a minimum of four sub-pixels per axis were used in the hologram generation.

Finite array This hologram type is a subset of the *defective array* type and contains only those pixel layouts that have a defect ratio of 0%. Hence, it serves as another ordered reference case. Moreover, this hologram type produces phase-only holograms.

For each pixel size of this type, all 6 lattice constant variations (Figure 8.1c) were used to generate the final hologram. The initial hologram consisted of random phase values, since numerical experiments indicated that this typically maximizes the image quality of phase-only holograms.

Note that the *infinite array* and *defective array* hologram types have the same number of unique transmission coefficients and both produce amplitude-and-phase holograms, which furthers a fair comparison of their performance. However, the *finite array* contains a substantially smaller number of unique transmission coefficients, which represents a smaller information capacity that generally manifests in a lower image quality. Moreover, phase-only holograms typically produce a large number of isolated zeros in the electric field, which are difficult to remove and lead to stagnation in the iterative Fourier transform algorithm [215]. Hence, it can be expected that the image quality of the *finite array* is generally worse than that of the other hologram types. Nevertheless, comparisons with simulations and the *defective array* may still allow for an assessment of the influence of positional disorder on the hologram performance.

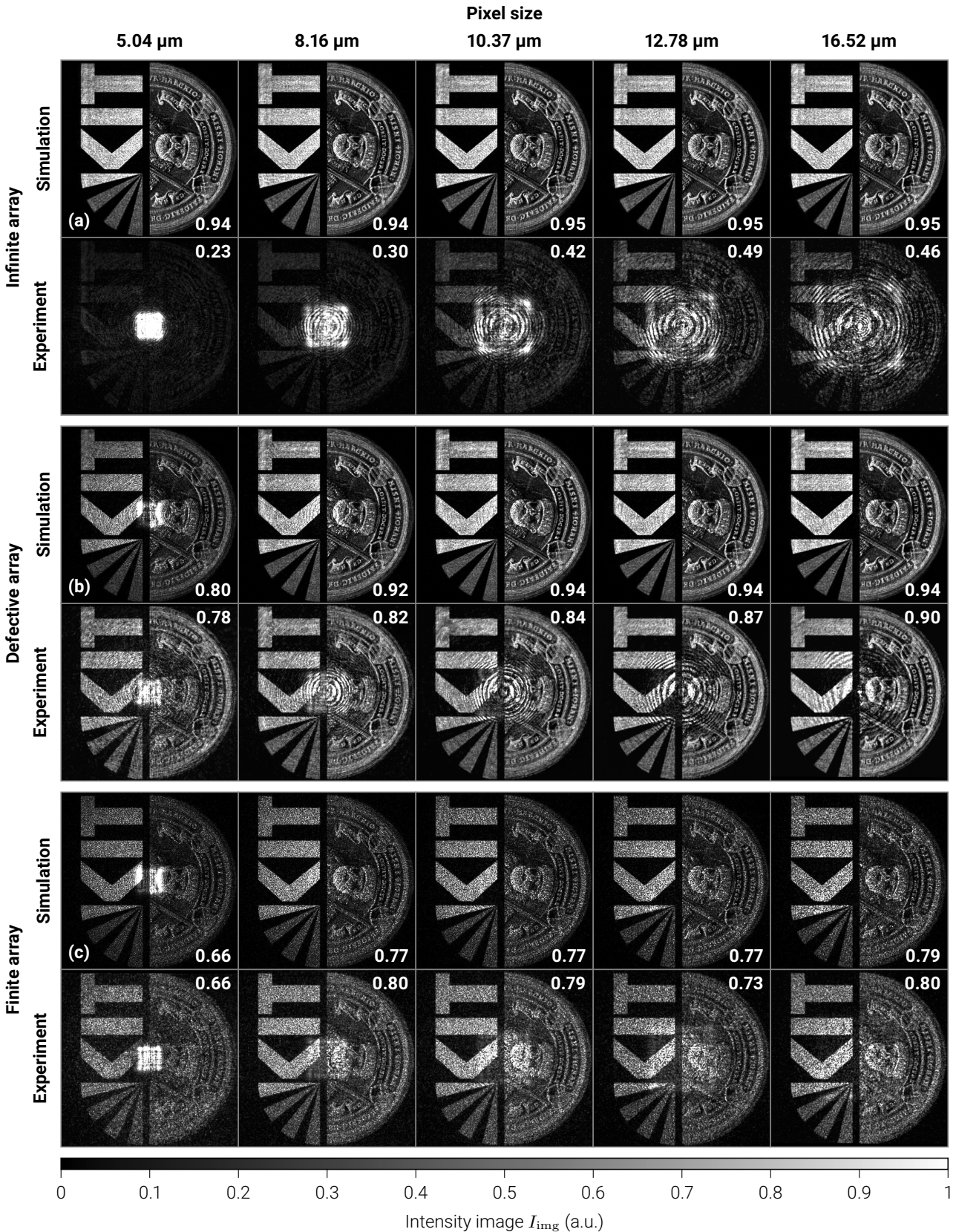


Fig. 8.2 | Intensity images for all hologram types and pixel sizes. Simulated and experimental intensity images of the (a) infinite array, (b) defective array, and (c) finite array hologram type for all pixel sizes (column titles). The intensity in each subplot is normalized with respect to its 99th percentile. Overlays display the ZNCC of each image with respect to the target image. Each image has an actual side length of 10 mm and originates from an (a,b) amplitude-and-phase or (c) phase-only hologram. The experimental data in (a) is dominated by systematic errors. See Table 8.1 and Fig. 8.1 for further details.

8.2. Experimental results

Figure 8.2 shows simulated and experimental intensity images and their zero-normalized cross correlation ZNCC (Eq. (5.15)) for all hologram types and pixel sizes. The experiments were conducted in a setup similar to that in Fig. 6.1, but without any lenses and by placing the camera (Xenics Xeva-1.7-640-TE3; square pixels with 20 μm side length) directly into the hologram's image plane.

Unfortunately, the experimental data of the *infinite array* (Fig. 8.2a) is dominated by systematic errors that were introduced during fabrication. The electron-beam lithography system did not correct for the *proximity effect*, which is the overexposure of dense structures due to scattered electrons. Since several pixels of the *infinite array* possess high filling fractions, which means a large nanocylinder radius paired with a small lattice constant (bottom right corner of Fig. 8.1e), their radii turned out larger than anticipated and their transmission coefficients changed considerably. As a result, the holograms scattered less light out of the incident wave, and the recorded images were dominated by the diffraction pattern of the square aperture that surrounds each hologram. However, note that the chosen design parameters did indeed lead to a nearly constant simulated ZNCC for all pixel sizes. Hence, if the proximity effect is properly taken into account, future experimental measurements of the *infinite array* will be able to quantify by how much the image quality deteriorates due to unaccounted-for scattering from the pixel boundaries as the pixel size is reduced.

Nevertheless, the fabrication process was optimized for a filling fraction that corresponds to $r = 245$ nm and $a = 0.80$ μm , which was ideal for the *defective array* and *finite array* (Figs. 8.2b,c). The simulated and experimental ZNCC of these hologram types are in good agreement and only decrease with the pixel size due to the inherently less favorable distributions of available transmission coefficients in the complex plane (cf. Figs. 8.1b,c).

The *defective array* (Fig. 8.2b) shows a slightly lower ZNCC in the experiments than in the simulations. Unfortunately, it is difficult to identify the main cause for this observation. For smaller pixel sizes, the presence of speckles in supposedly dark regions of the target image is an indication for scattered light that was not accounted for in the design, which means that it must originate from the pixel boundaries or residual fabrication errors. For larger pixel sizes, the lower ZNCC is likely due to the presence of interference artifacts in the image centers. To understand this, one may imagine that the image is formed by the superposition of two waves, namely the diffraction of the incident wave at the square aperture (background wave) and the wave generated by the hologram (scattered wave). Since the interference artifacts are reminiscent of Newton's rings, it is likely that either the background wave or the scattered wave obtained a small global phase shift or a slightly curved wavefront. This may be due to fabrication tolerances in the particle geometry, deviations from the refractive index data that was used in the simulations, or due to the fact that in the experiments, the incident wave is better described by a Gaussian beam than by a plane wave.

Remarkably though, as the pixel size is reduced from 10.37 μm over 8.16 μm to 5.04 μm , the experimental ZNCC of the *infinite array* roughly reduces in steps of 0.10, whereas that of the *defective array* only reduces in steps of about 0.03, which in turn could indicate that the *defective array* might indeed successfully suppress scattering from the pixel boundaries and thus allow for smaller pixel sizes. Also note that even for the smallest pixel size of the *defective array*, the experimental and simulated ZNCC are not only very similar but also rather large, which indicates that the image quality is mainly limited by the available transmission coefficients. Considering that the *defective array* does not make use of all spatial degrees of freedom due to the four-fold symmetry and the underlying array, it might be possible to obtain a wider range of transmission coefficients with a more general type of positional disorder.

The *finite array* (Fig. 8.2c), on the other hand, sometimes even shows a larger ZNCC in the experiments than in the simulations. However, this is likely only a statistical effect due to the presence of strong speckles in the images. These speckles are typically more blurry in the experiments than in the simulations, which leads to a slightly smaller spatial standard deviation of intensities and thus to a slightly larger ZNCC. Hence, while phase-only holograms might not be useful for the study at hand, they demonstrate that the unaccounted-for scattering is less notable in the presence of speckles.

Although this study may be inconclusive about the influence of scattering from within a pixel on the image quality, it still addresses the issue of the pixel size and reveals the usefulness of positional disorder in holographic applications. In particular, Fig. 8.2b suggests that if the systematic experimental errors are corrected, a pixel size of about $8\ \mu\text{m}$, which corresponds to about 10^2 particles per pixel, could already be large enough to widely overcome the unaccounted-for scattering. Moreover, the high image quality obtained via the *defective array*, and the complications encountered in the fabrication of the *infinite array*, demonstrate that positional disorder is a valuable alternative design parameter in the realization of amplitude-and-phase holograms.

Lastly, future studies that investigate the influence of a pixel's scattering profile on the performance of holographic devices may benefit from positionally disordered Huygens' metasurfaces that are operated at or near the disorder-induced phase transition. This provides nearly-Lambertian scattering profiles and naturally suppresses the transmission of the incident wave along the zeroth order, which could be used to enhance the numerical aperture and the intensity homogeneity of in-line holograms and related imaging applications.

9. Conclusion and Outlook

The high complexity of disorder, and the theoretical and technological complications that it entails, may seem a mere nuisance at the first glance, but on the second sight, it quickly becomes apparent that it is the very complexity that harbors novel physical phenomena. Furthermore, since research has only just started to unravel these phenomena, more profound studies on disordered structures will certainly continue to be well worth their effort for many years to come.

This thesis aims to provide a basic theoretical understanding and an experimental characterization of the optical effects that can be observed in positionally disordered Huygens' metasurfaces. Moreover, the presented metasurfaces demonstrate their applicability as wavelength-selective optical diffusers, wavefront-shaping devices, or holograms.

With the modifications and extensions made to the numerical methods in Chapter 4, it is possible to generate homogeneous particle distributions with prescribed short-range and long-range order. Although the collective coordinate method is much more general and versatile, Matérn-type distributions can be easier to implement and are, in some situations, faster to generate. With the presented collective coordinate method it is also possible to synthesize a pixelated metasurface, where each pixel contains a distinct homogeneous particle distribution, and discontinuities near the pixel boundaries can be avoided by filling the pixels sequentially while keeping previously generated particles fixed.

Future research could generalize the collective coordinate method to generate truly inhomogeneous particle distributions, which would eliminate the need for pixelation, thus avoid detrimental boundary effects, and perfectly align with the theoretical description of the optical response of a particle cluster: If the effective multipole moments of one particle are mostly determined by its nearest neighbors, then it should be possible to tune the effective multipole moments in each particle of the cluster via the spatial degrees of freedom that are available in the short-range order, while the long-range order determines the collective farfield response of the entire cluster. Ultimately, a combination of the collective coordinate method and the local-coordinate T-matrix method could yield a very powerful inverse design method, which in turn would facilitate systematic studies on how exactly the optical response of a positionally disordered Huygens' metasurface depends on its particle statistics.

In Chapter 5, the iterative Fourier transform algorithm was extended by the possibility to apply constraints on the transmission coefficients of a hologram. The proposed *discrete* constraint forces the optimizer to only consider a predefined finite set of transmission coefficients, which is of advantage in situations where it would otherwise be impossible or too demanding to find or fabricate a nanostructure that exactly yields the (arbitrary) transmission coefficient requested by the optimizer. Moreover, it was shown how a set of provided transmission coefficients can be reduced to contain only the most significant ones, and how sub-pixel information can be included as to account for scattering effects that originate from within a pixel.

The zeroth-order transmission and reflection of positionally disordered Huygens' metasurfaces was presented in Sec. 7.3. More specifically, in Sec. 7.3.1, experimental transmittance spectra for oblique incidence showed that the generalized Brewster effect in the *array* can be used to obtain a device that only transmits for a specific incidence angle. The *uniform*-type metasurfaces, on the other hand, showed a high insensitivity with respect to the incidence angle and polarization of the incident wave, which allows a device to accept more complex electromagnetic input fields.

In Sec. 7.3.2, the disorder-induced phase transition in the transmission coefficient was investigated on a rather phenomenological level: At the resonance wavelength and for a critical degree of positional disorder, the zeroth-order transmittance equals zero and the phase abruptly changes from normal to anomalous dispersion. At the same time, however, the zeroth-order reflectance remains zero, which implies that all light must be scattered along diffuse directions. Away from the resonance wavelength, a very low reflectance and a high transmittance were observed. This confirmed the wavelength-selective diffuser functionality of positionally disordered Huygens' metasurfaces.

Section 7.3.3 presented spatial statistics of optical properties for normal incidence. While experimental measurements of the transmission coefficient profiles confirmed that disordered Huygens' metasurfaces are suitable for wavefront-shaping applications, simulations of the induced effective dipole moments supported the presented theoretical model that explains the manifestation of the disorder-induced phase transition.

The question of how positionally disordered Huygens' metasurfaces redistribute incident light across the diffuse directions was answered in Sec. 7.4. Here, simulations and experimental measurements of the directional scatterance showed that the *uniform*-type metasurfaces possess a scattering profile that is comparable to a Lambertian surface, is almost independent of the incident polarization, and can be maintained for incidence angles of up to about 30° .

It is expected that the directional scatterance of a positionally disordered Huygens' metasurface can be fine-tuned via the particle distribution and/or the introduction of higher-order multipoles.

The experiments in Chapter 8 confirmed that disordered Huygens' metasurfaces are also suitable for holographic applications. In particular, the experimental performance of disordered holograms matched the simulated performance of ordered holograms. Unfortunately, a direct experimental comparison was not possible due to systematic fabrication errors in the ordered holograms, which were caused by the need to vary the nanocylinder radius and the neglect of the proximity effect. However, this circumstance ironically demonstrates that positional disorder is not only a valuable degree of freedom in the design, but that it can also permit the use of simpler and less error-prone fabrication protocols.

In summary, this thesis documents several intriguing properties of disordered Huygens' metasurfaces, discusses them on the basis of a simple theoretical model, and provides adapted numerical methods that may serve as a foundation for future investigations. In future, it would be most delightful to obtain an answer to the profound question of how exactly the optical response of a positionally disordered Huygens' metasurface depends both on the particle statistics and higher-order multipole moments. Aside from its high intellectual value, this knowledge will certainly also enable the realization of truly inhomogeneous Huygens' metasurfaces with fully tailored directional transmission and reflection.

A. Definitions and Derivations

A.1. Directional scatterance of ideal scatterers

Inspired by Lambert's cosine law $dI(\theta, \phi) \propto I_0 \cos(\theta) d\Omega$ and the intensity $dI(\theta, \phi) \propto I_0 \cos^2(\theta) d\Omega$ of a Hertzian dipole that is oriented perpendicular to the polar axis [176], the directional scatterance of a Lambertian surface (superscript L) and that of a Hertzian dipole (superscript H)

$$Q_{\Omega}^L(\theta, \phi) = \frac{1}{2\pi} \quad Q_{\Omega}^H(\theta, \phi) = \frac{3}{4\pi} |\cos(\theta)| \quad (\text{A.1})$$

were found by comparing their directional intensity with Eq. (3.82) and choosing the proportionality factors such that the total scatterance is correctly normalized to $Q = 1$. With this, the azimuthal and polar scatterance read as

$$Q_{\phi}^L(\phi) = \frac{1}{2\pi} \quad Q_{\phi}^H(\phi) = \frac{1}{2\pi} \quad (\text{A.2})$$

$$Q_{\theta}^L(\theta) = \sin(\theta) |\cos(\theta)| \quad Q_{\theta}^H(\theta) = \frac{3}{2} \sin(\theta) \cos^2(\theta) \quad (\text{A.3})$$

and the sectorial scatterance

$$Q^L(\theta) = \begin{cases} \frac{1}{2} \sin^2(\theta) & \theta \leq \frac{\pi}{2} \\ 1 - \frac{1}{2} \sin^2(\theta) & \theta > \frac{\pi}{2} \end{cases} \quad Q^H(\theta) = \frac{1 - \cos^3(\theta)}{2} \quad (\text{A.4})$$

satisfies $Q^{L,H}(\frac{\pi}{2}) = \frac{1}{2}$ and $Q^{L,H}(\pi) = 1$.

A.2. Spherical vector wave functions

Orthogonality conditions The orthogonality conditions of the spherical vector wave functions are based on the orthogonality conditions of the following functions [216, 1.17.ii, 14.17.iii]

$$\int_0^{2\pi} e^{\mathbf{i}(m-m')\phi} d\phi = 2\pi \delta_{m,m'} \quad (\text{A.5})$$

$$\int_0^{\pi} P_{n'}^m(\cos \theta) P_n^m(\cos \theta) \sin(\theta) d\theta = \frac{1}{2\pi n(n+1) (\Psi_n^m)^2} \delta_{n,n'} \quad (\text{A.6})$$

$$\int_0^{\infty} j_n(kr) j_n(k'r) r^2 dr = \frac{\pi}{2k^2} \delta(k - k') \quad (\text{A.7})$$

and on the following special integrals

$$m \int_0^{\pi} (P_{n'}^m [\partial_{\theta} P_n^m] + [\partial_{\theta} P_{n'}^m] P_n^m) d\theta = 0 \quad (\text{A.8})$$

$$\int_0^{\pi} \left(\frac{m^2}{\sin^2 \theta} P_{n'}^m P_n^m + [\partial_{\theta} P_{n'}^m] [\partial_{\theta} P_n^m] \right) \sin \theta d\theta = \frac{1}{2\pi (\Psi_n^m)^2} \delta_{n,n'} \quad (\text{A.9})$$

which can be solved with the help of Eq. (B.22) and the following identities

$$P_{n'}^m [\partial_{\theta} P_n^m] + [\partial_{\theta} P_{n'}^m] P_n^m = \partial_{\theta} [P_{n'}^m P_n^m] \quad (\text{A.10})$$

$$\left(\frac{m^2}{\sin^2 \theta} P_{n'}^m P_n^m + [\partial_{\theta} P_{n'}^m] [\partial_{\theta} P_n^m] \right) \sin \theta = \frac{n(n+1) + n'(n'+1)}{2} P_{n'}^m P_n^m \sin \theta + \frac{1}{2} \partial_{\theta} [\sin \theta \partial_{\theta} [P_{n'}^m P_n^m]] \quad (\text{A.11})$$

where the arguments of the associated Legendre polynomials were omitted for readability.

To avoid the need of evaluating differentials or dealing with undefined expressions at $r = 0$, the spherical Bessel and Hankel functions can be simplified to [216, 10.51]:

$$\frac{\zeta_n(kr; i)}{kr} = \frac{\zeta_{n-1}(kr; i) + \zeta_{n+1}(kr; i)}{2n+1} \quad (\text{A.12})$$

$$\frac{[r\partial_r + 1]\zeta_n(kr; i)}{kr} = \frac{(n+1)\zeta_{n-1}(kr; i) - n\zeta_{n+1}(kr; i)}{2n+1} \quad (\text{A.13})$$

Lastly, the following identity for spherical Hankel functions of the first kind

$$\text{Im}\left[\overline{\zeta_{n\pm 1}(x; 3)}\zeta_n(x; 3)\right] = \pm x^{-2} \quad x \in \mathbb{R} \quad (\text{A.14})$$

relies on the cross-product identity $j_{n+1}(z)y_n(z) - j_n(z)y_{n+1}(z) = z^{-2}$ for $z \in \mathbb{C}$ [216, 10.50].

Multipole expansion based on impulse response In order to find a representation of $\mathbf{I}\delta(\mathbf{r} - \mathbf{r}')$ in terms of the spherical vector wave functions, the following ansatz can be made

$$\mathbf{I}\delta(\mathbf{r} - \mathbf{r}') = \frac{2}{\pi} \sum_{n=1}^{\infty} \sum_{m=-n}^n \int_0^{\infty} \left[\mathbf{a}_n^m(\mathbf{r}; k) \overline{\mathbf{M}_n^m(\mathbf{r}'; k, 1)} + \mathbf{b}_n^m(\mathbf{r}; k) \overline{\mathbf{N}_n^m(\mathbf{r}'; k, 1)} \right] k^2 dk \quad (\text{A.15})$$

where \mathbf{a}_n^m and \mathbf{b}_n^m are vector functions that need to be determined. By dot-multiplying this equation from the right with $\mathbf{M}_n^m(\mathbf{r}'; k', 1)$ or $\mathbf{N}_n^m(\mathbf{r}'; k', 1)$, integrating over all \mathbf{r}' and using Eqs. (3.103,106), the sought-for vector functions are found to equal:

$$\mathbf{a}_n^m(\mathbf{r}; k) = \mathbf{M}_n^m(\mathbf{r}; k, 1) \quad \mathbf{b}_n^m(\mathbf{r}; k) = \mathbf{N}_n^m(\mathbf{r}; k, 1) \quad (\text{A.16})$$

Similarly, it can be assumed that

$$\mathbf{G}(\mathbf{r}, \mathbf{r}') = \frac{2}{\pi} \sum_{n=1}^{\infty} \sum_{m=-n}^n \int_0^{\infty} \left[\mathbf{c}_n^m(\mathbf{r}; k) \overline{\mathbf{M}_n^m(\mathbf{r}'; k, 1)} + \mathbf{d}_n^m(\mathbf{r}; k) \overline{\mathbf{N}_n^m(\mathbf{r}'; k, 1)} \right] k^2 dk \quad (\text{A.17})$$

and after inserting this expression into $[\nabla^2 + k_b^2] \mathbf{G}(\mathbf{r}, \mathbf{r}') = -\mathbf{I}\delta(\mathbf{r} - \mathbf{r}')$ and comparing the series terms on both sides, it is found that:

$$[\nabla^2 + k_b^2] \mathbf{c}_n^m(\mathbf{r}; k) = -\mathbf{M}_n^m(\mathbf{r}; k, 1) \quad [\nabla^2 + k_b^2] \mathbf{d}_n^m(\mathbf{r}; k) = -\mathbf{N}_n^m(\mathbf{r}; k, 1) \quad (\text{A.18})$$

However, since $[\nabla^2 + k_b^2] \mathbf{M} = -(k^2 - k_b^2) \mathbf{M}$ holds by definition (similarly for \mathbf{N}), it follows that:

$$\mathbf{c}_n^m(\mathbf{r}; k) = \frac{1}{k^2 - k_b^2} \mathbf{M}_n^m(\mathbf{r}; k, 1) \quad \mathbf{d}_n^m(\mathbf{r}; k) = \frac{1}{k^2 - k_b^2} \mathbf{N}_n^m(\mathbf{r}; k, 1) \quad (\text{A.19})$$

With this, the explicit form of $\mathbf{G}(\mathbf{r}, \mathbf{r}')$ is now known, but since the k -integral is difficult to treat numerically, it is best to perform it analytically. To this end, two types of integrals that originate from $\mathbf{M}_n^m(\mathbf{r}; k, 1) \overline{\mathbf{M}_n^m(\mathbf{r}'; k, 1)} \rightarrow I_M$ and $\mathbf{N}_n^m(\mathbf{r}; k, 1) \overline{\mathbf{N}_n^m(\mathbf{r}'; k, 1)} \rightarrow I_N$ must be evaluated [38]:

$$I_M = \int_0^{\infty} j_n(kr) j_n(kr') \frac{k^2}{k^2 - k_b^2} dk \quad (\text{A.20})$$

$$I_N = \int_0^{\infty} j_n(kr) j_n(kr') \frac{1}{k^2 - k_b^2} dk \quad (\text{A.21})$$

Note that in the process of determining I_N , the spatial derivatives of the form $[r\partial_r + 1]$ were pulled out of the k -integral. These integrals can be solved with the help of the residue theorem and the following identities and large-argument approximations [216, 10.47.v, 10.52]

$$j_n(z) = \frac{1}{2} \left[h_n^{(1)}(z) + h_n^{(2)}(z) \right] \quad (\text{A.22})$$

$$h_n^{(2)}(-z) j_n(-z') = h_n^{(1)}(z) j_n(z') \quad (\text{A.23})$$

$$h_n^{(1)}(z) j_n(z') \approx \mathbb{i}^{-n-1} \frac{\sin(z' - \frac{\pi}{2}n) e^{\mathbb{i}z}}{z'z} \quad \text{for } z \rightarrow \infty \quad (\text{A.24})$$

where $z, z' \in \mathbb{C}$.

It is important to note that $h_n^{(1)}(z)j_n(z')$ vanishes sufficiently quickly on the upper half-space only if $z/z' \geq 1$. With this, the integrals are first extended over the entire real axis by expressing $j_n(kr)$ in terms of spherical Hankel functions. Then, the complex integration path needed in the residue theorem is closed over the upper half-space to yield

$$I_M = \frac{1}{2} \int_{-\infty}^{\infty} h_n^{(1)}(kr) j_n(kr') \frac{k^2}{k^2 - k_b^2} dk = \mathbf{i} \frac{\pi}{2} k_b h_n^{(1)}(k_b r) j_n(k_b r') \quad \text{for } r \geq r' \quad (\text{A.25})$$

$$I_N = \frac{1}{2} \int_{-\infty}^{\infty} h_n^{(1)}(kr) j_n(kr') \frac{1}{k^2 - k_b^2} dk = \mathbf{i} \frac{\pi}{2} \frac{1}{k_b} h_n^{(1)}(k_b r) j_n(k_b r') \quad \text{for } r \geq r' \quad (\text{A.26})$$

where the singularity at $k = 0$ can be lifted and therefore does not contribute, and the positive and negative poles $k = \pm k_s$ are chosen to lie within and outside of the integration path, respectively, before the detours around the poles are contracted. Alternatively, one may argue that k_s has an infinitesimally small positive imaginary part such that the negative pole does not contribute. Ultimately, this allows the Green's dyadic to be written in a substantially simpler form

$$\mathbf{G}(\mathbf{r}, \mathbf{r}') = \mathbf{i} k_b \sum_{n=1}^{\infty} \sum_{m=-n}^n \left[\mathbf{M}_n^m(\mathbf{r}; k_b, 3) \overline{\mathbf{M}_n^m(\mathbf{r}'; k_b, 1)} + \mathbf{N}_n^m(\mathbf{r}; k_b, 3) \overline{\mathbf{N}_n^m(\mathbf{r}'; k_b, 1)} \right] \quad (\text{A.27})$$

which, however, is only valid for $r \geq r'$.

Farfield along the polar axis To obtain farfield approximations of the spherical vector wave functions along the polar axis ($\cos(\theta) = \pm 1, \phi = 0$), it is necessary to investigate the corresponding limits of the associated Legendre polynomials (cf. Eqs. (B.23,24))

$$\lim_{\cos \theta \rightarrow \pm 1} \partial_\theta \Psi_n^m P_n^m(\cos \theta) = (\pm 1)^n \Psi_n^{-1} \frac{1}{2} [\delta_{m,-1} - \delta_{m,1}] \quad (\text{A.28})$$

$$\lim_{\cos \theta \rightarrow \pm 1} \frac{m}{\sin \theta} \Psi_n^m P_n^m(\cos \theta) = \mp (\pm 1)^n \Psi_n^{-1} \frac{1}{2} [\delta_{m,-1} + \delta_{m,1}] \quad (\text{A.29})$$

where it is convenient to readily account for Ψ_n^m (Eq. (3.99)). Large-argument approximations of expressions involving the Hankel function of first kind (see [217] and [216, 10.52])

$$\lim_{r \rightarrow \infty} \check{\mathfrak{z}}_n(kr; 3) \approx \mathbf{i}^{-n-1} \frac{e^{\mathbf{i}kr}}{kr} \quad (\text{A.30})$$

$$\lim_{r \rightarrow \infty} \frac{\check{\mathfrak{z}}_n(kr; 3)}{kr} \approx 0 \quad (\text{A.31})$$

$$\lim_{r \rightarrow \infty} \frac{[r\partial_r + 1] \check{\mathfrak{z}}_n(kr; 3)}{kr} \approx \mathbf{i}^{-n} \frac{e^{\mathbf{i}kr}}{kr} \quad (\text{A.32})$$

indicate that in the farfield, the radial dependency of each spherical vector wave function takes the shape of a spherical wave. With this, the farfield approximations of the spherical vector wave functions (Eqs. (3.100,101)) along the polar axis can be written as

$$\lim_{\substack{r \rightarrow \infty \\ \cos \theta \rightarrow \pm 1}} \mathbf{M}_n^m(\mathbf{r}; k, 3) \approx \mp \mathbf{i}^{\mp n} \Psi_n^{-1} \frac{e^{\mathbf{i}kr}}{kr} \frac{1}{\sqrt{2}} [\delta_{m,-1} \hat{\mathbf{c}}^\mp + \delta_{m,1} \hat{\mathbf{c}}^\pm] \quad (\text{A.33})$$

$$\lim_{\substack{r \rightarrow \infty \\ \cos \theta \rightarrow \pm 1}} \mathbf{N}_n^m(\mathbf{r}; k, 3) \approx \mathbf{i}^{\mp n} \Psi_n^{-1} \frac{e^{\mathbf{i}kr}}{kr} \frac{1}{\sqrt{2}} [\delta_{m,-1} \hat{\mathbf{c}}^\mp - \delta_{m,1} \hat{\mathbf{c}}^\pm] \quad (\text{A.34})$$

where the unit vectors $\hat{\mathbf{c}}^+$ and $\hat{\mathbf{c}}^-$ are defined as:

$$\hat{\mathbf{c}}^\pm = \frac{\hat{\boldsymbol{\theta}} \pm \mathbf{i} \hat{\boldsymbol{\phi}}}{\sqrt{2}} \quad \hat{\mathbf{c}}^\mp \times \hat{\mathbf{c}}^\pm = \pm \mathbf{i} \hat{\mathbf{r}} \quad \hat{\mathbf{c}}^\mp \cdot \hat{\mathbf{c}}^\pm = 1 \quad \hat{\mathbf{c}}^\pm \cdot \hat{\mathbf{c}}^\pm = 0 \quad (\text{A.35})$$

These vectors resemble the Jones vectors of circularly polarized waves, and since $\hat{\boldsymbol{\theta}} = \pm \hat{\mathbf{x}}$ and $\hat{\boldsymbol{\phi}} = \hat{\mathbf{y}}$ along the polar axis, one may associate $\hat{\mathbf{c}}^+$ with left-circular and $\hat{\mathbf{c}}^-$ with right-circular polarization. Note that only the multipoles with azimuthal orders of $m = \pm 1$ are able to generate non-vanishing electromagnetic fields in the farfield along the polar axis. Consequently, based on Eq. (3.115), the polarization state of an arbitrary scattered field in the farfield along the polar axis is fully characterized by a sum of such circularly polarized waves.

In analogy to Eqs. (3.123,124), the differential energy flux along the polar axis may be defined as

$$\frac{dP_s^\pm}{d\Omega} = \lim_{\substack{r \rightarrow \infty \\ \cos \theta \rightarrow \pm 1}} \frac{1}{2} \operatorname{Re} \left\{ \left[\mathbf{E}_s \times \overline{\mathbf{H}_s} \right] \cdot \hat{\mathbf{r}} \right\} r^2 \quad (\text{A.36})$$

where the upper signs indicate forward direction ($\theta = 0$) and the lower signs backward direction ($\theta = \pi$), and the differential scattering cross section along the polar axis follows as

$$\frac{dC_s^\pm}{d\Omega} = \frac{1}{I_0} \frac{dP_s^\pm}{d\Omega} \quad I_0 = \frac{|E_0|^2 n_b}{2c_0 \mu_0 \mu_b} \quad (\text{A.37})$$

where I_0 is again the incident intensity of an arbitrarily polarized plane wave. After evaluating all previously defined expressions, it is found that:

$$\frac{dC_s^\pm}{d\Omega} = \frac{1}{2k_b^2} \left[\left| \sum_{n=1}^{\infty} \mathbf{i}^{\mp n} \Psi_n^{-1} (a_n^{-1} \mp b_n^{-1}) \right|^2 + \left| \sum_{n=1}^{\infty} \mathbf{i}^{\mp n} \Psi_n^{-1} (a_n^1 \pm b_n^1) \right|^2 \right] \quad (\text{A.38})$$

If the scattered field only contains dipolar contributions, this simplifies to

$$\frac{dC_s^\pm}{d\Omega} = \frac{3}{8\pi k_b^2} \left[\left| a_1^{-1} \mp b_1^{-1} \right|^2 + \left| a_1^1 \pm b_1^1 \right|^2 \right] \quad (\text{A.39})$$

and it can be concluded that in this case, the differential scattering cross section only vanishes along the polar axis if the multipole coefficients satisfy $a_1^{-1} = \pm b_1^{-1}$ and $a_1^1 = \mp b_1^1$.

A.3. Radial structure factor and pair correlation function

The radial structure factor $S(k)$ and the radial pair correlation function $g(r)$ can be defined as the average of $S(\mathbf{k})$ and $g(\mathbf{r})$ with respect to the full solid angle. To avoid repetitions in the following discussion, f may stand for either S or g , and \mathbf{u} for \mathbf{k} or \mathbf{r} , respectively. Given that the unit vector $\hat{\mathbf{u}}$ is expressed in terms of D -dimensional spherical coordinates [218]

$$\hat{\mathbf{u}} = \sum_{d=1}^D \hat{\mathbf{e}}_d \cos(\phi_d) \prod_{i=1}^{d-1} \sin(\phi_i) \quad (\phi_1, \dots, \phi_{D-1}) \in [0, \pi]^{D-2} \times [0, 2\pi] \quad \phi_D = 0 \quad (\text{A.40})$$

where $\hat{\mathbf{e}}_d$ is a Cartesian basis vector, the radial function $f(u)$ can be defined as

$$f(u) = \frac{1}{\Omega_D} \int f(u\hat{\mathbf{u}}) d\Omega \quad \Omega_D = \frac{2\pi^{\frac{D}{2}}}{\Gamma(\frac{D}{2})} \quad d\Omega = d\phi_{D-1} \prod_{i=2}^{D-1} \sin^{i-1}(\phi_{D-i}) d\phi_{D-i} \quad (\text{A.41})$$

where Ω_D is the full solid angle of a D -dimensional sphere and $d\Omega$ is the corresponding unit solid angle. In two dimensions, the radial function can be written as

$$f(u) = \frac{1}{2\pi} \int_0^{2\pi} f(u [\cos(\phi) \hat{\mathbf{e}}_1 + \sin(\phi) \hat{\mathbf{e}}_2]) d\phi \quad (\text{A.42})$$

which is simply the average along the azimuthal angle $\phi = \phi_1$.

A.4. Probability density functions

The standard \bar{f} , folded \check{f} , and wrapped \mathring{f} normal distributions of a random variable $x \in \mathbb{D}$ (cf. [219]) may be defined as

$$\bar{f}(x; \mu, \sigma) = \frac{1}{\sqrt{2\pi\sigma^2}} \exp\left(-\frac{(x-\mu)^2}{2\sigma^2}\right) \quad \mathbb{D} =]-\infty, \infty[\quad (\text{A.43})$$

$$\check{f}(x; \mu, \sigma) = \bar{f}(x; \mu, \sigma) + \bar{f}(x; -\mu, \sigma) \quad \mathbb{D} = [0, \infty[\quad (\text{A.44})$$

$$\mathring{f}(x; \mu, \sigma) = \sum_{n=-\infty}^{\infty} \bar{f}(x; \mu - 2\pi n, \sigma) \quad \mathbb{D} = [-\pi, \pi] \quad (\text{A.45})$$

where the folding and wrapping is meant in a quite literal sense. The folded normal distribution mirrors and adds the part of the standard normal distribution that lies on the negative half-space onto the positive half-space. The wrapped normal distribution splits the standard normal distribution modulo 2π and adds up all periods. Hence, the folded and wrapped normal distributions are suitable for the description of amplitudes and angles of normally distributed quantities. Note that the wrapped normal distribution turns from a standard normal distribution into a uniform distribution as the standard deviation σ increases.

The first raw moment (mean) μ_x and the second central moment (variance) σ_x^2 of x are defined as

$$\mu_x = \int_{\mathbb{D}} x f(x) dx \quad \approx \frac{1}{N} \sum_{n=1}^N x_n \quad (\text{A.46})$$

$$\sigma_x^2 = \int_{\mathbb{D}} (x - \mu_x)^2 f(x) dx \quad \approx \frac{1}{N} \sum_{n=1}^N (x_n - \mu_x)^2 \quad (\text{A.47})$$

where f is an arbitrary probability density function and the estimates require N samples x_n of x . The mean μ_x and variance σ_x^2 of the folded normal distribution are related to the mean μ and variance σ^2 of the underlying standard normal distribution via a transcendental system of equations

$$\mu_x = \sqrt{\frac{2\sigma^2}{\pi}} \exp\left(-\frac{\mu}{2\sigma^2}\right) + \mu \operatorname{erf}\left(\frac{\mu}{\sqrt{2\sigma^2}}\right) \quad (\text{A.48})$$

$$\sigma_x^2 = \sigma^2 + \mu^2 - \mu_x^2 \quad (\text{A.49})$$

where $\operatorname{erf}(\cdot)$ is the error function.

The circular mean μ_z of the wrapped normal distribution is not defined as the first raw moment of x , but instead as the first raw moment of the complex number $z = e^{\mathbf{i}x}$:

$$\mu_z = \int_{\mathbb{D}} e^{\mathbf{i}x} \mathring{f}(x; \mu, \sigma) dx = e^{-\frac{\sigma^2}{2} + \mathbf{i}\mu} \approx \frac{1}{N} \sum_{n=1}^N e^{\mathbf{i}x_n} \quad (\text{A.50})$$

The mean angle $\hat{\mu}_x$ and the circular variance $\hat{\sigma}_x^2$ of x are derived from μ_z via

$$\hat{\mu}_x = \mu = \arg(\mu_z) \quad \hat{\sigma}_x^2 = \sigma^2 = -2 \ln(|\mu_z|) \quad (\text{A.51})$$

and are defined to be identical to the mean μ and variance σ^2 of the underlying standard normal distribution.

In this thesis, each kernel density estimation of a two-dimensional probability density function $f(x, y)$ used the following uncorrelated bivariate standard normal distribution as kernel

$$f(x, y) \approx \frac{1}{N} \sum_{n=1}^N \bar{f}(x; x_n, h_x) \bar{f}(y; y_n, h_y) \quad (\text{A.52})$$

where (x_n, y_n) are N samples of (x, y) , and the constants h_x and h_y are carefully-chosen kernel bandwidths. The sum was evaluated with a fast nonuniform Fourier transformation, and the result was folded or wrapped whenever f was expected to be a folded or wrapped normal distribution.

A.5. Disordered Huygens' metasurfaces

The discussion in this section was mainly developed by Rahimzadegan [28], can also be found in [32], and was replicated here to support the interpretation of data shown in this thesis.

Effective dipole moments The maximum electric p_0 and magnetic m_0 dipole moment that can be induced in a spherical particle equals to

$$p_0 = \frac{6\pi\mathbf{i}E_0\varepsilon}{k^3} \quad m_0 = \frac{6\pi\mathbf{i}E_0}{k^3Z} \quad (\text{A.53})$$

where E_0 is the amplitude of an incident plane wave that excites the sphere, and k and $Z = \sqrt{\mu/\varepsilon}$ are the wavenumber and impedance of the homogeneous background medium. These moments will serve as normalization constants.

In a particle cluster, the effective electric \mathbf{p}_{eff} and magnetic \mathbf{m}_{eff} dipole moment of a particle can be computed from its effective electric $\mathbf{a}_{1,\text{eff}}$ and magnetic $\mathbf{b}_{1,\text{eff}}$ multipole coefficients ($n = 1$) [220]

$$\mathbf{p}_{\text{eff}} = \frac{-\mathbf{i}\varepsilon\sqrt{6\pi}}{k^3} \mathbf{F}_1 \cdot \mathbf{a}_{1,\text{eff}} \quad \mathbf{m}_{\text{eff}} = \frac{-\mathbf{i}\sqrt{6\pi}}{Zk^3} \mathbf{F}_1 \cdot \mathbf{b}_{1,\text{eff}} \quad \mathbf{F}_1 = \frac{1}{\sqrt{2}} \begin{pmatrix} 1 & 0 & -1 \\ -\mathbf{i} & 0 & -\mathbf{i} \\ 0 & \sqrt{2} & 0 \end{pmatrix} \quad (\text{A.54})$$

where the dipole moment vectors are given in a Cartesian standard basis (x, y, z) , the elements in the multipole coefficient vectors are arranged in the sequence of increasing azimuthal orders $m = -n, \dots, n$, and the matrix \mathbf{F}_1 represents a basis transformation from spherical to Cartesian coordinates.

Ordered Huygens' metasurfaces The zeroth-order transmission t and reflection r coefficient of an array of dipolar particles, that is excited by a y -polarized plane wave, can be written as [221]

$$t = 1 - \frac{3\pi}{k^2 A} \left(\frac{p_{y,\text{eff}}}{p_0} - \frac{m_{x,\text{eff}}}{m_0} \right) \quad (\text{A.55})$$

$$r = -\frac{3\pi}{k^2 A} \left(\frac{p_{y,\text{eff}}}{p_0} + \frac{m_{x,\text{eff}}}{m_0} \right) \quad (\text{A.56})$$

where A is the unit cell area, and $p_{y,\text{eff}}$ and $m_{x,\text{eff}}$ are vector components of the effective dipole moments in each particle. In an ordered Huygens' metasurface, the effective dipole moments satisfy the Kerker condition $p_{y,\text{eff}}/p_0 = -m_{x,\text{eff}}/m_0$ for all wavelengths, which results in $r = 0$, and $|t| = 1$ due to energy conservation. At the resonance wavelength, the effective dipole moments take on their maximum values $p_{y,\text{eff}}/p_0 = k^2 A/(3\pi)$ and $m_{x,\text{eff}}/m_0 = -k^2 A/(3\pi)$, and generate a scattered wave that exceeds the incident wave by a factor of two in amplitude and is shifted by π in phase ($t = 1 + 2e^{i\pi} = -1$). In other words, the scattered wave not only cancels the incident wave, but also replaces it by a phase-shifted version of it. Lastly, note that if the particles support only one of the two dipole types at the resonance wavelength, it follows that $|r| = 1$ and $t = 0$.

Disordered Huygens' metasurface If the dipolar particles are then brought into an arrangement with uniform disorder, the zeroth-order transmission and reflection coefficient may be estimated via

$$t \approx 1 - \frac{3\pi}{k^2} \left\langle \frac{p_{x,\text{eff}}}{p_0} + \frac{m_{y,\text{eff}}}{m_0} + \frac{p_{y,\text{eff}}}{p_0} - \frac{m_{x,\text{eff}}}{m_0} \right\rangle_A \quad (\text{A.57})$$

$$r \approx -\frac{3\pi}{k^2} \left\langle \frac{p_{x,\text{eff}}}{p_0} - \frac{m_{y,\text{eff}}}{m_0} + \frac{p_{y,\text{eff}}}{p_0} + \frac{m_{x,\text{eff}}}{m_0} \right\rangle_A \quad (\text{A.58})$$

where $\langle \cdot \rangle_A$ denotes the area average of the effective dipole moments in all particles. However, for resonant excitation, experimental and numerical evidence suggests that certain effective dipole moments, or combinations thereof, vanish in average:

$$\left\langle \frac{p_{x,\text{eff}}}{p_0} \right\rangle_A \approx 0 \quad \left\langle \frac{m_{y,\text{eff}}}{m_0} \right\rangle_A \approx 0 \quad \left\langle \frac{p_{y,\text{eff}}}{p_0} + \frac{m_{x,\text{eff}}}{m_0} \right\rangle_A \approx 0 \quad (\text{A.59})$$

The effective dipole moments that are cross-polarized ($p_{x,\text{eff}}$ and $m_{y,\text{eff}}$) with respect to the y -polarized incident wave are due to local random anisotropy in the particle arrangement. Hence, it can be expected that these moments follow a mean-free normal distribution. The sum term $p_{y,\text{eff}}/p_0 + m_{x,\text{eff}}/m_0$, on the other hand, vanishes in average since increasing positional disorder mainly reduces the magnitudes of the effective dipole moments (Fig. 7.10c), but leaves their values in a relationship that still satisfies the Kerker condition (Fig. 7.10e). In other words, the majority of the particles still sustain Huygens sources, but they do not radiate as strongly as in the ordered case.

Hence, for resonant excitation, the transmission and reflection coefficients reduce to:

$$t \approx 1 - \frac{3\pi}{k^2} \left\langle \frac{p_{y,\text{eff}}}{p_0} - \frac{m_{x,\text{eff}}}{m_0} \right\rangle_A \quad (\text{A.60})$$

$$r \approx 0 \quad (\text{A.61})$$

Figure 7.6e demonstrates a very low reflectance over the entire spectrum and, in particular, $r = 0$ exactly at the resonance wavelength $\lambda = 1.38 \mu\text{m}$. Furthermore, since increasing positional disorder reduces the magnitude of the effective dipole moments in average (Fig. 7.10c), it is possible to obtain $t = 0$ at resonance for a critical degree of positional disorder (Fig. 7.7a). More precisely, the average magnitude of the effective dipole moments must reduce to one half of that in the ordered case, such that the zeroth-order component of the scattered wave cancels the incident wave ($t = 1 + e^{i\pi} = 0$).

B. Numerical Methods

B.1. Computation of spherical Bessel functions

Spherical Bessel functions of integer order $n \in \mathbb{Z}_{\geq 0}$ satisfy for $z \in \mathbb{C}$ [216, 10.51]:

$$\check{\delta}_{n-1}(z) - \frac{2n+1}{z}\check{\delta}_n(z) + \check{\delta}_{n+1}(z) = 0 \quad (\text{B.1})$$

$$n\check{\delta}_{n-1}(z) - (2n+1)\check{\delta}'_n(z) - (n+1)\check{\delta}_{n+1}(z) = 0 \quad (\text{B.2})$$

Downward recurrence is stable for j_n and j'_n :

$$j_n(z) = \frac{n+2}{z}j_{n+1}(z) + j'_{n+1}(z) \quad (\text{B.3})$$

$$j'_n(z) = \frac{n}{z}j_n(z) - j_{n+1}(z) \quad (\text{B.4})$$

Upward recurrence is stable for y_n and y'_n :

$$y_n(z) = \frac{n-1}{z}y_{n-1}(z) - y'_{n-1}(z) \quad (\text{B.5})$$

$$y'_n(z) = y_{n-1}(z) - \frac{n+1}{z}y_n(z) \quad (\text{B.6})$$

While the upward recurrences for y_n and y'_n can be initialized with known analytic expressions for small orders, the downward recurrences for j_n and j'_n require a secondary method for the computation of large-order initial values. One possibility is to utilize the logarithmic derivative of j_n

$$\frac{j'_n(z)}{j_n(z)} = \frac{n}{z} - \frac{j_{n+1}(z)}{j_n(z)} \quad (\text{B.7})$$

and to evaluate the resulting continued fraction

$$\frac{j'_n(z)}{j_n(z)} = \frac{n}{z} + \mathop{\text{K}}_{i=1}^{\infty} \frac{-1}{[2(n+i)+1]z^{-1}} \quad b_0 + \mathop{\text{K}}_{i=1}^{\infty} \frac{a_i}{b_i} = b_0 + \frac{a_1}{b_1 + \frac{a_2}{b_2 + \dots}} \quad (\text{B.8})$$

with the Lentz-Thompson algorithm [222] to obtain an initial value for the ratio j'_n/j_n . After completing the recurrence with this ratio as initial value, all intermediate results can be renormalized by comparison with j'_0/j_0 or other small-order identities. For reference, the first few orders read as

$$j_0(z) = \frac{\sin(z)}{z} \quad j_1(z) = -j'_0(z) \quad (\text{B.9})$$

$$j'_0(z) = \frac{z \cos(z) - \sin(z)}{z^2} \quad j'_1(z) = \frac{\sin(z) + 2j'_0(z)}{z} \quad (\text{B.10})$$

$$y_0(z) = -\frac{\cos(z)}{z} \quad y_1(z) = -y'_0(z) \quad (\text{B.11})$$

$$y'_0(z) = \frac{z \sin(z) + \cos(z)}{z^2} \quad y'_1(z) = -\frac{\cos(z) - 2y'_0(z)}{z} \quad (\text{B.12})$$

and the point $z = 0$ must be treated analytically:

$$\lim_{z \rightarrow 0} j_n(z) = \delta_{n,0} \quad \lim_{z \rightarrow 0} y_n(z) = -\infty \quad (\text{B.13})$$

$$\lim_{z \rightarrow 0} j'_n(z) = \frac{1}{3}\delta_{n,1} \quad \lim_{z \rightarrow 0} y'_n(z) = +\infty \quad (\text{B.14})$$

$$\lim_{z \rightarrow 0} \frac{1}{z}j_n(z) = +\infty\delta_{n,0} + \frac{1}{3}\delta_{n,1} \quad \lim_{z \rightarrow 0} \frac{1}{z}y_n(z) = -\infty \quad (\text{B.15})$$

With this, the numerical values for all j_n, j'_n and y_n, y'_n are now available up to a desired order n .

B.2. Computation of associated Legendre polynomials

The following discussion is restricted to associated Legendre polynomials $P_n^m(\cos \theta)$ of integer order $n = 0, 1, \dots$ and integer degree $m = -n, \dots, n$ on the real-valued domain $\theta \in [0, \pi]$ (see [216, 14]).

The following upward recurrence is stable for negative $m = -(n-2), -(n-3), \dots, 0$ with $n = 2, 3, \dots$:

$$P_n^m(\cos \theta) = -2 \frac{m-1}{\tan \theta} P_n^{m-1}(\cos \theta) - (n-m+2)(n+m-1) P_n^{m-2}(\cos \theta) \quad (\text{B.16})$$

Initial values for this recurrence can be generated with the help of the following two identities

$$P_n^{-n}(\cos \theta) = \frac{1}{n!} \left(\frac{\sin \theta}{2} \right)^n \quad (\text{B.17})$$

$$P_n^{-(n-1)}(\cos \theta) = \cos(\theta) P_{(n-1)}^{-(n-1)}(\cos \theta) \quad (\text{B.18})$$

which may as well be computed recursively by iterating over $n = 1, 2, \dots$ with:

$$P_n^{-n}(\cos \theta) = \frac{1}{n} \left(\frac{\sin \theta}{2} \right) P_{(n-1)}^{-(n-1)}(\cos \theta) \quad P_0^0(\cos \theta) = 1 \quad (\text{B.19})$$

$$P_n^{-(n-1)}(\cos \theta) = \cos(\theta) P_{(n-1)}^{-(n-1)}(\cos \theta) \quad (\text{B.20})$$

Once all P_n^m with negative m are obtained, the corresponding derivatives $\partial_\theta P_n^m$ can be computed by iterating over $n = 1, 2, \dots$ and $m = 0, -1, \dots, -n$ with:

$$\partial_\theta P_n^m(\cos \theta) = \frac{n}{\tan \theta} P_n^m(\cos \theta) - \frac{n+m}{\sin \theta} P_{n-1}^m(\cos \theta) \quad \partial_\theta P_0^0(\cos \theta) = 0 \quad (\text{B.21})$$

Note that $P_n^m = 0$ for $|m| > n$. Moreover, since all recurrence relations exhibit singularities at $\sin \theta = 0$, the following special points must be treated analytically:

$$\lim_{\cos \theta \rightarrow \pm 1} P_n^m(\cos \theta) = (\pm 1)^n \delta_{m,0} \quad (\text{B.22})$$

$$\lim_{\cos \theta \rightarrow \pm 1} \partial_\theta P_n^m(\cos \theta) = (\pm 1)^n \frac{1}{2} [\delta_{m,-1} - n(n+1) \delta_{m,1}] \quad (\text{B.23})$$

$$\lim_{\cos \theta \rightarrow \pm 1} \frac{m}{\sin \theta} P_n^m(\cos \theta) = -(\pm 1)^{n+1} \frac{1}{2} [\delta_{m,-1} + n(n+1) \delta_{m,1}] \quad (\text{B.24})$$

The positive and negative m are connected via

$$P_n^m(\cos \theta) = (-1)^m \frac{(n+m)!}{(n-m)!} P_n^{-m}(\cos \theta) \quad (\text{B.25})$$

which, once again, can be evaluated recursively for each $n = 1, 2, \dots$ by iterating over $m = 1, \dots, n$ and performing the following mapping from negative to positive m :

$$a_n^m = -(n-m+1)(n+m) a_n^{m-1} \quad a_n^0 = 1 \quad (\text{B.26})$$

$$P_n^m(\cos \theta) = a_n^m P_n^{-m}(\cos \theta) \quad (\text{B.27})$$

$$\partial_\theta P_n^m(\cos \theta) = a_n^m \partial_\theta P_n^{-m}(\cos \theta) \quad (\text{B.28})$$

With this, the numerical values for all P_n^m and $\partial_\theta P_n^m$ are now available up to a desired order n .

B.3. Simulation of planar multilayer systems

Consider a planar multilayer system consisting of $\ell = 1, \dots, L$ layers of linear, isotropic, homogeneous media with refractive indices n_ℓ , where the outermost layers extend to infinity. The layers are separated by $i = 1, \dots, L+1$ interfaces, where the outermost interfaces represent the input and output plane and only account for additional phase terms due to propagation within the outermost layers. The position

vector is parameterized in the form of $\mathbf{r}(\mathbf{t}, d) = \mathbf{t} + d\hat{\mathbf{n}}$, where the plane $\mathbf{t} \cdot \hat{\mathbf{n}} = 0$ is oriented parallel to the interfaces, and the base point of an interface $\mathbf{r}_i = \mathbf{r}(\mathbf{0}, d_i)$ lies in a distance of d_i with respect to the origin. The layers are enumerated in ascending order along the direction of $\hat{\mathbf{n}}$ such that the phase $\varphi_\ell = k_\ell(d_{\ell+1} - d_\ell) \cos(\theta_\ell)$ has a positive imaginary part for forward-propagating waves. The incident wavevector \mathbf{k}_1 points towards the first interface, which means that the incidence angle is limited to $\text{Re } \theta_1 \in [0, \frac{\pi}{2}]$. Moreover, with the reflections of the plane wave unit vectors from Eqs. (3.53,54), it is possible to express reflected plane waves in terms of:

$$\mathbf{M}_{\mathcal{R}\mathbf{k}}(\mathbf{r}) = \mathbf{M}_{\mathbf{k}}(\mathbf{t}) e^{-\mathbf{i}k d \cos(\theta)} \quad \mathbf{N}_{\mathcal{R}\mathbf{k}}(\mathbf{r}) = -\mathcal{R}\mathbf{N}_{\mathbf{k}}(\mathbf{t}) e^{-\mathbf{i}k d \cos(\theta)} \quad (\text{B.29})$$

In each layer, the electric field and its associated magnetic field consist of a superposition of forward-propagating and reflected, TE and TM polarized, plane waves

$$\mathbf{E}_\ell(\mathbf{r}) = \{A_\ell \mathbf{M}_{\mathbf{k}_\ell}(\mathbf{r} - \mathbf{r}_\ell) + B_\ell \mathbf{M}_{\mathcal{R}\mathbf{k}_\ell}(\mathbf{r} - \mathbf{r}_{\ell+1}) + C_\ell \mathbf{N}_{\mathbf{k}_\ell}(\mathbf{r} - \mathbf{r}_\ell) + D_\ell \mathbf{N}_{\mathcal{R}\mathbf{k}_\ell}(\mathbf{r} - \mathbf{r}_{\ell+1})\} \quad (\text{B.30})$$

$$\mathbf{H}_\ell(\mathbf{r}) = \{A_\ell \mathbf{N}_{\mathbf{k}_\ell}(\mathbf{r} - \mathbf{r}_\ell) + B_\ell \mathbf{N}_{\mathcal{R}\mathbf{k}_\ell}(\mathbf{r} - \mathbf{r}_{\ell+1}) + C_\ell \mathbf{M}_{\mathbf{k}_\ell}(\mathbf{r} - \mathbf{r}_\ell) + D_\ell \mathbf{M}_{\mathcal{R}\mathbf{k}_\ell}(\mathbf{r} - \mathbf{r}_{\ell+1})\} \frac{-\mathbf{i}n_\ell}{c_0 \mu_0 \mu_\ell} \quad (\text{B.31})$$

where $A_\ell, B_\ell, C_\ell, D_\ell \in \mathbb{C}$ are arbitrary electric field amplitudes that remain to be determined. Note that the spatial dependency separates into $\mathbf{E}_\ell(\mathbf{r}) = \mathbf{E}_\ell(d\hat{\mathbf{n}}) e^{\mathbf{i}\mathbf{k}_\ell \cdot \mathbf{t}}$ and $\mathbf{H}_\ell(\mathbf{r}) = \mathbf{H}_\ell(d\hat{\mathbf{n}}) e^{\mathbf{i}\mathbf{k}_\ell \cdot \mathbf{t}}$. When these expressions are inserted into the boundary conditions of Maxwell's equations (Eqs. (3.27,28)), it is found that the spatially-dependent term $\exp(\mathbf{i}(\mathbf{k}_\ell - \mathbf{k}_{\ell+1}) \cdot \mathbf{t})$ must equal a constant, which is only possible if the tangential wavevector components $\mathcal{P}_\parallel(\mathbf{k}_\ell - \mathbf{k}_{\ell+1}) = \mathbf{0}$ are conserved throughout the multilayer system. Moreover, since the "magnitude" $\mathbf{k}_\ell^2 = k_\ell^2$ is fixed, it immediately follows that the polar propagation angles are related via Snell's law $n_{\ell+1} \sin(\theta_{\ell+1}) = n_\ell \sin(\theta_\ell)$ and that the wavevectors and unit vectors of refracted plane waves satisfy

$$\mathbf{k}_b = \left[\mathcal{P}_\parallel + \frac{n_b \cos(\theta_b)}{n_a \cos(\theta_a)} \mathcal{P}_\perp \right] \mathbf{k}_a \quad \hat{\mathbf{M}}_{\mathbf{k}_b} = \hat{\mathbf{M}}_{\mathbf{k}_a} \quad \hat{\mathbf{N}}_{\mathbf{k}_b} = \left[\frac{\cos(\theta_b)}{\cos(\theta_a)} \mathcal{P}_\parallel + \frac{n_a}{n_b} \mathcal{P}_\perp \right] \hat{\mathbf{N}}_{\mathbf{k}_a} \quad (\text{B.32})$$

where a and b stand for any two layers of the system. To determine the electric field amplitudes, it suffices then to consider the electromagnetic fields on either side at the base point of an interface:

$$\mathbf{E}_\ell(\mathbf{r}_{\ell+1}) = \left\{ [A_\ell e^{\mathbf{i}\varphi_\ell} + B_\ell] \hat{\mathbf{M}}_{\mathbf{k}_\ell} + [C_\ell e^{\mathbf{i}\varphi_\ell} - D_\ell \mathcal{R}] \hat{\mathbf{N}}_{\mathbf{k}_\ell} \right\} \quad (\text{B.33})$$

$$\mathbf{H}_\ell(\mathbf{r}_{\ell+1}) = \left\{ [A_\ell e^{\mathbf{i}\varphi_\ell} - B_\ell \mathcal{R}] \hat{\mathbf{N}}_{\mathbf{k}_\ell} + [C_\ell e^{\mathbf{i}\varphi_\ell} + D_\ell] \hat{\mathbf{M}}_{\mathbf{k}_\ell} \right\} \frac{-\mathbf{i}n_\ell}{c_0 \mu_0 \mu_\ell} \quad (\text{B.34})$$

$$\mathbf{E}_{\ell+1}(\mathbf{r}_{\ell+1}) = \left\{ [A_{\ell+1} + B_{\ell+1} e^{\mathbf{i}\varphi_{\ell+1}}] \hat{\mathbf{M}}_{\mathbf{k}_{\ell+1}} + [C_{\ell+1} - D_{\ell+1} e^{\mathbf{i}\varphi_{\ell+1}} \mathcal{R}] \hat{\mathbf{N}}_{\mathbf{k}_{\ell+1}} \right\} \quad (\text{B.35})$$

$$\mathbf{H}_{\ell+1}(\mathbf{r}_{\ell+1}) = \left\{ [A_{\ell+1} - B_{\ell+1} e^{\mathbf{i}\varphi_{\ell+1}} \mathcal{R}] \hat{\mathbf{N}}_{\mathbf{k}_{\ell+1}} + [C_{\ell+1} + D_{\ell+1} e^{\mathbf{i}\varphi_{\ell+1}}] \hat{\mathbf{M}}_{\mathbf{k}_{\ell+1}} \right\} \frac{-\mathbf{i}n_{\ell+1}}{c_0 \mu_0 \mu_{\ell+1}} \quad (\text{B.36})$$

Since the TE and TM components of a plane wave are orthogonal, the tangential boundary conditions of Maxwell's equations (Eq. (3.27)) separate into four unique equations

$$\text{TE: } \begin{pmatrix} 1 & 1 \\ 1 & -1 \end{pmatrix} \cdot \begin{pmatrix} 1 & 0 \\ 0 & e^{\mathbf{i}\varphi_{\ell+1}} \end{pmatrix} \cdot \begin{pmatrix} A_{\ell+1} \\ B_{\ell+1} \end{pmatrix} = \begin{pmatrix} 1 & 0 \\ 0 & \frac{\eta_\ell \cos(\theta_\ell)}{\eta_{\ell+1} \cos(\theta_{\ell+1})} \end{pmatrix} \cdot \begin{pmatrix} 1 & 1 \\ 1 & -1 \end{pmatrix} \cdot \begin{pmatrix} e^{\mathbf{i}\varphi_\ell} & 0 \\ 0 & 1 \end{pmatrix} \cdot \begin{pmatrix} A_\ell \\ B_\ell \end{pmatrix} \quad (\text{B.37})$$

$$\text{TM: } \begin{pmatrix} 1 & 1 \\ 1 & -1 \end{pmatrix} \cdot \begin{pmatrix} 1 & 0 \\ 0 & e^{\mathbf{i}\varphi_{\ell+1}} \end{pmatrix} \cdot \begin{pmatrix} C_{\ell+1} \\ D_{\ell+1} \end{pmatrix} = \begin{pmatrix} \frac{\eta_\ell}{\eta_{\ell+1}} & 0 \\ 0 & \frac{\cos(\theta_\ell)}{\cos(\theta_{\ell+1})} \end{pmatrix} \cdot \begin{pmatrix} 1 & 1 \\ 1 & -1 \end{pmatrix} \cdot \begin{pmatrix} e^{\mathbf{i}\varphi_\ell} & 0 \\ 0 & 1 \end{pmatrix} \cdot \begin{pmatrix} C_\ell \\ D_\ell \end{pmatrix} \quad (\text{B.38})$$

where $\eta_\ell = n_\ell / \mu_\ell$. The normal boundary conditions of Maxwell's equations (Eq. (3.28)) result in two equations that are already contained in the preceding matrix equations. These matrix equations can then be rearranged according to the following templates

$$\mathbf{T}_{ab} = \mathbf{S}_{ab}^* \quad \text{TE: } \begin{pmatrix} A_b \\ B_b \end{pmatrix} = \mathbf{T}_{ab} \cdot \begin{pmatrix} A_a \\ B_a \end{pmatrix} \quad \text{TM: } \begin{pmatrix} C_b \\ D_b \end{pmatrix} = \mathbf{T}_{ab} \cdot \begin{pmatrix} C_a \\ D_a \end{pmatrix} \quad (\text{B.39})$$

$$\mathbf{S}_{ab} = \mathbf{T}_{ab}^* = \begin{pmatrix} t_{ab} & r_{ba} \\ r_{ab} & t_{ba} \end{pmatrix} \quad \text{TE: } \begin{pmatrix} A_b \\ B_a \end{pmatrix} = \mathbf{S}_{ab} \cdot \begin{pmatrix} A_a \\ B_b \end{pmatrix} \quad \text{TM: } \begin{pmatrix} C_b \\ D_b \end{pmatrix} = \mathbf{S}_{ab} \cdot \begin{pmatrix} C_a \\ D_b \end{pmatrix} \quad (\text{B.40})$$

where the transfer matrix \mathbf{T}_{ab} transforms the electric field amplitudes of layer a into those of layer b , the elements of the scattering matrix \mathbf{S}_{ab} represent transmission coefficients t and reflection coefficients r in forward (subscript ab) and reverse (subscript ba) direction for the propagation from layer a to b , and the star operator can be written as

$$\mathbf{A}^* = \frac{1}{A_{22}} \begin{pmatrix} \det(\mathbf{A}) & A_{12} \\ -A_{21} & 1 \end{pmatrix} \quad (\text{B.41})$$

where \mathbf{A} is an arbitrary matrix. Given that a, b, c are three consecutive layers, the combined transfer matrix can be computed from the transfer matrices of the individual interfaces: $\mathbf{T}_{ac} = \mathbf{T}_{bc} \cdot \mathbf{T}_{ab}$. While such chained matrix products are particularly simple to perform, they can become numerically unstable if certain elements of the transfer matrices are much larger in magnitude than others. This issue can be avoided by making use of the fact that the elements of the scattering matrix are limited in their magnitude due to energy conservation. The combined scattering matrix can be computed from

$$\mathbf{S}_{ac} = (\mathbf{S}_{bc}^* \cdot \mathbf{S}_{ab}^*)^* = \frac{1}{1 - r_{ba}r_{bc}} \begin{pmatrix} t_{ab}t_{bc} & r_{cb} + \det(\mathbf{S}_{bc})r_{ba} \\ r_{ab} + \det(\mathbf{S}_{ab})r_{bc} & t_{cb}t_{ba} \end{pmatrix} \quad (\text{B.42})$$

with the scattering matrix of a single interface

$$\text{TE: } \mathbf{S}_{\ell, \ell+1} = \begin{pmatrix} \frac{2\eta_\ell \cos(\theta_\ell)}{\eta_\ell \cos(\theta_\ell) + \eta_{\ell+1} \cos(\theta_{\ell+1})} & -\frac{\eta_\ell \cos(\theta_\ell) - \eta_{\ell+1} \cos(\theta_{\ell+1})}{\eta_\ell \cos(\theta_\ell) + \eta_{\ell+1} \cos(\theta_{\ell+1})} \\ \frac{\eta_\ell \cos(\theta_\ell) - \eta_{\ell+1} \cos(\theta_{\ell+1})}{\eta_\ell \cos(\theta_\ell) + \eta_{\ell+1} \cos(\theta_{\ell+1})} & \frac{2\eta_{\ell+1} \cos(\theta_{\ell+1})}{\eta_\ell \cos(\theta_\ell) + \eta_{\ell+1} \cos(\theta_{\ell+1})} \end{pmatrix} \cdot \begin{pmatrix} e^{i\varphi_\ell} & 0 \\ 0 & e^{i\varphi_{\ell+1}} \end{pmatrix} \quad (\text{B.43})$$

$$\text{TM: } \mathbf{S}_{\ell, \ell+1} = \begin{pmatrix} \frac{2\eta_\ell \cos(\theta_\ell)}{\eta_{\ell+1} \cos(\theta_\ell) + \eta_\ell \cos(\theta_{\ell+1})} & -\frac{\eta_{\ell+1} \cos(\theta_\ell) - \eta_\ell \cos(\theta_{\ell+1})}{\eta_{\ell+1} \cos(\theta_\ell) + \eta_\ell \cos(\theta_{\ell+1})} \\ \frac{\eta_{\ell+1} \cos(\theta_\ell) - \eta_\ell \cos(\theta_{\ell+1})}{\eta_{\ell+1} \cos(\theta_\ell) + \eta_\ell \cos(\theta_{\ell+1})} & \frac{2\eta_{\ell+1} \cos(\theta_{\ell+1})}{\eta_{\ell+1} \cos(\theta_\ell) + \eta_\ell \cos(\theta_{\ell+1})} \end{pmatrix} \cdot \begin{pmatrix} e^{i\varphi_\ell} & 0 \\ 0 & e^{i\varphi_{\ell+1}} \end{pmatrix} \quad (\text{B.44})$$

where $\eta_\ell = n_\ell/\mu_\ell$, the left matrices are known as Fresnel's equations, the right matrices are phase terms due to propagation throughout the thickness of a layer, and the polar propagation angle θ_ℓ is fully determined by Snell's law:

$$\theta_\ell = \arcsin\left(\frac{n_1}{n_\ell} \sin(\theta_1)\right) \quad (\text{B.45})$$

Note that θ_ℓ is generally complex-valued if n_ℓ is complex-valued. If n_1 and θ_1 are real-valued, it is necessary that $n_\ell \sin(\theta_\ell)$ is also real-valued, which is the same as requiring $\text{Im } \mathcal{P}_{\parallel} \mathbf{k}_\ell = \mathbf{0}$ as mentioned in the derivation of Eqs. (3.56,57). On the other hand, if n_1 is complex-valued and n_ℓ is real-valued, θ_ℓ can become complex-valued. To avoid the combination of real-valued n_ℓ and complex-valued θ_ℓ , one may persist on $\text{Im } \mathcal{P}_{\parallel} \mathbf{k}_\ell = \mathbf{0}$. Equation (B.45) automatically fulfills this condition if $n_1, \theta_1 \in \mathbb{R}$. Otherwise, θ_ℓ must be chosen such that $\tanh(\text{Im } \theta_\ell) = -\tan(\arg(n_\ell)) \tan(\text{Re } \theta_\ell)$.

Lastly, the transmittance T and reflectance R are defined as the ratio of the transmitted or reflected intensity with respect to the incident intensity. For the special case of $\mu \in \mathbb{R}$, Eq. (3.71) provides an expression for the intensity in each layer, where the spatial dependency along the normal direction is readily contained in the phase terms of the scattering matrices. With this, the transmittance T_{ab} and reflectance R_{ab} from layer a to b can be written as

$$T_{ab} = \frac{p_b \text{Re}(\eta_b \cos(\theta_b))}{p_a \text{Re}(\eta_a \cos(\theta_a))} |t_{ab}|^2 \quad R_{ab} = |r_{ab}|^2 \quad p_\ell = \begin{cases} 1 & \text{TE} \\ \cosh(2 \text{Im } \theta_\ell) & \text{TM} \end{cases} \quad (\text{B.46})$$

where a and b can be interchanged to yield T_{ba} and R_{ba} , and the polarization-dependency ($p_\ell \approx 1$) is usually neglected in media with weak gain or loss ($\text{Im } \theta_\ell \approx 0$).

B.4. Algorithmic determination of diffraction orders

This section presents a numerical method that determines the diffraction orders that can be excited in an arbitrary two-dimensional lattice for a given range of polar and azimuthal incidence angles. Certain simulation software require this information to perform parameter sweeps of the incidence angles. The presented method also allows for a visual representation of the reciprocal space.

In a two-dimensional infinite lattice, the electromagnetic fields must satisfy periodic boundary conditions. Given the electric field \mathbf{E} and wavevector \mathbf{k} of a plane wave, and the lattice vector $\mathbf{R}_i = (\mathbf{a}_1, \mathbf{a}_2) \cdot \mathbf{i}$ with multi-index $\mathbf{i} = (i_1, i_2) \in \mathbb{Z}^2$ and basis vectors $\mathbf{a}_1, \mathbf{a}_2$, the Floquet-Bloch boundary condition reads as

$$\mathbf{E}(\mathbf{r} + \mathbf{R}_i) = \mathbf{E}(\mathbf{r}) e^{i[\mathbf{k} + \mathbf{K}_j] \cdot \mathbf{R}_i} \quad \mathbf{K}_j \cdot \mathbf{R}_i = 0 \pmod{2\pi} \quad (\text{B.47})$$

where the reciprocal lattice vector $\mathbf{K}_j = (\mathbf{b}_1, \mathbf{b}_2) \cdot \mathbf{j}$ with multi-index $\mathbf{j} = (j_1, j_2) \in \mathbb{Z}^2$ is given by the (pseudo)inverse $(\mathbf{b}_1, \mathbf{b}_2) = 2\pi[(\mathbf{a}_1, \mathbf{a}_2)^{-1}]^\top$. Without loss of generality, it can be assumed that \mathbf{k} points towards the origin of a spherical coordinate system with polar $\theta \in [0, \frac{\pi}{2}]$ and azimuthal $\phi \in [-\pi, \pi]$ angles, where the θ -axis coincides with the unit normal $\hat{\mathbf{n}} = (\hat{\mathbf{a}}_1 \times \hat{\mathbf{a}}_2) / \sin(\phi_2 - \phi_1)$ and the basis vectors $\mathbf{a}_1, \mathbf{a}_2$ are specified in terms of their magnitudes a_1, a_2 and azimuthal angles ϕ_1, ϕ_2 , which are measured with respect to the same axis as ϕ and are restricted to $(\phi_2 - \phi_1) \in]0, \pi[$ to avoid ambiguities. With this, the tangential components of the main vectors can be written as

$$\mathcal{P}_{\parallel} \mathbf{k} = -k \sin(\theta) \begin{pmatrix} \cos(\phi) \\ \sin(\phi) \end{pmatrix} \quad k = \frac{2\pi}{\lambda} n \quad (\text{B.48})$$

$$\mathbf{R}_i = \begin{pmatrix} \cos(\phi_1) & \cos(\phi_2) \\ \sin(\phi_1) & \sin(\phi_2) \end{pmatrix} \cdot \begin{pmatrix} a_1 & 0 \\ 0 & a_2 \end{pmatrix} \cdot \mathbf{i} \quad (\text{B.49})$$

$$\mathbf{K}_j = \frac{2\pi}{\sin(\phi_2 - \phi_1)} \begin{pmatrix} \sin(\phi_2) & -\sin(\phi_1) \\ -\cos(\phi_2) & \cos(\phi_1) \end{pmatrix} \cdot \begin{pmatrix} \frac{1}{a_1} & 0 \\ 0 & \frac{1}{a_2} \end{pmatrix} \cdot \mathbf{j} \quad (\text{B.50})$$

where λ is the vacuum wavelength, n is the refractive index on the respective side of the lattice plane, and $\mathcal{P}_{\parallel} \mathbf{k}$ is the projection of the wavevector onto the lattice plane (cf. Eq. (3.29)). Since $\mathcal{P}_{\parallel} \mathbf{k}$ is preserved in planar systems (cf. Appendix B.3), this quantity represents both the incident wave and the zeroth order of a diffracted wave. If the incident wave originates from another medium $(n_{\text{inc}}, \theta_{\text{inc}})$, all θ angles must be computed from Snell's law: $n \sin(\theta) = n_{\text{inc}} \sin(\theta_{\text{inc}})$ (cf. Eq. (B.45)). In general, the tangential wavevector component of a diffracted wave may be written as $\mathcal{P}_{\parallel} \mathbf{k}_j = \mathcal{P}_{\parallel} \mathbf{k} + \mathbf{K}_j$ and its normal component is restricted to $(\mathcal{P}_{\perp} \mathbf{k}_j)^2 = k^2 - (\mathcal{P}_{\parallel} \mathbf{k}_j)^2$. For real-valued n , this readily shows that the normal component is either purely real (propagating wave) or purely imaginary (evanescent wave). For complex-valued n , one would have to define a threshold value to distinguish between diffraction orders with weak and strong attenuation. However, it often suffices to simply use the real part of n in the following method. With this, all diffraction orders \mathbf{j} that satisfy $(\mathcal{P}_{\parallel} \mathbf{k}_j)^2 \leq k^2$ can be regarded as propagating waves, which can be written in a more concise form

$$\mathbf{U}_j^2(\theta, \phi) \leq 1 \quad \theta \in [\theta_{\min}, \theta_{\max}] \quad \phi \in [\phi_{\min}, \phi_{\max}] \quad \lambda, n, a_1, a_2, \phi_1, \phi_2: \text{constant} \quad (\text{B.51})$$

by introducing the following vector functions and constants

$$\mathbf{U}_j(\theta, \phi) = \mathbf{u}_j - \sin(\theta) \begin{pmatrix} \cos(\phi - \Sigma) \\ \sin(\phi - \Sigma) \end{pmatrix} \quad \Sigma = \frac{\phi_2 + \phi_1}{2} \quad (\text{B.52})$$

$$\mathbf{u}_j = \frac{\lambda}{n} \begin{pmatrix} \frac{1}{2 \cos(\Delta)} & 0 \\ 0 & \frac{1}{2 \sin(\Delta)} \end{pmatrix} \cdot \begin{pmatrix} 1 & 1 \\ -1 & 1 \end{pmatrix} \cdot \begin{pmatrix} \frac{1}{a_1} & 0 \\ 0 & \frac{1}{a_2} \end{pmatrix} \cdot \mathbf{j} \quad \Delta = \frac{\phi_2 - \phi_1}{2} \quad (\text{B.53})$$

where \mathbf{u}_j is a transformed reciprocal lattice vector, and $\mathbf{U}_j(\theta, \phi)$ describes an annular sector around \mathbf{u}_j . Hence, the intersection of this annular sector with the unit disk $\mathbf{U}_j \leq 1$ (cf. Eq. (B.51)) defines the subset of incidence angles for which a fixed diffraction order \mathbf{j} is considered to be a propagating wave.

However, since the goal of this method is to determine whether a fixed diffraction order propagates for *any* of the given incidence angles, it is not necessary to specify the resulting subset and it suffices to test whether an intersection occurs. Moreover, it already suffices to test for each \mathbf{j} if the point of the annular sector that is closest to the origin is contained within the unit disk. To this end, it is convenient to parameterize $\mathbf{u}_{\mathbf{j}}$ in terms of polar coordinates $u, \psi \in \mathbb{R}$

$$\mathbf{u}_{\mathbf{j}}(u, \psi) = u \begin{pmatrix} \cos(\psi) \\ \sin(\psi) \end{pmatrix} \quad u = \sqrt{\mathbf{u}_{\mathbf{j}}^2} \quad \psi = \arctan\left(\frac{u_{2,\mathbf{j}}}{u_{1,\mathbf{j}}}\right) \quad (\text{B.54})$$

where the \mathbf{j} -subscript of u and ψ is dropped for readability, and the problem of finding the point of the annular sector that is closest to the origin can be stated as a constrained minimization problem

$$\underset{(\theta, \phi)}{\operatorname{argmin}} \mathbf{U}_{\mathbf{j}}^2(\theta, \phi) \quad \theta \in [\theta_{\min}, \theta_{\max}] \quad \phi \in \{x \mid \text{isWithin}(x; \phi_{\min}, \phi_{\max})\} \quad (\text{B.55})$$

from which it is found that the global minimum is located along the direction of $\phi_0 = (\psi + \Sigma)_{[-\pi, \pi]}$ in a distance of $\sin(\theta_0) = u$, and the following functions allow ϕ to wrap around its domain of definition:

$$\text{isWithin}(x; a, b) = a \leq x \leq b \vee a > b \wedge (x \leq b \vee x \geq a) \quad (\text{B.56})$$

$$(x)_{[-\pi, \pi]} = x - 2\pi \left\lfloor \frac{x + \pi}{2\pi} \right\rfloor \quad (\text{B.57})$$

If ϕ_0 is not within the given interval, i.e. that the global minimum is not within the annular sector, then there must be a constrained minimum at the interval limit closest to ϕ_0 :

$$\cos(\phi_{\text{con}} - \phi_0) = \begin{cases} 1 & \text{isWithin}(\phi_0; \phi_{\min}, \phi_{\max}) \\ \max\{\cos(\phi_{\min} - \phi_0); \cos(\phi_{\max} - \phi_0)\} & \text{otherwise} \end{cases} \quad (\text{B.58})$$

$$\sin(\theta_{\text{con}}) = \max\{\sin(\theta_{\min}); \min\{\sin(\theta_{\max}); u \cos(\phi_{\text{con}} - \phi_0)\}\} \quad (\text{B.59})$$

Finally, if the following inequality holds true, it follows that the currently selected diffraction order \mathbf{j} is a propagating wave for at least some of the given incidence angles:

$$u^2 - 2u \cos(\phi_{\text{con}} - \phi_0) \sin(\theta_{\text{con}}) + \sin^2(\theta_{\text{con}}) \leq 1 \quad (\text{B.60})$$

This inequality further suggests that only those diffraction orders need to be tested that lie within the circle $u \leq 2$, or within the more practical rectangle $|j_{1,2}| \leq 2na_{1,2}/\lambda$.

Wavelength dependency Equation (B.51) can also be solved for the wavelength $\lambda(\mathbf{j}, \theta, \phi)$

$$\frac{\lambda}{n} \leq \sin(2\Delta) \frac{\cos(\phi - \psi - \Sigma) \sin(\theta) + \sqrt{1 - \sin^2(\phi - \psi - \Sigma) \sin^2(\theta)}}{\sqrt{\left(\frac{j_1}{a_1}\right)^2 + \left(\frac{j_2}{a_2}\right)^2 - 2\frac{j_1 j_2}{a_1 a_2} \cos(2\Delta)}} \quad (\text{B.61})$$

where the secondary solution of the initial quadratic equation never takes effect and can thus be ignored. Note that for strong dispersion ($|\partial_{\lambda} n| \gg 0$), this inequality must be solved numerically for λ . For the special case of a square array ($a_1 = a_2 = a$, $\phi_1 = 0$, $\phi_2 = \frac{\pi}{2}$) it is found that

$$\frac{\lambda}{n} \leq a \frac{\cos(\phi - \psi') \sin(\theta) + \sqrt{1 - \sin^2(\phi - \psi') \sin^2(\theta)}}{\sqrt{j_1^2 + j_2^2}} \quad \psi' = \arctan\left(\frac{j_2 - j_1}{j_2 + j_1}\right) + \frac{\pi}{4} \quad (\text{B.62})$$

and if $\phi = \psi'$ is aligned with the j_1 -axis ($j_2 = 0, \psi' = 0$) or j_2 -axis ($j_1 = 0, \psi' = \frac{\pi}{2}$), this reduces to

$$\frac{\lambda}{n} \leq a \frac{\sin(\theta) + 1}{|j_{1,2}|} \quad (\text{B.63})$$

where $j_{1,2}$ is the diffraction order along the j_1 or j_2 axis.

Visualization To visualize the region that contains all propagating diffraction orders for the given incidence angle ranges, it is convenient to introduce a new parameterization such that $\mathbf{U}_{\mathbf{j}}^2 = 1$:

$$\mathbf{U}_{\mathbf{j}}(\Psi) = \begin{pmatrix} \cos(\Psi - \Sigma) \\ \sin(\Psi - \Sigma) \end{pmatrix} \quad (\text{B.64})$$

Then, by solving $\mathbf{U}_{\mathbf{j}}$ for \mathbf{j} , all curves can be plotted in the Cartesian plane $\mathbf{j} \in \mathbb{R}^2$:

$$\mathbf{j}(\Psi, \theta, \phi) = \frac{n}{\lambda} \begin{pmatrix} a_1 & 0 \\ 0 & a_2 \end{pmatrix} \cdot \left[\begin{pmatrix} \cos(\Psi - \phi_1) \\ \cos(\Psi - \phi_2) \end{pmatrix} + \sin(\theta) \begin{pmatrix} \cos(\phi - \phi_1) \\ \cos(\phi - \phi_2) \end{pmatrix} \right] \quad (\text{B.65})$$

The first vector in the square brackets represents an ellipse (the mapping of the unit disk into the \mathbf{j} -plane), and the second vector an elliptical annular sector (the mapping of the θ - ϕ -range). One may imagine that the annular sector is stationary while the ellipse is shifted continuously across it. In this picture, the sought-for region is the union of all ellipses. However, it suffices to find the boundary curve of this region. As the boundary of the annular sector is traced out, Ψ must simultaneously be chosen such that the tangential vector of the ellipse is always parallel to that of the annular sector. From the tangential vectors $\partial_{\Psi}\mathbf{j}$, $\partial_{\theta}\mathbf{j}$, $\partial_{\phi}\mathbf{j}$ it is found that $\Psi = \phi$ if ϕ is varying, and that $\Psi = \phi - \frac{\pi}{2}$ if θ is varying. Table B.1 summarizes the parameter combinations that generate the main segments of the boundary curve. As illustrated in Fig. B.1, the interior points can be removed by testing all points of the curve against $\mathbf{U}_{\mathbf{j}}^2 \leq 1 - \epsilon$ for a small ϵ . Note that if n/λ is increased, the spacing of the underlying \mathbf{j} -grid increases uniformly while the shape of the curve remains. This generally means that less diffraction orders can be excited. Hence, the distance of a diffraction order to the curve provides a visual cue to whether the diffraction order will be excited if the wavelength is changed by a small amount.

#	Ψ		θ	ϕ	
	start	end		start	end
1	$\phi_{\min} - 90^\circ$	ϕ_{\min}	θ_{\max}	ϕ_{\min}	
2	ϕ_{\min}	ϕ_{\max}	θ_{\max}	ϕ_{\min}	ϕ_{\max}
3	ϕ_{\max}	$\phi_{\max} + 90^\circ$	θ_{\max}	ϕ_{\max}	
4	$\phi_{\max} + 90^\circ$	$\phi_{\max} + 180^\circ$	θ_{\min}	ϕ_{\max}	
5	$\phi_{\max} + 180^\circ$	$\phi_{\min} + 180^\circ$	θ_{\min}	ϕ_{\max}	ϕ_{\min}
6	$\phi_{\min} + 180^\circ$	$\phi_{\min} + 270^\circ$	θ_{\min}	ϕ_{\min}	

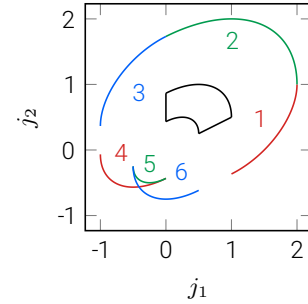


Table B.1 | The parameters of the main segments of the region that contains all propagating diffraction orders. A missing “end”-value indicates that the parameter is held constant. The segments 3/4 and 6/1 are connected by straight lines. The graph illustrates all segments (colored) and the boundary of the θ - ϕ range (black) for an incident wave with $\theta \in [30^\circ, 90^\circ]$, $\phi \in [0^\circ, 90^\circ]$, $n = \lambda = 1$, and a skew lattice with $\phi_1 = 0^\circ$, $\phi_2 = 60^\circ$, $a_1 = a_2 = 1$.

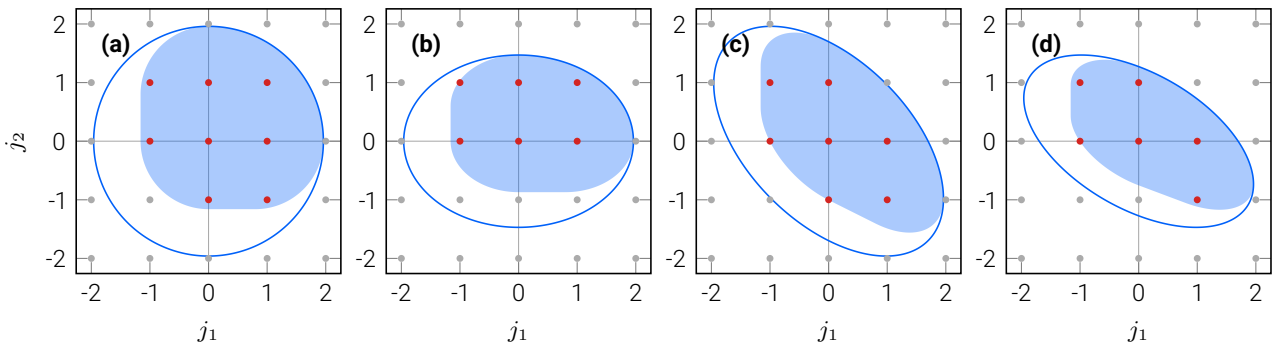


Fig. B.1 | A demonstration of the visualization. (a,b) Rectangular ($\phi_2 = 90^\circ$) and (c,d) hexagonal ($\phi_2 = 120^\circ$) lattices with common parameters $a_1 = 0.8$, $\phi_1 = 0^\circ$, $\theta_{\text{inc}} \in [0^\circ, 90^\circ]$, $\phi_{\text{inc}} \in [0^\circ, 90^\circ]$, $\lambda = 1$, $n = 1.45$, and $n_{\text{inc}} = 1$, except for (a,c) $a_2 = 0.8$ and (b,d) $a_2 = 0.6$. Red and gray dots indicate propagating and evanescent diffraction orders, respectively. Blue areas and ellipses encompass the current set and the largest possible set of excitable diffraction orders, respectively.

B.5. Computation of structure factor and pair correlation function

One major drawback in the numerical computation of the pair correlation function $g(\mathbf{r})$ from the microscopic structure factor $\tilde{S}(\mathbf{k})$ via Eqs. (4.9,10) is that g must be sampled across the entire extent of the bounding box that encloses all particle coordinates \mathbf{R}^N , while the required spatial resolution is typically much smaller than the average pair distance of neighboring particles. This can demand large amounts of memory and often one is not even interested in knowing g at very large pair distances, or equivalently, knowing S with a very fine spectral resolution. In the following, it is explained how g can be computed across a smaller spatial extent by taking into account aliasing effects in \tilde{S} , but unfortunately, this approach turns out to be not very time-efficient.

Given the size $\mathbf{w} \in \mathbb{R}_{>0}^D$ of a D -dimensional window that exactly divides the bounding box into a rectangular grid of $\mathbf{I} \in \mathbb{Z}_{>0}^D$ cells, the set $\mathcal{R}_\mathbf{i}$ of particle coordinates $\mathbf{R}_{\mathbf{i},n}$ that are contained within a cell with multi-index $\mathbf{0} \leq \mathbf{i} \leq \mathbf{I} - \mathbf{1}$ can be written as

$$\mathcal{R}_\mathbf{i} = \{\mathbf{R}_{\mathbf{i},1}, \dots, \mathbf{R}_{\mathbf{i},N_i}\} = \left\{ \mathbf{R}_n \mid \mathbf{i} = \left\lfloor \frac{\mathbf{R}_n}{\mathbf{w}} \right\rfloor \wedge n = 1, \dots, N \right\} \quad \mathcal{R}_{\mathbf{i}+\mathbf{j}\circ\mathbf{I}} = \mathcal{R}_\mathbf{i} \text{ for } \mathbf{j} \in \mathbb{Z} \quad (\text{B.66})$$

where $N_i = |\mathcal{R}_\mathbf{i}|$ is the number of particle coordinates within cell \mathbf{i} , and the rectangular grid must be made \mathbf{I} -periodic since the definitions of g and \tilde{S} are only valid for homogeneous systems. With this, the microscopic particle density $\tilde{\rho}$ from Eq. (4.10) can be written as

$$\tilde{\rho}(\mathbf{k}) = \sum_{\mathbf{i}=\mathbf{0}}^{\mathbf{I}-\mathbf{1}} \tilde{\rho}_\mathbf{i}(\mathbf{k}) e^{-\mathbf{i}\mathbf{k}\cdot[\mathbf{w}\circ\mathbf{i}]} \quad \tilde{\rho}_\mathbf{i}(\mathbf{k}) = \sum_{n=1}^{N_i} e^{-\mathbf{i}\mathbf{k}\cdot[\mathbf{R}_{\mathbf{i},n}-\mathbf{w}\circ\mathbf{i}]} \quad (\text{B.67})$$

where $\tilde{\rho}_\mathbf{i}$ is the microscopic particle density of cell \mathbf{i} . In the following, these expressions are inserted into \tilde{S} from Eq. (4.10), and it is important to note that the amplitude square in the definition of \tilde{S} is equivalent to an autocorrelation of $\tilde{\rho}$. Moreover, from Eq. (4.11) it can be seen that larger pair distances produce higher instantaneous frequencies in \tilde{S} , which means that the largest pair distance $\Delta\mathbf{R}_{\max}$ determines the required spectral resolution $\Delta\mathbf{k}$ due to the Nyquist theorem $\Delta\mathbf{k} \circ \Delta\mathbf{R}_{\max} \leq \pi$. Consequently, the domain of g can be reduced to $-2\mathbf{w} \leq \mathbf{r} \leq 2\mathbf{w}$ if all high-frequency contributions to \tilde{S} that would lead to aliasing are excluded, which can be achieved by considering only the nearest neighborhood of each cell that yields a maximum pair distance of $\Delta\mathbf{R}_{\max} = 2\mathbf{w}$.

More precisely, the number of sample points \mathbf{L} , the actual spatial resolution $\Delta\mathbf{r}$, and the spectral resolution $\Delta\mathbf{k}$ are given by

$$\mathbf{L} = \left\lceil \frac{4\mathbf{w}}{\Delta\mathbf{r}'} \right\rceil \quad \Delta\mathbf{r} = \frac{4\mathbf{w}}{\mathbf{L}} \quad \Delta\mathbf{k} = \frac{2\pi}{4\mathbf{w}} \quad (\text{B.68})$$

where $\Delta\mathbf{r}'$ is the desired spatial resolution. With this, \tilde{S} from Eq. (4.10) can be written as

$$\tilde{S}(\mathbf{k}) = \frac{1}{N} \sum_{\mathbf{i}=\mathbf{0}}^{\mathbf{I}-\mathbf{1}} \tilde{\rho}_\mathbf{i}(\mathbf{k}) \sum_{\mathbf{j}=\mathbf{0}}^{\mathbf{I}-\mathbf{1}} \overline{\tilde{\rho}_\mathbf{j}(\mathbf{k})} e^{-\mathbf{i}\mathbf{k}\cdot[\mathbf{w}\circ(\mathbf{i}-\mathbf{j})]} \quad \text{Exact} \quad (\text{B.69})$$

$$\approx \frac{1}{N} \sum_{\mathbf{i}=\mathbf{0}}^{\mathbf{I}-\mathbf{1}} \tilde{\rho}_\mathbf{i}(\mathbf{k}) \sum_{\mathbf{j}=-\mathbf{1}}^{\mathbf{1}} \overline{\tilde{\rho}_{\mathbf{i}+\mathbf{j}}(\mathbf{k})} e^{\mathbf{i}\mathbf{k}\cdot[\mathbf{w}\circ\mathbf{j}]} \quad \text{Avoid aliasing} \quad (\text{B.70})$$

$$\approx \frac{1}{N} \sum_{\mathbf{i}=\mathbf{0}}^{\mathbf{I}-\mathbf{1}} |\tilde{\rho}_\mathbf{i}(\mathbf{k})|^2 + \frac{1}{N} \sum_{\mathbf{j} \in \square} e^{\mathbf{i}\mathbf{k}\cdot[\mathbf{w}\circ\mathbf{j}]} \sum_{\mathbf{i}=\mathbf{0}}^{\mathbf{I}-\mathbf{1}} \tilde{\rho}_\mathbf{i}(\mathbf{k}) \overline{\tilde{\rho}_{\mathbf{i}+\mathbf{j}}(\mathbf{k})} \quad \text{Separate neighborhood} \quad (\text{B.71})$$

$$\approx \frac{1}{N} \sum_{\mathbf{i}=\mathbf{0}}^{\mathbf{I}-\mathbf{1}} |\tilde{\rho}_\mathbf{i}(\mathbf{k})|^2 + \frac{2}{N} \operatorname{Re} \left[\sum_{\mathbf{j} \in \Delta} e^{\mathbf{i}\mathbf{k}\cdot[\mathbf{w}\circ\mathbf{j}]} \sum_{\mathbf{i}=\mathbf{0}}^{\mathbf{I}-\mathbf{1}} \tilde{\rho}_\mathbf{i}(\mathbf{k}) \overline{\tilde{\rho}_{\mathbf{i}+\mathbf{j}}(\mathbf{k})} \right] \quad \text{Uni-directional pairs} \quad (\text{B.72})$$

where the box set $\square = \{\mathbf{i} \mid -\mathbf{1} \leq \mathbf{i} \leq \mathbf{1} \wedge \mathbf{i} \neq \mathbf{0}\}$ represents the index offsets that point to the nearest neighbors of a cell, and the triangle set Δ is implicitly defined via $\square \setminus \Delta = -\Delta$, where the minus operator negates all set elements $-\Delta = \{-\mathbf{i} \mid \mathbf{i} \in \Delta\}$. Note that in higher dimensions $D > 1$, there are multiple valid choices for the triangle set. For example, in two dimensions, one may choose $\Delta = \{(1, -1), (1, 0), (1, 1), (0, 1)\}$, or $\Delta = \{(1, 0), (1, 1), (0, 1), (-1, 1)\}$, and so on.

A more detailed discussion of each derivation step is in order:

Exact This expression is identical to Eq. (4.10), but its direct evaluation requires the same amount of memory and its time complexity $T_1 = N |\log_{10}(\epsilon)|^D + IL [\log_2 L + I]$ is always higher than the time complexity $T_0 = N |\log_{10}(\epsilon)|^D + IL \frac{1}{4} [\log_2(IL) - 1]$ of Eq. (4.10), where ϵ is the precision of the fast nonuniform Fourier transformation, L is the total number of sample points, and I is the total number of cells.

Avoid aliasing All pair distances that span over more than one adjacent cell are ignored as they would cause aliasing in \tilde{S} . The approximate sign is kept as a reminder for this type of rejection of high-frequency information, which has a similar effect as the convolution of \tilde{S} with a low-pass filter, or the multiplication of g with a box function.

Separate neighborhood In preparation for the next step it is convenient to separate the autocorrelation of a cell from the cross-correlations with its nearest neighbors. In fact, if \mathbf{w} is very large and one is only interested in characterizing a given set of particle coordinates in an approximate sense, all cross-correlations may even be ignored. Then, it suffices to use $L/2$ sample points, and all cells can be processed independently. However, this approximation cannot be used in the collective coordinate method, as it would completely decouple all cells.

Uni-directional pairs In the previous steps, pair distances that start and end in different cells are always evaluated twice. Here, these pair distances are evaluated only once. This not only reduces the computational effort, but also allows for an easier determination of the derivative of \tilde{S} with respect to a given particle coordinate. Note that not all $\tilde{\rho}_i$ need to be held in memory simultaneously, but unfortunately, the time complexity of this expression $T_2 = N |\log_{10}(\epsilon)|^D + IL \left[\log_2 L + 1 + \frac{3^D - 1}{2} \right]$ is unlikely to out-perform T_0 in any real-case scenario, as it would require $I \geq 8 \cdot 4^{3^D} L^3$.

In summary, the direct evaluation of Eq. (4.10) is always the most efficient approach if sufficient memory is available, and for completeness, the derivative of Eq. (B.72) with respect to a given particle coordinate $\mathbf{R}_{i,n}$ can be written as

$$\frac{d\tilde{S}(\mathbf{k})}{d\mathbf{R}_{i,n}} = -\frac{2}{N} \mathbf{k} \operatorname{Im} \left[\left(\tilde{\rho}_i(\mathbf{k}) + \sum_{\mathbf{j} \in \Delta} \tilde{\rho}_{i+\mathbf{j}}(\mathbf{k}) e^{-i\mathbf{k} \cdot [\mathbf{w} \circ \mathbf{j}]} \right) e^{i\mathbf{k} \cdot [\mathbf{R}_{i,n} - \mathbf{w} \circ \mathbf{i}]} \right] \quad (\text{B.73})$$

where intermediate results from Eq. (B.72) could be reused by rearranging the sum over \mathbf{j} .

C. Supplementary Data

In addition to the simulated (Fig. 7.11) and experimental (Fig. 7.12) scatterance for TE polarized excitation, the following figures show the corresponding simulated (Fig. C.1) and experimental (Fig. C.2) scatterance for TM polarized excitation.

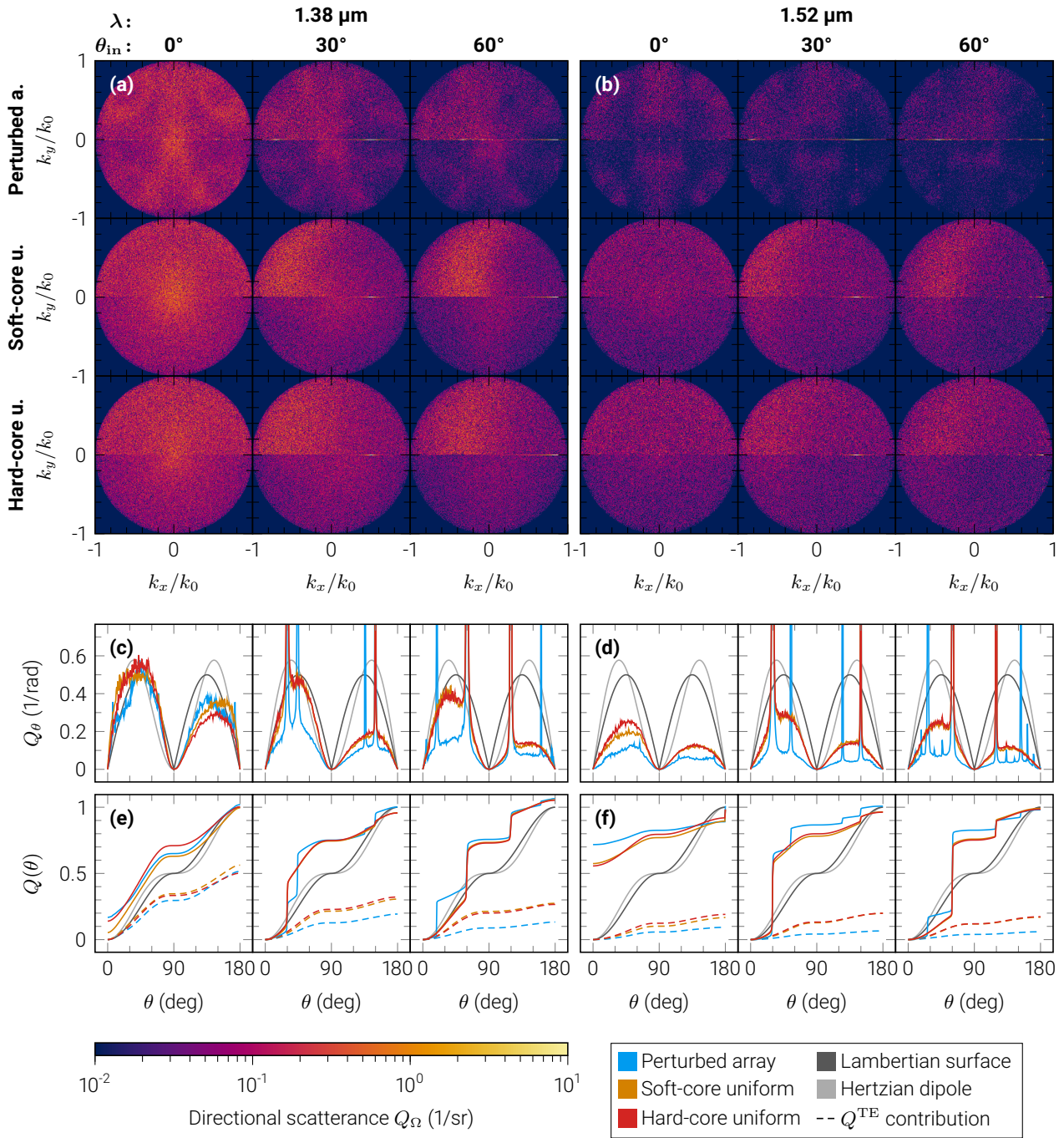


Fig. C.1 | Simulated scattering for TM polarized excitation. The (a,b) directional Q_Ω , (c,d) polar Q_θ and (e,f) sectorial $Q(\theta)$ scattering of the perturbed array, soft-core uniform and hard-core uniform metasurface type for the overlapping resonance case with (a,c,e) resonant ($\lambda = 1.38 \mu\text{m}$) or (b,d,f) off-resonant ($\lambda = 1.52 \mu\text{m}$) excitation by a TM polarized plane wave incident under $\theta_{\text{in}} \in \{0^\circ, 30^\circ, 60^\circ\}$. Column and row titles indicate all parameter combinations. In (a,b), $k_y > 0$ shows transmission and $k_y < 0$ reflection. In (e,f), Q^{TE} shows the contribution of cross-polarized light to $Q = Q^{\text{TE}} + Q^{\text{TM}}$. All wavenumbers are normalized with respect to the magnitude of the wavevector k_0 in silicon dioxide.

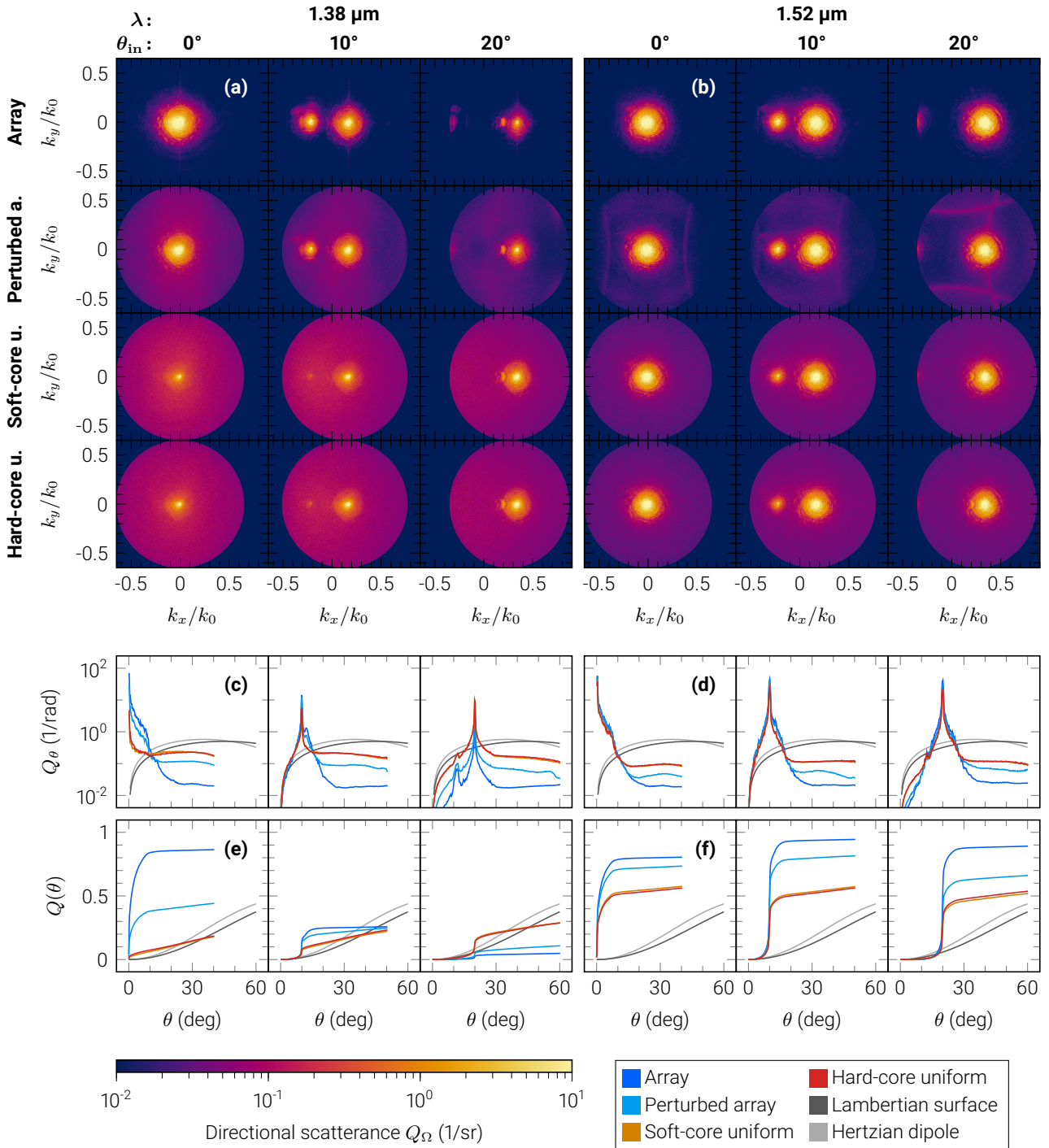


Fig. C.2 | Experimental scatterance for TM polarized excitation. The (a,b) directional Q_Ω , (c,d) polar Q_θ and (e,f) sectorial $Q(\theta)$ scatterance of the array, perturbed array, soft-core uniform and hard-core uniform metasurface type for the overlapping resonance case with (a,c,e) resonant ($\lambda = 1.38 \mu\text{m}$) or (b,d,f) off-resonant ($\lambda = 1.52 \mu\text{m}$) excitation by a TM polarized plane wave incident under $\theta_{\text{in}} \in \{0^\circ, 10^\circ, 20^\circ\}$. All graphs show transmission ($k_z \geq 0, \theta \leq 90^\circ$). Column and row titles indicate all parameter combinations. All wavenumbers are normalized with respect to the magnitude of the wavevector k_0 in air.

List of Publications

Journal articles (presented in this thesis)

- [30] D. Arslan, K. E. Chong, A. E. Miroshnichenko, D.-Y. Choi, D. N. Neshev, T. Pertsch, Y. S. Kivshar, I. Staude, “Angle-selective all-dielectric Huygens’ metasurfaces”, *J. Phys. D: Appl. Phys.* **2017**, *50*, 434002.
- [31] A. Rahimzadegan*, D. Arslan*, R. N. S. Suryadharma, S. Fasold, M. Falkner, T. Pertsch, I. Staude, C. Rockstuhl, “Disorder-induced phase transitions in the transmission of dielectric metasurfaces”, *Phys. Rev. Lett.* **2019**, *122*, 015702.
- [32] D. Arslan*, A. Rahimzadegan*, S. Fasold, M. Falkner, W. Zhou, M. Kroychuk, C. Rockstuhl, T. Pertsch, I. Staude, “Toward perfect optical diffusers: Dielectric Huygens’ metasurfaces with critical positional disorder”, *Adv. Mater.* **2021**, *34*, 2105868.

* Contributed equally.

Journal articles (not presented in this thesis)

1. C. Jin, M. Afsharnia, R. Berlich, S. Fasold, C. Zou, D. Arslan, I. Staude, T. Pertsch, F. Setzpfandt, “Dielectric metasurfaces for distance measurements and three-dimensional imaging”, *Adv. Photonics* **2019**, *1*, 1.
2. A. Rahimzadegan, D. Arslan, D. Dams, A. Groner, X. Garcia-Santiago, R. Alaei, I. Fernandez-Corbaton, T. Pertsch, I. Staude, C. Rockstuhl, “Beyond dipolar Huygens’ metasurfaces for full-phase coverage and unity transmittance”, *Nanophotonics* **2019**, *9*, 75.
3. K. Tanaka, D. Arslan, S. Fasold, M. Steinert, J. Sautter, M. Falkner, T. Pertsch, M. Decker, I. Staude, “Chiral bilayer all-dielectric metasurfaces”, *ACS Nano* **2020**, *14*, 15926.
4. T. Santiago-Cruz, A. Fedotova, V. Sultanov, M. A. Weissflog, D. Arslan, M. Younesi, T. Pertsch, I. Staude, F. Setzpfandt, M. Chekhova, “Photon pairs from resonant metasurfaces”, *Nano Lett.* **2021**, *21*, 4423.
5. N. Abbasirad, A. Barreda, D. Arslan, M. Steinert, S. Fasold, C. Rockstuhl, I. Staude, F. Setzpfandt, T. Pertsch, “Investigation of dipole emission near a dielectric metasurface using a dual-tip scanning near-field optical microscope”, *Nanophotonics* **2021**, *10*, 4511.

Conference presentations

1. D. Arslan, K. E. Chong, D. N. Neshev *et al.*, “Silicon Huygens’ metasurfaces at oblique incidence”, in *CLEO Europe*, Munich, Germany, June **2017** (Talk).
2. D. Arslan, A. Rahimzadegan, S. Fasold *et al.*, “Mie-resonant all-dielectric metasurfaces with tailored positional disorder”, in *DPG Spring Meeting*, Berlin, Germany, Mar. **2018** (Talk).
3. D. Arslan, I. Staude, S. Fasold *et al.*, “Tailoring the optical properties of metasurfaces by deterministic structural disorder”, in *MRS Spring Meeting*, Phoenix, USA, Apr. **2018** (Talk).
4. D. Arslan, S. Fasold, A. Rahimzadegan *et al.*, “Tailored structural disorder in optical metasurfaces”, in *CLEO Pacific Rim*, Hong Kong, China, July **2018** (Invited talk).
5. D. Arslan, A. Rahimzadegan, S. Fasold *et al.*, “Silicon metasurfaces with positional disorder at oblique incidence”, in *DisoMAT*, Potsdam, Germany, Sept. **2019** (Talk).

Bibliography

- [1] J. M. Ziman, “Models of disorder”, Cambridge University Press, **2013**.
- [2] P. Stollmann, “Caught by disorder”, Birkhäuser Boston, **2001**.
- [3] Editorial: “Disordered times”, *Nat. Photonics* **2013**, *7*, 161.
- [4] C. Conti, E. DelRe, “Photonics and the Nobel Prize in physics”, *Nat. Photonics* **2021**, *16*, 6.
- [5] S. Torquato, F. H. Stillinger, “Jammed hard-particle packings: From Kepler to Bernal and beyond”, *Rev. Mod. Phys.* **2010**, *82*, 2633.
- [6] I. Brener, S. Liu, I. Staude, J. Valentine, C. Holloway, “Dielectric metamaterials”, Woodhead Publishing, **2020**.
- [7] N. Muller, J. Haberko, C. Marichy, F. Scheffold, “Silicon hyperuniform disordered photonic materials with a pronounced gap in the shortwave infrared”, *Adv. Opt. Mater.* **2013**, *2*, 115.
- [8] A. F. Koenderink, A. Alù, A. Polman, “Nanophotonics: Shrinking light-based technology”, *Science* **2015**, *348*, 516.
- [9] R. Verre, L. Shao, N. O. Länk, P. Karpinski, A. B. Yankovich, T. J. Antosiewicz, E. Olsson, M. Käll, “Metasurfaces and colloidal suspensions composed of 3D chiral Si nanoresonators”, *Adv. Mater.* **2017**, *29*, 1701352.
- [10] P. M. Piechulla, B. Fuhrmann, E. Slivina, C. Rockstuhl, R. B. Wehrspohn, A. N. Sprafke, “Tailored light scattering through hyperuniform disorder in self-organized arrays of high-index nanodisks”, *Adv. Opt. Mater.* **2021**, 2100186.
- [11] M. Rothhammer, C. Zollfrank, K. Busch, G. Freymann, “Tailored disorder in photonics: Learning from nature”, *Adv. Opt. Mater.* **2021**, *9*, 2100787.
- [12] D. R. Smith, J. B. Pendry, M. C. K. Wiltshire, “Metamaterials and negative refractive index”, *Science* **2004**, *305*, 788.
- [13] A. I. Kuznetsov, A. E. Miroshnichenko, Y. H. Fu, J. Zhang, B. Luk’yanchuk, “Magnetic light”, *Sci. Rep.* **2012**, *2*, 1.
- [14] B. Redding, S. F. Liew, R. Sarma, H. Cao, “Compact spectrometer based on a disordered photonic chip”, *Nat. Photonics* **2013**, *7*, 746.
- [15] H. Chu, Q. Li, B. Liu, J. Luo, S. Sun, Z. H. Hang, L. Zhou, Y. Lai, “A hybrid invisibility cloak based on integration of transparent metasurfaces and zero-index materials”, *Light: Sci. Appl.* **2018**, *7*, 1.
- [16] A. Cordaro, H. Kwon, D. Sounas, A. F. Koenderink, A. Alù, A. Polman, “High-index dielectric metasurfaces performing mathematical operations”, *Nano Lett.* **2019**, *19*, 8418.
- [17] S. Zeng, K. V. Sreekanth, J. Shang, T. Yu, C.-K. Chen, F. Yin, D. Baillargeat, P. Coquet, H.-P. Ho, A. V. Kabashin, K.-T. Yong, “Graphene-gold metasurface architectures for ultrasensitive plasmonic biosensing”, *Adv. Mater.* **2015**, *27*, 6163.
- [18] Z. Fusco, M. Rahmani, R. Bo, R. Verre, N. Motta, M. Käll, D. Neshev, A. Tricoli, “Nanostructured dielectric fractals on resonant plasmonic metasurfaces for selective and sensitive optical sensing of volatile compounds”, *Adv. Mater.* **2018**, *30*, 1800931.
- [19] Y. Fan, N.-H. Shen, F. Zhang, Q. Zhao, H. Wu, Q. Fu, Z. Wei, H. Li, C. M. Soukoulis, “Graphene plasmonics: A platform for 2D optics”, *Adv. Opt. Mater.* **2018**, *7*, 1800537.
- [20] I. Staude, J. Schilling, “Metamaterial-inspired silicon nanophotonics”, *Nat. Photonics* **2017**, *11*, 274.

- [21] M. Decker, I. Staude, “Resonant dielectric nanostructures: A low-loss platform for functional nanophotonics”, *J. Opt.* **2016**, *18*, 103001.
- [22] M. Decker, I. Staude, M. Falkner, J. Dominguez, D. N. Neshev, I. Brener, T. Pertsch, Y. S. Kivshar, “High-efficiency dielectric Huygens’ surfaces”, *Adv. Opt. Mater.* **2015**, *3*, 813.
- [23] K. E. Chong, L. Wang, I. Staude, A. R. James, J. Dominguez, S. Liu, G. S. Subramania, M. Decker, D. N. Neshev, I. Brener, Y. S. Kivshar, “Efficient polarization-insensitive complex wavefront control using Huygens’ metasurfaces based on dielectric resonant meta-atoms”, *ACS Photonics* **2016**, *3*, 514.
- [24] W. Zhao, H. Jiang, B. Liu, J. Song, Y. Jiang, C. Tang, J. Li, “Dielectric Huygens’ metasurface for high-efficiency hologram operating in transmission mode”, *Sci. Rep.* **2016**, *6*, 30613.
- [25] I. M. Vellekoop, A. Lagendijk, A. P. Mosk, “Exploiting disorder for perfect focusing”, *Nat. Photonics* **2010**, *4*, 320.
- [26] H. Yu, K. Lee, J. Park, Y. Park, “Ultrahigh-definition dynamic 3D holographic display by active control of volume speckle fields”, *Nat. Photonics* **2017**, *11*, 186.
- [27] M. Jang, Y. Horie, A. Shibukawa, J. Brake, Y. Liu, S. M. Kamali, A. Arbabi, H. Ruan, A. Faraon, C. Yang, “Wavefront shaping with disorder-engineered metasurfaces”, *Nat. Photonics* **2018**, *12*, 84.
- [28] A. Rahimzadegan, “Multipolar analysis of ordered and disordered metasurfaces”, *PhD thesis*, Karlsruhe Institute of Technology, **2021**.
- [29] T. A. Germer, J. C. Zwinkels, B. K. Tsai, “Theoretical concepts in spectrophotometric measurements”, in *Experimental methods in the physical sciences*, Elsevier, **2014**.
- [30] D. Arslan, K. E. Chong, A. E. Miroshnichenko, D.-Y. Choi, D. N. Neshev, T. Pertsch, Y. S. Kivshar, I. Staude, “Angle-selective all-dielectric Huygens’ metasurfaces”, *J. Phys. D: Appl. Phys.* **2017**, *50*, 434002.
- [31] A. Rahimzadegan, D. Arslan, R. N. S. Suryadharma, S. Fasold, M. Falkner, T. Pertsch, I. Staude, C. Rockstuhl, “Disorder-induced phase transitions in the transmission of dielectric metasurfaces”, *Phys. Rev. Lett.* **2019**, *122*, 015702.
- [32] D. Arslan, A. Rahimzadegan, S. Fasold, M. Falkner, W. Zhou, M. Kroychuk, C. Rockstuhl, T. Pertsch, I. Staude, “Toward perfect optical diffusers: Dielectric Huygens’ metasurfaces with critical positional disorder”, *Adv. Mater.* **2021**, *34*, 2105868.
- [33] A. I. Kuznetsov, A. E. Miroshnichenko, M. L. Brongersma, Y. S. Kivshar, B. Luk’yanchuk, “Optically resonant dielectric nanostructures”, *Science* **2016**, *354*, aag2472.
- [34] C. F. Bohren, D. R. Huffman, “Absorption and scattering of light by small particles”, Wiley, **1998**.
- [35] N. Yu, F. Capasso, “Flat optics with designer metasurfaces”, *Nat. Mater.* **2014**, *13*, 139.
- [36] J. N. Mait, D. W. Prather, N. C. Gallagher, “Subwavelength diffractive optical elements”, in *Holography for the New Millennium*, Springer, **2002**.
- [37] G. Mie, “Beiträge zur Optik trüber Medien, speziell kolloidaler Metallösungen”, *Ann. Phys.* **1908**, *330*, 377.
- [38] W. C. Chew, “Waves and fields in inhomogeneous media”, IEEE Press, **1995**.
- [39] M. I. Mishchenko, L. D. Travis, A. A. Lacis, “Scattering, absorption, and emission of light by small particles”, Cambridge University Press, **2002**.
- [40] B. A. Slovick, Z. G. Yu, S. Krishnamurthy, “Generalized effective-medium theory for metamaterials”, *Phys. Rev. B* **2014**, *89*, 155118.

- [41] A. A. Siraji, Y. Zhao, “Simple effective medium approximation with Rayleigh scattering”, *Opt. Lett.* **2017**, *42*, 1860.
- [42] A. Rahimzadegan, R. Alaee, C. Rockstuhl, R. W. Boyd, “Minimalist Mie coefficient model”, *Opt. Express* **2020**, *28*, 16511.
- [43] R. Alaee, C. Rockstuhl, I. Fernandez-Corbaton, “Exact multipolar decompositions with applications in nanophotonics”, *Adv. Opt. Mater.* **2018**, *7*, 1800783.
- [44] A. Rahimzadegan, D. Arslan, D. Dams, A. Groner, X. Garcia-Santiago, R. Alaee, I. Fernandez-Corbaton, T. Pertsch, I. Staude, C. Rockstuhl, “Beyond dipolar Huygens’ metasurfaces for full-phase coverage and unity transmittance”, *Nanophotonics* **2019**, *9*, 75.
- [45] H.-H. Hsiao, C. H. Chu, D. P. Tsai, “Fundamentals and applications of metasurfaces”, *Small Methods* **2017**, *1*, 1600064.
- [46] Y. F. Yu, A. Y. Zhu, R. Paniagua-Domínguez, Y. H. Fu, B. Luk’yanchuk, A. I. Kuznetsov, “High-transmission dielectric metasurface with 2π phase control at visible wavelengths”, *Laser Photonics Rev.* **2015**, *9*, 412.
- [47] M. I. Shalaev, J. Sun, A. Tsukernik, A. Pandey, K. Nikolskiy, N. M. Litchinitser, “High-efficiency all-dielectric metasurfaces for ultracompact beam manipulation in transmission mode”, *Nano Lett.* **2015**, *15*, 6261.
- [48] M. Principe, M. Consales, A. Micco, A. Crescitelli, G. Castaldi, E. Esposito, V. L. Ferrara, A. Cutolo, V. Galdi, A. Cusano, “Optical fiber meta-tips”, *Light: Sci. Appl.* **2016**, *6*, e16226.
- [49] E. Nazemosadat, M. Mazur, S. Kruk, I. Kravchenko, J. Carpenter, J. Schröder, P. A. Andrekson, M. Karlsson, Y. Kivshar, “Dielectric broadband metasurfaces for fiber mode-multiplexed communications”, *Adv. Opt. Mater.* **2019**, *7*, 1801679.
- [50] M. F. Picardi, A. V. Zayats, F. J. Rodríguez-Fortuño, “Janus and Huygens dipoles: Near-field directionality beyond spin-momentum locking”, *Phys. Rev. Lett.* **2018**, *120*, 117402.
- [51] T. X. Hoang, S. T. Ha, Z. Pan, W. K. Phua, R. Paniagua-Domínguez, C. E. Png, H.-S. Chu, A. I. Kuznetsov, “Collective Mie resonances for directional on-chip nanolasers”, *Nano Lett.* **2020**, *20*, 5655.
- [52] K. Tanaka, D. Arslan, S. Fasold, M. Steinert, J. Sautter, M. Falkner, T. Pertsch, M. Decker, I. Staude, “Chiral bilayer all-dielectric metasurfaces”, *ACS Nano* **2020**, *14*, 15926.
- [53] S. Wen, C. Jin, Y. Yang, “Multilayer Huygens’ metasurface absorber toward snapshot multispectral imaging”, *J. Opt.* **2021**, *23*, 044001.
- [54] C. Gigli, Q. Li, P. Chavel, G. Leo, M. L. Brongersma, P. Lalanne, “Fundamental limitations of Huygens’ metasurfaces for optical beam shaping”, *Laser Photonics Rev.* **2021**, *15*, 2000448.
- [55] J. Courtial, “Wave plates and the Pancharatnam phase”, *Opt. Commun.* **1999**, *171*, 179.
- [56] E. Cohen, H. Larocque, F. Bouchard, F. Nejdassattari, Y. Gefen, E. Karimi, “Geometric phase from Aharonov–Bohm to Pancharatnam–Berry and beyond”, *Nat. Rev. Phys.* **2019**, *1*, 437.
- [57] E. Maguid, I. Yulevich, M. Yannai, V. Kleiner, M. L. Brongersma, E. Hasman, “Multifunctional interleaved geometric-phase dielectric metasurfaces”, *Light: Sci. Appl.* **2017**, *6*, e17027.
- [58] S. A. Maier, “Plasmonics”, Springer, **2007**.
- [59] E. Rahimi, R. Gordon, “Nonlinear plasmonic metasurfaces”, *Adv. Opt. Mater.* **2018**, *6*, 1800274.
- [60] J. Zhang, M. ElKabbash, R. Wei, S. C. Singh, B. Lam, C. Guo, “Plasmonic metasurfaces with 42.3% transmission efficiency in the visible”, *Light: Sci. Appl.* **2019**, *8*, 1.

- [61] E. Karimi, S. A. Schulz, I. D. Leon, H. Qassim, J. Upham, R. W. Boyd, “Generating optical orbital angular momentum at visible wavelengths using a plasmonic metasurface”, *Light: Sci. Appl.* **2014**, *3*, e167.
- [62] Y. Zhang, Z. Li, W. Liu, Z. Li, H. Cheng, S. Chen, J. Tian, “Spin-selective and wavelength-selective demultiplexing based on waveguide-integrated all-dielectric metasurfaces”, *Adv. Opt. Mater.* **2019**, *7*, 1801273.
- [63] Y. Sun, L. Zhang, H. Xia, S. Cao, L. Wang, S. Yang, Y. Wu, R. Tai, “Integrated silicon metasurface polarization beam splitter on a standard SOI substrate”, *Optik* **2021**, *227*, 166096.
- [64] C. Zou, J. Sautter, F. Setzpfandt, I. Staude, “Resonant dielectric metasurfaces: Active tuning and nonlinear effects”, *J. Phys. D: Appl. Phys.* **2019**, *52*, 373002.
- [65] S. Liu, P. P. Vabishchevich, A. Vaskin, J. L. Reno, G. A. Keeler, M. B. Sinclair, I. Staude, I. Brener, “An all-dielectric metasurface as a broadband optical frequency mixer”, *Nat. Commun.* **2018**, *9*, 1.
- [66] J. D. Sautter, L. Xu, A. E. Miroshnichenko, M. Lysevych, I. Volkovskaya, D. A. Smirnova, R. Camacho-Morales, K. Z. Kamali, F. Karouta, K. Vora, H. H. Tan, M. Kauranen, I. Staude, C. Jagadish, D. N. Neshev, M. Rahmani, “Tailoring second-harmonic emission from (111)-GaAs nanoantennas”, *Nano Lett.* **2019**, *19*, 3905.
- [67] A. Fedotova, M. Younesi, J. Sautter, A. Vaskin, F. J. F. Löchner, M. Steinert, R. Geiss, T. Pertsch, I. Staude, F. Setzpfandt, “Second-harmonic generation in resonant nonlinear metasurfaces based on lithium niobate”, *Nano Lett.* **2020**, *20*, 8608.
- [68] A. Vaskin, J. Bohn, K. E. Chong, T. Bucher, M. Zilk, D.-Y. Choi, D. N. Neshev, Y. S. Kivshar, T. Pertsch, I. Staude, “Directional and spectral shaping of light emission with Mie-resonant silicon nanoantenna arrays”, *ACS Photonics* **2018**, *5*, 1359.
- [69] A. Vaskin, S. Mashhadi, M. Steinert, K. E. Chong, D. Keene, S. Nanz, A. Abass, E. Rusak, D.-Y. Choi, I. Fernandez-Corbaton, T. Pertsch, C. Rockstuhl, M. A. Noginov, Y. S. Kivshar, D. N. Neshev, N. Noginova, I. Staude, “Manipulation of magnetic dipole emission from Eu^{3+} with Mie-resonant dielectric metasurfaces”, *Nano Lett.* **2019**, *19*, 1015.
- [70] T. Bucher, A. Vaskin, R. Mupparapu, F. J. F. Löchner, A. George, K. E. Chong, S. Fasold, C. Neumann, D.-Y. Choi, F. Eilenberger, F. Setzpfandt, Y. S. Kivshar, T. Pertsch, A. Turchanin, I. Staude, “Tailoring photoluminescence from MoS_2 monolayers by Mie-resonant metasurfaces”, *ACS Photonics* **2019**, *6*, 1002.
- [71] A. Vaskin, R. Kolkowski, A. F. Koenderink, I. Staude, “Light-emitting metasurfaces”, *Nanophotonics* **2019**, *8*, 1151.
- [72] J. Sautter, I. Staude, M. Decker, E. Rusak, D. N. Neshev, I. Brener, Y. S. Kivshar, “Active tuning of all-dielectric metasurfaces”, *ACS Nano* **2015**, *9*, 4308.
- [73] M. R. Shcherbakov, S. Liu, V. V. Zubyuk, A. Vaskin, P. P. Vabishchevich, G. Keeler, T. Pertsch, T. V. Dolgova, I. Staude, I. Brener, A. A. Fedyanin, “Ultrafast all-optical tuning of direct-gap semiconductor metasurfaces”, *Nat. Commun.* **2017**, *8*, 1.
- [74] J. Bohn, T. Bucher, K. E. Chong, A. Komar, D.-Y. Choi, D. N. Neshev, Y. S. Kivshar, T. Pertsch, I. Staude, “Active tuning of spontaneous emission by Mie-resonant dielectric metasurfaces”, *Nano Lett.* **2018**, *18*, 3461.
- [75] C. Zou, C. Amaya, S. Fasold, A. A. Muravsky, A. A. Murauski, T. Pertsch, I. Staude, “Multiresponsive dielectric metasurfaces”, *ACS Photonics* **2021**, *8*, 1775.
- [76] S. M. Kamali, E. Arbabi, A. Arbabi, A. Faraon, “A review of dielectric optical metasurfaces for wavefront control”, *Nanophotonics* **2018**, *7*, 1041.

- [77] W. T. Chen, A. Y. Zhu, F. Capasso, “Flat optics with dispersion-engineered metasurfaces”, *Nat. Rev. Mater.* **2020**, *5*, 604.
- [78] A. H. Dorrah, F. Capasso, “Tunable structured light with flat optics”, *Science* **2022**, *376*, 6591.
- [79] A. Rahimzadegan, T. D. Karamanos, R. Alaei, A. G. Lamprianidis, D. Beutel, R. W. Boyd, C. Rockstuhl, “A comprehensive multipolar theory for periodic metasurfaces”, *Adv. Opt. Mater.* **2022**, *10*, 2102059.
- [80] K. E. Chong, I. Staude, A. James, J. Dominguez, S. Liu, S. Campione, G. S. Subramania, T. S. Luk, M. Decker, D. N. Neshev, I. Brener, Y. S. Kivshar, “Polarization-independent silicon metadevices for efficient optical wavefront control”, *Nano Lett.* **2015**, *15*, 5369.
- [81] V. I. Zakomirnyi, S. V. Karpov, H. Ågren, I. L. Rasskazov, “Collective lattice resonances in disordered and quasi-random all-dielectric metasurfaces”, *J. Opt. Soc. Am. B* **2019**, *36*, E21.
- [82] F. Zhang, F. Tang, X. Xu, P.-M. Adam, J. Martin, J. Plain, “Influence of order-to-disorder transitions on the optical properties of the aluminum plasmonic metasurface”, *Nanoscale* **2020**, *12*, 23173.
- [83] H. Cao, Y. Eliezer, “Harnessing disorder for photonic device applications”, *Appl. Phys. Rev.* **2022**, *9*, 011309.
- [84] E. Maguid, M. Yannai, A. Faerman, I. Yulevich, V. Kleiner, E. Hasman, “Disorder-induced optical transition from spin Hall to random Rashba effect”, *Science* **2017**, *358*, 1411.
- [85] M. A. Klatt, J. Kim, S. Torquato, “Cloaking the underlying long-range order of randomly perturbed lattices”, *Phys. Rev. E* **2020**, *101*, 032118.
- [86] S. Yu, C.-W. Qiu, Y. Chong, S. Torquato, N. Park, “Engineered disorder in photonics”, *Nat. Rev. Mater.* **2020**, *6*, 226.
- [87] M. Xu, Q. He, M. Pu, F. Zhang, L. Li, D. Sang, Y. Guo, R. Zhang, X. Li, X. Ma, X. Luo, “Emerging long-range order from a freeform disordered metasurface”, *Adv. Mater.* **2022**, *34*, 2108709.
- [88] C. Helgert, C. Rockstuhl, C. Etrich, E.-B. Kley, A. Tünnermann, F. Lederer, T. Pertsch, “Effects of anisotropic disorder in an optical metamaterial”, *Appl. Phys. A* **2010**, *103*, 591.
- [89] S. S. Kruk, C. Helgert, M. Decker, I. Staude, C. Menzel, C. Etrich, C. Rockstuhl, C. Jagadish, T. Pertsch, D. N. Neshev, Y. S. Kivshar, “Optical metamaterials with quasicrystalline symmetry: Symmetry-induced optical isotropy”, *Phys. Rev. B* **2013**, *88*, 20.
- [90] M. Albooyeh, S. Kruk, C. Menzel, C. Helgert, M. Kroll, A. Krysinski, M. Decker, D. N. Neshev, T. Pertsch, C. Etrich, C. Rockstuhl, S. A. Tretyakov, C. R. Simovski, Y. S. Kivshar, “Resonant metasurfaces at oblique incidence: Interplay of order and disorder”, *Sci. Rep.* **2014**, *4*, 4484.
- [91] S. Torquato, “Hyperuniform states of matter”, *Phys. Rep.* **2018**, *745*, 1.
- [92] M. Castro-Lopez, M. Gaio, S. Sellers, G. Gkantzounis, M. Florescu, R. Sapienza, “Reciprocal space engineering with hyperuniform gold disordered surfaces”, *APL Photonics* **2017**, *2*, 061302.
- [93] H. Bertin, Y. Brûlé, G. Magno, T. Lopez, P. Gogol, L. Pradere, B. Gralak, D. Barat, G. Demésy, B. Dagens, “Correlated disordered plasmonic nanostructures arrays for augmented reality”, *ACS Photonics* **2018**, *5*, 2661.
- [94] F. Sterl, E. Herkert, S. Both, T. Weiss, H. Giessen, “Shaping the color and angular appearance of plasmonic metasurfaces with tailored disorder”, *ACS Nano* **2021**, *15*, 10318.
- [95] P. M. Piechulla, E. Slivina, D. Bätzner, I. Fernandez-Corbaton, P. Dhawan, R. B. Wehrspohn, A. N. Sprafke, C. Rockstuhl, “Antireflective Huygens’ metasurface with correlated disorder made from high-index disks implemented into silicon heterojunction solar cells”, *ACS Photonics* **2021**, *8*, 3476.

- [96] D. Veksler, E. Maguid, N. Shitrit, D. Ozeri, V. Kleiner, E. Hasman, “Multiple wavefront shaping by metasurface based on mixed random antenna groups”, *ACS Photonics* **2015**, *2*, 661.
- [97] M. Yannai, E. Maguid, A. Faerman, Q. Li, J.-H. Song, V. Kleiner, M. L. Brongersma, E. Hasman, “Order and disorder embedded in a spectrally interleaved metasurface”, *ACS Photonics* **2018**, *5*, 4764.
- [98] M. Haghtalab, M. Tamagnone, A. Y. Zhu, S. Safavi-Naeini, F. Capasso, “Ultrahigh angular selectivity of disorder-engineered metasurfaces”, *ACS Photonics* **2020**, *7*, 991.
- [99] H. Chu, X. Xiong, Y.-J. Gao, J. Luo, H. Jing, C.-Y. Li, R. Peng, M. Wang, Y. Lai, “Diffuse reflection and reciprocity-protected transmission via a random-flip metasurface”, *Sci. Adv.* **2021**, *7*, 37.
- [100] A. Pors, F. Ding, Y. Chen, I. P. Radko, S. I. Bozhevolnyi, “Random-phase metasurfaces at optical wavelengths”, *Sci. Rep.* **2016**, *6*, 28448.
- [101] S. Fasold, S. Linß, T. Kawde, M. Falkner, M. Decker, T. Pertsch, I. Staude, “Disorder-enabled pure chirality in bilayer plasmonic metasurfaces”, *ACS Photonics* **2018**, *5*, 1773.
- [102] R. H. Siddique, J. Mertens, H. Hölscher, S. Vignolini, “Scalable and controlled self-assembly of aluminum-based random plasmonic metasurfaces”, *Light: Sci. Appl.* **2017**, *6*, e17015.
- [103] A. K. González-Alcalde, A. Reyes-Coronado, “Large angle-independent structural colors based on all-dielectric random metasurfaces”, *Opt. Commun.* **2020**, *475*, 126289.
- [104] K. Lee, J. Lee, E. Kim, J.-I. Lee, D.-H. Cho, J. T. Lim, C. W. Joo, J. Y. Kim, S. Yoo, B.-K. Ju, J. Moon, “Simultaneously enhanced device efficiency, stabilized chromaticity of organic light emitting diodes with lambertian emission characteristic by random convex lenses”, *Nanotechnology* **2016**, *27*, 075202.
- [105] M. Dupré, L. Hsu, B. Kanté, “On the design of random metasurface based devices”, *Sci. Rep.* **2018**, *8*, 1.
- [106] M. Odeh, M. Dupré, K. Kim, B. Kanté, “Optical response of jammed rectangular nanostructures”, *Nanophotonics* **2020**, *10*, 705.
- [107] K. Vynck, M. Burrese, F. Riboli, D. S. Wiersma, “Photon management in two-dimensional disordered media”, *Nat. Mater.* **2012**.
- [108] G. M. Conley, M. Burrese, F. Pratesi, K. Vynck, D. S. Wiersma, “Light transport and localization in two-dimensional correlated disorder”, *Phys. Rev. Lett.* **2014**, *112*, 14.
- [109] L. S. Froufe-Pérez, M. Engel, P. F. Damasceno, N. Muller, J. Haberko, S. C. Glotzer, F. Scheffold, “Role of short-range order and hyperuniformity in the formation of band gaps in disordered photonic materials”, *Phys. Rev. Lett.* **2016**, *117*, 053902.
- [110] L. S. Froufe-Pérez, M. Engel, J. J. Sáenz, F. Scheffold, “Band gap formation and Anderson localization in disordered photonic materials with structural correlations”, *Proc. Natl. Acad. Sci.* **2017**, *114*, 9570.
- [111] A. Egel, U. Lemmer, “Dipole emission in stratified media with multiple spherical scatterers: Enhanced outcoupling from OLEDs”, *J. Quant. Spectrosc. Radiat. Transf.* **2014**, *148*, 165.
- [112] Y. Y. Kim, J. J. Park, S. J. Ye, W. J. Hyun, H.-G. Im, B.-S. Bae, O. O. Park, “Novel microlens arrays with embedded Al₂O₃ nanoparticles for enhancing efficiency and stability of flexible polymer light-emitting diodes”, *RSC Adv.* **2016**, *6*, 65450.
- [113] J. Bertolotti, E. G. Putten, C. Blum, A. Lagendijk, W. L. Vos, A. P. Mosk, “Non-invasive imaging through opaque scattering layers”, *Nature* **2012**, *491*, 232.
- [114] H. Yilmaz, E. G. Putten, J. Bertolotti, A. Lagendijk, W. L. Vos, A. P. Mosk, “Speckle correlation resolution enhancement of wide-field fluorescence imaging”, *Optica* **2015**, *2*, 424.

- [115] M. A. Golub, A. Averbuch, M. Nathan, V. A. Zheludev, J. Hauser, S. Gurevitch, R. Malinsky, A. Kagan, “Compressed sensing snapshot spectral imaging by a regular digital camera with an added optical diffuser”, *Appl. Opt.* **2016**, *55*, 432.
- [116] G. Kim, “A PMMA composite as an optical diffuser in a liquid crystal display backlighting unit (BLU)”, *Eur. Polym. J.* **2005**, *41*, 1729.
- [117] R. A. Hoover, R. G. Hoover, “Light diffuser for optical microscopes replacing condenser with opal glass to produce near-Koehler illumination”, *U.S. pat.* US6963445B2, **2003**.
- [118] N. Antipa, G. Kuo, R. Heckel, B. Mildenhall, E. Bostan, R. Ng, L. Waller, “DiffuserCam: Lensless single-exposure 3D imaging”, *Optica* **2018**, *5*, 1.
- [119] L. Lu, J. Sun, J. Zhang, Y. Fan, Q. Chen, C. Zuo, “Quantitative phase imaging camera with a weak diffuser”, *Front. Phys.* **2019**, *7*, 77.
- [120] P. Song, S. Jiang, H. Zhang, Z. Bian, C. Guo, K. Hoshino, G. Zheng, “Super-resolution microscopy via ptychographic structured modulation of a diffuser”, *Opt. Lett.* **2019**, *44*, 3645.
- [121] Z. Cai, J. Chen, G. Pedrini, W. Osten, X. Liu, X. Peng, “Lensless light-field imaging through diffuser encoding”, *Light: Sci. Appl.* **2020**, *9*, 143.
- [122] W. Yang, S. Xiao, Q. Song, Y. Liu, Y. Wu, S. Wang, J. Yu, J. Han, D.-P. Tsai, “All-dielectric metasurface for high-performance structural color”, *Nat. Commun.* **2020**, *11*, 1864.
- [123] R. Zhao, L. Huang, Y. Wang, “Recent advances in multi-dimensional metasurfaces holographic technologies”, *Photonix* **2020**, *1*, 1.
- [124] R. French, S. Gigan, O. L. Muskens, “Speckle-based hyperspectral imaging combining multiple scattering and compressive sensing in nanowire mats”, *Opt. Lett.* **2017**, *42*, 1820.
- [125] S. K. Sahoo, D. Tang, C. Dang, “Single-shot multispectral imaging with a monochromatic camera”, *Optica* **2017**, *4*, 1209.
- [126] K. Monakhova, K. Yanny, N. Aggarwal, L. Waller, “Spectral DiffuserCam: Lensless snapshot hyperspectral imaging with a spectral filter array”, *Optica* **2020**, *7*, 1298.
- [127] Z. Fang, H. Zhu, Y. Yuan, D. Ha, S. Zhu, C. Preston, Q. Chen, Y. Li, X. Han, S. Lee, G. Chen, T. Li, J. Munday, J. Huang, L. Hu, “Novel nanostructured paper with ultrahigh transparency and ultrahigh haze for solar cells”, *Nano Lett.* **2014**, *14*, 765.
- [128] T. G. Deepak, G. S. Anjusree, S. Thomas, T. A. Arun, S. V. Nair, A. S. Nair, “A review on materials for light scattering in dye-sensitized solar cells”, *RSC Adv.* **2014**, *4*, 17615.
- [129] W. Wu, N. G. Tassi, H. Zhu, Z. Fang, L. Hu, “Nanocellulose-based translucent diffuser for optoelectronic device applications with dramatic improvement of light coupling”, *ACS Appl. Mater. Interfaces* **2015**, *7*, 26860.
- [130] A. P. Mosk, A. Lagendijk, G. Lerosey, M. Fink, “Controlling waves in space and time for imaging and focusing in complex media”, *Nat. Photonics* **2012**, *6*, 283.
- [131] R. Schittny, A. Niemeyer, F. Mayer, A. Naber, M. Kadic, M. Wegener, “Invisibility cloaking in light-scattering media”, *Laser Photonics Rev.* **2016**, *10*, 382.
- [132] H. Butt, A. K. Yetisen, A. A. Khan, K. M. Knowles, M. M. Qasim, S. H. Yun, T. D. Wilkinson, “Electrically tunable scattering from devitrite-liquid crystal hybrid devices”, *Adv. Opt. Mater.* **2016**, *5*, 1600414.
- [133] W. Smith, “Modern optical engineering: The design of optical systems”, McGraw-Hill, **2007**.
- [134] M. D. Fairchild, “Color appearance models”, Wiley, **2013**.
- [135] P. Genevet, F. Capasso, F. Aieta, M. Khorasaninejad, R. Devlin, “Recent advances in planar optics: From plasmonic to dielectric metasurfaces”, *Optica* **2017**, *4*, 139.

- [136] P. Lalanne, P. Chavel, “Metalenses at visible wavelengths: Past, present, perspectives”, *Laser Photonics Rev.* **2017**, *11*, 1600295.
- [137] W. T. Chen, F. Capasso, “Will flat optics appear in everyday life anytime soon?”, *Appl. Phys. Lett.* **2021**, *118*, 100503.
- [138] A. Colombo, F. Tassone, F. Santolini, N. Contiello, A. Gambirasio, R. Simonutti, “Nanoparticle-doped large area PMMA plates with controlled optical diffusion”, *J. Mater. Chem. C: Mater. Opt. Electron. Devices* **2013**, *1*, 2927.
- [139] S. M. Mahpeykar, Y. Zhao, X. Li, Z. Yang, Q. Xu, Z.-H. Lu, E. H. Sargent, X. Wang, “Cellulose nanocrystal: Polymer hybrid optical diffusers for index-matching-free light management in optoelectronic devices”, *Adv. Opt. Mater.* **2017**, *5*, 1700430.
- [140] M. S. Toivonen, O. D. Onelli, G. Jacucci, V. Lovikka, O. J. Rojas, O. Ikkala, S. Vignolini, “Anomalous-diffusion-assisted brightness in white cellulose nanofibril membranes”, *Adv. Mater.* **2018**, *30*, 1704050.
- [141] S.-I. Chang, J.-B. Yoon, H. Kim, J.-J. Kim, B.-K. Lee, D. H. Shin, “Microlens array diffuser for a light-emitting diode backlight system”, *Opt. Lett.* **2006**, *31*, 3016.
- [142] T. Ohzono, K. Suzuki, T. Yamaguchi, N. Fukuda, “Tunable optical diffuser based on deformable wrinkles”, *Adv. Opt. Mater.* **2013**, *1*, 374.
- [143] S. M. Mahpeykar, Q. Xiong, J. Wei, L. Meng, B. K. Russell, P. Hermansen, A. V. Singhal, X. Wang, “Stretchable hexagonal diffraction gratings as optical diffusers for in situ tunable broadband photon management”, *Adv. Opt. Mater.* **2016**, *4*, 1106.
- [144] T. Alqurashi, H. Butt, “Highly flexible, stretchable, and tunable optical diffusers with mechanically switchable wettability surfaces”, *ACS Cent. Sci.* **2019**, *5*, 1002.
- [145] F. Lin, L. Zhu, S. Yang, “Effective optical diffuser based on interfacial hydrogen-bonding polymer complexation”, *ACS Appl. Polym. Mater.* **2020**, *2*, 3805.
- [146] R. Pawluczyk, “Holographic diffusers”, in *Photopolymers and Applications in Holography, Optical Data Storage, Optical Sensors, and Interconnects*, Jan. **1994**.
- [147] S. Wadle, D. Wuest, J. Cantalupo, R. S. Lakes, “Holographic diffusers”, *Opt. Eng.* **1994**, *33*, 213.
- [148] C. Gu, J. Hong, J.-R. Lien, F. Dai, “Diffraction properties of volume holographic diffusers”, *J. Opt. Soc. Am. A* **1996**, *13*, 1704.
- [149] S. I. Kim, Y. S. Choi, Y. N. Ham, C. Y. Park, J. M. Kim, “Holographic diffuser by use of a silver halide sensitized gelatin process”, *Appl. Opt.* **2003**, *42*, 2482.
- [150] G. Savant, T. Jansson, J. Jansson, “Diffuser display screen”, in *Holography for the New Millennium*, Springer, **2002**.
- [151] D. Yap, H. Sharifi, D. F. Weston, R. D. Rajavel, “Wavelength selective optical diffuser”, *U.S. pat.* US9709711B1, **2013**.
- [152] M.-L. Piao, K.-C. Kwon, H.-J. Kang, K.-Y. Lee, N. Kim, “Full-color holographic diffuser using time-scheduled iterative exposure”, *Appl. Opt.* **2015**, *54*, 5252.
- [153] D. S. Wiersma, “Disordered photonics”, *Nat. Photonics* **2013**, *7*, 188.
- [154] G. Osnabrugge, R. Horstmeyer, I. N. Papadopoulos, B. Judkewitz, I. M. Vellekoop, “Generalized optical memory effect”, *Optica* **2017**, *4*, 886.
- [155] A. P. Ravishankar, M. A. J. Tilburg, F. Vennberg, D. Visser, S. Anand, “Color generation from self-organized metallo-dielectric nanopillar arrays”, *Nanophotonics* **2019**, *8*, 1771.
- [156] J. A. Mignaco, “Electromagnetic duality, charges, monopoles, topology, ...” *Braz. J. Phys.* **2001**, *31*, 2.

- [157] I. Fernandez-Corbaton, “Helicity and duality symmetry in light matter interactions: Theory and applications”, *PhD thesis*, Macquarie University, **2014**.
- [158] A. Rahimzadegan, M. Fruhnert, R. Alaei, I. Fernandez-Corbaton, C. Rockstuhl, “Optical force and torque on dipolar dual chiral particles”, *Phys. Rev. B* **2016**, *94*, 125123.
- [159] P. Hariharan, “Optical holography”, Cambridge University Press, **2004**.
- [160] P. Hariharan, “Basics of holography”, Cambridge University Press, **2011**.
- [161] D. Gabor, “A new microscopic principle”, *Nature* **1948**, *161*, 777.
- [162] D. Gabor, “Microscopy by reconstructed wave-fronts”, *Proc. R. Soc. Lond. A* **1949**, *197*, 454.
- [163] D. Gabor, “Microscopy by reconstructed wave fronts: II”, *Proc. Phys. Soc. B* **1951**, *64*, 449.
- [164] O. Bryngdahl, F. Wyrowski, “I Digital holography – Computer-generated holograms”, in *Progress in Optics*, Elsevier, **1990**.
- [165] “Holography for the new millennium”, Springer, **2002**.
- [166] U. Schnars, C. Falldorf, J. Watson, W. Jüptner, “Digital holography and wavefront sensing”, Springer, **2014**.
- [167] B. Walther, C. Helgert, C. Rockstuhl, F. Setzpfandt, F. Eilenberger, E.-B. Kley, F. Lederer, A. Tünnermann, T. Pertsch, “Spatial and spectral light shaping with metamaterials”, *Adv. Mater.* **2012**, *24*, 6300.
- [168] Q. Wei, L. Huang, T. Zentgraf, Y. Wang, “Optical wavefront shaping based on functional metasurfaces”, *Nanophotonics* **2020**, *9*, 987.
- [169] E. G. Putten, I. M. Vellekoop, A. P. Mosk, “Spatial amplitude and phase modulation using commercial twisted nematic LCDs”, *Appl. Opt.* **2008**, *47*, 2076.
- [170] L. Zhu, J. Wang, “Arbitrary manipulation of spatial amplitude and phase using phase-only spatial light modulators”, *Sci. Rep.* **2014**, *4*, 1.
- [171] E. Otte, C. Schlickriede, C. Alpmann, C. Denz, “Complex light fields enter a new dimension: Holographic modulation of polarization in addition to amplitude and phase”, in *Complex Light and Optical Forces IX*, Mar. **2015**.
- [172] L. Huang, S. Zhang, T. Zentgraf, “Metasurface holography: From fundamentals to applications”, *Nanophotonics* **2018**, *7*, 1169.
- [173] B. E. A. Saleh, M. C. Teich, “Fundamentals of photonics”, Wiley, **2007**.
- [174] M. Frigo, S. G. Johnson, “The design and implementation of FFTW3”, *Proc. IEEE* **2005**, *93*, 216.
- [175] A. H. Barnett, J. Magland, L. Klinteberg, “A parallel nonuniform fast Fourier transform library based on an "exponential of semicircle" kernel”, *SIAM J. Sci. Comput.* **2019**, *41*, C479.
- [176] M. Born, E. Wolf, “Principles of optics”, Cambridge University Press, **2002**.
- [177] P. M. Morse, H. Feshbach, “Methods of theoretical physics, Part I”, McGraw-Hill, **1953**.
- [178] P. M. Morse, H. Feshbach, “Methods of theoretical physics, Part II”, McGraw-Hill, **1953**.
- [179] A. Sard, “The measure of the critical values of differentiable maps”, *Bull. Am. Math. Soc.* **1942**, *48*, 883.
- [180] J.-P. Hansen, I. R. McDonald, “Theory of simple liquids”, Elsevier, **2006**.
- [181] O. U. Uche, F. H. Stillinger, S. Torquato, “Constraints on collective density variables: Two dimensions”, *Phys. Rev. E* **2004**, *70*, 046122.
- [182] O. U. Uche, S. Torquato, F. H. Stillinger, “Collective coordinate control of density distributions”, *Phys. Rev. E* **2006**, *74*, 031104.

- [183] G. Zhang, S. Torquato, “Realizable hyperuniform and nonhyperuniform particle configurations with targeted spectral functions via effective pair interactions”, *Phys. Rev. E* **2020**, *101*, 032124.
- [184] R. Fletcher, “A new approach to variable metric algorithms”, *Comput. J.* **1970**, *13*, 317.
- [185] C. G. Broyden, “The convergence of a class of double-rank minimization algorithms 1. General considerations”, *IMA J. Appl. Math.* **1970**, *6*, 76.
- [186] D. Goldfarb, “A family of variable-metric methods derived by variational means”, *Math. Comput.* **1970**, *24*, 23.
- [187] D. F. Shanno, “Conditioning of quasi-Newton methods for function minimization”, *Math. Comput.* **1970**, *24*, 647.
- [188] J. Møller, M. L. Huber, R. L. Wolpert, “Perfect simulation and moment properties for the Matérn type III process”, *Stoch. Process. their Appl.* **2010**, *120*, 2142.
- [189] J. Teichmann, F. Ballani, K. G. Boogaart, “Generalizations of Matérn’s hard-core point processes”, *Spat. Stat.* **2013**, *3*, 33.
- [190] U. S. Inan, R. A. Marshall, “Numerical electromagnetics”, Cambridge University Press, **2011**.
- [191] P. Monk, “Finite element methods for Maxwell’s equations”, Oxford University Press, **2003**.
- [192] M. G. Larson, F. Bengzon, “The finite element method: Theory, implementation, and applications”, Springer, **2013**.
- [193] G. Demésy, J.-C. Auger, B. Stout, “Scattering matrix of arbitrarily shaped objects: Combining finite elements and vector partial waves”, *J. Opt. Soc. Am. A* **2018**, *35*, 1401.
- [194] S. Stein, “Addition theorems for spherical wave functions”, *Q. Appl. Math.* **1961**, *19*, 15.
- [195] Y.-l. Xu, “Electromagnetic scattering by an aggregate of spheres”, *Appl. Opt.* **1995**, *34*, 4573.
- [196] K. Matsushima, T. Shimobaba, “Band-limited angular spectrum method for numerical simulation of free-space propagation in far and near fields”, *Opt. Express* **2009**, *17*, 19662.
- [197] X. Yu, T. Xiahui, Q. Yingxiong, P. Hao, W. Wei, “Band-limited angular spectrum numerical propagation method with selective scaling of observation window size and sample number”, *J. Opt. Soc. Am. A* **2012**, *29*, 2415.
- [198] R. W. Gerchberg, W. O. Saxton, “A practical algorithm for the determination of the phase from image and diffraction plane pictures”, *Optik* **1972**, *35*, 237.
- [199] J. R. Fienup, “Phase retrieval algorithms: A comparison”, *Appl. Opt.* **1982**, *21*, 2758.
- [200] V. Kettunen, “Review of iterative Fourier-transform algorithms for beam shaping applications”, *Opt. Eng.* **2004**, *43*, 2549.
- [201] J. R. Fienup, “Phase retrieval algorithms: A personal tour [invited]”, *Appl. Opt.* **2012**, *52*, 45.
- [202] P. Hariharan, “Basics of interferometry”, Academic Press, **2012**.
- [203] J. E. Greivenkamp, “Generalized data reduction for heterodyne interferometry”, *Opt. Eng.* **1984**, *23*, 4.
- [204] P. Carré, “Installation et utilisation du comparateur photoélectrique et interférentiel du Bureau International des Poids et Mesures”, *Metrologia* **1966**, *2*, 13.
- [205] J. Li, L. Zhong, S. Liu, Y. Zhou, J. Xu, J. Tian, X. Lu, “An advanced phase retrieval algorithm in N-step phase-shifting interferometry with unknown phase shifts”, *Sci. Rep.* **2017**, *7*, 44307.
- [206] M. Kerker, D.-S. Wang, C. L. Giles, “Electromagnetic scattering by magnetic spheres”, *J. Opt. Soc. Am.* **1983**, *73*, 765.
- [207] R. Alaei, R. Filter, D. Lehr, F. Lederer, C. Rockstuhl, “A generalized Kerker condition for highly directive nanoantennas”, *Opt. Lett.* **2015**, *40*, 2645.

-
- [208] V. E. Babicheva, A. B. Evlyukhin, “Resonant lattice Kerker effect in metasurfaces with electric and magnetic optical responses”, *Laser Photonics Rev.* **2017**, *11*, 1700132.
- [209] R. Paniagua-Domínguez, Y. F. Yu, A. E. Miroschnichenko, L. A. Krivitsky, Y. H. Fu, V. Valuckas, L. Gonzaga, Y. T. Toh, A. Y. S. Kay, B. Luk’yanchuk, A. I. Kuznetsov, “Generalized Brewster effect in dielectric metasurfaces”, *Nat. Commun.* **2016**, *7*, 10362.
- [210] E. Pshenay-Severin, F. Setzpfandt, C. Helgert, U. Hübner, C. Menzel, A. Chipouline, C. Rockstuhl, A. Tünnermann, F. Lederer, T. Pertsch, “Experimental determination of the dispersion relation of light in metamaterials by white-light interferometry”, *J. Opt. Soc. Am. B* **2010**, *27*, 660.
- [211] E. Pshenay-Severin, M. Falkner, C. Helgert, T. Pertsch, “Ultra broadband phase measurements on nanostructured metasurfaces”, *Appl. Phys. Lett.* **2014**, *104*, 221906.
- [212] G. Strang, “Computational science and engineering”, Wellesley-Cambridge Press, **2007**.
- [213] P. Hansen, L. Hesselink, “Accurate adjoint design sensitivities for nano metal optics”, *Opt. Express* **2015**, *23*, 23899.
- [214] I. Fernandez-Corbaton, “Forward and backward helicity scattering coefficients for systems with discrete rotational symmetry”, *Opt. Express* **2013**, *21*, 29885.
- [215] F. Wyrowski, O. Bryngdahl, “Iterative Fourier-transform algorithm applied to computer holography”, *J. Opt. Soc. Am. A* **1988**, *5*, 1058.
- [216] F. W. J. Olver, A. B. Olde Daalhuis, D. W. Lozier, B. I. Schneider, R. F. Boisvert, C. W. Clark, B. R. Miller, B. V. Saunders, H. S. Cohl, M. A. McClain, “NIST Digital library of mathematical functions”, Mar. **2022**, <http://dlmf.nist.gov/> (Accessed: June 2022).
- [217] I. S. Gradshteyn, I. M. Ryzhik, “Table of integrals, series, and products”, Elsevier, **2014**.
- [218] L. E. Blumenson, “A derivation of n-dimensional spherical coordinates”, *Am. Math. Mon.* **1960**, *67*, 63.
- [219] J. K. Patel, “Handbook of the normal distribution”, M. Dekker, **1982**.
- [220] J. Mun, S. So, J. Jang, J. Rho, “Describing meta-atoms using the exact higher-order polarizability tensors”, *ACS Photonics* **2020**, *7*, 1153.
- [221] A. B. Evlyukhin, C. Reinhardt, A. Seidel, B. S. Luk’yanchuk, B. N. Chichkov, “Optical response features of Si-nanoparticle arrays”, *Phys. Rev. B* **2010**, *82*, 4.
- [222] K. Bartschat, “Computational atomic physics”, Springer, **1996**.